# SCALABLE PRODUCTION OF 3D MICROTISSUES USING NOVEL MICROFLUIDIC TECHNOLOGIES

S.R. van Loo

# SCALABLE PRODUCTION OF 3D MICROTISSUES USING NOVEL MICROFLUIDIC TECHNOLOGIES

Sebastiaan Robert van Loo

2024

**Graduation Committee**

| | |
|---|---|
| Prof. dr. J.C.H. Leijten (promotor) | University of Twente |
| Prof. dr. H.B.J. Karperien (promotor) | University of Twente |
| Prof. dr. ir. P. Jonkheijm | University of Twente |
| Prof. dr. P.C.J.J. Passier | University of Twente |
| Prof. dr. G.J.V.M. van Osch | Erasmus University Rotterdam |
| Prof. dr. G.J.C. Veenstra | Radboud University |
| Prof. dr. L. Moroni | Maastricht University |

**SCALABLE PRODUCTION OF 3D MICROTISSUES USING NOVEL MICROFLUIDIC TECHNOLOGIES**

Sebastiaan Robert van Loo, 2024

Cover design: Rutger Klunder

# SCALABLE PRODUCTION OF 3D MICROTISSUES USING NOVEL MICROFLUIDIC TECHNOLOGIES

**DISSERTATION**

to obtain
the degree of doctor at the University of Twente,
on the authority of the rector magnificus,
prof. dr. A. Veldkamp
on account of the decision of the graduation committee,
to be publicly defended
on Friday, February 16th 2024 at 16.45

by

**Sebastiaan Robert van Loo**

Born on January 13th, 1993
in Apeldoorn, The Netherlands

**This dissertation has been approved by:**

prof. dr. J.C.H. Leijten (promotor)
prof. dr. H.B.J. Karperien (promotor)

# Summary

Tissue engineering approaches are widely studied with the goal to replace or repair human tissues. However, while studies are often promising in a laboratory environment, there remain difficulties in the translation of laboratory-based studies towards clinical applications due to low in vivo efficiency and/or complex impractical procedures.An interesting strategy for improving therapy effectiveness is by evolving from conventional 2D cell culture to more biomimetic 3D cell culture approaches. While therapy efficiency can be greatly improved  using 3D cell culture, current 3D microtissue production techniques are often non-scalable batch processes, limiting clinical and industrial translation. A continuous production method is needed in order to improve the microtissue production rate and improve the feasibility of clinical application.

Microfluidics offers the possibility to evolve microtissue production towards a continuous process. Using conventional on-chip microfluidics, microtissues can be produced in a controlled and continuous manner by cell encapsulation in hollow microcapsules. However, conventional on-chip microfluidics offers challenges such as complex multistep processes, the use of potentially harmful oils and surfactants and often low throughputs, which are currently hampering widespread clinical and industrial translation of microfluidically produced microtissues. There is therefore a need to evolve microfluidics towards a clean, fast and single step scalable approach to fulfill the clinical requirements for tissue engineering approaches that take advantage of 3D microtissues.

This thesis describes multiple microfluidic solutions that focus on overcoming these challenges hampering the widespread clinical and industrial use of microtissues. A reusable, cleanroom-free, multifunctional microfluidic device is developed using standard cutting and abrasion technology, which allows the production of microtissue-laden microcapsules in a single step-manner. This on-chip process is then evolved towards an off-chip jetting approach which allows for the production of microtissue-laden microcapsules in an ultra-high throughput manner (>10 ml/min) without the need of potentially harmful oils and surfactants. This in-air microfluidic approach is also utilized for mass production of microtissues in larger compartmentalized hydrogels, which are used for the production of large clinical-sized tissues. A multitude of microtissues are formed using these described microfluidic technologies such as human mesenchymal stem cell spheroids, chondrocyte spheroids, fibroblast spheroids, cholangiocyte and cholangiocarcinoma organoids, lumen-forming embryoid bodies, contracting cardiospheres, and clinical sized cartilage tissues.

To summarize, this thesis introduces multiple microfluidic systems for scalable microcapsule and microtissue production with the aim to remove the hurdles towards clinical and industrial translation of 3D microtissues.

# Samenvatting

Weefselengineering wordt uitgebreid bestudeerd met als doel menselijke weefsels te vervangen of te herstellen. Hoewel onderzoeken vaak veelbelovend zijn in een laboratoriumomgeving, blijven er moeilijkheden bestaan bij de vertaling van op laboratorium gebaseerde onderzoeken naar klinische toepassingen door lage in vivo (in een levend organisme) -efficiëntie en/of complexe onpraktische procedures. Een interessante strategie om de effectiviteit van de therapie te verbeteren is door over te stappen van conventionele 2D-celkweek naar meer bio-mimetische 3D-celkweektechnieken. Hoewel de efficiëntie van de therapie kan worden verhoogd met behulp van 3D-celkweek zijn huidige technieken voor 3D-microweefselproductie vaak niet-schaalbare, meerstaps batchprocessen die klinische en industriële translatie limiteren. Een continue productiemethode is nodig om de productiesnelheid van microweefsels te verbeteren, waardoor de haalbaarheid van klinische toepassing zal worden verbeterd.

Microfluïdica biedt de mogelijkheid om microweefsel productie te evolueren naar een continu proces. Met behulp van conventionele op-chip microfluïdica kunnen microweefsels op een gecontroleerde, continue manier worden geproduceerd door celencapsulering in holle microcapsules. Echter, conventionele op-chip microfluïdica biedt uitdagingen zoals, onder andere, complexe multistaps processen, het gebruik van potentieel schadelijke oliën en oppervlakteactieve stoffen en vaak lage productie snelheden, welke momenteel brede klinische en industriële translatie van microfluïdisch geproduceerde microweefsels belemmeren. Er is daarom behoefte aan een evolutie van microfluïdica naar een schone, snelle en eenvoudige schaalbare aanpak om te voldoen aan de klinische eisen voor weefselengineering die gebruik maken van 3D-microweefsels.

Dit proefschrift beschrijft meerdere microfluïdische oplossingen die zich richten op deze uitdagingen die de brede klinische en industriële toepassing van microweefsels belemmeren. Een herbruikbaar, cleanroom-vrij, multifunctioneel microfluïdisch systeem is ontwikkeld met behulp van standaard snij- en schuurtechnologie, waardoor de productie van microweefsel-geladen microcapsules op een enkel-staps manier mogelijk is. Dit op-chip proces is vervolgens geëvolueerd naar een off-chip jetting-benadering, waardoor de productie van microweefsel-geladen microcapsules op een zeer hoge doorvoersnelheid (>10 ml/min) mogelijk is zonder de noodzaak tot gebruik van mogelijk schadelijke oliën en oppervlakteactieve stoffen. Deze in-air microfluïdische aanpak is ook gebruikt voor massaproductie van microweefsels in grote gecompartimentaliseerde hydrogels, die worden gebruikt voor de productie van weefsels van klinisch-relevante grote. Een veelvoud aan microweefsels zijn gevormd met behulp van deze beschreven microfluïdische technologieën, zoals menselijke mesenchymale stamcel-sferoïden, chondrocyte-sferoïden, fibroblast-sferoïden, cholangiocyten- en cholangiocarcinoom-organoïden, lumen-vormende embryoide-lichamen, samentrekkende cardiosferen, en kraakbeenweefsels van klinisch-relevante grote.
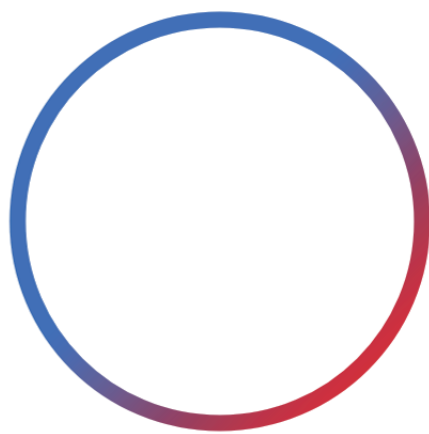
Samengevat introduceert dit proefschrift de meerdere microfluïdische systemen voor schaalbare productie van microcapsules en microweefsels, met als doel de obstakels voor klinische en industriële vertaling van 3D-microweefsels weg te nemen.

# Contents

# 1

## Introduction and Motivation

1

## Introduction

### 1.1.1 Tissue engineering

Tissue engineering is an interdisciplinary field that applies the principles of biology, chemistry, and engineering to fabricate biological tissue substitutes utilizing cells, materials, or a combination thereof. Tissue substitutes can be used for repairing or replacing tissues and organs, advancing drug screening capabilities, and enabling new insights into developmental and cellular biology.[1]

Typically, cells are acquired from a donor and cultured and multiplied using culture flasks. In these culture flasks cells are plated on a 2D plastic surface upon which cell culture medium is deposited. In this way, cells can multiply in a simple manner until sufficient cell quantities are acquired to perform desired experiments or therapies.

However, this conventional method of cell culture is artificial in its nature as it does not reflect the 3D *in vivo* environment. In the 3D *in vivo* environment, cells undergo intensive cell-cell contact, which is an important regulator of a plethora of intracellular functions. Besides cell-cell interactions, cells also adhere to their surrounding extracellular matrix. These adhesions are offered in a three-dimensional manner with low stiffnesses (kPa range), which is distinct form the x-y plane adhesions with high stiffness (GPa range) that are offered in plastic-adherent 2D cultures that associate with unnatural cell polarities. Furthermore, the 3D *in vivo* environment contains gradients of soluble factors, which do not occur in 2D culture.[2]

The artificial simplification of the before mentioned microenvironment in a 2D culture plastic environment alters the cell phenotype, resulting in impaired cell function.[3,4] While 2D cultured cells are useful for gaining basic knowledge on cell biology, the use of impaired behavior of cell sources are limiting the effectiveness of cell-based applications and obscures natural behaviors thus limiting clinical and industrial translation. There is therefore a need to advance cell culture towards biomimetic 3D environments, which can mimic the *in vivo* physiological conditions more closely and offer cell sources with less-impaired *in vivo*-like function.

A common method for 3D cell culture is the encapsulation of cells within hydrogels, which possesses high water content and aims to mimic matrix properties of our tissues.[5] The benefit of 3D hydrogel cultures is exemplified in that chondrocytes with 2D culture-induce impaired function are able to be restored in its functionality through culture in a 3D hydrogel environment.[6] Indeed, hydrogels have become a gold standard as a 3D cell culture environments. However, despite offering designer cell-matrix interactions, cell-laden hydrogels typically still only offer only limited cell-cell interaction as the cells are homogeneously dispersed throughout the 3D hydrogel and require both hydrogel remodeling and cellular migration to establish new cell-cell contacts. While hydrogels represent an important step towards more

biologically relevant 3D cell cultures, an approach with more biomimetic cell-cell and cell-matrix interactions has remained preferred.

## 1.1.2 Microtissues

The formation and culture of 3D microtissues offers an alternative 3D cell culture approach that is characterized by both cell-cell and cell-matrix interactions. In these microtissues, cells are aggregated together in single monolithic tissues. Dependent on the specialized cell type or mixture of cell types, a microenvironment can be created that more faithfully emulates the native microenvironment of natural tissues.[7–9]

Microtissues such as cellular spheroids and organoids have played an essential role in our comprehension of tissue development and homeostasis and represent an essential tool to understand cell-cell interdependence regarding biological variables such as viability, migration, and differentiation.[2,8,9] Spheroids are typically cellular aggregates a single type of specialized cells, while organoids are composed of multiple cell-type that could potentially have their origin from a single cell source (e.g., pluripotent stem cells).[10] While spheroids are often relatively homogeneous in nature, organoids can self-organize towards native-tissue like structures and therefore have an extra layer of complexity and are therefore argued to be more native-like for most tissue applications.[10–12]

The natural design of spheroids makes this culture technique a popular approach for a multitude of applications in tissue engineering and drug screening, which has yielded various important advances. For example, spheroids have been found to outperform 2D cultured cells for the formation of tissues such as cartilage[13–15], bone[16], and heart muscle[17], allow for the engineering of complex macroscopic tissue constructs[18–21], and have proven to facilitate drug target discovery[22–24]. The complexity of organoids provide the ability to closely study developmental biology and are widely studied for personalized drug screening[25–32].

## 1.1.3 Technological State of the Art

Despite the immense progress in the development of cell-based models, clinical and industrial translation of microtissues is currently hindered due to the limited scalability of the microtissue production processes. This scalability is important as target applications such as pharmacological screenings and cell-based therapeutical strategies require large amounts of microtissues. The existing technologies currently only offer low production rates at high microtissue quality (e.g., monodispersity) or high production rates at low microtissue quality. Moreover, all current techniques necessitate extensive manual labor, which associates with low cost-effectiveness, which limits clinical and industrial translation. Additionally, achieving consistently reproducibility at high production rates monodispersity is important when aiming for clinical or industrial use of microtissues owing to standardization benchmarks and quality assessments. Current microtissue

**1**

production processes are often limited in these aspects due to their reliance on batch production, which offer limited control or limited throughput in microtissue formation. Therefore, in order to unleash the clinical and industrial potential of microtissues, there is a unmet need for techniques offering scalable high quality microtissue production.
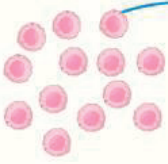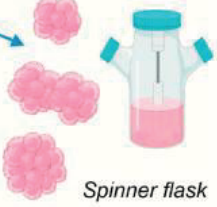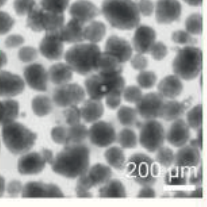
## 1.2 Microtissue Production Process

### 1.2.1 Batch Production

Conventionally, microtissues have been produced with batch processes such as suspension, microwell, or non-adherent plate cultures. Although these methods often associate with poorly controlled aggregate size and shape inhomogeneity, microtissue production in suspension cultures can be optimized by incorporating complementary rotation and spinning methods[33–35]. While large-scale bioreactors are being investigated and have shown to be successful in producing large amounts of microtissues, it is consistently reported that free-floating microtissues conventionally produced inside these bioreactors tend to fuse with each and thus results in uncontrolled final microtissue size (**Figure 1.1**)[36,37]. This may lead to highly variable biological performance of produced microtissues as it is well known that microtissue size is critical to its biological function[14,38]. Not surprisingly, tight control over biological performance, and by extension microtissue size, is highly desirable for clinical and industrial translation of microtissues[39].

In contrast, aqueous compartmentalization techniques such as hanging-drop cultures offer more control over the size distribution by preventing microtissue merging, with the added benefit that no specialized equipment or reagents are required[40,41]. However, this technique only offers very limited throughput as compared to other 3D culturing platforms. Alternatively, microwells, micropatterned gels, U-shaped chips, or microporous membranes have emerged as a valid batch-process technique to produce cell microtissues[42]. These platforms represent a minimal and simplistic approach, that offers accurate control over microtissue size and shape, substantially increased throughputs, and predictable spatial placement of microtissues. Specifically, cell-seeded microwell arrays have emerged as promising 3D substrates for the production of reproducible ce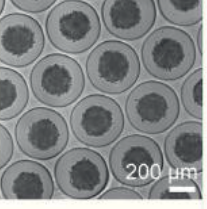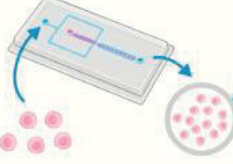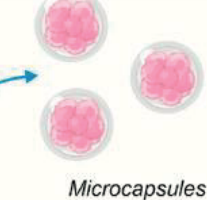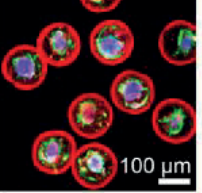ll aggregates in amounts that are readily suitable for the screening of a limited amounts of drugs[43–45] and performing of in vivo studies using small animal models[13,14]. However, although these conventional batch techniques produce hundreds to thousands of microtissues per batch, translation to the industrial/clinical setting of these technologies has been challenging[46].

In order to allow clinical and industrial translation of microtissues, requirements such as a high-throughput production process[47], minimal batch-to-batch variation[48] have to be met. Unfortunately, aforementioned conventional batch processes such as low-adherent culture plates[49–52], micropatterning[53,54], microwells[13,55–58], hanging-drop techniques[17,59–62], and bioreactors[36,37] do not comply with these requirements. There is therefore a need to go from a batch process towards a scalable, highly

**Figure 1.1. Microencapsulation is required to translate microtissues to industrial/clinical scale applications.** To expand cells into larger quantities and/or more complex modalities, encapsulation using continuous microfluidics provides an ideal balance between scalability and uniformity. Traditional methods to produce microtissues rely on the culture of cells without compartmentalization (e.g., in spinner flasks) or with batch compartmentalization (e.g., in microwells), leading to low uniformity due to fusion and low throughput, respectively. By compartmentalizing cells in microcapsules using high-throughput microfluidics, microtissues can be produced in large quantities while maintaining microtissue uniformity. Moreover, microtissues produced in this manner can still be cultured in large bioreactors due to the physical barrier provided by the (semi-permeable) microcapsule, preventing microtissue fusion. Figures adapted with permission from[37,63,64].

controlled continuous process as they have the inherent ability to offer greater throughputs.

## 1.2.2 Continuous production: Microfluidics

Microfluidics is extensively investigated due to its potential to revolutionize scalable continuous production processes of microtissues. Utilizing precise and efficient handling of fluids with predictable flow behavior, microfluidics can be used to produce micromaterials with controlled size, shape and composition in a high-throughput continuous manner. By compartmentalizing cells in these continuously produced micromaterials, it is possible to produce microtissues in a highly controlled manner, with minimal batch-to-batch variations and, most notably, in a scalable

**1**

manner, making microfluidics an attractive technology for the clinical and industrial translation of microtissues.

Microfluidic production of microtissues typically involves two critical steps: (1) dispersion of a liquid cell-laden particle precursor solution into discrete droplets; and (2) solidification of droplets through in situ crosslinking or precipitation. Droplets can be formed via patterning[65–68], molding on/in solid substrates[66], emulsification in an (immiscible) liquid[69–74], or atomization in a gas[75–80]. Here, emulsification (i.e., liquid-liquid) and atomization (i.e., liquid-air) are continuous droplet formation processes compatible with microfluidics with inherently high throughputs and therefore suitable for scalable production of microtissues.

Droplet emulsions are typically produced by flowing two immiscible fluids (i.e., a (cell-laden) water-phase and an oil-phase) in a coaxial[73,74], T-junction[71,72], or flow focusing[69,70] configuration (**Figure 1.2a**), which can be stabilized with surfactants[81]. The discrete aqueous droplets within the emulsion can be solidified into cell-laden micromaterials via a wide range of mechanisms including ionic-[82–84], enzymatic-[64], photo-[85–87], or thermal-crosslinking[88]. These cell-laden micromaterials can be cultured as individual living microtissues, but can also be assembled into clinically sized, modular, living microtissues.

The most intuitive form of microfluidically produced micromaterials is solid microspheres, where a polymer precursor solution is emulsified into droplets that are fully solidified[89–91]. The introduction of cells into the precursor solution results in either single-cell-laden solid microgels[85,89,92], or multiple-cell-laden solid microgels[90,91], which can in turn be used as building blocks for bottom-up engineered tissues. However, these solid microgel systems hinder cell-cell contact of encapsulated cells, which is known to be an important factor in the benefits of 3D cell culture[93]. Building on the principles utilized in creating solid microspheres, it is possible to create hollow, compartmentalized microgels by using, for example, multi-emulsions[94]. By introduction of cells in the hollow compartment of core-shell microgels, cells are encapsulated in a manner in which cell-cell contact is enabled, which allows for the formation of cellular spheroids and more complex organoids[64,95].

The most common method for continuous droplet formation for production of the aforementioned cell-laden micromaterials are operated in the dripping regime. These systems have been shown to be successful for the fabrication of microtissues at typically low production rates (< 1 ml/min)[96]. Jetting and spraying technologies allow for higher throughputs (up to 100 ml/min)[78], which makes them more suitable for scalable production of cell-laden microcapsules and microtissues[96] (**Figure 1.2a,b**). However, unassisted techniques such as air-induced spraying and electrospraying offer poor resolution control and result in polydisperse microparticle populations[97,98] (**Figure 1.2c**). Therefore, efforts have been made in order to achieve monodisperse microparticles in the jetting regime by for instance jet cutting or by applying microvibrations using piezoelectric elements in both liquid-liquid with vibrating jet technology[99–101] and liquid-air configurations in both inkjet and vibrating jet technology[102–104], and in the spraying regime by applying (submerged)

**1**
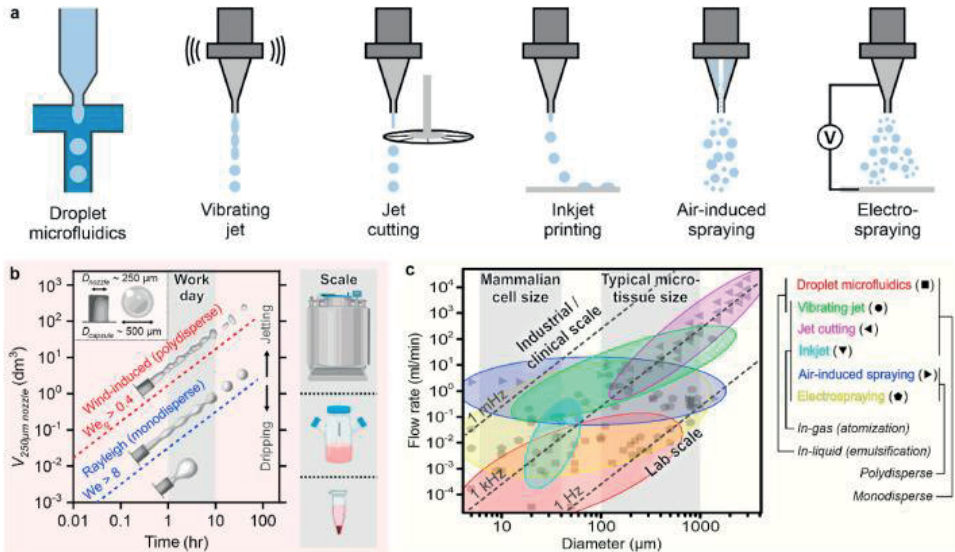
**Figure 1.2. Continuous microcapsule production methods and their potential for translation to clinical/industrial settings**. **a.** Schematic representation of various continuous production methods to produce (cell-laden) microcapsules. **b.** Typical throughputs of continuous production techniques calculated for varying regimes including from dripping; Weber number (We) < 8 to jetting (We > 8) into and from Rayleigh induced break up (gas Weber number (We$_g$) < 0.4) to wind-induced breakup (We$_g$ > 0.4). A capsule size of 500 µm is chosen for the calculations as a representative example. On the right y-axis, container sizes are indicated to illustrate the required time to fill a specific volume ranging from lab scale (Eppendorf tube) to industrial scale (bioreactor). **c.** Overview of various continuous production methods and their throughputs (flow rate) as a function of droplet size. Typical mammalian cell size and microtissue sizes are indicated to outline methods of interest. The indicated production regimes are based on data points obtained from the following references: droplet microfluidics[84,105–112], vibrating jet[113], jet cutting[103,114], inkjet[102,104,115], air-induced spraying[103,116–119], and electrospraying[103,120,121]. Figure adapted with permission from[122].

electromagnetic fields for both liquid-liquid electrospraying[123,124] and liquid-air electrospraying configurations[76,77,80].

In contrast to liquid-liquid, liquid-air systems such as sprays or droplets that fly in the air do neither require the use of a potentially sample contaminating immiscible phase (e.g., oil) or surfactants (e.g. amphiphiles) to form droplets while allowing for considerably higher production rates. However, the produced droplets only remain separated until they collide onto their receiving collector, or coalesce in-flight, which necessitates their in-flight stabilization using, for example, extremely rapid (milliseconds) crosslinking mechanisms. In practice, atomization is therefore almost exclusively combined with ionic crosslinking strategies such as alginate with divalent cations[78,79], rapid heating (i.e., spray drying) or cooling (i.e., spray freeze drying) strategies, which is in contrast with lower throughput systems which beside ionic crosslinking materials can utilize materials with slower crosslinking mechanisms such as enzymatic and photo crosslinking. Several complex micromaterial structures have been produced using in-air microfluidics, such as solid microgels, core-shell microgels, Janus micromaterials and microfiber structures[78,79]. Jetting technologies

are starting to emerge for microtissue production as well, but are as of yet associated with poor microtissue size control with low resolution, again limiting clinical and industrial translation[97,98].

## 1.3 Motivation: Challenges and aim of this thesis

### 1.3.1 Challenge: Towards Clinical and Industrial Translation of 3D Microtissues

Unleashing the clinical and industrial potential of microtissues is currently hindered by the limited scalability of microtissues production process. Target applications such as pharmacological screenings, cruelty-free meat production, and cell-based therapeutical strategies require large amounts of high quality microtissues in order to be of clinical or industrial use. While microfluidics offers scalable continuous microtissue production processes, it is clear that as of yet no perfect technology exists. Overall, it can be stated that the following requirements have to be met in order to truly allow clinical and industrial translation of microfluidically produced microtissues:

- Continuous process, since this allows for scalability and minimal batch-to-batch variation.
- High throughputs to be able to produce relevant quantities of microtissues.
- Viable cell encapsulation and microtissue formation (spheroids and organoids).
- A clean process without the use of potential harmful oils and surfactants.
- High control over produced microtissue size with high monodispersity and high resolution.
- No need for complex and costly cleanroom environments to produce the microfluidic setup. Off-the-shelve setups would be preferable.
- While single-purpose devices are the current standard, multi-purpose devices could allow for easier adaptation of microfluidic technologies.
- Simple one-step procedures would be preferable over multi-step procedures.

Although conventional production methods in the dripping regime allow for excellent control and monodisperse microparticle formation, their low production rates (< 1 ml/min)[96] are inhibitive for clinical and industrial translation (**Figure 1.2**). Hence, innovations such as parallelization are required in order to achieve commercially relevant throughputs[125–127]. Moreover, disadvantages of the single-use and enclosed nature of these systems limits their scalability for the production of microtissues[128]. These disadvantages include the need for advanced lithographic infrastructure to produce the microfluidic systems and their association with significant wastage of (e.g., clogged) microfluidic devices.

In comparison with these dripping regime chip-based strategies, newly upcoming jetting and spraying technologies overcome the throughput challenges, but are currently still associated with lower microtissue size control and resolution[75,97,98], again limiting clinical and industrial translation. While these technologies are already being used for simple microtissue production[75,97,98], there is as of yet still no proof-of-concept of jetting/spraying methods to produce more complex microtissues such as organoids. It is therefore clear that both on-chip dripping and in-air jetting possess inherent challenges that have to be met in order to allow true clinical and industrial translation of microtissues (**Table 1.1**).

**Table 1: Comparison of dripping and jetting/spraying regime technologies.**

|  | **Conventional on-chip dripping regime technologies**[69–74] | **Off-chip Jetting/spraying regime technologies**[75,78,79,97,98] |
|---|---|---|
| **Continuous process** | Yes | Yes |
| **Throughput** | Low (<1 ml/min) | High (1-100 ml/min) |
| **Spheroid production** | Yes | Yes |
| **Organoid production** | Yes | No |
| **Clean process** | Oils and surfactants needed | No oils and surfactants needed |
| **Control** | High | Low |
| **Microtissue monodispersity** | High | Dependent on throughput |
| **Microtissue resolution** | High | Low |
| **Cleanroom technology** | Yes | No |
| **Can be used multiple times** | No | Yes |
| **Multi-purpose** | No | Yes |
| **Single-step procedure** | No | Yes |

## 1.3.2 Aim of this Thesis

In brief, the aim of this thesis is to overcome the challenges accompanied with the use of the continuous microfluidics, which is anticipated to facilitate the clinical and industrial translation of 3D microtissues. As detailed in the introduction above, microfluidic systems in the dripping regime and the jetting/spraying regime both have their respective advantages and disadvantages. This thesis sets-out to introduce new microfluidic systems to realize the scalable production of microtissue in both the dripping and jetting/spraying regime to overcome the limiting disadvantages of each regime, while retaining their inherent advantages. Consequently, this thesis aims to contribute to the progress towards fulfilling the requirements necessary for the clinical and industrial translation of 3D microtissues.

### 1.3.3 Thesis Outline

In the current chapter, the reader is provided with an introduction on the benefits of 3D microtissue culture for, for instance, tissue engineering applications. Challenges concerning conventional cellular microtissue production techniques that hamper the widespread clinical and industrial translation of microtissues are highlighted. Based on this chapter, the argument is made that a clean, continuous production processes with high throughput is needed, and the benefits and disadvantages of current continuous microfluidic technologies are reviewed.

In chapter 2, a microfluidic manufacturing platform is presented that overcomes the before mentioned translational challenges for the use of microfluidic platforms in the dripping regime for continuous microtissue production. An on-the-fly exchangeable nozzle concept that operates in a transparent, 3D, and reusable microfluidic device produced without cleanroom technology is presented. This novel microfluidic platform allows for the controlled fabrication of multiple micromaterials such as solid and core-shell microspheres, microfibers, and Janus micromaterials.

In chapter 3, cellular spheroids or microaggregates, are produced utilizing the microfluidic platform described in chapter 2. Enzymatic outside-in crosslinking of (cell-laden) tyramine-conjugated polymer droplets enabled single-step cellular spheroid production with high cytocompatibility. The use of physically controlled enzymatic crosslinking process improved reproducibility, operational window, and throughput of cell-laden microcapsule formation.

In chapter 4, the production of organoids in a continuous manner is demonstrated. Produced intrahepatic cholangiocyte organoids are of similar quality compared to the golden standard batch process technique. The high quantity and the encapsulated nature allows for easy processing for scalable personalized drug screening.

In chapter 5, an innovative microfluidic system is presented that overcomes the before mentioned translational challenges for the use of microfluidics platforms in the jetting regime for continuous spheroid production. Specifically, In Air microfluidics is explored for ultra-high throughput production of human embryonic stem cell-laden microcapsules for continuous microtissue production in an oil-free, chip-free, jet-based manner. The microcapsules provided a lumenogenic microenvironment for undifferentiated pluripotent embryoid bodies, while myocardial differentiation enabled the formation of unparalleled amounts of functional (i.e., contracting) cardiospheres.

In chapter 6, the scalability of In Air microfluidic produced cellular spheroids is further highlighted through single step biofabrication of large *in situ* spheroid forming tissue constructs via the 3D printing of multi-compartmentalized hydrogels. Spheroid forming hydrogels with different complexities are achieved utilizing either handheld freeform bioprinting or 3D print technology. Due to the ultra-high spheroid

production rates it now becomes possible to produce clinical sized cellular cartilage tissues with excellent shape stability in a fast, clean and feasible manner.

In chapter 7, the future perspectives concerning microfluidic hollow micromaterials for high-throughput cellular microtissue formation are discussed. The in this thesis presented microfluidic systems are discussed and compared with each other with regards to multiple applications in the field of tissue engineering.

**1**

## References

1.    Langer, R. & Vacanti, J. P. Tissue Engineering. *Science (80-. ).* **260**, 920–926 (1993).
2.    Baker, B. M. & Chen, C. S. Deconstructing the third dimension – how 3D culture microenvironments alter cellular cues. *J. Cell Sci.* **125**, 3015 LP – 3024 (2012).
3.    VON DER MARK, K., GAUSS, V., VON DER MARK, H. & MÜLLER, P. Relationship between cell shape and type of collagen synthesised as chondrocytes lose their cartilage phenotype in culture. *Nature* **267**, 531–532 (1977).
4.    Petersen, O. W., Rønnov-Jessen, L., Howlett, A. R. & Bissell, M. J. Interaction with basement membrane serves to rapidly distinguish growth and differentiation pattern of normal and malignant human breast epithelial cells. *Proc. Natl. Acad. Sci. U. S. A.* **89**, 9064–9068 (1992).
5.    Mantha, S. *et al.* Smart Hydrogels in Tissue Engineering and Regenerative Medicine. *Mater. (Basel, Switzerland)* **12**, (2019).
6.    Benya, P. D. & Shaffer, J. D. Dedifferentiated chondrocytes reexpress the differentiated collagen phenotype when cultured in agarose gels. *Cell* **30**, 215–224 (1982).
7.    Edmondson, R., Broglie, J. J., Adcock, A. F. & Yang, L. Three-Dimensional Cell Culture Systems and Their Applications in Drug Discovery and Cell-Based Biosensors. *Assay Drug Dev. Technol.* **12**, 207–218 (2014).
8.    Shamir, E. R. & Ewald, A. J. Three-dimensional organotypic culture: experimental models of mammalian biology and disease. *Nat. Rev. Mol. Cell Biol.* **15**, 647 (2014).
9.    Fitzgerald, K. A., Malhotra, M., Curtin, C. M., O' Brien, F. J. & O' Driscoll, C. M. Life in 3D is never flat: 3D models to optimise drug delivery. *J. Control. Release* **215**, 39–54 (2015).
10.   Clevers, H. Modeling Development and Disease with Organoids. *Cell* **165**, 1586–1597 (2016).
11.   Lancaster, M. A. & Knoblich, J. A. Organogenesis in a dish: modeling development and disease using organoid technologies. *Science* **345**, 1247125 (2014).
12.   Dutta, D., Heo, I. & Clevers, H. Disease Modeling in Stem Cell-Derived 3D Organoid Systems. *Trends Mol. Med.* **23**, 393–410 (2017).
13.   Moreira Teixeira, L. S. *et al.* High throughput generated micro-aggregates of chondrocytes stimulate cartilage formation in vitro and in vivo. *Eur. Cell. Mater.* **23**, 387–399 (2012).
14.   Leijten, J. *et al.* Bioinspired seeding of biomaterials using three dimensional microtissues induces chondrogenic stem cell differentiation and cartilage formation under growth factor free conditions. *Sci. Rep.* **6**, 36011 (2016).
15.   Wolf, F. *et al.* Cartilage tissue engineering using pre-aggregated human articular chondrocytes. *Eur. Cell. Mater.* **16**, 92–99 (2008).
16.   Bolander, J. *et al.* Healing of a Large Long-Bone Defect through Serum-Free In-Vitro Priming of Human Periosteum-Derived Cells. *Stem Cell Reports* **8**, 758–772 (2017).
17.   Beauchamp, P. *et al.* Development and Characterization of a Scaffold-Free 3D Spheroid Model of Induced Pluripotent Stem Cell-Derived Human Cardiomyocytes. *Tissue Eng. - Part C Methods* **21**, 852–861 (2015).
18.   Vrij, E. *et al.* Directed Assembly and Development of Material-Free Tissues with Complex Architectures. *Adv. Mater.* **28**, 4032–4039 (2016).
19.   Rivron, N. C. *et al.* Tissue deformation spatially modulates VEGF signaling and angiogenesis. *Proc. Natl. Acad. Sci.* **109**, 6886–6891 (2012).
20.   Matsunaga, Y. T., Morimoto, Y. & Takeuchi, S. Molding Cell Beads for Rapid Construction of Macroscopic 3D Tissue Architecture. *Adv. Mater.* **23**, H90–H94 (2011).
21.   Lin, H., Li, Q. & Lei, Y. Three-dimensional tissues using human pluripotent stem cell spheroids as biofabrication building blocks. *Biofabrication* **9**, 25007 (2017).
22.   Langhans, S. A. Three-Dimensional in Vitro Cell Culture Models in Drug Discovery and Drug Repositioning. *Frontiers in Pharmacology* **9**, (2018).
23.   Thoma, C. R., Zimmermann, M., Agarkova, I., Kelm, J. M. & Krek, W. 3D cell culture systems modeling tumor growth determinants in cancer target discovery. *Adv. Drug Deliv. Rev.* **69**–**70**, 29–41 (2014).
24.   Hoffmann, O. I. *et al.* Impact of the spheroid model complexity on drug response. *J. Biotechnol.*

**205**, 14–23 (2015).

25. McCracken, K. W. *et al.* Modelling human development and disease in pluripotent stem-cell-derived gastric organoids. *Nature* **516**, 400–404 (2014).

26. Lancaster, M. A. *et al.* Cerebral organoids model human brain development and microcephaly. *Nature* **501**, 373–379 (2013).

27. Gao, D. *et al.* Organoid cultures derived from patients with advanced prostate cancer. *Cell* **159**, 176–187 (2014).

28. Eiraku, M. & Sasai, Y. Self-formation of layered neural structures in three-dimensional culture of ES cells. *Curr. Opin. Neurobiol.* **22**, 768–777 (2012).

29. Drakhlis, L. *et al.* Human heart-forming organoids recapitulate early heart and foregut development. *Nat. Biotechnol.* **39**, 737–746 (2021).

30. Dekkers, J. F. *et al.* Characterizing responses to CFTR-modulating drugs using rectal organoids derived from subjects with cystic fibrosis. *Sci. Transl. Med.* **8**, 344ra84 (2016).

31. Richards, D. J. *et al.* Human cardiac organoids for the modelling of myocardial infarction and drug cardiotoxicity. *Nat. Biomed. Eng.* **4**, 446–462 (2020).

32. Sahu, S. & Sharan, S. K. Translating Embryogenesis to Generate Organoids: Novel Approaches to Personalized Medicine. *iScience* **23**, 101485 (2020).

33. Li, X. *et al.* A fully defined static suspension culture system for large-scale human embryonic stem cell production. *Cell Death Dis.* **9**, 892 (2018).

34. Hammond, T. G. *et al.* Cell spinpods are a simple inexpensive suspension culture device to deliver fluid shear stress to renal proximal tubular cells. *Sci. Rep.* **11**, 21296 (2021).

35. Carpenedo, R. L., Sargent, C. Y. & McDevitt, T. C. Rotary Suspension Culture Enhances the Efficiency, Yield, and Homogeneity of Embryoid Body Differentiation. *Stem Cells* **25**, 2224–2234 (2007).

36. Sumi, S. *et al.* A multiple-funnels cell culture insert for the scale-up production of uniform cell spheroids. *Regen. Ther.* **7**, 52–60 (2017).

37. Allen, L. M., Matyas, J., Ungrin, M., Hart, D. A. & Sen, A. Serum-Free Culture of Human Mesenchymal Stem Cell Aggregates in Suspension Bioreactors for Tissue Engineering Applications. *Stem Cells Int.* **2019**, 4607461 (2019).

38. Lee, J., Lee, S., Kim, S. M. & Shin, H. Size-controlled human adipose-derived stem cell spheroids hybridized with single-segmented nanofibers and their effect on viability and stem cell differentiation. *Biomater. Res.* **25**, 14 (2021).

39. Mehta, G., Hsiao, A. Y., Ingram, M., Luker, G. D. & Takayama, S. Opportunities and challenges for use of tumor spheroids as models to test drug delivery and efficacy. *J. Control. release Off. J. Control. Release Soc.* **164**, 192–204 (2012).

40. Wang, S. *et al.* Application of Hanging Drop Technique for Kidney Tissue Culture. *Kidney Blood Press. Res.* **42**, 220–231 (2017).

41. Frey, O., Misun, P. M., Fluri, D. A., Hengstler, J. G. & Hierlemann, A. Reconfigurable microfluidic hanging drop network for multi-tissue interaction and analysis. *Nat. Commun.* **5**, 4250 (2014).

42. Moshksayan, K. *et al.* Spheroids-on-a-chip: Recent advances and design considerations in microfluidic platforms for spheroid formation and culture. *Sensors Actuators B Chem.* **263**, 151–176 (2018).

43. Mosaad, E. O., Chambers, K. F., Futrega, K., Clements, J. A. & Doran, M. R. The Microwell-mesh: A high-throughput 3D prostate cancer spheroid and drug-testing platform. *Sci. Rep.* **8**, 253 (2018).

44. Wu, K.-W., Kuo, C.-T. & Tu, T.-Y. A Highly Reproducible Micro U-Well Array Plate Facilitating High-Throughput Tumor Spheroid Culture and Drug Assessment. *Glob. Challenges* **5**, 2000056 (2021).

45. Yeh, S. I. *et al.* Development of a simple static microwell array with uniform cell seeding and a chemical concentration gradient. *Microfluid. Nanofluidics* **21**, 80 (2017).

46. Gonzalez-Fernandez, T., Tenorio, A. J. & Leach, J. K. Three-Dimensional Printed Stamps for the Fabrication of Patterned Microwells and High-Throughput Production of Homogeneous Cell Spheroids. *3D Print. Addit. Manuf.* **7**, 139–147 (2020).

47. Menasché, P. Cell therapy trials for heart regeneration — lessons learned and future directions. *Nat. Rev. Cardiol.* **15**, 659–671 (2018).

48. de Souza, N. Organoid variability examined. *Nat. Methods* **14**, 655 (2017).

49. Sutherland, R. M., Inch, W. R., McCredie, J. A. & Kruuv, J. A Multi-component Radiation Survival Curve Using an in Vitro Tumour Model. *Int. J. Radiat. Biol. Relat. Stud. Physics, Chem. Med.* **18**, 491–495 (1970).

50. Li, X., Ootani, A. & Kuo, C. An Air–Liquid Interface Culture System for 3D Organoid Culture of Diverse Primary Gastrointestinal Tissues BT - Gastrointestinal Physiology and Diseases: Methods and Protocols. in (ed. Ivanov, A. I.) 33–40 (Springer New York, 2016). doi:10.1007/978-1-4939-3603-8_4

51. Kelm, J. M., Timmins, N. E., Brown, C. J., Fussenegger, M. & Nielsen, L. K. Method for generation of homogeneous multicellular tumor spheroids applicable to a wide variety of cell types. *Biotechnol. Bioeng.* **83**, 173–180 (2003).

52. Yuhas, J. M., Li, A. P., Martinez, A. O. & Ladman, A. J. A Simplified Method for Production and Growth of Multicellular Tumor Spheroids. *Cancer Res.* **37**, 3639–3643 (1977).

1

53. Nelson, C. M., VanDuijn, M. M., Inman, J. L., Fletcher, D. A. & Bissell, M. J. Tissue geometry determines sites of mammary branching morphogenesis in organotypic cultures. *Science (80-. ).* **314**, 298–300 (2006).

54. Warmflash, A., Sorre, B., Etoc, F., Siggia, E. D. & Brivanlou, A. H. A method to recapitulate early embryonic spatial patterning in human embryonic stem cells. *Nat. Methods* **11**, 847–854 (2014).

55. Hu, Y. *et al.* Lung cancer organoids analyzed on microwell arrays predict drug responses of patients within a week. *Nat. Commun.* **12**, 2581 (2021).

56. Branco, M. A. *et al.* Transcriptomic analysis of 3D Cardiac Differentiation of Human Induced Pluripotent Stem Cells Reveals Faster Cardiomyocyte Maturation Compared to 2D Culture. *Sci. Rep.* **9**, (2019).

57. Rivron, N. C. *et al.* Blastocyst-like structures generated solely from stem cells. *Nature* **557**, 106–111 (2018).

58. Sozen, B. *et al.* Self-assembly of embryonic and two extra-embryonic stem cell types into gastrulating embryo-like structures. *Nat. Cell Biol.* **20**, 979–989 (2018).

59. Kuo, C.-T. *et al.* Three-dimensional spheroid culture targeting versatile tissue bioassays using a PDMS-based hanging drop array. *Sci. Rep.* **7**, 4363 (2017).

60. Tung, Y.-C. *et al.* High-throughput 3D spheroid culture and drug testing using a 384 hanging drop array. *Analyst* **136**, 473–478 (2011).

61. Hsiao, A. Y. *et al.* Micro-ring structures stabilize microdroplets to enable long term spheroid culture in 384 hanging drop array plates. *Biomed. Microdevices* **14**, 313–323 (2012).

62. Lin, B. *et al.* Surface Tension Guided Hanging-Drop: Producing Controllable 3D Spheroid of High-Passaged Human Dermal Papilla Cells and Forming Inductive Microtissues for Hair-Follicle Regeneration. *ACS Appl. Mater. Interfaces* **8**, 5906–5916 (2016).

63. Girgin, M. U., Broguiere, N., Mattolini, L. & Lutolf, M. P. Gastruloids generated without exogenous Wnt activation develop anterior neural tissues. *Stem cell reports* **16**, 1143–1155 (2021).

64. van Loo, B. *et al.* Enzymatic outside-in cross-linking enables single-step microcapsule production for high-throughput three-dimensional cell microaggregate formation. *Mater. Today Bio* **6**, 100047 (2020).

65. Feng, W., Li, L., Du, X., Welle, A. & Levkin, P. A. Single-Step Fabrication of High-Density Microdroplet Arrays of Low-Surface-Tension Liquids. *Adv. Mater.* **28**, 3202–3208 (2016).

66. Jackman, R. J., Duffy, D. C., Ostuni, E., Willmore, N. D. & Whitesides, G. M. Fabricating Large Arrays of Microwells with Arbitrary Dimensions and Filling Them Using Discontinuous Dewetting. *Anal. Chem.* **70**, 2280–2287 (1998).

67. Kobaku, S. P. R., Kota, A. K., Lee, D. H., Mabry, J. M. & Tuteja, A. Patterned Superomniphobic–Superomniphilic Surfaces: Templates for Site-Selective Self-Assembly. *Angew. Chemie Int. Ed.* **51**, 10109–10113 (2012).

68. Debuisson, D., Senez, V. & Arscott, S. SU-8 micropatterning for microfluidic droplet and microparticle focusing. *J. Micromechanics Microengineering* **21**, 65011 (2011).

69. Anna, S. L., Bontoux, N. & Stone, H. A. Formation of dispersions using "flow focusing" in microchannels. *Appl. Phys. Lett.* **82**, 364–366 (2003).

70. Theberge, A. B. *et al.* Microdroplets in Microfluidics: An Evolving Platform for Discoveries in Chemistry and Biology. *Angew. Chemie Int. Ed.* **49**, 5846–5868 (2010).

71. Nisisako, T., Torii, T. & Higuchi, T. Droplet formation in a microchannel network. *Lab Chip* **2**, 24–26 (2002).

72. Garstecki, P., Fuerstman, M. J., Stone, H. A. & Whitesides, G. M. Formation of droplets and bubbles in a microfluidic T-junction—scaling and mechanism of break-up. *Lab Chip* **6**, 437–446 (2006).

73. Cramer, C., Fischer, P. & Windhab, E. J. Drop formation in a co-flowing ambient fluid. *Chem. Eng. Sci.* **59**, 3045–3058 (2004).

74. Tran, T. M., Cater, S. & Abate, A. R. Coaxial flow focusing in poly(dimethylsiloxane) microfluidic devices. *Biomicrofluidics* **8**, 16502 (2014).

75. Doméjean, H. *et al.* Controlled production of sub-millimeter liquid core hydrogel capsules for parallelized 3D cell culture. *Lab Chip* **17**, 110–119 (2017).

76. Zhao, S. *et al.* Coaxial electrospray of liquid core-hydrogel shell microcapsules for encapsulation and miniaturized 3D culture of pluripotent stem cells. *Integr. Biol. (Camb).* **6**, 874–884 (2014).

77. Song, Y., Chan, Y. K., Ma, Q., Liu, Z. & Shum, H. C. All-Aqueous Electrosprayed Emulsion for Templated Fabrication of Cytocompatible Microcapsules. *ACS Appl. Mater. Interfaces* **7**, 13925–13933 (2015).

78. Visser, C. W., Kamperman, T., Karbaat, L. P., Lohse, D. & Karperien, M. In-air microfluidics enables rapid fabrication of emulsions, suspensions, and 3D modular (bio)materials. *Sci. Adv.* **4**, eaao1175 (2023).

79. Kamperman, T., Trikalitis, V. D., Karperien, M., Visser, C. W. & Leijten, J. Ultrahigh-Throughput Production of Monodisperse and Multifunctional Janus Microparticles Using in-Air Microfluidics. *ACS Appl. Mater. Interfaces* **10**, 23433–23438 (2018).

80. Braghirolli, D. I. *et al.* Bio-electrospraying of human mesenchymal stem cells: An alternative for tissue engineering. *Biomicrofluidics* **7**, 44130 (2013).

81. Baret, J.-C. Surfactants in droplet-based microfluidics. *Lab Chip* **12**, 422–433 (2012).
82. Tan, W.-H. & Takeuchi, S. Monodisperse Alginate Hydrogel Microbeads for Cell Encapsulation. *Adv. Mater.* **19**, 2696–2701 (2007).
83. Lim, F. & Sun, A. M. Microencapsulated Islets as Bioartificial Endocrine Pancreas. *Science (80-. ).* **210**, 908–910 (1980).
84. Utech, S. *et al.* Microfluidic Generation of Monodisperse, Structurally Homogeneous Alginate Microgels for Cell Encapsulation and 3D Cell Culture. *Adv. Healthc. Mater.* **4**, 1628–1633 (2015).
85. Kamperman, T. *et al.* Single Cell Microgel Based Modular Bioinks for Uncoupled Cellular Micro- and Macroenvironments. *Adv. Healthc. Mater.* **6**, 1600913 (2017).
86. Kamperman, T. *et al.* On-the-fly exchangeable microfluidic nozzles for facile production of various monodisperse micromaterials. *Lab Chip* **19**, 1977–1984 (2019).
87. Wang, S. *et al.* An in-situ photocrosslinking microfluidic technique to generate non-spherical, cytocompatible, degradable, monodisperse alginate microgels for chondrocyte encapsulation. *Biomicrofluidics* **12**, 14106 (2018).
88. Flueckiger, J. & Cheung, K. C. Microfluidic System for Controlled Gelation of a Thermally Reversible Hydrogel. *IEEE Trans. Biomed. Circuits Syst.* **3**, 195–201 (2009).
89. Kamperman, T., Henke, S., Visser, C. W., Karperien, M. & Leijten, J. Centering Single Cells in Microgels via Delayed Crosslinking Supports Long-Term 3D Culture by Preventing Cell Escape. *Small* **13**, 1–10 (2017).
90. Henke, S. *et al.* Enzymatic Crosslinking of Polymer Conjugates is Superior over Ionic or UV Crosslinking for the On-Chip Production of Cell-Laden Microgels. *Macromol. Biosci.* 1524–1532 (2016). doi:10.1002/mabi.201600174
91. Ma, T., Gao, X., Dong, H., He, H. & Cao, X. High-throughput generation of hyaluronic acid microgels via microfluidics-assisted enzymatic crosslinking and/or Diels–Alder click chemistry for cell encapsulation and delivery. *Appl. Mater. Today* **9**, 49–59 (2017).
92. Kamperman, T. *et al.* Tethering Cells via Enzymatic Oxidative Crosslinking Enables Mechanotransduction in Non-Cell-Adhesive Materials. *Adv. Mater.* **33**, 2102660 (2021).
93. Mueller, M., Rasoulinejad, S., Garg, S. & Wegner, S. V. The Importance of Cell–Cell Interaction Dynamics in Bottom-Up Tissue Engineering: Concepts of Colloidal Self-Assembly in the Fabrication of Multicellular Architectures. *Nano Lett.* **20**, 2257–2263 (2020).
94. Chu, L.-Y., Utada, A. S., Shah, R. K., Kim, J.-W. & Weitz, D. A. Controllable Monodisperse Multiple Emulsions. *Angew. Chemie Int. Ed.* **46**, 8970–8974 (2007).
95. Agarwal, P. *et al.* One-step microfluidic generation of pre-hatching embryo-like core-shell microcapsules for miniaturized 3D culture of pluripotent stem cells. *Lab Chip* **13**, 4525–4533 (2013).
96. Utada, A. S., Fernandez-Nieves, A., Stone, H. A. & Weitz, D. A. Dripping to Jetting Transitions in Coflowing Liquid Streams. *Phys. Rev. Lett.* **99**, 94502 (2007).
97. Alessandri, K. *et al.* A 3D printed microfluidic device for production of functionalized hydrogel microcapsules for culture and differentiation of human Neuronal Stem Cells (hNSC). *Lab Chip* **16**, 1593–1604 (2016).
98. Alessandri, K. *et al.* Cellular capsules as a tool for multicellular spheroid production and for investigating the mechanics of tumor progression in vitro. *Proc. Natl. Acad. Sci. U. S. A.* **110**, 14843–14848 (2013).
99. Ziemecka, I. *et al.* Monodisperse hydrogel microspheres by forced droplet formation in aqueous two-phase systems. *Lab Chip* **11**, 620–624 (2011).
100. Yin, Z., Huang, Z., Lin, X., Gao, X. & Bao, F. Droplet Generation in a Flow-Focusing Microfluidic Device with External Mechanical Vibration. *Micromachines* **11**, (2020).
101. Bransky, A., Korin, N., Khoury, M. & Levenberg, S. A microfluidic droplet generator based on a piezoelectric actuator. *Lab Chip* **9**, 516–520 (2009).
102. Nakamura, M. *et al.* Biocompatible Inkjet Printing Technique for Designed Seeding of Individual Living Cells. *Tissue Eng.* **11**, 1658–1666 (2005).
103. Prüsse, U. *et al.* Comparison of different technologies for alginate beads production. *Chem. Pap.* **62**, 364–374 (2008).
104. Xu, T., Kincaid, H., Atala, A. & Yoo, J. J. High-Throughput Production of Single-Cell Microparticles Using an Inkjet Printing Technology. *J. Manuf. Sci. Eng.* **130**, (2008).
105. Zhang, H. *et al.* Microfluidic Production of Biopolymer Microcapsules with Controlled Morphology. *J. Am. Chem. Soc.* **128**, 12205–12210 (2006).
106. Tumarkin, E. *et al.* High-throughput combinatorial cell co-culture using microfluidics. *Integr. Biol.* **3**, 653–662 (2011).
107. Liu, K., Ding, H.-J., Liu, J., Chen, Y. & Zhao, X.-Z. Shape-Controlled Production of Biodegradable Calcium Alginate Gel Microparticles Using a Novel Microfluidic Device. *Langmuir* **22**, 9453–9457 (2006).
108. Lin, Y.-S., Yang, C.-H., Hsu, Y.-Y. & Hsieh, C.-L. Microfluidic synthesis of tail-shaped alginate microparticles using slow sedimentation. *Electrophoresis* **34**, 425–431 (2013).
109. Kemna, E. W. M. *et al.* High-yield cell ordering and deterministic cell-in-droplet encapsulation using Dean flow in a curved microchannel. *Lab Chip* **12**, 2881–2887 (2012).

110. Femmer, T. *et al.* High-Throughput Generation of Emulsions and Microgels in Parallelized Microfluidic Drop-Makers Prepared by Rapid Prototyping. *ACS Appl. Mater. Interfaces* **7**, 12635–12638 (2015).

111. Dendukuri, D. & Doyle, P. S. The Synthesis and Assembly of Polymeric Microparticles Using Microfluidics. *Adv. Mater.* **21**, 4071–4086 (2009).

112. Yobas, L., Martens, S., Ong, W.-L. & Ranganathan, N. High-performance flow-focusing geometry for spontaneous generation of monodispersed droplets. *Lab Chip* **6**, 1073–1079 (2006).

113. Visser, C. W., Kamperman, T., Karbaat, L. P., Lohse, D. & Karperien, M. In-air microfluidics enables rapid fabrication of emulsions, suspensions, and 3D modular (bio)materials. *Sci. Adv.* **4**, (2018).

114. Prüße, U., Dalluhn, J., Breford, J. & Vorlop, K.-D. Production of Spherical Beads by JetCutting. *Chem. Eng. Technol.* **23**, 1105–1110 (2000).

115. Wijshoff, H. The dynamics of the piezo inkjet printhead operation. *Phys. Rep.* **491**, 77–177 (2010).

116. Kwok, K. K., Groves, M. J. & Burgess, D. J. Production of 5–15 μm Diameter Alginate-Polylysine Microcapsules by an Air-Atomization Technique. *Pharm. Res.* **8**, 341–344 (1991).

117. Cui, J.-H., Goh, J.-S., Park, S.-Y., Kim, P.-H. & Lee, B.-J. Preparation and Physical Characterization of Alginate Microparticles Using Air Atomization Method. *Drug Dev. Ind. Pharm.* **27**, 309–319 (2001).

118. Strasdat, B. & Bunjes, H. Incorporation of lipid nanoparticles into calcium alginate beads and characterization of the encapsulated particles by differential scanning calorimetry. *Food Hydrocoll.* **30**, 567–575 (2013).

119. Hendriks, J. *et al.* Optimizing cell viability in droplet-based cell deposition. *Sci. Rep.* **5**, 11304 (2015).

120. Gañán-Calvo, A. M., Dávila, J. & Barrero, A. Current and droplet size in the electrospraying of liquids. Scaling laws. *J. Aerosol Sci.* **28**, 249–275 (1997).

121. Jaworek, A. Electrostatic micro- and nanoencapsulation and electroemulsification: A brief review. *J. Microencapsul.* **25**, 443–468 (2008).

122. Kamperman, T., Karperien, M., Le Gac, S. & Leijten, J. Single-Cell Microgels: Technology, Challenges, and Applications. *Trends Biotechnol.* **36**, 850–865 (2018).

123. Marín, Á. G., Loscertales, I. G. & Barrero, A. Surface tension effects on submerged electrosprays. *Biomicrofluidics* **6**, 44104 (2012).

124. Young, C. J., Poole-Warren, L. A. & Martens, P. J. Combining submerged electrospray and UV photopolymerization for production of synthetic hydrogel microspheres for cell encapsulation. *Biotechnol. Bioeng.* **109**, 1561–1570 (2012).

125. Nisisako, T. & Torii, T. Microfluidic large-scale integration on a chip for mass production of monodisperse droplets and particles. *Lab Chip* **8**, 287–293 (2008).

126. Yadavali, S., Jeong, H.-H., Lee, D. & Issadore, D. Silicon and glass very large scale microfluidic droplet integration for terascale generation of polymer microparticles. *Nat. Commun.* **9**, 1222 (2018).

127. Kamperman, T. *et al.* Engineering 3D parallelized microfluidic droplet generators with equal flow profiles by computational fluid dynamics and stereolithographic printing. *Lab Chip* **20**, 490–495 (2020).

128. Schot, M., Araújo-Gomes, N., van Loo, B., Kamperman, T. & Leijten, J. Scalable fabrication, compartmentalization and applications of living microtissues. *Bioact. Mater.* **19**, 392–405 (2023).

**1**
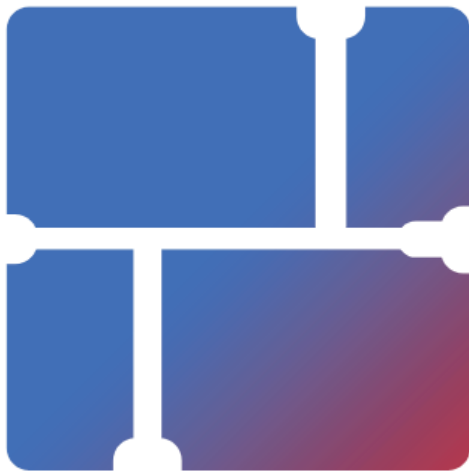
# 2

## On-the-fly Exchangeable Microfluidic Nozzles for Facile Production of Various Monodisperse Micromaterial

Microfluidic manufacturing platforms have advanced the production of monodisperse, shape-controlled, and chemically defined micromaterials. However, conventional microfabrication platforms are typically designed and fabricated as single-purpose and single-use tools, which limits their efficiency, versatility, and overall potential. We here present an on-the-fly exchangeable nozzle concept that operates in a transparent, 3D, and reusable microfluidic device produced without cleanroom technology. The facile exchange and repositioning of the nozzles readily enables the production of monodisperse water-in-oil and oil-in-water emulsions, solid and core–shell microspheres, microfibers, and even Janus type micromaterials with controlled diameters ranging from 10 to 1000 μm using a single microfluidic device.

Bas van Loo[†], Tom Kamperman[†], Melvin Gurian, Sieger Henke, Marcel Karperien, and Jeroen Leijten.
[†] Authors contributed equally to this work.
Contribution BvL: experimental design, experimental performance, data interpretation and manuscript writing.

## 2.1 Introduction

Microfluidic devices offer predictable (i.e., laminar) flow behaviour, in-line manipulation, and monitoring of liquids.[1] This control over liquids has enabled the production of micromaterials with controlled size, shape, and composition.[2–4] Microfluidic devices are typically produced as channels that are permanently formed and/or enclosed within glass or transparent polymer using a covalent bonding strategy such as plasma bonding, gluing, or fusing via partial melting or dissolving.[5,6] The non-reversible nature of these conventional microfluidic device fabrication methods limits their use to a single specific application. In particular, device dimensions and surface wetting properties need to be optimized per application, with little to no flexibility for efficient adaptation to other applications.[7,8] Conventional microfluidic devices are also inefficient during design optimization strategies, as their non-adaptable nature hampers swift iterations towards a functional device. On top, conventional microdevices are considered as single-use disposables. Cleaning difficulties of permanently bonded devices contributes to significant wastage of (e.g., clogged) chips, which is highly cost-inefficient considering the high-end materials, skilled personnel, and advanced lithographic infrastructure that are typically required for manufacturing of microfluidic devices. These limitations have jointly been hampering the rapid and widespread adoption of microfluidic technologies into other scientific disciplines as well as translation into clinical and industrial applications.[9,10]

Opportunely, microfluidic devices with on-demand adaptable channels represent a straightforward flexible solution to expand the versatility and efficiency of microfluidic devices. Reusable 'off-the-shelf' microfluidic devices made from plastic parts and steel needles have been explored to this end. These devices have been successfully used for flow focusing applications,[11] generation and splitting of water-in-oil (W/O) droplets,[12,13] and liposome generation.[14] However, the nontransparent nature of current devices impaired the direct monitoring that is required for controlled droplet formation and manipulation processes. Nozzle positioning has, for example, a major effect on the droplet size.[15] Furthermore, microfluidic device transparency is critical for the on-chip photocrosslinking of various polymers.[16] The pressing need for on-the-fly adoptable microfluidic devices is furthermore reflected by the recent development of several modular microfluidic systems.[17–20] Regardless of their promise, current adaptable microfluidic devices are not yet readily compatible with the production of solid micromaterials.

In this work, we demonstrate the fabrication of monodisperse micrometer-sized droplets, beads, and fibers using a fully transparent multifunctional 3D microfluidic device with exchangeable nozzles. The microfluidic device was manufactured without cleanroom technology and could be configured on-the-fly to operate in a T-junction, coaxial flow, and flow focusing manner. Combining this multifunctional microfluidic production platform with various classes of in situ crosslinkable polymers
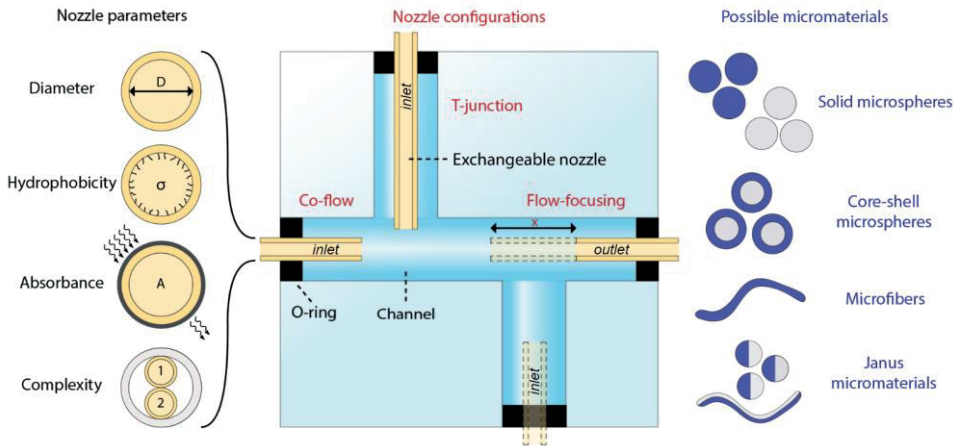
**Figure 2.1. Schematic concept of exchangeable nozzles within a multifunctional 3D microfluidic device for versatile monodisperse micromaterials production.** Sealed connections between the device, tubing, and nozzles enable the on-the-fly exchange of nozzles. This allows for the on-demand switching between nozzles with different diameters, hydrophobicity, absorbance, and complexity. Furthermore, the nozzle placement can be temporally controlled to switch between T-junction, co-flow, and flow-focusing configurations. The multifunctional nature of this microfluidic device enables facile tuning towards the fabrication of various micromaterials including microspheres and microfibers.

enabled the straightforward micromanufacturing of myriad micromaterials with controlled size, shape, composition, and complexity (**Figure. 2.1**).

## 2.2 Materials and Methods

### 2.2.1 Materials

Polymethylmethacrylate (PMMA) and O-rings (Viton, #1: inner diameter 0.74 mm, outer diameter 2.78 mm, #2: inner diameter 1.07 mm, outer diameter 3.61 mm) were provided by the University of Twente. Fluorinated ethylene propylene tubing (FEP, inner diameter 500 µm, outer diameter 1/16'') was purchased from IDEX Health & Science. Polyimide-coated fused silica capillaries (TSP type, various inner diameters, outer diameter 360 µm) were purchased from Polymicro Technologies. Borosilicate capillaries (inner diameter 700 µm, outer diameter 870 µm were purchased from CM Scientific. Quick-set epoxy adhesive (RS 850-956) was purchased from RS Components. Polydimethylsiloxane (PDMS, Sylgard 184) was purchased from Dow Corning. Silicone tubing (inner diameter 310 µm, outer diameter 640 µm) was purchased from Helix Medical. Abrasive (Cif) was purchased from Unilever. Fluorinated silane (Aquapel) was purchased from Vulcavite. Hexadecane, Span 80, sodium dodecyl sulphate (SDS), phosphate-buffered saline (PBS), horseradish peroxidase (HRP; type IV), $H_2O_2$ (with inhibitor), acetic acid, polyethylene glycol diacrylate (PEGDA; 575 Da), 2- Hydroxy-4'-(2-hydroxyethoxy)-2-methylpropiophenone (I2959), polyethylene glycol (PEG; 12 kDa), $CaCl_2$, and

dextran-FITC (2000 kDa) were purchased from Sigma-Aldrich / Merck. Dextran-tyramine (Dex-TA; ~20 kDa) with 15 tyramine moieties per 100 repetitive units was synthesized as previously described.35 Alginate (80 to 120 cP) and catalase (from bovine liver) were purchased from Wako Chemicals. CaCO3 nanoparticles were purchased from Nanomaterials Technology. Red fluorescent particles (0.6 µm polystyrene Fluoro-Max) were purchased from Thermo Fisher Scientific.

### 2.2.1 Microfluidic device production and operation

The microfluidic device was designed using SolidWorks software and manufactured by cutting using a belt saw and drilling using a column drill. Drilling was done at a relatively low rotational frequency (<1000 rpm) in the presence of concentrated soap (Dreft, Procter & Gamble) solution to prevent cracking of the PMMA. To recover transparency, the inside of the device was polished by pulling a knotted cotton thread soaked in abrasive through the center channel. Nozzles were manufactured by hand-cutting fused silica or borosilicate capillaries using a tungsten-carbide glass cutting knife. Optionally, the nozzles were chemically or physically modified as follows. Hydrophobic nozzles were produced by oxygen plasma treatment (PDC-002, Harrick Plasma) for 1 minute at (21% $O_2$, 30 W, 0.2 mbar) followed by coating with fluorinated silane solution. UV-transparent nozzles were produced by flaming off the fused silica capillary's polyimide coating. Absorbance of 365 nm light was measured using an optical power meter (1916-C with 818-ST-UV sensor, Newport). The nozzles were either glued into tubing using quick-set epoxy adhesive or inserted in tightly fitting silicone tubing that self-sealed to the nozzle through hydrophobic interactions. Multi-bore nozzles were fabricated by gluing multiple fused silica capillaries into a borosilicate capillary using PDMS. Tubing and nozzles were sealed to the microfluidic device using tight-fitting O-rings. Tubing was connected to syringes (Gastight, Hamilton) that were controlled by low-pressure syringe pumps (neMESYS, Cetoni). On-the-fly nozzle exchange was performed by sequentially pausing the syringe pump, pulling out the original nozzle, inserting a distinct nozzle, starting the syringe pump, and recalibrating the flow rate to obtain a Capillary number at which stable droplet production was achieved. For droplet production, typical dispersed flow rates for the 75, 200, and 700 µm nozzles were 5, 30, and 200 µl/min, respectively. Total flow rates can be calculated from the capillary numbers as plotted in Figure 3.

### 2.2.2 Micromaterial production:

To produce microemulsions, water or water with 5% (w/v) Dex-TA was emulsified in hexadecane with 1% (w/v) Span 80 using a pristine or hydrophobic fused silica nozzle in T-junction, coaxial flow, or flow focusing configuration. Alternatively, hexadecane was emulsified in water with 1% (w/v) SDS using a pristine or hydrophobic fused silica nozzle in flow focusing configuration. To produce all-aqueous two-phase flows, water with 1% (w/v) alginate was injected in water with 30% (w/v) PEG using a combination of a pristine fused silica nozzle (inlet) in combination with a borosilicate glass nozzle in coaxial flow and flow focusing

configuration, respectively. To produce solid Dex-TA microspheres, 5% (w/v) Dex-TA and 25 U/ml HRP in PBS was emulsified in hexadecane with 1% (w/v) Span 80 using a hydrophobic fused silica nozzle in flow focusing configuration connected to a silicone tubing. The silicone tubing was submerged in 30% (w/w) $H_2O_2$, which diffused through the silicone and the oil phase into the Dex-TA precursor microemulsion, thereby inducing the enzymatic crosslinking of the tyramine-conjugated polymer to yield Dex-TA microspheres, as previously described.[21] To produce core-shell Dex-TA microspheres, the protocol for solid Dex-TA microspheres was used, but with addition of 83000 U/ml catalase to the hydrogel precursor solution. To produce PEGDA microspheres, 25% (v/v) PEGDA and 0.25% (w/v) I2959 in water was emulsified in hexadecane with 1% (w/v) Span 80 using a hydrophobic polyimide-coated fused silica nozzle in flow focusing configuration connected to a silicone tubing. The microfluidic device was placed under a UV light source (365 nm, ~50 mW/cm$^2$; LC8 Lightningcure L9588, Hamamatsu), enabling the on-chip photocrosslinking of the microemulsion into PEGDA microspheres. Emulsions were broken by multiple hexadecane washes (i.e., to reduce the concentration of Span 80 surfactant) in the presence of water or PBS. To produce alginate microparticles, a solution of 0.5% (w/v) alginate and 1 g/l $CaCO_3$ in water was emulsified in a 50/50 hexadecane/mineral oil mixture with 1% (w/v) Span 80, and subsequently injected in the same oil solution supplemented with 2 µl/ml acetic acid using a combination of a pristine fused silica nozzle and a hydrophobic fused silica nozzle in coaxial and flow focusing configuration. Diffusion of the acid through the intermediate oil flow enabled controlled dissolution of the $CaCO_3$ into $Ca^{2+}$ that induced the ionic crosslinking of alginate. To produce alginate microfibers, water with 1% (w/v) alginate was injected in water with 30% (w/v) PEG, which was focused by a flow of water with 30% (w/v) PEG and 100 mM $CaCl_2$ using a combination of a pristine fused silica nozzle (inlet) in combination with a borosilicate glass nozzle in coaxial flow and flow focusing configuration, respectively. Diffusion of the $Ca^{2+}$ ions through the intermediate PEG flow enabled controlled ionic crosslinking of the alginate, resulting in smooth alginate microfibers. Replacing the single-core inlet nozzle by a multi-core inlet nozzle enabled the formation of a multimaterial Janus type alginate microfiber.

## 2.2.3 Staining, visualization, and image analysis

On-chip multiphase flows were visualized using a stereomicroscope setup (Nikon SMZ800 equipped with Leica DFC300 FX camera). Collected micromaterials were imaged using standard phase contrast microscopy. Alginate microfibers were stained by adding fluorescent particles and/or dextran-FITC and visualized using fluorescence microscopy (EVOS FL, Thermo Fisher Scientific). Size distribution analysis of droplets and particles was done using ImageJ software. The droplet production rate ($f_{droplet}$) in Hz was determined from a microscopic timelapse recording of the droplet generator.

## 2.2.4 Statistics

All droplet diameters were determined from at least 30, 30, and 5 samples for the 75 µm, 200 µm, and 700 µm nozzles, respectively, and were reported as the average ± standard deviation or as a histogram with the coefficient of variation (CV = standard deviation / average). The relative transmissions in Figure 4e and Figure S1 were determined from at least three measurements and reported as the average ± standard deviation. The droplet frequencies in Figure 4g for t=0-30 s were determined from 3 samples and for t=30-300 s from one sample, and (where possible) reported as the average ± standard deviation. All micromaterials diameters were determined based on at least 12 samples and reported as a histogram with the CV. All linear regression analyses were performed in OriginPro2016.

### 2.2.5 Schematics

All graphs were made using OriginPro 2016 software. All schematics were made using Solid Works 2017, Adobe Illustrator CS6, and Microsoft PowerPoint software CorelDRAW X7 software.

## 2.3 Results and Discussion

### 2.3.1 Design and fabrication of multifunctional microfluidic device with exchangeable nozzles

The microfluidic device design consisted of a center channel and two side channels that essentially formed two serially connected T-junctions (**Figure 2.2a**). This design was compatible with the user-defined assembly of a variety of nozzles into the three most used nozzle configurations, namely T-junction, coaxial flow, and flow focusing, and thus acted as a universal platform for the fabrication of a variety of micromaterials. The device was fabricated in polymethylmethacrylate (PMMA), as this material is transparent, widely available, and biocompatible, but also mechanically robust while easily adaptable using standard cutting and abrasion methods. Channels were micromilled in the presence of concentrated soap solution that acted as a coolant and prevented heat induced cracking of the PMMA, resulting in precise and highly reproducible microfluidic device fabrication (**Figure 2.2b**).[22] Channels were measured to be 0.9 mm in diameter, which allowed for the insertion of a wide variety of commercially available capillaries. The device inlets and outlets consisted of 1.6 mm wide holes that enabled the insertion of 1/16" (i.e., ~1.59 mm) outer diameter tubing, which is commonly used in microfluidic applications. After micromilling, the transparency of the center channel was increased by >2.5-fold through abrasion using a knotted thread and polish (**Figure 2.2c and S2.1**). Fused silica capillaries were selected as nozzles, as they are readily available with inner diameters ranging from 2 ± 1 to 700 ± 10 µm and outer diameters ranging from 90 ± 6 to 850 ± 20 µm, thus nearly spanning the entire micrometer regime. Furthermore, fused silica capillaries can be pre-coated with, for example, a
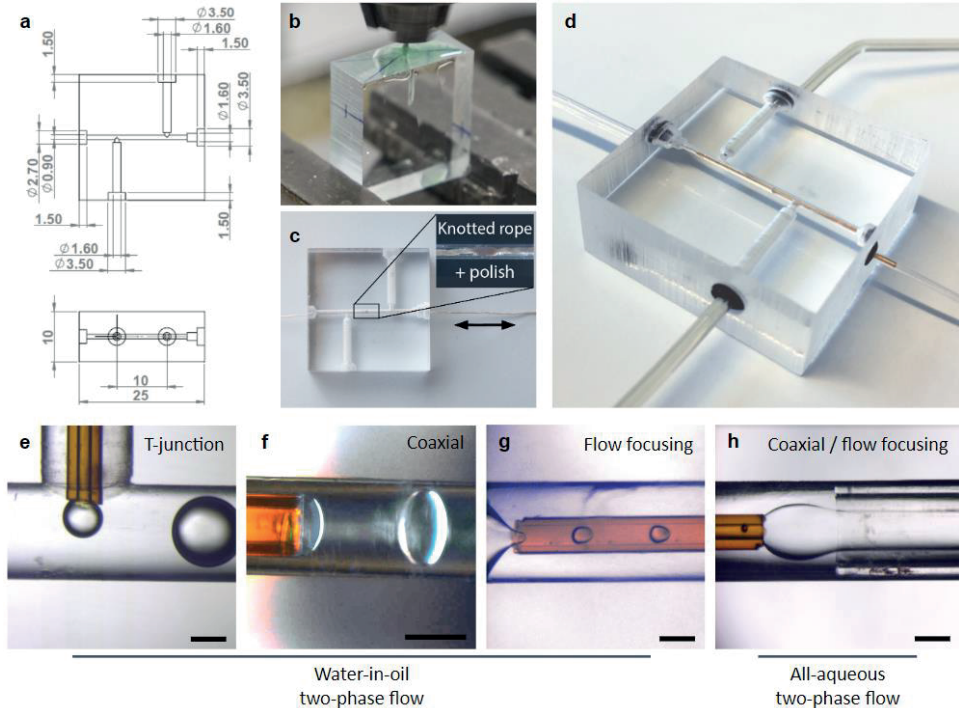
**Figure 2.2. Engineering a microfluidic device with exchangeable nozzles.** (a) Computer-aided design (CAD) of the multifunctional 3D microfluidic device. The device was fabricated in PMMA using standard (b) cutting (i.e., sawing and drilling) and (c) abrasion (i.e., polishing) techniques. (d) Tubing and nozzles were sealed to the PMMA device using rubber O-rings that auto-aligned inserted nozzles. The adaptable nature of the microfluidic device enabled the straightforward generation of water-in-oil and all-aqueous two-phase flows using (e) T-junction, (f) coaxial, (g) flow focusing, and (h) coaxial / flow focusing nozzle configurations. Scale bars indicate 350 μm.

polyimide layer to improve durability and provide UV-protection. Exchangeable nozzles were fabricated by gluing a fused silica capillary into 1/16″ tubing (i.e., for T-junction and coaxial flow) or by inserting it into silicone tubing (i.e., for flow focusing), which acted as outlet tubing (**Figure S2.2**). The transparent and semi-permeable nature of the silicone outlet tubing enabled in-line monitoring, photo-irradiation of the flowing materials, and diffusion-based delivery of small molecules such as reactive hydrogen peroxide to induce or control chemical reactions.[23] The microfluidic device inlets and outlets were partially widened to hold elastic O-rings that formed liquid tight seals and ensured centering of the exchangeable nozzles and/or tubing in the microfluidic device's channels. Optionally, a borosilicate glass capillary spacer was used to enable sealing of the silicone tubing into the device. As expected, the PMMA device and rubber O-rings enabled the facile connection of tubing and fused silica nozzles in various configurations, as confirmed by successful demonstration of W/O emulsification using T-junction, coaxial, and flow focusing modes, as well as the formation of a focused aqueous two-phase coaxial flow (**Figure 2.2d–h**).

**2**

## 2.3.2 Expanding the microfluidic droplet production regime using exchangeable nozzles

Microfluidic droplets can be leveraged as templates for the controlled fabrication of microspheres.[24] The size of such microfluidic-generated materials strongly depends on the nozzle width, the flow ratio of the dispersed and continuous phases, and (for droplet and particles) the capillary number of the continuous phase $Ca = \eta_c v_c / \gamma$, where $\eta_c$ is the viscosity of the continuous phase, $v_c$ is the average velocity of the continuous phase, and $\gamma$ is the interfacial tension between the dispersed and continuous phases.[25] Tuning the flow rates of the dispersed and continuous phases is thus a potent strategy to control the droplet size. However, stable production of monodisperse droplets is limited to the squeezing and dripping regimes.[26,27] Therefore, droplet size can only be fine-tuned within a relatively small regime, typically limited to an order of magnitude in diameter.[28–30] We hypothesized that the production regime of a single microfluidic device could be significantly expanded in terms of droplet size by controlling the nozzle diameter on-the-fly. To demonstrate this, our microfluidic device was successively equipped with three different nozzles ($D_{nozzle}$ = 75, 200, 700 µm) during a continuous experiment. On-the-fly exchange of the nozzles readily enabled the production of monodisperse microdroplets with diameters exceeding an order of magnitude, as demonstrated by emulsification of water in a 1% Span 80 containing hexadecane solution (**Figure. 2.3a**). The rubber O-rings enabled facile and swift nozzle exchange by guaranteeing instant sealing and auto-centering of the nozzles, which allowed for the switching between different droplet size production regimes in less than a minute (F**igure 2.3b, Movie S2.1**). As expected, with every nozzle the droplet size could be fine-tuned by controlling the capillary number. Specifically, increasing the capillary number by increasing the continuous phase flow rate resulted in reduction of the droplet size (**Figure 2.3c–e**). Furthermore, the exact position of nozzles significantly affected the droplet production regime, which could be uniquely simultaneously fine-tuned and monitored through on-the-fly repositioning of the nozzles within our transparent microfluidic device (**Fig. S3**). Microdroplets over the entire size regime were characterized by a monodisperse size distribution as confirmed by coefficients of variation CV < 5%. (**Fig. 3f**). Similar size control was achieved with all-aqueous two-phase co-flows, which is key for the microfabrication of, for example, microfibers with controlled diameters (**Fig. S4**).

## 2.3.3 Chemical and physical nozzle tuning for micromaterial production

Controlling microfluidic nozzle wettability is key to achieve successful generation of droplets. The fused silica nozzles used in this work contain siloxane bridges that bind water via chemisorption to form silanol groups, which adsorb polar compounds
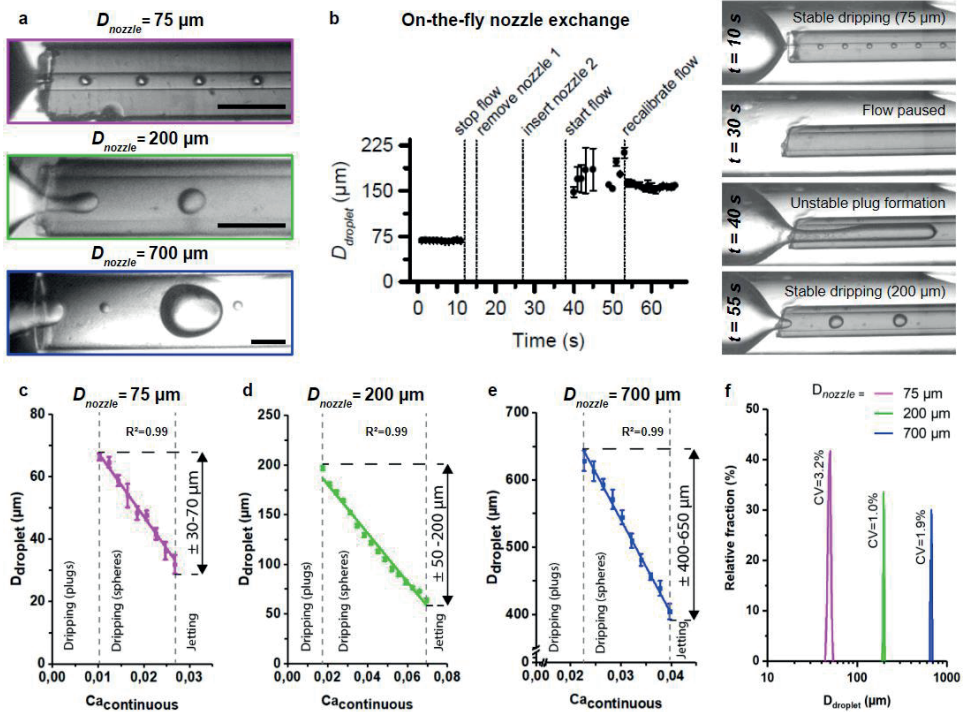
**Figure 2.3. Characterization of microdroplets production with on-the-fly nozzle exchange.** (a) Coaxially flowing water in oil using nozzles with different inner diameters enabled the formation of droplets with diameters spanning more than an order of magnitude. (b) Switching between two stable droplet production size regimes by exchanging the nozzle was achieved within one minute. (c–e) Per nozzle, the droplet size was fine-tuned by tuning the flow rate of the continuous phase and thereby the capillary number. (f) All nozzles were compatible with the production of monodisperse (CV < 5%) droplets. Scale bars indicate 350 µm.

including water molecules allowing it to act as a hydrophilic surface.[31] Consequently, fused silica is inherently hydrophilic in its native state, which was confirmed by contact angle measurements ($\theta = 27 \pm 5°$) using the capillary rise method (**Figure 2.4a**).[32] Fused silica nozzles were therefore readily compatible with production of oil-in-water (O/W) emulsions such as hexadecane in a 1% sodium dodecyl sulphate (SDS) containing water solution. However, the nozzles' hydrophilic nature also hampered the stable formation of W/O emulsions. Moreover, aqueous wetting of fused silica was exacerbated in the presence of water-soluble polymers such as dextran, which hindered the formation of microsphere precursor droplets (**Figure 2.4a**). To enable polymer microsphere formation through microfluidic emulsion templating using our microfluidic platform, fused silica nozzles were deactivated by chemically coupling fluorinated silane to the available silanol groups (**Figure 2.4b**). The fluorinated fused silica nozzles were significantly less hydrophilic ($\theta = 52 \pm 2°$) than pristine fused silica nozzles and were
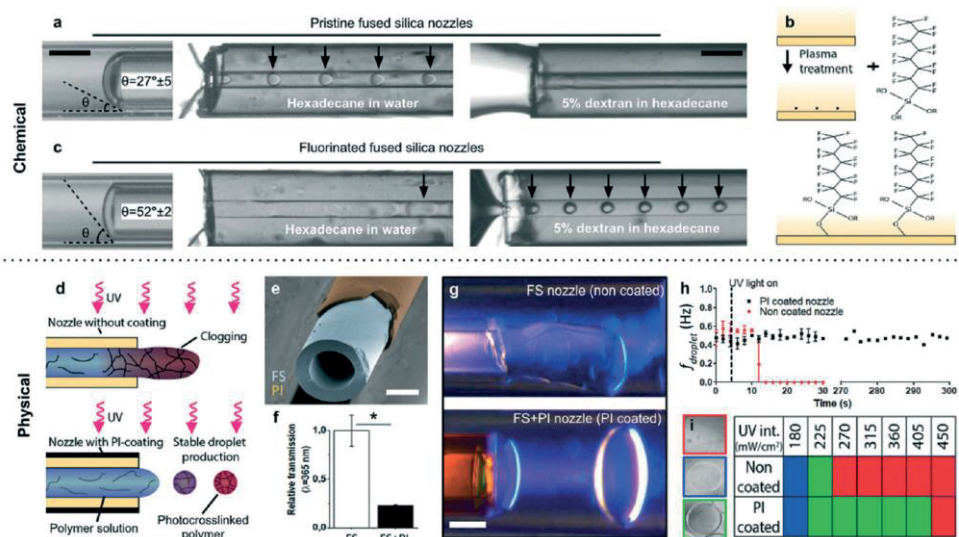
**Figure 2.4. Chemical and physical optimization of exchangeable nozzles to enable the processing of polymers solutions.** (a) Pristine fused silica nozzles were hydrophilic, which readily enabled the formation of O/W emulsions, but impaired the formation of polymer-laden W/O emulsions such as dextran solution in hexadecane. (b) Chemically treating the fused silica with fluorinated silane (c) resulted in less hydrophilic nozzles that were compatible with the production of polymer-laden W/O emulsions. (d and e) Alternatively, fused silica (FS) nozzles could be physically modified with a UV-protective polyimide (PI) coating to prevent nozzle clogging during processing of photocrosslinkable polymers. (f) The polyimide coating reduced the relative UV transmission by more than 4-fold and enabled (g and h) continuous and stable production of photocrosslinked polymer microspheres under UV irradiation by preventing nozzle clogging (i) over a wide range of UV intensities as compared to non-coated nozzles. Nozzle clogging, incomplete PEGDA photocrosslinking, and complete PEGDA photocrosslinking are indicated with red, blue, and green squares, respectively. Scale bars indicate 200 μm. * indicates significance with p < 0.01.

proven to be compatible with the W/O emulsification of 5% dextran solution (**Figure 2.4c**). Besides chemical modification, exchangeable nozzles could also be physically optimized for the processing of polymer precursor solutions. For example, selectively modifying the optical properties of nozzles offers the possibility to optimize the microfluidic system for processing photocrosslinkable polymers. An ongoing challenge in on-chip photocrosslinking strategies is microfluidic channel clogging due to photocrosslinking of polymers by strayed UV light.[33–35] To overcome UV-induced clogging, we exchanged the conventionally used glass or borosilicate capillaries by polyimide-coated fused silica capillaries that acted as UV-protected nozzles (**Figure 2.4d,e**). Absorption spectrometry confirmed that polyimide-coated nozzles absorbed significantly more UV light (λ = 365 nm) than pristine fused silica nozzles (**Fig. 4f**). Advantageously, the polyimide-coated nozzles enabled the continuous and stable on-chip production of polyethylene glycol diacrylate (PEGDA) microdroplets in the presence of UV light, while the pristine nozzle mainly associated with clogging (**Figure 2.4g,h**). Moreover, the use of polyimide-coated

nozzles significantly widened the operational window for the production of completely photocrosslinked PEGDA microspheres (**Figure 2.4i**).

## 2.3.4 On-demand fabrication of a wide variety of micromaterials

To demonstrate the universal nature of the microfluidic device, it was combined with a variety of nozzles in different configurations to produce various different classes of micromaterials. To this end, several combinations of distinct (i) polymers (natural and synthetic); (ii) crosslinking mechanisms (chemical and physical); (iii) morphologies (spherical and fiber); and (iv) complexities (isotropic solid, Janus solid, and core–shell) were produced (**Figure 2.5**). A flow focusing configuration of a fluorinated fused silica nozzle enabled the stable production of isotropic solid and core–shell dextran microspheres (**Figure 2.5a**). Specifically, a mixture of dextran–tyramine (Dex–TA) and horseradish peroxidase (HRP) was emulsified with hexadecane that contained Span 80, and flown through a semi-permeable silicone tubing that was submerged in H2O2. Diffusion-based supplementation of H2O2 into the polymer droplets initiated the enzymatic crosslinking of the tyramine moieties resulting in the formation of monodisperse dextran microspheres.[23] Core–shell microspheres were produced by adding the H2O2 consuming enzyme catalase to the polymer solution,[36,37] which prevented crosslinking of the droplet center. A polyimide-coated capillary in coaxial flow mode was used as a UV-shielded nozzle to demonstrate the stable production of photocrosslinked PEGDA microspheres (**Figure 2.5b**). Acrylate moieties of PEGDA can be covalently coupled through free-radical polymerization upon irradiation of a photoinitiator such as 2-hydroxy-4'-(2-hydroxyethoxy)-2- methylpropiophenone (I2959). Straightforward W/O emulsification of a PEGDA and I2959 containing solution using a UV-irradiated coaxial flow nozzle resulted in the stable and clog-free formation of monodisperse PEGDA microspheres. A combination of coaxial flow and flow focusing was used to generate alginate microspheres (**Figure 2.5c**). Specifically, this nozzle arrangement enabled the formation of a laminar three-layered co-flow of CaCO3 nanoparticles in alginate, Span 80 in hexadecane, and Span 80 and acetic acid in hexadecane. The alginate droplets were ionically crosslinked using divalent calcium cations, which were released upon the acid-induced dissolution of CaCO3.[38] The middle oil flow acted as a liquid barrier between the CaCO3 and the acetic acid, which prevented clogging of the microfluidic device. Alginate microfibers were produced using the same nozzle configuration by co-flowing solutions of alginate, polyethylene glycol (PEG) and CaCl2. The middle PEG flow acted as a liquid barrier between the divalent calcium ions and the alginate, which prevented microfluidic device clogging. Inserting a multibore nozzle readily provided an extra level of complexity, as demonstrated by the production of Janus type microfibers (**Figure 2.5c and S2.5**).

**2**
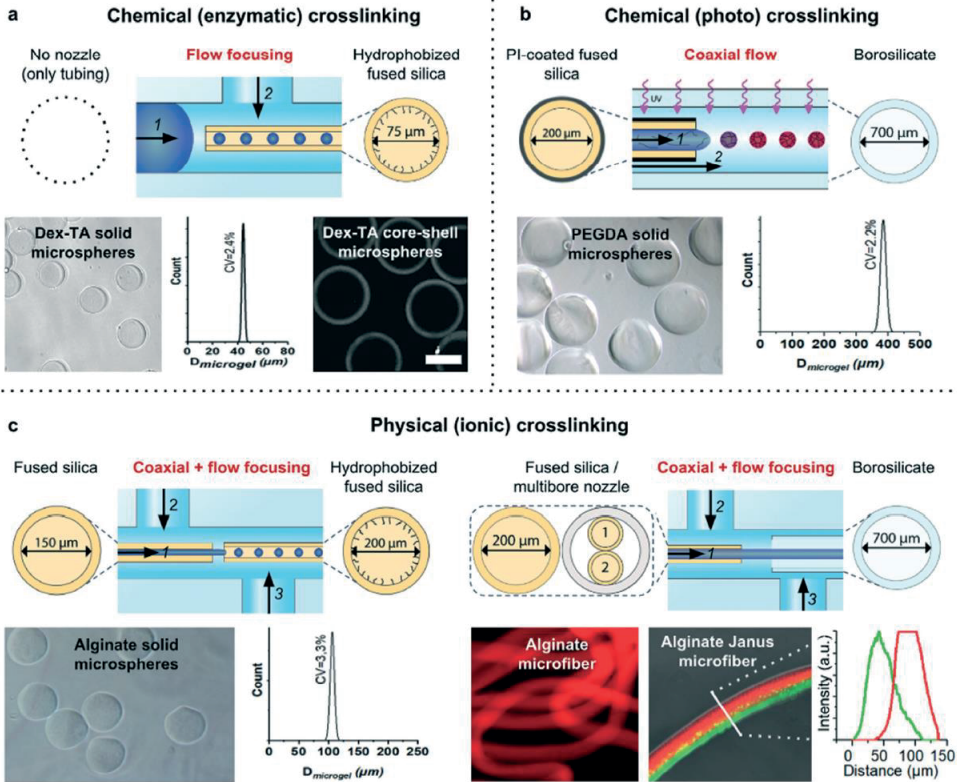


**Figure 2.5. Various examples of monodisperse micromaterials produced using the multifunctional 3D microfluidic device with different optimized nozzle configurations.** (a) Flow focusing an enzymatically crosslinkable Dex-TA and HRP containing solution (*1*) in hexadecane with Span 80 (2) using a fluorinated fused silica nozzle enabled the production of monodisperse solid dextran-based microspheres. (b) Coaxially flowing a photocrosslinkable PEGDA and I2959 containing solution (*1*) in hexadecane with Span 80 (2) using a polyimide-coated fused silica nozzle enabled the production of monodisperse PEG-based microspheres. (c) Focusing coaxially flowing alginate (*1*) and PEG (2) containing solutions in a calcium chloride containing solution (3) using a combination of single and multi-bore capillaries enabled the production of monodisperse simple and Janus type microfibers. Scale bar indicates 200 µm.

## 2.4 Conclusion

Microfluidic platforms for micromaterial production typically rely on permanently enclosed single-use devices with limited operational freedom. In this work, we presented a re-usable microfluidic device with disposable exchangeable nozzles, which enabled the controlled production of a wide variety of micromaterials. The device was fabricated in PMMA using standard cutting and abrasion methods that do not demand clean-room infrastructures. Reversible exchange of the tubing, nozzles, and device was enabled in a rapid, straightforward, and leak-free manner. On-the-fly nozzle exchange enabled the continuous generation of microfluidic

products over a size range far exceeding the production limits of conventional fixed nozzle devices. Furthermore, nozzle exchange readily allowed for the tuning of surface wetting properties, which enabled swift iteration towards functional micromanufacturing protocols for various materials. Various nozzle configurations, materials, and crosslinking methods have been efficiently and successfully combined to demonstrate the user-friendly manufacturing of a myriad of micromaterials. Uniquely, equipping the transparent microfluidic device with UV-protected nozzles enabled the stable production of photocrosslinked polymer microspheres. The universal and facile nature of the transparent 3D microfluidic device with exchangeable nozzles is expected to facilitate the controlled production of micromaterials, thereby aiding its widespread adoption.

**2**

## 2.5 Supplementary Information
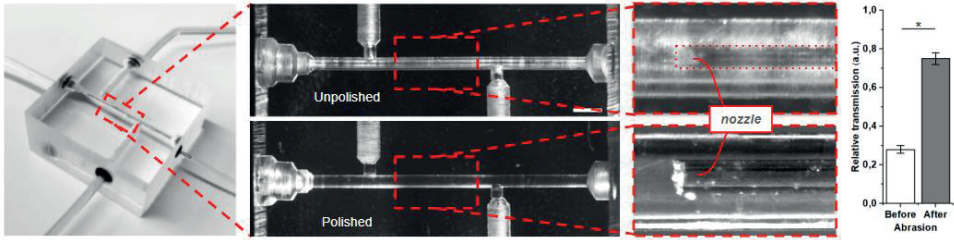


**Figure S2.1. Polished versus unpolished microfluidic device channels.** Polishing the PMMA based microfluidic device significantly increased transparency, thereby enabling on-chip monitoring of the nozzle. * indicates significance with $p < 0.0001$.
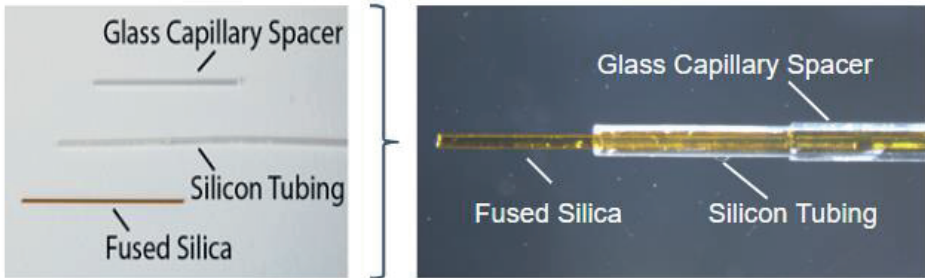


**Figure S2.2. Exchangeable nozzle assembly.** To assemble an exchangeable nozzle, a fused silica capillary was inserted into a silicone tubing, which was inserted into a glass capillary spacer.
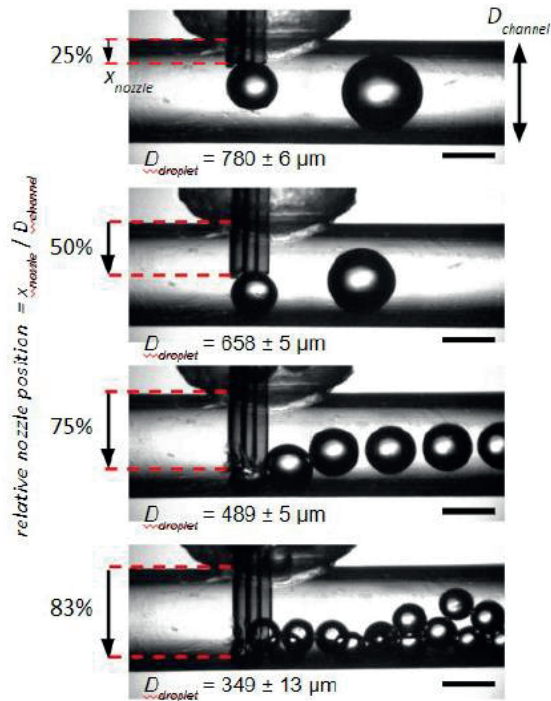
**Figure S2.3. On-the-fly fine-tuning of nozzle position controls droplet size.** All microphotographs were taken during emulsification of water (10 µl/min) in hexadecane with 1% Span 80 (100 µl/min) using a 150 µm nozzle in T-junction configuration. The size of droplets was largely determined by the position of the nozzle within the channel. On-the-fly nozzle repositioning within a transparent microfluidic device thus enables the swift iteration towards a functional droplet generator that operates within the desired production regime. Scale bars indicate 500 µm.
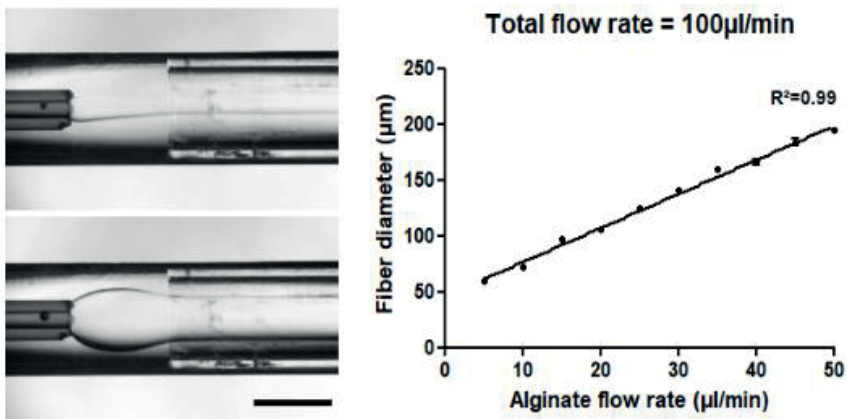


**Figure S2.4. All aqueous two-phase flow generation control.** The diameter of alginate flow and resulting microfibers could be linearly ($R^2$=0.99) controlled by the ratio of alginate to the total flow rate. Scale bar indicates 700 µm.
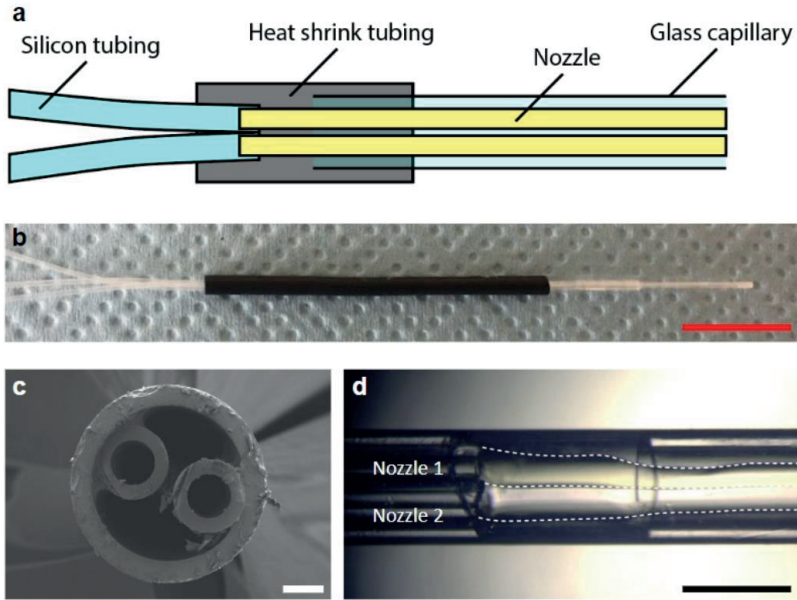
**Figure S2.5. Assembly and operation of multibore nozzle for the production of Janus micromaterials.** (**a**) Schematic overview, (**b**) photograph, and (**c**) scanning electron microscopy image of the multibore nozzle assembly that was used to generate (**d**) focused multiphase aqueous co-flows for the production of Janus type microfibers. Red scale bar indicates 1 cm. White scale bar indicates 200 μm. Black scale bar indicates 1 mm.
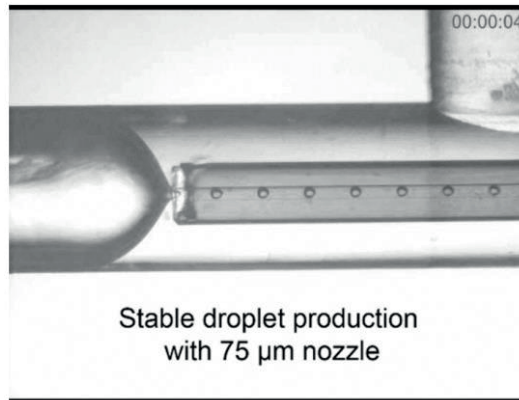


**Movie S2.1 (still). On-the-fly nozzle exchange allows for a switch in droplet size production regime within 1 minute.** t = 0-10s: droplets are produced using a nozzle with a diameter of 200 μm. t = 10s: flow is paused. t = 13s: 200 μm diameter nozzle is retracted. t = 25s: nozzle with a diameter of 75 μm is inserted. t = 35s: flow is restarted. t = 40-50s: flow rates are adjusted. t = 52s: stable droplet production achieved with 75 μm nozzle.

# References

1.  Whitesides, G. M. The origins and the future of microfluidics. *Nature* **442,** 368 (2006).
2.  Ma, S. *et al.* Fabrication of Microgel Particles with Complex Shape via Selective Polymerization of Aqueous Two-Phase Systems. *Small* **8,** 2356–2360 (2012).
3.  Kang, E. *et al.* Digitally tunable physicochemical coding of material composition and topography in continuous microfibres. *Nat. Mater.* **10,** 877 (2011).
4.  Xu, S. *et al.* Generation of Monodisperse Particles by Using Microfluidics: Control over Size, Shape, and Composition. *Angew. Chemie Int. Ed.* **44,** 724–728 (2005).
5.  Temiz, Y., Lovchik, R. D., Kaigala, G. V & Delamarche, E. Lab-on-a-chip devices: How to close and plug the lab? *Microelectron. Eng.* **132,** 156–175 (2015).
6.  Fiorini, G. S. & Chiu, D. T. Disposable microfluidic devices: fabrication, function, and application. *Biotechniques* **38,** 429–446 (2005).
7.  Bauer, W.-A. C., Fischlechner, M., Abell, C. & Huck, W. T. S. Hydrophilic PDMS microchannels for high-throughput formation of oil-in-water microdroplets and water-in-oil-in-water double emulsions. *Lab Chip* **10,** 1814–1819 (2010).
8.  Anna, S. L. Droplets and Bubbles in Microfluidic Devices. *Annu. Rev. Fluid Mech.* **48,** 285–309 (2016).
9.  Holtze, C. Large-scale droplet production in microfluidic devices{\textemdash}an industrial perspective. *J. Phys. D. Appl. Phys.* **46,** 114008 (2013).
10. Holtze, C., Weisse, S. A. & Vranceanu, M. Commercial Value and Challenges of Drop-Based Microfluidic Screening Platforms–An Opinion. *Micromachines* **8,** 193 (2017).
11. Terray, A. & Hart, S. J. 'Off-the-shelf' 3-D microfluidic nozzle. *Lab Chip* **10,** 1729–1731 (2010).
12. Li, T., Zhao, L., Liu, W., Xu, J. & Wang, J. Simple and reusable off-the-shelf microfluidic devices for the versatile generation of droplets. *Lab Chip* **16,** 4718–4724 (2016).
13. Wang, Y. *et al.* Controllable geometry-mediated droplet fission using 'off-the-shelf' capillary microfluidics device. *RSC Adv.* **4,** 31184–31187 (2014).
14. Bottaro, E. & Nastruzzi, C. 'Off-the-shelf' microfluidic devices for the production of liposomes for drug delivery. *Mater. Sci. Eng. C. Mater. Biol. Appl.* **64,** 29–33 (2016).
15. Wang, K., Lu, Y. C., Xu, J. H., Tan, J. & Luo, G. S. Generation of micromonodispersed droplets and bubbles in the capillary embedded T-junction microfluidic devices. *AIChE J.* **57,** 299–306 (2011).
16. Kamperman, T. *et al.* Single Cell Microgel Based Modular Bioinks for Uncoupled Cellular Micro- and Macroenvironments. *Adv. Healthc. Mater.* **6,** 1600913 (2017).
17. Dekker, S. *et al.* Standardized and modular microfluidic platform for fast Lab on Chip system development. *Sensors Actuators B Chem.* **272,** 468–478 (2018).
18. Vittayarukskul, K. & Lee, A. P. A truly Lego®-like modular microfluidics platform. *J. Micromechanics Microengineering* **27,** 35004 (2017).
19. Owens, C. E. & Hart, A. J. High-precision modular microfluidics by micromilling of interlocking injection-molded blocks. *Lab Chip* **18,** 890–901 (2018).
20. Bhargava, K. C., Thompson, B. & Malmstadt, N. Discrete elements for 3D microfluidics. *Proc. Natl. Acad. Sci.* **111,** 15013 LP – 15018 (2014).
21. Jin, R. *et al.* Enzymatically-crosslinked injectable hydrogels based on biomimetic dextran–hyaluronic acid conjugates for cartilage tissue engineering. *Biomaterials* **31,** 3103–3113 (2010).
22. Guckenberger, D. J., de Groot, T. E., Wan, A. M. D., Beebe, D. J. & Young, E. W. K. Micromilling: a method for ultra-rapid prototyping of plastic microfluidic devices. *Lab Chip* **15,** 2364–2378 (2015).
23. Kamperman, T., Henke, S., Visser, C. W., Karperien, M. & Leijten, J. Centering Single Cells in Microgels via Delayed Crosslinking Supports Long-Term 3D Culture by Preventing Cell Escape. *Small* **13,** 1603711 (2017).
24. Park, J. Il, Saffari, A., Kumar, S., Günther, A. & Kumacheva, E. Microfluidic Synthesis of Polymer and Inorganic Particulate Materials. *Annu. Rev. Mater. Res.* **40,** 415–443 (2010).
25. Christopher, G. F., Noharuddin, N. N., Taylor, J. A. & Anna, S. L. Experimental observations of the squeezing-to-dripping transition in T-shaped microfluidic junctions. *Phys. Rev. E* **78,** 36317 (2008).
26. Nunes, J. K., Tsai, S. S. H., Wan, J. & Stone, H. A. Dripping and jetting in microfluidic multiphase flows applied to particle and fiber synthesis. *J. Phys. D. Appl. Phys.* **46,** (2013).
27. Zagnoni, M., Anderson, J. & Cooper, J. M. Hysteresis in Multiphase Microfluidics at a T-Junction. *Langmuir* **26,** 9416–9422 (2010).

28.  Yobas, L., Martens, S., Ong, W.-L. & Ranganathan, N. High-performance flow-focusing geometry for spontaneous generation of monodispersed droplets. *Lab Chip* **6,** 1073–1079 (2006).

29.  Anna, S. L., Bontoux, N. & Stone, H. A. Formation of dispersions using 'flow focusing' in microchannels. *Appl. Phys. Lett.* **82,** 364–366 (2003).

30.  Wacker, J., Parashar, V. K. & Gijs, M. A. M. Influence of Oil Type and Viscosity on Droplet Size in a Flow Focusing Microfluidic Device. *Procedia Chem.* **1,** 1083–1086 (2009).

31.  Papirer, E. *Adsorption on Silica Surfaces*. (CRC Press, 2000).

32.  Ogden, M. W. & Mcnair, H. Characterization of fused-silica capillary tubing by contact angle measurements. *J. Chromatogr. A* **354,** 7–18 (1986).

33.  Seiffert, S., Dubbert, J., Richtering, W. & Weitz, D. A. Reduced UV light scattering in PDMS microfluidic devices. *Lab Chip* **11,** 966–968 (2011).

34.  Wang, S. *et al.* An in-situ photocrosslinking microfluidic technique to generate non-spherical, cytocompatible, degradable, monodisperse alginate microgels for chondrocyte encapsulation. *Biomicrofluidics* **12,** 14106 (2018).

35.  Wang, S., Shankles, P., Retterer, S., Kang, Y. T. & Choi, C. K. A Very Low-Cost, Labor-Efficient, and Simple Method to Block Scattered Ultraviolet Light in PDMS Microfluidic Devices by Inserting Aluminum Foil Strips. *J. Therm. Sci. Eng. Appl.* **11,** 14501–14503 (2018).

36.  Kamperman, T. *et al.* Nanoemulsion-induced enzymatic crosslinking of tyramine-functionalized polymer droplets. *J. Mater. Chem. B* **5,** 4835–4844 (2017).

37.  Ashida, T., Sakai, S. & Taya, M. Competing two enzymatic reactions realizing one-step preparation of cell-enclosing duplex microcapsules. *Biotechnol. Prog.* **29,** 1528–1534 (2013).

38.  Tan, W.-H. & Takeuchi, S. Monodisperse Alginate Hydrogel Microbeads for Cell Encapsulation. *Adv. Mater.* **19,** 2696–2701 (2007).

**2**
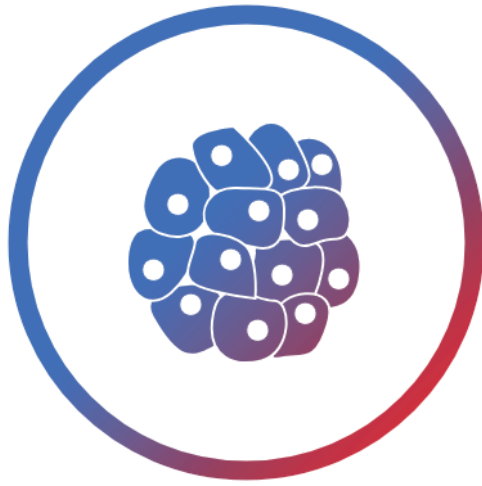
# 3

## Enzymatic Outside-In Cross-Linking Enables Single-Step Microcapsule Production for High-Throughput Three-Dimensional Cell Microaggregate Formation

Cell-laden hydrogel microcapsules enable the high-throughput production of cell aggregates, which are relevant for three-dimensional tissue engineering and drug screening applications. However, current microcapsule production strategies are limited by their throughput, multistep protocols, and limited amount of compatible biomaterials. We here present a single-step process for the controlled microfluidic production of single-core microcapsules using enzymatic outside-in cross-linking of tyramine-conjugated polymers. It was hypothesized that a physically, instead of the conventionally explored biochemically, controlled enzymatic cross-linking process would improve the reproducibility, operational window, and throughput of shell formation. Droplets were flown through a silicone delay line, which allowed for highly controlled diffusion of the enzymatic cross-linking initiator. The microcapsules' cross-linking density and shell thickness is strictly depended on the droplet's retention time in the delay line, which is predictably controlled by flow rate. The here presented hydrogel cross-linking method allows for facile and cytocompatible production of cell-laden microcapsules compatible with the formation and biorthogonal isolation of long-term viable cellular spheroids for tissue engineering and drug screening applications.

Bas van Loo, Seyedeh Sara Salehi, Sieger Henke, Amir Shamloo, Tom Kamperman[1], Marcel Karperien, and Jeroen Leijten.
Contribution BvL: experimental design, experimental performance, data interpretation and manuscript writing.

## 3.1 Introduction

The field of microfluidics has emerged as a powerful platform for the manufacturing of advanced micromaterials. The possibility to manipulate liquids using predictable flows allows for the production of cross-linkable droplets with controlled size, shape, and composition for biomedical applications[1–4]. For example, microfluidic droplet generation has been leveraged for the production of hollow core-shell micrometer-sized hydrogels (i.e. microcapsules). The microcapsules' hollow compartment can be used for controlled aggregation of cells into three-dimensional (3D) microtissues such as organoids and microaggregates[5–11].

Cellular microaggregates offer numerous advantages for tissue engineering and drug screening strategies owing to their 3D biomimetic design, which enhances cellular functions in comparison with conventional two-dimensional monolayer cultures[12–14]. For example, microaggregates have been reported to improve stem cell differentiation, facilitate drug target discovery, and enable engineering of macroscopic tissue constructs[15–19]. Cell microaggregates were originally generated using flat non-adherent tissue culture plates, which resulted in microaggregates of polydisperse sizes owing to the lack of geometrical control during the cells' self-assembly process[20]. Consequently, U-shaped multiwell plates[21], conical tubes[22], hanging drops[22], and microwells[18,19,23] have been developed to yield monodisperse spherical microaggregates. However, the inefficient and batch-type nature of these production methods only offered limited quantities of microaggregates, which has hindered their upscaling to industrial and clinical production scales.

In recent years, various microfluidic processes have been explored for the continuous production of monodisperse cell-laden microcapsules[5–11]. Despite significant progress, the microfluidic production of microcapsules has remained a complex, inefficient, and labor intensive process, which has hampered its widespread adoption. Specifically, a multistep process has been used in which a sacrificial microgel is produced, coated with distinct biomaterial, and subsequently turned into a microcapsule by enzymatic degradation of the sacrificial core[9,11]. Other methods are, for example, based on multiple emulsion strategies or multistep formation of external shells via layer-by-layer assembly of positively and negatively charged polyelectrolytes[5,7,11]. Moreover, most of these approaches have relied on the ionic cross-linking of alginate, which can be unstable owing to the inherently reversible nature of this physical cross-link and the gradual loss of divalent ions from the cross-linked biomaterial[24]. More straightforward single-step microcapsule production methods have been developed based on competitive enzymatic cross-linking of phenolic compounds. Specifically, tyramine-functionalized polymers droplets can form microcapsules by preventing enzymatic cross-linking of the core using the $H_2O_2$ (i.e. cross-linking initiator) consuming enzyme catalase[25–27]. Although monodisperse microcapsules were produced in a single cytocompatible step, competitive enzymatic cross-linking remains a delicate biochemical process that

depends on balanced activities of cross-linking inducing and inhibiting enzymes, which results in a suboptimal production process (i.e. encapsulation efficiency and shell thickness), restricted level of cross-linking tunability, and limited rate of production. Previously, gradients of $H_2O_2$-initiated enzymatic cross-linking were observed across semipermeable silicone microfluidic channels[28]. We hypothesized that such cross-linker gradients could be leveraged for the continuous microfluidic formation of microcapsules in the absence of a polymerization inhibitor, thereby providing more control over the reproducibility, operational window, and throughput of microcapsule production than conventional competitive enzymatic cross-linking platforms.

In this study, we present a single-step microfluidic strategy that enabled the high-throughput production of monodisperse hydrogel microcapsules via enzymatic outside-in cross-linking of tyramine-conjugated polymer droplets. Outside-in cross-linking was achieved by supplementing hydrogel precursor droplets with the enzymatic cross-linking initiator $H_2O_2$ via diffusion through a semipermeable silicone tubing. This method, which involves only a single enzymatic reaction, provided control over the shell thickness and facilitated microcapsule optimization for cell encapsulation. Specifically, dextran-based microcapsules were fine-tuned to enable the cytocompatible encapsulation, aggregation, long-term culture, and on-demand release of mesenchymal stem cells.

## 3.2 Materials and Methods

### 3.2.1 Materials

Dextran-tyramine (Dex-TA; ~20 kDa) was synthesized as previously described [29]. The resulting Dex-TA contained 14 tyramine moieties per 100 repetitive units. N-hexadecane, Span 80, horseradish peroxidase (HRP; type IV), hydrogen peroxide ($H_2O_2$; with inhibitor), dextran-FITC (10-2000 kDa), fetal bovine serum (FBS), ascorbic acid, iodixanol (Optiprep), calcein AM, ethidium homodimer-1 (EthD-1), Triton X-100, dexamethasone, proline, buffered formalin, and dextranase from penicillium sp. were purchased from Sigma-Aldrich / Merck. 4',6-diamidino-2-phenylindole (DAPI) was purchased form Thermo Scientific. Minimal essential medium a with nucleosides(α-MEM), penicillin, streptomycin, L-glutamine, and trypsin-EDTA were purchased from Gibco. Phosphate-buffered saline (PBS) was purchased from Lonza. Basic fibroblast growth factor (ISOKine bFGF) was purchased from Neuromics. Phalloidin-AF488 was purchased from Molecular Probes. Catalase (from bovine liver) were purchased from Wako Chemicals. Polymethylmethacrylate (PMMA) microfluidic chip was produced as previously described [27]. Polymethylmethacrylate (PMMA) and O-rings (#1: inner diameter 0.74 mm, outer diameter 2.78 mm, #2: inner diameter 1.07 mm, outer diameter 3.61 mm) were purchased by Viton. Fluorinated ethylene propylene tubing (FEP, inner diameter 500 µm, outer diameter 1/16''), Gastight syringes (Hamilton), and connectors were purchased from IDEX Health & Science. Polyimide-coated fused silica capillaries

(TSP type, various inner diameters, outer diameter 360 μm) were purchased from Polymicro Technologies. Borosilicate capillaries (inner diameter 700 μm, outer diameter 870 μm were purchased from CM Scientific. Silicone tubing (inner diameter 300 μm, outer diameter 640 μm, thickness 170 μm) was purchased from Helix Medical. Abrasive (Cif) was purchased from Unilever. Fluorinated silane (Aquapel) was purchased from Vulcavite. Low-pressure syringe pumps (neMESYS) were purchased from Cetoni.

### 3.2.2 Microfluidic Chip Production

A 3D microfluidic glass capillary device was used to produce droplets as described by Kamperman et al. [27] In short, a polymethylmethacrylate (PMMA) device was fabricated using standard cutting and abrasion methods. Fused silica capillaries with an inner diameter of 200 μm were used as nozzles in a flow focusing setup. These nozzles were fabricated by inserting it into silicone tubing which has a transparent and semi-permeable nature, enabling in-line monitoring and diffusion-based delivery of small molecules such as reactive $H_2O_2$ to induce or control chemical reactions.

### 3.2.3 Hydrogen Peroxide Diffusion

First, a 0.5X 3,3'-diaminobenzodine (DAB) solution containing 20 U/ml of HRP was flown through a silicone tube in a hydrogen peroxide diffusion bath at a rate of 100 μl/min. The poly(DAB) that precipitated inside the silicone tube was imaged macroscopically. Next, droplets containing 0.5X DAB solution containing 20 U/ml of HRP were produced in an oil phase composed of N-hexadecane and 1% Span 80 at a 1:10 flow rate ratio. Droplets were produced with varying hydrogen peroxide immersion times, ranging from 4-20 s. Absorption of collected droplets was measured using a Multiskan Go Microplate Spectrophotometer (Thermo Scientific) at 540 nm.

### 3.2.4 Microgel Formation

Dextran-Tyramine (Dex-TA) conjugates were prepared as described previously [29]. Dex-TA was used with a degree of substitution of 15. Droplets containing 5% of Dex-TA and 250 U/ml of Horseradish Peroxidase (HRP) were produced in an oil phase, containing N-Hexadecane supplemented with 1% Span 80 as surfactant. Droplets were then transported through ~20 cm silicone tubing that was immersed in a $H_2O_2$ bath containing 30% of $H_2O_2$. The outside-in crosslinking of the droplets was induced by $H_2O_2$ that diffused through the tubing and oil and into the Dex-TA and HRP containing droplets. The microdroplet's residence time in the $H_2O_2$ bath can be altered by increasing the total flow rate while keeping the water:oil ratio constant at 1:10. Unless otherwise written, the total flow rate used was ~100 μl/min, which relates to a residence time of 8.5 seconds. The produced microgels were collected in oil, and the emulsion was broken by three consecutive washes using hexadecane and subsequent wash with phosphate buffered saline (PBS). To further investigate the stable hollow microgel production window, microgels were produced using

10%, 20% and 30% $H_2O_2$ baths, using total flow rates ranging from 11 µl/min to 154 µl/min while keeping the water:oil ratio constant at 1:10. To compare outside-in crosslinking with the catalase based method described by Sakai et al. [9], 83.000 U/ml catalase was added to the Dex-TA HRP solution. Microgels were then produced at total flow rates of 11 µl/min to 110 µl/min. Microgels were then stained with EthD-1 as described before and analyzed by confocal microscopy. In an attempt to increase the production window lower concentrations of 40.000 and 20.000 U/ml catalase were also used.

## 3.2.5 Microgel Characterization

For assessment of the microgels' size and monodispersity, brightfield microphotographs were taken and analyzed using ImageJ. For visualizing the crosslinked polymer shell and determining its thickness, microgels were stained with ethidium homodimer (EthD-1) at a concentration of 30 µM in PBS, imaged with a confocal microscope (Nikon A1 confocal) at a confocal depth with the highest ferret diameter of the microcapsules and analyzed using ImageJ. The permeability of the microgels was tested by incubating them in FITC-conjugated dextrans with molecular weights of 10, 20, 40, 70 (40 mg/ml), 150, 500, 2000 kDa (20 mg/ml) for 24 hours after which fluorescence intensity in the center of the gel was measured by confocal images.

## 3.2.6 Cell Culture

Bone marrow derived human Mesenchymal Stem Cells (hMSCs) were isolated from bone marrow as described previously[30]. The cells were cultured in proliferation medium, containing Alfa-MEM, supplemented with 10% FBS, 2 mM L-glutamine, 0.2 mM ascorbic acid, 1 ng/ml basic fibroblast growth factor, and 100 U/ml penicillin and 100 µg/ml streptomycin. This culture medium was changed biweekly, when 80% confluency was reached. Cells were kept in a humidified environment at 37 °C with 5% $CO_2$ and used until passage 5.

## 3.2.7 Cell Encapsulation

To produce cell-laden microgels, detached cells were washed with medium, flown through a 40 µm cell strainer, and suspended in the hydrogel precursor solution at a concentration of $2*10^7$ cells/ml. In addition, 8% Optiprep was added in order to obtain ρ = 1.05 g/l. The cell-laden hydrogel precursor solution was loaded into an ice-cooled gastight syringe where it was continually agitated in order to prevent cell clump formation. The emulsion was broken by washing three times with surfactant free n-hexadecane oil and subsequent supplementation of culture medium. Culture medium was refreshed twice a week. Cell viability of cell-laden hollow microgels were studied by calcein AM and ethidium homodimer-1 staining according to manufacturer's protocol (Invitrogen) and imaging using a digital fluorescence microscope (EVOS FL Imaging System, ThermoFisher) in multiple independent experiments. DAPI was used to allow nuclei detection to determine cell number in microaggregates. Live/dead cells were counted such that a

percentage of viability could be obtained. For additional analyses, cell-laden microgels were first washed with PBS and fixated using a 10% formalin solution. Cells were permeabilized using 0.1% Triton X-100 and subsequently stained with 2.5 U/ml of phalloidin-AF488, 10 of µg/ml DAPI, and 4 µM of EthD-1 to stain F-actin, nuclei and Dex-TA respectively and analyzed by confocal microscopy (Nikon confocal A1). Isolation of cell aggregates was performed by incubating microaggregate containing microcapsules with 100 U/ml of dextranase at 37 °C for 5 minutes.

### 3.2.8 Statistics
Shown results were determined from at least 10 measurements and reported as the average ± standard deviation. Sample size per experiment is reported in figure descriptions. Significance was determined based on one-way Anova analysis. Significance of $p < 0.05$ is indicated by *. All statistical analyses were performed in OriginPro2017.

### 3.2.9 Schematics
All graphs were drawn using OriginPro 2017 software. All schematics were composed using ChemDraw Professional 16.0 software and Adobe Illustrator CC 2017 software.

## 3.3 Results and Discussion

### 3.3.1 Microfluidic Platform for Diffusion-Based Delivery of Cross-Link Initiator to Microdroplets
A schematic of the microfluidic platform for diffusion-based delivery of the cross-linker to microdroplets is presented in **Figure 3.1a** and **Figure 3.1b**. In short, a 3D microfluidic glass capillary device was manufactured out of polymethylmethacrylate using a recently reported clean-room independent method to enable the generation of polymer solution droplets (**Figure 3.1c**)[27]. By applying a 1:10 hydrogel precursor:oil ratio at a production flow rate of 100 µl/min while using a 200 µm inner diameter nozzle, droplets were produced at a production rate of approximately 132 Hz (**Figure 3.1d**). Flowing the polymer solution droplets through a semipermeable silicone tube, which was submerged in a hydrogen peroxide bath (**Figure 3.1e** and **Figure 3.1f**), allowed for the diffusion of hydrogen peroxide into the microdroplets.

To prove the diffusion-based delivery of hydrogen peroxide through the silicone tubing, 3,3'-diaminobenzidine (DAB) was used. In the presence of the enzyme horseradish peroxidase (HRP) and hydrogen peroxide, DAB reacts into poly(DAB) which can be observed as a brown precipitate (Fig. 1g). When flowing DAB + HRP solution through a silicone tube submerged in a hydrogen peroxide bath, the formation of brown precipitate was observed, which indicated the diffusion of hydrogen peroxide through the silicone tubing into the solution. Moreover, the
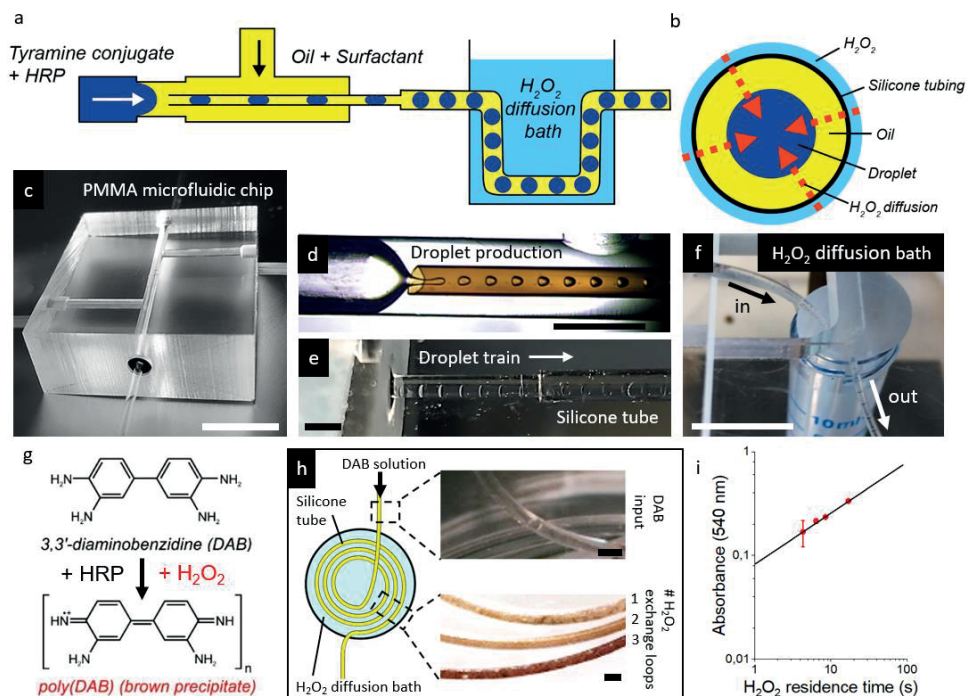
**Figure 3.1: Microfluidic platform for outside-in diffusion-based delivery of crosslinker to water-in-oil microdroplets.** (a) Schematic representation of hydrogel microcapsule production via delayed outside-in crosslinking of water-in-oil polymer microdroplet by transporting the droplets through a silicone tubing submerged in a $H_2O_2$ bath. (b) $H_2O_2$ diffuses through the silicone tubing, through the oil phase, and into microdroplets. (c) Polymethylmethacrylate (PMMA) microfluidic 3D glass capillary device in which (d) microdroplets are formed using a flow-focus nozzle setup. (e) Droplets are then transported off-chip through a silicone tube, which is (f) immersed in a hydrogen peroxide diffusion bath for diffusion of hydrogen peroxide into the droplets. (g) DAB forms brown precipitate (poly(DAB)) in presence of HRP and hydrogen peroxide. (h) DAB solution was flown through a silicone tube that was immersed in a hydrogen peroxide diffusion bath, which demonstrated the time-dependent nature of the diffusion-based hydrogen peroxide availability. (i) Longer hydrogen peroxide residence times resulted in higher absorbance at 540 nm, indicating higher poly(DAB) production and thus higher hydrogen peroxide availability (n=2). White scale bar indicates 1 cm. Black scale bar indicates 1 mm.

quantity of diffused hydrogen peroxide could be predictably controlled as the solution's metachromatic color positively correlated with the solution's residence time in the diffusion bath (**Figure 3.1h**). To validate this finding, microdroplets containing DAB were produced and transported through the hydrogen peroxide diffusion bath with varying residence times. Again, it was observed that longer residence time resulted in a predictable increase in poly(DAB) formation, indicated by the higher absorbance, which was in line with Fick's second law of diffusion. (**Figure 3.1i**).

### 3.3.2 Outside-In Cross-Linking for the Production of Hydrogel Microcapsules

Hydrogels were prepared by the HRP-mediated coupling of phenol moieties of tyramine conjugates (**Figure 3.2a**). As an example material, dextran-tyramine (Dex-TA) was used. Flowing a 5% polymer solution droplets through the submerged silicone tubing for ~8.5 s resulted in the monodisperse production of outside-in cross-linked microgels with a diameter of 123.6 ± 4.9 μm (CV = 3.8) (**Figure 3.2b**). By varying the water:oil ratios and/or different nozzle diameters, microcapsules with diameters ranging from 80 μm to 300 μm could be produced in a monodisperse manner (**Figure 3.2c,d**). Confocal analysis of ethidium homodimer stained microgels confirmed that these microgels were formulated as single core microcapsules (**Figure 3.2c**). To illustrate the possibility to use multiple materials, single core microcapsules were also produced of tyramine-conjugated hyaluronic acid (HA-TA) (**Figure S3.1**).

Control over the local hydrogen peroxide concentration proved to be of essential importance to successfully produce microcapsules using the outside-in cross-linking strategy. When exposing the polymer precursor to a too low hydrogen peroxide concentration it resulted in incomplete cross-linking of microgels' shell (**Figure 3.2e**), which resulted in microgel rupture during the subsequent washing step. Cross-linking the microdroplet with a higher hydrogen peroxide concentration resulted in formation of robust microcapsules (**Figure 3.2e**). Exposure to a too high hydrogen peroxide concentration also resulted in the formation of conformal microcapsules, but associated with the cross-linking of polymer droplet's core thus giving rise to soft-core or solid-core microgels (**Figure 3.2e**). Quantitative analysis of shell thickness and ethidium homodimer intensity of these soft-core microgels confirmed that the polymer cross-linking became gradually less intense in an outside-in manner. This was in contrast to the microcapsules, which revealed a sharp decline in cross-linking density (**Figure 3.2f**).

We then mapped under which parameters partially cross-linked, hollow core, or soft-core microgels would be formed by varying the emulsion's flow rates and the hydrogen peroxide bath's concentration (Fig. 2g, Fig. S2). As expected, decreasing the flow through rate and increasing the hydrogen peroxide concentration associated with increased cross-linking. Microcapsules could be produced at a wide range of emulsion flow rates, which spanned nearly an order of magnitude, with the highest measured microcapsule production rate being measured using an emulsion flow rate of 99 μl/min and a bath concentration of 30% of hydrogen peroxide. This associated with a maximum possible microcapsule production rate of ~132 Hz. In comparison, previously reported catalase-based microcapsule formation strategies based on inside-out hydrogen peroxide scavenging[25], could only form microcapsules in a notably smaller window of operation and at a substantially lower emulsion flow through rate, which offered a maximal microcapsule production rate of only ~29 Hz (**Figure 3.2g,h**).
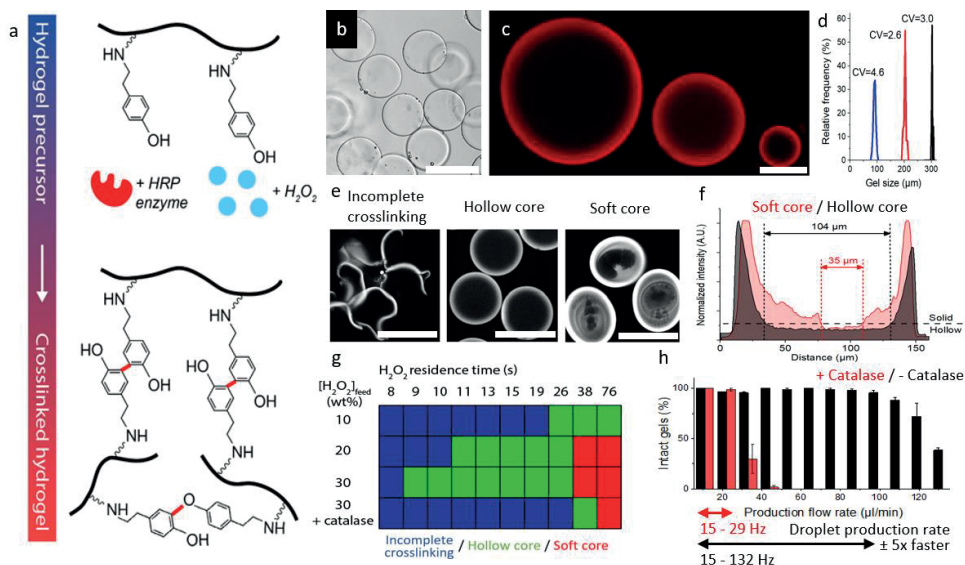
**Figure 3.2: Outside-In crosslinking of polymer containing water-in-oil microdroplets produces hydrogel microcapsules.** (a) Tyramine-conjugated polymer is crosslinked by HRP in the presence of hydrogen peroxide. (b) Delayed outside-in crosslinking results in microgels. (c) EthD-1 staining proves microgels of different sizes contain a hollow core and can be defined as microcapsules. (d) Size distribution of produced microcapsules show monodisperse production in different size regions with a CV<5 (N≥10). (e) Three distinct production regimes, being incomplete crosslinking, hollow microgels, and soft-core microgels, were identified. (f) Histogram of soft-core (red) and hollow core microgels (black), with soft-core microgels containing hollow compartments significantly smaller in comparison with the hollow compartments of stable hollow microgels. (g) Qualification of Dex-TA crosslinking regime as function of hydrogen peroxide concentration, hydrogen peroxide residence time, and the presence of catalase resulting in incomplete crosslinking (blue), stable hollow microgels (green), and soft-core microgels (red). (h) Producing microcapsules without catalase enables higher total flow rates and thus a higher production rate before reaching the incomplete crosslinking regime, as indicated by a low percentage of intact gels (<95%) after crosslinking (N≥20). Scale bar indicates 100 µm.

It is likely that delayed outside-in cross-linking can achieve this large production window and higher production, as compared with catalase-based strategies, by avoiding the delicate balance between initiation and inhibition of cross-linking (**Table S3.1**). Advantageously, the ability to form microgels using fewer components (e.g. without catalase) not only improves the cross-linking control and rate but also results in a cleaner, more chemically defined production process, which is of relevance for clinical and biomedical applications. In addition, rheological characteristics of the microcapsules can be altered by varying the Dex-TA concentration in the hydrogel precursor solution (**Figure S3.3**).

### 3.3.3 Optimization of Microcapsules Shell Thickness for Cytocompatible Cell Encapsulation

As a concrete example for a biomedical application of the presented delayed outside-in cross-linked microcapsule technique, cell encapsulation experiments were performed. Mixing human mesenchymal stem cells (hMSCs) into the hydrogel

**3**

precursor solution readily allowed for the production of cell-laden microcapsules. However, it was observed that the supplementation of cells to the polymer solution consistently altered the cross-linking of the microdroplets. For example, while cell-free microdroplets produced at a production flow rate of 100 µl/min and cross-linked using a 30% hydrogen peroxide concentration yield hollow microgels, microdroplets containing $2*10^7$ cells/ml resulted in the production of soft-core microgels (**Figure 3.3a,b**). We then demonstrated that cell-laden microdroplets required higher production flow rates than their cell-free counterparts to form microcapsules (**Figure 3.3a**). Advantageously, this allowed for the production of microcapsules at emulsion flow through rates as high as 180 µl/min (**Figure 3.3c**), which resulted in thinner shells with a thickness of 16.7 ± 2.7 µm (**Figure 3.3d**). This increased flow rate equates to a production rate of ~230 Hz, which is almost double the maximum production rate of cell-free microcapsules, and ~8× faster than catalase-dependent microcapsule production.

The microgel's shell thickness is of great importance for cell encapsulation as it positively correlates with cells becoming entrapped in the shell. Moreover, although cell death was negligible within the hollow compartment, it was observed that cell death of entrapped cells in the shell was relatively high (**Figure 3.3e**) being 67 ± 5% after 14 days of culture. However, by adjusting the production flow rate from 100 µl/min to 180 µl/min we were able to lower the amount of entrapped cells from 15% to 0,2% (**Figure 3.3f**) effectively optimizing the cytocompatible cell encapsulation within the microcapsules.

The number of encapsulated cells could be controlled by tuning the cell concentration in the hydrogel precursor solution. For example, single-cell hollow microcapsules were produced using a concentration of $2*10^5$ cells/ml (**Fig. 3g**). Specifically, a single cell was present in 35% of the microcapsules, whereas only 2% of the hollow microgels contained two or more cells. This strategy thus represents an effective approach to study individual cells within soft, hollow, and 3D microenvironments, which can be composed of spatiotemporally responsive materials[31].

The number of cells per microgel scaled in a predictable manner with the cell concentration used in the hydrogel precursor solution, which thus also enabled the production of microcapsules that contained multiple cells (**Figure 3.3h,i**). Delayed outside-in cross-linking of 120 µm diameter microdroplets composed of $2*10^7$ cells/ml polymer solution resulted in the monodisperse encapsulation of 34.4 ± 3.1 cells per microcapsule (CV = 9.2%). Increasing the cell concentration further associated with a linear increase in the number of encapsulated cells within the microcapsule, which corroborated the predictable nature of the encapsulation process (**Figure 3.3j**). Besides the cell concentration in the hydrogel precursor solution, the amount of cells per microcapsule could also be tuned by producing microcapsules of different sizes. For example, production of microcapsules of 298 ± 9 µm resulted in 101 ± 8 cells per gel (**Figure S3.4**).
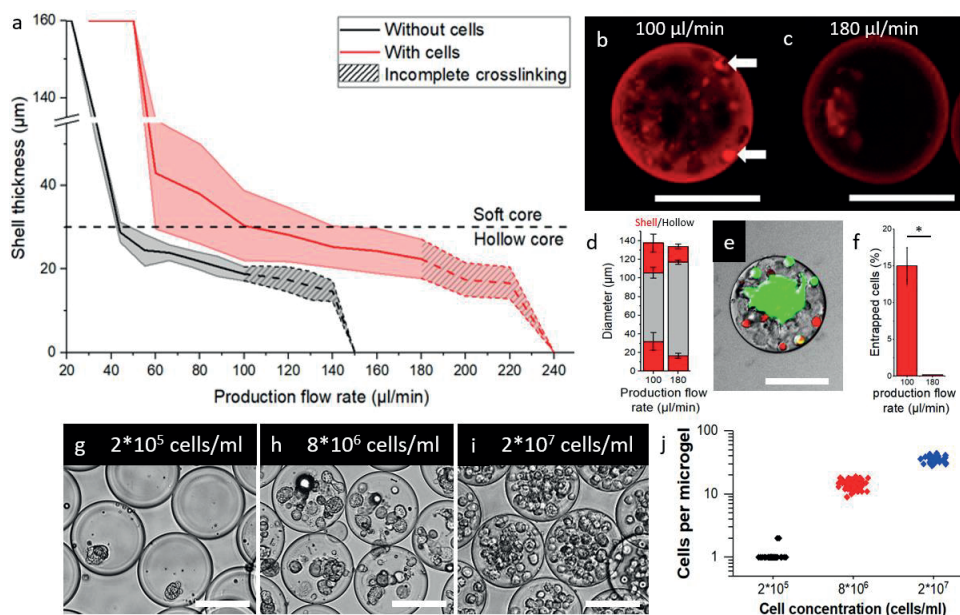
**Figure 3.3: Optimization of microcapsules shell thickness for efficient cell encapsulation.** (a) Quantification of shell thickness at different production flow rates with and without $2*10^7$ of hMSCs in the polymer solution. (N≥20). (b) Cell-laden microcapsules produced at a production flow rate of 100 μl/min resulted in soft-core microgels with cell entrapment in the shell, as indicated by white arrows (c) Cell-laden hollow core microcapsules were obtained when produced with a production flow rate of 180 μl/min. (d) Shell size decreases with increasing production flow rates (N≥15). (e) Live/dead assay of cell-laden microcapsules showed that dead cells (shown in red) tend to be entrapped in the microgel's shell. (f) Number of cells entrapped in the shell drop from 15% to 0.2% with higher production flow rates. (g) Cell encapsulation with a cell concentration of $2*10^5$ cells/ml in the hydrogel precursor solution for single cell encapsulation. Further increasing the cell concentration in the polymer solution to (h) $8*10^6$ or (i) $2*10^7$ cells/ml resulted in the encapsulation of a predictable amount of multiple cells. (j) Quantification of the number of cells per microcapsule for different cell concentrations in the hydrogel precursor solution (N≥30). Scale bar indicates 100 μm. * Indicates significance with $p<0.05$.

## 3.3.4 Long-Term Culture of Cell-Laden Microcapsules Enable In Situ Formation of Stem Cell-Based 3D Microtissues

The semipermeable nature of the microcapsules was studied with diffusion experiments using fluorescein isothiocyanate-conjugated dextrans of various molecular weights, which illustrated that molecules up to 150 kDa were are able to diffuse into the microcapsule (**Figure S3.5**). Relevant molecules such as growth factors, nutrients and waste products, can thus diffuse freely through the microcapsules' shell. This indicated that long-term cell culture is most likely possible within the microcapsules.

hMSC containing microcapsules were produced and cultured for up to 28 days (**Figure 3.4a–c**). Cells rapidly aggregated into 3D microtissues within the hollow

**3**
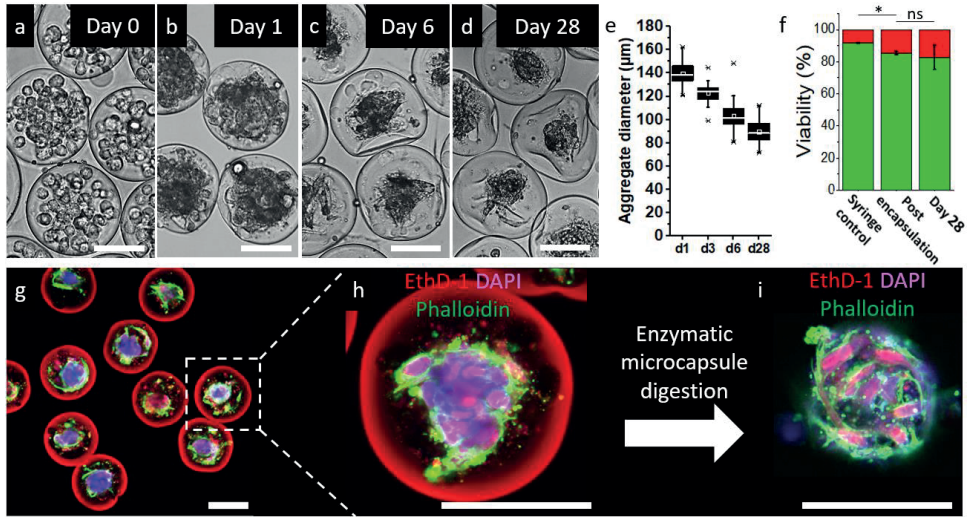


**Figure 3.4: Cell-laden microcapsules enable in situ formation, formation, and biorthogonal isolation of stem cell based 3D microtissues.** Encapsulated cells in microcapsules (a) immediately after crosslinking, (b) after 1 day of culture, (c) after 6 days of culture, (d) and after 28 days of culture. (e) Quantification of the size of the microtissues formed within the microcapsules. (f) Quantification of live/dead assays of used hMSCs at various point in time (N≥20). (g) Confocal images of microaggregates in microcapsules after 14 days of culture, stained with EthD-1 (red), DAPI (magenta), and Phalloidin (green). (h) High resolution confocal microphotograph of a single microaggregate in a microcapsule after 14 days of culture. (i) Enzymatic degradation of Dex-TA microgels using dextranase allowed for biorthogonal microaggregate isolation. Scale bar represents 100 μm. * Indicates significance with p<0.05.

compartment of the microcapsules. These microaggregates could be maintained within the microcapsules for the entire duration of experimentation without any notable level of cell egression. As with conventionally cultured stem cell microaggregates, the cellular spheroids decreased (e.g. 62% reduction in 28 days) in diameter over time (**Figure 3.4d**)[19,23]. This observation is likely explained by cellular compaction within the microaggregate, as previously reported[18], as cell viability consistently remained high directly after encapsulation and after a culture period of 28 days in multiple experiments (n = 4), with a viability of 86 ± 1% 5 h after encapsulation and 83 ± 7% of cells surviving after 28 days of culture (**Figure 3.4e, Figure S3.6**). This indicated that the diffused hydrogen peroxide was offered to the cell-laden microdroplet in a non-toxic concentration as the hydrogen peroxide–free syringe control associated with a comparable level of cell survival. This was likely mediated via the outside-in consumption of hydrogen peroxide during the cross-linking reaction, which effectively shielded the cells in the droplets core from exposure to cytotoxic levels of hydrogen peroxide. This emphasized the cytocompatible nature of the delayed outside-in cross-linking process. Moreover, fluorescent confocal analysis revealed that the microfluidic encapsulation procedure prevented cells from being at the peripheral side of the microcapsules,

thus effectively locating the cells within the microcapsules core and allowing the formation of conformal and continuous shells (**Figure 3.4f**). Interestingly, evidence was found that cells could originally reside on the proximal side of the microcapsule's shell and vacate their position after cross-linking. (**Figure 3.4g**). Furthermore, enzymatic digestion of the Dex-TA microcapsules using dextranase allowed for biorthogonal isolation of the produced microaggregates (**Figure 3.4h**).

## 3.4 Discussion

Here, we present a robust and straightforward method to produce hydrogel-based hollow single-core microcapsules. Our method relies on the enzymatic cross-linking of polymer-tyramine conjugates in an enzymatic reaction that is cytocompatible, achieved in seconds, and controlled via outside-in diffusion of a cross-link activator (e.g. hydrogen peroxide). By exposing polymer solution microdroplets to outside-in diffusion of low amounts of hydrogen peroxide, which can be controlled by adjusting the production flow rate, hydrogen peroxide concentration and possibly by varying the thickness of the silicone tubing, microcapsules are effectively formed as the hydrogen peroxide will be consumed in the cross-linking reaction before being able to reach the microdroplet's core.

Compared with previously reported strategies, such as those based on the spatial competition between an inducer (e.g. hydrogen peroxide) and an inhibitor (e.g. catalase) of polymer cross-linking[25], our system offers several advantages that are a consequence from its activator-only–based design. Specifically, it is a cleaner, more chemically defined production process, which is favorable when taking possible future clinical studies into account. In addition, as no inhibitors are used, the microcapsules could be produced at a substantially higher production rate while offering a wider window of operation. Furthermore, as our system relies on delayed cross-linking, the cross-linking of polymer at the droplet generator's nozzle is avoided, which lowers the chance on microdevice failure[27]. Moreover, several other previously published methods described for production of microcapsules demand access to nano and microfabrication technologies and dedicated infrastructures, whereas our method relies on the use of off-the-shelve components and readily available non–clean-room–based production processes, thus being suitable for a much wider target audience as it includes non-specialized end-users[27].

The enzymatic cross-linking of Dex-TA has been used for various biomedical applications and can be combined with distinct production techniques[26–29,31–33]. Dex-TA is thus chosen as a model material as it represents an effective, versatile, inert, and cytocompatible biomaterial. Regardless, the presented method for microcapsule production is compatible with a wide variety of polymers. Numerous natural and synthetic tyramine polymer conjugates to form hydrogel networks have previously been reported. Beside Dex-TA, conjugates of hyaluronic acid[29], poly(ethylene glycol)[34], heparin[33], chitosan[35], alginate[36], gelatin[37], Poly Vinyl

Alcohol[38], and peptides[39] have been reported. These conjugates and their combination thereof, each with their own biological and physicochemical properties, are all suited for outside-in enzymatic cross-linking. Hence, it will be possible to tailor the biological and physicochemical properties of the microcapsule's shell by selecting distinct polymer conjugates and stimulating moieties. To demonstrate this, microcapsules consisting of different concentrations of Dex-TA and HA-TA were produced as described earlier.

Encapsulating cells using outside-in cross-linking associated with excellent cell survival, despite the silicone delay line being submerged in a bath composed for 30% of hydrogen peroxide. Indeed, it is widely known that too high concentrations of hydrogen peroxide cause acute cell death[40]. However, it is also known this cytotoxicity depends on both dose and incubation time. For example, decreasing the $H_2O_2$ concentration from 500 to 30 μm required, respectively, 1 h and 48 h to show cytotoxic effects[40]. In contrast, in our enzymatically cross-linking system, $H_2O_2$ is rapidly consumed (seconds) and thus allow for extremely short incubation times. Extensive research has shown that these extremely short $H_2O_2$ exposure times allow for high cell viability and long-term cell function without any detectable functional effect[28,32,33,35,41,42]. In fact, it was recently demonstrated that our enzymatic cross-linking material system was more cytocompatible than any of the previously studied material systems used for microfluidic generation of microgels[32]. Moreover, the amount of hydrogen peroxide that diffuses through the silicone tubing, through the continuous oil phase, and into the polymer droplet is both limited and controlled and is rapidly consumed by the enzyme HRP to cross-link the polymer into a macromolecular network. Within a few micrometer of diffusion into the microdroplet, the $H_2O_2$ has decreased to such a low level that it was no longer able to cross-link the microdroplet into a microgel, hence the formation of hollow microcapsules. Consequently, the levels of $H_2O_2$ within the bulk/core of the microdroplets — where the cells reside — are well within the cytocompatible level. This logic is substantiated by our viability experiments that allowed high cell survival after encapsulation and long-term cell culture. Advantageously, owing to hydrodynamic focusing of microparticles (e.g. cells) inside of aqueous solution (e.g. polymer microdroplets), the cells are transported away from the droplet's shell and toward its core[28]. Indeed, using the delayed cross-linking strategy, no cell were present in the peripheral side of the microcapsules' shell, which likely contributed to the excellent postencapsulation survival rates by spatially shielding it from the outside-in diffusing hydrogen peroxide.

When cells were encapsulated, the microcapsules functioned as microbioreactors that enabled the formation of monodisperse 3D microtissues via cellular aggregation. This phenomenon occurs when cell-cell interactions are energetically more favorable as compared with the cell-substrate interactions, which thus requires biomaterials that present little or no cell binding motives. Controllably producing 3D microtissue has numerous application to, amongst others, study a variety of diseases, guide the differentiation of stem cells, and function as

microbuilding blocks in bottom-up tissue engineering[16,18–20]. Not surprisingly, several strategies have been developed to facilitate controlled cell microaggregation, which includes microwells, hanging drops, non-adhesive culture substrates[23]. Although being compatible with low throughput academic research, none of these platforms offers a production throughput that is readily suitable for clinical or industrial translation. Moreover, in many of these platforms, long-term cultures need to be protected from aggregate fusing or culture substrate attachment. In addition, changing media in many of these platforms is not a straightforward or facile exercise. Hydrogel microcapsules can overcome these challenges by allowing for facile culture and handling of 3D encapsulated microaggregates, which can be produced in a high-throughput manner. In addition, the biorthogonal isolation of the microaggregates allows for easy analysis and further downstream use of these microtissues.

Although the focus of this study was to produce microcapsules, we also identified regimes where soft-core microgels were produced using outside-in cross-linking of tyramine-conjugated polymers. These systems offer cells to be encapsulated in a soft 3D microenvironment, while being protected from undesired physical such as shear stress and/or compression. Moreover, it offers control over diffusion rates in a manner that is not directly dependent on the hydrodynamic properties of the microgels soft-core but rather on those of the microgel's protective shell. In addition, the shell can mitigate or prevent the cell egression that often challenge the culture of cells in soft microgels[28]. Soft-core microgels therefore represent an interesting tool for studying cell biology, development processes, and pathologies such as cancer. Importantly, as with the microcapsules, the soft-core microgels can be produced in high-throughput, which enables the drug screening using compound libraries[6,43,44].

## 3.5 Conclusion

In summary, delayed outside-in cross-linking is an effective, predictable, cytocompatible, universal, and high-throughput strategy for the formation of long-term viable 3D microtissues (e.g. stem cell microaggregates) that allows for biorthogonal purification for downstream biomedical applications such as tissue engineering and drug screening.

## 3.5 Supplementary Information
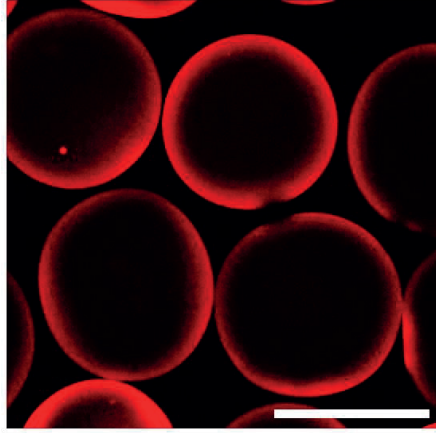


**Figure S3.1: Ethidium homodimer-1 stained HA-TA microcapsules.** Fluorescence confocal microphotograph of microcapsules composed of HA-TA. Scale bar indicates 200 μm.
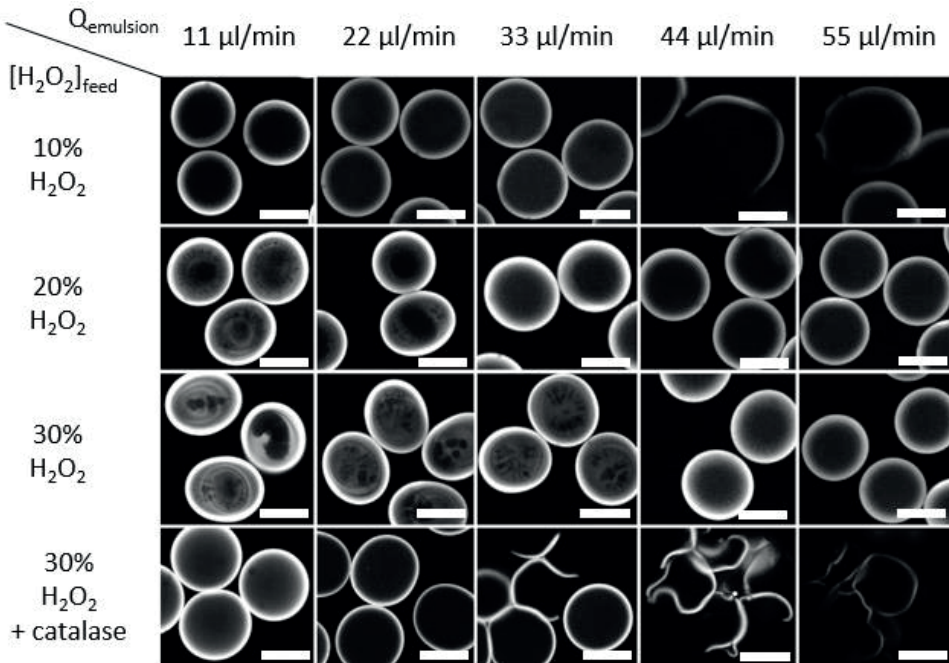


**Figure S3.2: Production regimes of hollow core-shell microgels using distinct $H_2O_2$ baths and total emulsion flow rates.** Representative fluorescence confocal microphotographs of ethidium homodimer-1 stained core-shell microgels. Scale bar indicates 100 μm.
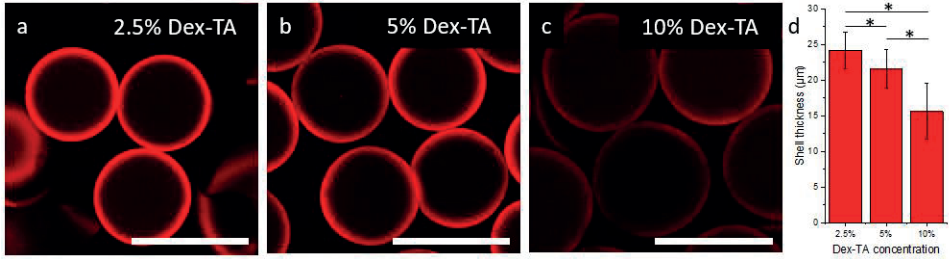
**Figure S3.3: Production of microcapsules with varying Dex-TA concentration.** Microcapsules produced with a Dex-TA concentration of (a) 2.5%, (b) 5% and (c) 10%. (d) Quantification of shell thickness of microcapsules with varying Dex-TA concentration (n>40). Scale bar indicates 100 μm. * Indicates significance with $p<0.05$.
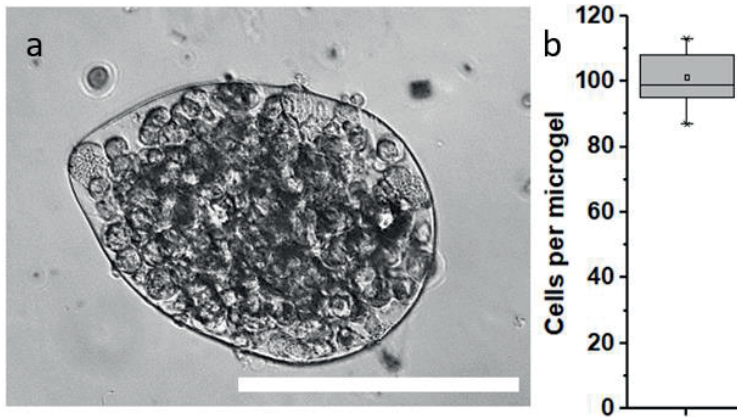


**Figure S3.4: Producing cell-laden hollow core-shell microgels with a distinct size.** (a) Hollow core-shell microgels of 300 μm containing $2*10^7$ cells/ml (b) allowed for the encapsulation of ~100 encapsulated cells per microcapsule (N=10). Scale bar indicates 300 μm.

3
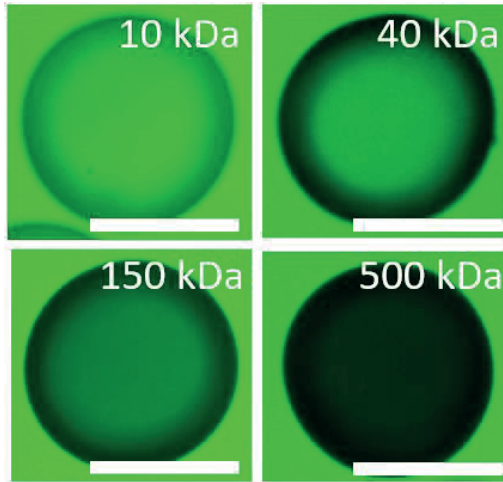
**Figure S3.5: Semipermeability of Dex-TA microcapsules.** Dex-TA microcapsules were incubated in solution with FITC-conjugated dextrans of various molecular weights. Microcapsules allowed diffusion of molecules with a molecular weight of at least 150 kDa. Scale bar indicates 100 µm.
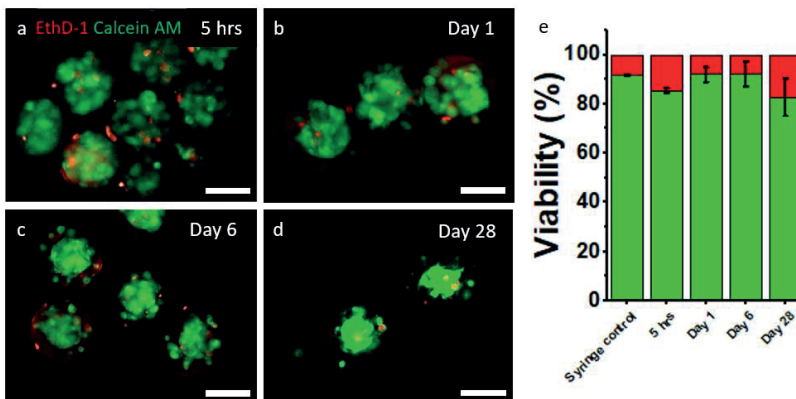


**Figure S3.6: Cell viability after long term culture in microcapsules.** Live/dead assay of cell-laden microcapsules (a) 5 hrs, (b) 1 day, (c) 6 days, and (d) 28 days post encapsulation showing live (green) and dead (red) cells. (e) Viability quantification during long term culture of cells in microcapsules. Scale bar indicates 100 µm.

**Table S3.1: Maximum flow rate for different concentrations of catalase.**

|  | 80k U/ml catalase | 40k U/ml catalase | 20k U/ml catalase |
|---|---|---|---|
| 10% $H_2O_2$ | 99 µl/min | - | - |
| 20% $H_2O_2$ | 77 µl/min | - | - |
| 30% $H_2O_2$ | 22 µl/min | 44 µl/min | 66 µl/min |

# References

1.  Ma, S. *et al.* Fabrication of Microgel Particles with Complex Shape via Selective Polymerization of Aqueous Two-Phase Systems. *Small* **8,** 2356–2360 (2012).
2.  Kang, E. *et al.* Digitally tunable physicochemical coding of material composition and topography in continuous microfibres. *Nat. Mater.* **10,** 877 (2011).
3.  Whitesides, G. M. The origins and the future of microfluidics. *Nature* **442,** 368 (2006).
4.  Xu, S. *et al.* Generation of Monodisperse Particles by Using Microfluidics: Control over Size, Shape, and Composition. *Angew. Chemie Int. Ed.* **44,** 724–728 (2005).
5.  Agarwal, P. *et al.* One-step microfluidic generation of pre-hatching embryo-like core-shell microcapsules for miniaturized 3D culture of pluripotent stem cells. *Lab Chip* **13,** 4525–4533 (2013).
6.  Alessandri, K. *et al.* Cellular capsules as a tool for multicellular spheroid production and for investigating the mechanics of tumor progression in vitro. *Proc. Natl. Acad. Sci. U. S. A.* **110,** 14843–14848 (2013).
7.  Chen, Q. *et al.* Controlled assembly of heterotypic cells in a core–shell scaffold: organ in a droplet. *Lab Chip* **16,** 1346–1349 (2016).
8.  Kim, C. *et al.* Generation of core-shell microcapsules with three-dimensional focusing device for efficient formation of cell spheroid. *Lab Chip* **11,** 246–252 (2011).
9.  Sakai, S. *et al.* Enzymatically fabricated and degradable microcapsules for production of multicellular spheroids with well-defined diameters of less than 150 microm. *Biomaterials* **30,** 5937–5942 (2009).
10. Yu, L., Ni, C., Grist, S. M., Bayly, C. & Cheung, K. C. Alginate core-shell beads for simplified three-dimensional tumor spheroid culture and drug screening. *Biomed. Microdevices* **17,** 33 (2015).
11. Correia, C. R., Bjørge, I. M., Zeng, J., Matsusaki, M. & Mano, J. F. Liquefied Microcapsules as Dual-Microcarriers for 3D+3D Bottom-Up Tissue Engineering. *Adv. Healthc. Mater.* **8,** 1901221 (2019).
12. Fitzgerald, K. A., Malhotra, M., Curtin, C. M., O' Brien, F. J. & O' Driscoll, C. M. Life in 3D is never flat: 3D models to optimise drug delivery. *J. Control. Release* **215,** 39–54 (2015).
13. Baker, B. M. & Chen, C. S. Deconstructing the third dimension – how 3D culture microenvironments alter cellular cues. *J. Cell Sci.* **125,** 3015 LP – 3024 (2012).
14. Shamir, E. R. & Ewald, A. J. Three-dimensional organotypic culture: experimental models of mammalian biology and disease. *Nat. Rev. Mol. Cell Biol.* **15,** 647 (2014).
15. Matsunaga, Y. T., Morimoto, Y. & Takeuchi, S. Molding Cell Beads for Rapid Construction of Macroscopic 3D Tissue Architecture. *Adv. Mater.* **23,** H90–H94 (2011).
16. Thoma, C. R., Zimmermann, M., Agarkova, I., Kelm, J. M. & Krek, W. 3D cell culture systems modeling tumor growth determinants in cancer target discovery. *Adv. Drug Deliv. Rev.* **69-70,** 29–41 (2014).
17. Hoffmann, O. I. *et al.* Impact of the spheroid model complexity on drug response. *J. Biotechnol.* **205,** 14–23 (2015).
18. Bolander, J. *et al.* Healing of a Large Long-Bone Defect through Serum-Free In-Vitro Priming of Human Periosteum-Derived Cells. *Stem Cell Reports* **8,** 758–772 (2017).
19. Leijten, J. *et al.* Bioinspired seeding of biomaterials using three dimensional microtissues induces chondrogenic stem cell differentiation and cartilage formation under growth factor free conditions. *Sci. Rep.* **6,** 36011 (2016).
20. Wolf, F. *et al.* Cartilage tissue engineering using pre-aggregated human articular chondrocytes. *Eur. Cell. Mater.* **16,** 92–99 (2008).
21. Friedrich, J., Seidel, C., Ebner, R. & Kunz-Schughart, L. A. Spheroid-based drug screen: considerations and practical approach. *Nat. Protoc.* **4,** 309–324 (2009).
22. Kurosawa, H. Methods for inducing embryoid body formation: in vitro differentiation system of embryonic stem cells. *J. Biosci. Bioeng.* **103,** 389–398 (2007).
23. Moreira Teixeira, L. S. *et al.* High throughput generated micro-aggregates of chondrocytes stimulate cartilage formation in vitro and in vivo. *Eur. Cell. Mater.* **23,** 387–399 (2012).
24. Lee, K. Y. & Mooney, D. J. Alginate: properties and biomedical applications. *Prog. Polym. Sci.* **37,** 106–126 (2012).
25. Ashida, T., Sakai, S. & Taya, M. Competing two enzymatic reactions realizing one-step preparation of cell-enclosing duplex microcapsules. *Biotechnol. Prog.* **29,** 1528–1534 (2013).
26. Kamperman, T. *et al.* Nanoemulsion-induced enzymatic crosslinking of tyramine-functionalized

**3**

polymer droplets. *J. Mater. Chem. B* **5,** 4835–4844 (2017).

27.    Kamperman, T. *et al.* On-the-fly exchangeable microfluidic nozzles for facile production of various monodisperse micromaterials. *Lab Chip* **19,** 1977–1984 (2019).

28.    Kamperman, T., Henke, S., Visser, C. W., Karperien, M. & Leijten, J. Centering Single Cells in Microgels via Delayed Crosslinking Supports Long-Term 3D Culture by Preventing Cell Escape. *Small* **13,** 1603711 (2017).

29.    Wennink, J. W. H. *et al.* Injectable Hydrogels by Enzymatic Co-Crosslinking of Dextran and Hyaluronic Acid Tyramine Conjugates. *Macromol. Symp.* **309-310,** 213–221 (2011).

30.    Both, S. K., van der Muijsenberg, A. J. C., van Blitterswijk, C. A., de Boer, J. & de Bruijn, J. D. A rapid and efficient method for expansion of human mesenchymal stem cells. *Tissue Eng.* **13,** 3–9 (2007).

31.    Kamperman, T. *et al.* Spatiotemporal material functionalization via competitive supramolecular complexation of avidin and biotin analogs. *Nat. Commun.* **10,** 4347 (2019).

32.    Henke, S. *et al.* Enzymatic Crosslinking of Polymer Conjugates is Superior over Ionic or UV Crosslinking for the On-Chip Production of Cell-Laden Microgels. *Macromol. Biosci.* 1524–1532 (2016). doi:10.1002/mabi.201600174

33.    Jin, R. *et al.* Chondrogenesis in injectable enzymatically crosslinked heparin/dextran hydrogels. *J. Control. Release* **152,** 186–195 (2011).

34.    Park, K. M., Ko, K. S., Joung, Y. K., Shin, H. & Park, K. D. In situ cross-linkable gelatin–poly(ethylene glycol)–tyramine hydrogel viaenzyme-mediated reaction for tissue regenerative medicine. *J. Mater. Chem.* **21,** 13180–13187 (2011).

35.    Jin, R. *et al.* Injectable chitosan-based hydrogels for cartilage tissue engineering. *Biomaterials* **30,** 2544–2551 (2009).

36.    Sakai, S. & Kawakami, K. Synthesis and characterization of both ionically and enzymatically cross-linkable alginate. *Acta Biomater.* **3,** 495–501 (2007).

37.    Sakai, S., Hirose, K., Taguchi, K., Ogushi, Y. & Kawakami, K. An injectable, in situ enzymatically gellable, gelatin derivative for drug delivery and tissue engineering. *Biomaterials* **30,** 3371–3377 (2009).

38.    Lim, K. S., Alves, M. H., Poole-Warren, L. A. & Martens, P. J. Covalent incorporation of non-chemically modified gelatin into degradable PVA-tyramine hydrogels. *Biomaterials* **34,** 7097–7105 (2013).

39.    Wang, L.-S. *et al.* Enzymatic conjugation of a bioactive peptide into an injectable hyaluronic acid-tyramine hydrogel system to promote the formation of functional vasculature. *Acta Biomater.* **10,** 2539–2550 (2014).

40.    Gülden, M., Jess, A., Kammann, J., Maser, E. & Seibert, H. Cytotoxic potency of $H_2O_2$ in cell cultures: Impact of cell concentration and exposure time. *Free Radic. Biol. Med.* **49,** 1298–1305 (2010).

41.    Lim, T. C., Toh, W. S., Wang, L.-S., Kurisawa, M. & Spector, M. The effect of injectable gelatin-hydroxyphenylpropionic acid hydrogel matrices on the proliferation, migration, differentiation and oxidative stress resistance of adult neural stem cells. *Biomaterials* **33,** 3446–3455 (2012).

42.    Toh, W. S., Lim, T. C., Kurisawa, M. & Spector, M. Modulation of mesenchymal stem cell chondrogenesis in a tunable hyaluronic acid hydrogel microenvironment. *Biomaterials* **33,** 3835–3845 (2012).

43.    Xu, F. & Burg, K. J. L. Three-dimensional polymeric systems for cancer cell studies. *Cytotechnology* **54,** 135–143 (2007).

44.    Kaemmerer, E. *et al.* Gelatine methacrylamide-based hydrogels: an alternative three-dimensional cancer cell culture system. *Acta Biomater.* **10,** 2551–2562 (2014).

3
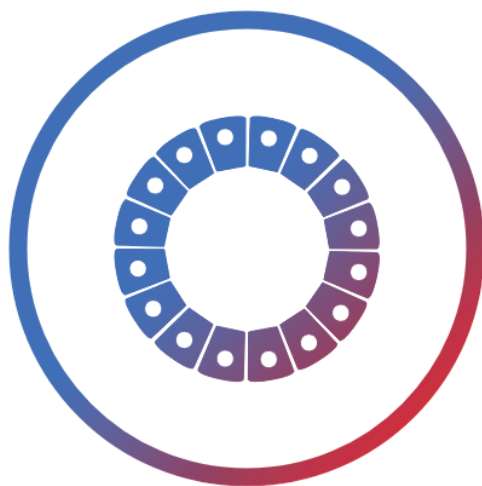
# 4

# Scalable Production of Size-Controlled Cholangiocyte and Cholangiocarcinoma Organoids within Liver Extracellular Matrix-Containing Microcapsules

Advances in biomaterials, particularly in combination with encapsulation strategies, have provided excellent opportunities to increase reproducibility and standardization for cell culture applications. Herein, hybrid microcapsules are produced in a flow-focusing microfluidic droplet generator combined with enzymatic outside-in crosslinking of dextran-tyramine, enriched with human liver extracellular matrix (ECM). The microcapsules provide a physiologically relevant microenvironment for the culture of intrahepatic cholangiocyte organoids (ICO) and patient-derived cholangiocarcinoma organoids (CCAO). Micro-encapsulation allowed for the scalable and size-standardized production of organoids with sustained proliferation for at least 21 days in vitro. Healthy ICO (n = 5) expressed cholangiocyte markers, including KRT7 and KRT19, similar to standard basement membrane extract cultures. The CCAO microcapsules (n = 3) showed retention of stem cell phenotype and expressed LGR5 and PROM1. Furthermore, ITGB1 was upregulated, indicative of increased cell adhesion to ECM in microcapsules. Encapsulated CCAO were amendable to drug screening assays, showing a dose-response response to the clinically relevant anti-cancer drugs gemcitabine and cisplatin. High-throughput drug testing identified both pan-effective drugs as well as patient-specific resistance patterns. The results described herein show the feasibility of this one-step encapsulation approach to create size-standardized organoids for scalable production. The liver extracellular matrix-containing microcapsules can provide a powerful platform to build mini healthy and tumor tissues for potential future transplantation or personalized medicine applications.

Bas van Loo,[†] Gilles S. van Tienderen,[†] Jorke Willemse,[†] Eline V. A. van Hengel, Jeroen de Jonge, Luc J. W. van der Laan, Jeroen Leijten, and Monique M. A. Verstegen.
[†] authors contributed equally to this work.

## 4.1 Introduction

Hepatobiliary organoids are valuable biomimetic ex vivo models for regenerative medicine and disease modeling purposes[1–3]. These three-dimensional organotypic cell structures recapitulate aspects of the native liver in vitro through complex cell–cell and cell–matrix interactions, which allow for self-organization[4,5]. Healthy donor-derived human cholangiocyte organoids used in a regenerative setting have shown the potential to restore damaged biliary epithelium in a preclinical model[6,7]. Simultaneously, patient-derived cholangiocyte and cholangiocarcinoma organoids offer an interesting platform for studying biliary diseases, particularly for drug screening applications[1,8–10]. However, the clinical and industrial translation of these organoids is currently limited by the use of mouse tumor-derived basement membrane extracts (BME).

Organoids are typically cultured in BME, which is a complex mixture of extracellular matrix (ECM) components derived from the mouse tumor mass produced by Englebreth-Holm-Swarm cells[11,12]. BME allows for self-organization of the cells into three-dimensional organotypic structures with maintenance of a proliferative status and can be used to create a tumor tissue-like microenvironment in vitro[5,13–15]. However, the process of cellular self-organization is uncontrolled, leading to relatively large inter-organoid disparity in size[16]. Organoid size is known to influence cell growth and division and thus introduces unwanted heterogeneity for standardization within translational applications of organoids[17,18]. This results in limited reproducibility of in vitro experiments. Furthermore, expansion of organoids in BME hemispheres is labor intensive and time consuming, which reduces scalability of the organoid cultures[19]. Thus, to overcome these limitations, there is a need for a controlled, continuous, high-throughput organoid production processes utilizing BME alternatives that are good clinical practice compliant[20].

We have recently shown that BME can be replaced by a hydrogel derived from decellularized human liver ECM[21]. This hydrogel supports the initiation and culture of cholangiocyte organoids and can unlock direct clinical applications for regenerative medicine purposes[15]. However, the use of this hydrogel does not resolve the high level of heterogeneity in organoid size and culture and still requires a time-consuming process. The incorporation of decellularized liver ECM with bioengineering encapsulation strategies could provide the necessary tools to comprehensively circumvent the persisting limitations.

In this study, we report on a microfluidic methodology for the controlled, high-throughput production of intrahepatic cholangiocyte organoids (ICO) and cholangiocarcinoma organoids (CCAO) in hybrid microcapsules containing decellularized liver-derived extracellular matrix[21]. In order to achieve this, primary human cholangiocyte and cholangiocarcinoma cells are encapsulated in a human liver extracellular matrix-containing dextran-tyramine microcapsules utilizing single-step enzymatic outside-in crosslinking in an off-the-shelf, reusable, flow-

focusing microfluidic device. Encapsulated organoids are of similar quality compared to standard BME-cultured organoids but show a high standardization with regard to size. In addition, this setup allows for the production of high quantities of tumor organoids that are similar in size and quality for scalable personalized drug screening.

## 4.2 Materials and Methods

### 4.2.1 Materials

Intrahepatic cholangiocyte organoids (ICO) (n = 5) were initiated from donor liver biopsies (0.5 cm$^3$–1 cm$^3$) following a previously published protocol[5,22]. The use of liver biopsies for research purposes was approved by the medical ethics committee of the Erasmus University Medical Center (MEC-2014-060). Cholangiocarcinoma (CCA) tumor tissue biopsies (n = 3) were obtained through liver resections performed at the Erasmus MC (MEC-2013-143) and CCAO were initiated as described previously[10]. All patients gave written informed consent to use their tissue for research purposes. In short, the biopsies were digested in 2.5 mg/mL collagenase type A (Sigma-Aldrich, St. Louis, MO, US) for 20–120 min at 37 °C. Next, the suspension was strained (70 µm cell strainer), washed with cold ADV+ (Table S1), resuspended in basement membrane extract (BME, Cultrex, R&D systems, Minneapolis, MN, United States), and plated in 25 µL droplets in 48-well suspension culture plates (Greiner Bio One, Alphen aan den Rijn, The Netherlands). The BME was allowed to solidify for 45–60 min at 37 °C before 250 µL startup expansion medium (SEM, Table S2) was added. After 72 h, SEM was replaced with Expansion Medium (EM, Table S2) and refreshed every 3 to 4 days. Organoids were passaged by mechanical dissociation every 7 days in 1:3 to 1:6 split ratios.

### 4.2.2 Human Liver for Decellularization and Hydrogel Preparation

Human livers (n = 4), deemed unsuitable for transplantation, were decellularized as previously described[23]. In short, livers were obtained after declination for liver transplantation by all transplant centers in the Eurotransplant zone. Informed consent for the use of these livers for research purposes was given to transplant coordinators of the Dutch Transplant Foundation by next of kin and was approved by the Erasmus MC medical ethics committee (MEC-2012-090).

Decellularization was achieved by continuous perfusion with Triton X-100 solution for 120 min, followed by nine 120 min reperfusion cycles with 10 L Tx100 solution. Afterward, the livers were flushed with 100 L dH2O and stored in dH2O for 10–14 days at 4 °C. This was followed by DNase treatment (10 mg/L DNase type I (Sigma) in 0.9% NaCl + 100 mM CaCl2 + 100 mM MgCl2) for eight hours at RT. Complete decellularization was confirmed based on histology and DNA quantification.

HLECM hydrogels were prepared as previously described[21]. In short, the ECM was lyophilized (Zirbus Technology Sublimator 400) and pulverized (Retsch ZM200). HLECM (40 mg/mL) was digested in 10% (W/W) Pepsin (Sigma, 3200–4500 U/mg) in

0.5 M Acetic Acid over a 72 h period at RT. Afterward, cold 10%(V/V) 10X PBS and cold 10% (V/V) ADV+ were added. PH was neutralized to 7.4–7.6 by the addition of 1 M NaOH. Solubilized HLECM concentration was measured using a Pierce BCA assay (ThermoFisher, Waltham, MA, United States) and, if needed, further diluted to 8 mg/mL. HLECM was stored at −20 °C.

### 4.2.3 Microfluidic Encapsulation

A reusable 3D microfluidic glass capillary platform was used for the production of droplets, as previously described[24]. A polymethylmethacrylate (PMMA) microfluidic device was fabricated using standard cutting and abrasion technology[24]. Fused silica capillaries (inner diameter of 200 μm; Polymicro Technologies, Phoenix, AZ, United States) were used to fabricate the nozzles by insertion into a transparent, semi-permeable silicone tubing (Helix Medical, Carpinteria, CA, United States) with a borosilicate capillary spacer (CM Scientific, Silsden, United Kingdom). The nozzles were operated in a flow-focusing configuration and enabled droplet formation, in-line monitoring of droplet formation, and allowed for diffusion-based delivery of $H_2O_2$ (Sigma-Aldrich) to controllably induce the enzymatic outside-in crosslinking of the formed droplets.

5% Dextran-tyramine (Dex-Ta) + 0.1% HLECM + 250 U/mL horseradish peroxidase (HRP) (Sigma-Aldrich) solutions were used as hydrogel precursor solution. The resulting Dex-Ta contained 14 tyramine moieties per 100 repetitive units. Droplets were produced in a N-Hexadecane (Sigma-Aldrich) oil phase supplemented with 1% Span 80 (Sigma-Aldrich) as a surfactant. Droplets were produced using a total flow rate of 100 μL/min with a water:oil ratio of 1:10 using a low-pressure syringe pump (neMESYS, Cetoni, Korbußen, Germany). The enzymatic outside-in crosslinking was induced through the transportation of droplets within a semi-permeable silicone tube that was immersed for 20 cm in a 30% $H_2O_2$ bath. Diffusion of $H_2O_2$ through the tubing and the oil phase into the Dex-Ta, HLECM, and HRP-containing droplets allowed for the formation of microcapsules. Produced microcapsules were collected in the oil. The emulsion was broken by five consecutive washes using N-Hexadecane and subsequent washes in phosphate-buffered saline (PBS).

For the production of organoid-laden microcapsules, cells were trypsinized, washed with medium, and collected using a 40 μm cell strainer. Cells were suspended in the hydrogel precursor solution at a concentration of $1 \times 10^6$ cells/mL, which was supplemented with 8% optiprep (Sigma-Aldrich) to obtain ρ = 1.05 g/L. The cell-laden hydrogel precursor solution was loaded in an ice-cooled gastight syringe (Hamilton) that was continually agitated using a small magnet in order to prevent the formation of cell clumps. Upon collection and washing, cell-laden microcapsules were divided into 12-well plates.

### 4.2.4 Cell Culture in Microcapsules

Encapsulated organoids were placed in EM, which was refreshed every 3–4 days. Cell viability was assessed using live dead staining. Organoids were incubated with

propidium iodide (50 µg/mL) and calceinAM (0.5 µM) at 37 °C and 5% $CO_2$ for 60 min. An EVOS microscope (ThermoFisher) was used to image cultures over time. The average diameter of ICO was measured using ImageJ (Version 1.53u, Bethesda, MD, USA).

At set time points (D7 and D21), organoids were fixed using 4% paraformaldehyde (Fresenius Kabi, Bad Homburg, Germany) or lysed in Qiazol (Qiagen, Hilden, Germany) lysis buffer. Lysed samples were stored at −80 °C.

### 4.2.5 FFPE Histology

Samples were washed in 1X PBS. The 1% (W/V) agarose was dissolved in PBS by heating the solution. Encapsulated organoids were placed in a 96-well plate, and PBS was removed. Agarose was added and allowed to solidify at 4 °C and subsequently embedded in paraffin. Paraffin blocks were sectioned at 4 µm thickness and stained with hematoxylin and eosin or used for immunohistological staining. For the latter, heat-induced epitope retrieval was performed using TRIS-EDTA buffer (pH = 8.0). Subsequently, slides were incubated in goat serum for 1 h before incubation of primary antibodies (listed in Table S3) overnight at 4 °C. Slides were washed using PBS before incubation (1 h, RT) with secondary antibodies (listed in Table S4). All slides were counterstained with DAPI (Vectashield anti-fade mounting medium with DAPI, Vectorlabs, Newark, CA, United States) and imaged on a Leica DM6000 CFS microscope with a LEICA TCS SP5 II confocal system. Data were processed and analyzed using ImageJ.

### 4.2.6 Whole Mount Confocal Microscopy

Fixated samples were permeabilized with 0.1% Triton X-100 in 1× PBS for 20 min. The 5% serum in 1× PBS was used to block samples for 60 min. Primary antibodies (Table S3) were incubated overnight at 4 °C. Secondary antibodies (Table S4) were incubated for 60 min. F-actin staining was performed by incubating samples with Alexa Fluor 488 Phalloidin (ThermoFisher) for 20 min at RT. All samples were counterstained with DAPI (Vectashield anti-fade mounting medium with DAPI, Vectorlabs). Samples were imaged using a Leica 20× water dipping lens on a Leica DM6000 CFS microscope with a LEICA TCS SP5 II confocal system. Data were processed and analyzed using ImageJ.

### 4.2.7 RT-qPCR

Qiazol samples were homogenized with a TissueRuptor (Qiagen, Hilden, Germany). RNA isolation was performed with the miRNeasy (Qiagen) kit according to the manufacturers' protocol, and RNA was measured on the Nanodrop 2000. cDNA (2 ng/µL) was prepared using 5x PrimeScript RT Master Mix and a 2730 Thermal cycler (Applied Biosystems, Waltham, MA, USA). RT-qPCR was performed using SYBR select master mix for SFX (Applied Biosystems) on a StepOnePlus RT PCR system (Applied Biosystems). The primers used are listed in Table S5.

### 4.2.8 In Vitro Drug Assay on Encapsulated CCAO

Preliminary to the drug response, encapsulated CCAO cell viability was measured using CellTiter-Glo (Promega, Madison, WI, USA) to equalize the relative amount of ATP in each organoid line to minimize drug response variability because of cell numbers. Next, encapsulated CCAO (n = 3) were plated out at a concentration of approximately 5000 cells/well in 96-well plates (Cellstar, Greiner Bio-One, Alphen aan den Rijn, The Netherlands). Encapsulated organoids were cultured for 24 h, and subsequently, a concentration dilution series of gemcitabine, range 0.01 µM–1000 µM (200 mg/5 mL, Sandoz, Basel, Switzerland), with a fixed concentration of cisplatin, 10 µM, (1 mg/mL, Accord) was added. Furthermore, a high-throughput drug screening using 51 drugs from the drug panel of approved oncology drugs (AOD X, NIH, dtp.cancer.gov, accessed on 15 May 2021) was added at a fixed concentration of 1 µM. After 72 h of incubation, cell viability was measured using CellTiter-Glo (Promega, Madison, WI, USA). An experimental concentration range was determined if possible, and dose-response curves were fitted using nonlinear least squares regression fitting.

### 4.2.9 Statistical Analysis

Data analysis was performed in Prism 8.0. Kruskal–Wallis test by ranks was performed on data sets with non-paired samples or different sample sizes. A Friedman test was performed on matched samples.

## 4.3 Results and Discussion

### 4.3.1 Preparation and Characterization of Crosslinker Nanoemulsion

ICO was produced by cholangiocyte cell encapsulation in microcapsules utilizing enzymatic outside-in crosslinking of cell-laden hydrogel precursor droplets as described by van Loo et al.[24] and as depicted in **Figure 4.1a,b**. Hydrogel precursor droplets flow through a semi-permeable silicone tubing, which allows for outside-in diffusion of hydrogen peroxide ($H_2O_2$), which initiates an outside-in crosslinking reaction that results in microcapsules (**Figure 4.1c,d)** with high monodispersity (coefficient of variation = 1.8%) (**Figure 4.1c,d** and **Figure S4.1a**).

The main advantage of the outside-in enzymatic crosslinking approach is the simple single-step continuous production process it utilizes, which is in contrast to multistep approaches such as microcapsules utilizing sacrificial cores[25,26], complex multiple emulsion strategies[27,28], or non-continuous layer-by-layer biofabrication[29]. Most of these complex approaches are based on ionic crosslinking of alginate hydrogels, which is considered unstable due to the inherently reversible non-covalent crosslink that is susceptible to gradual loss of divalent ions from the crosslinked alginate[30]. The
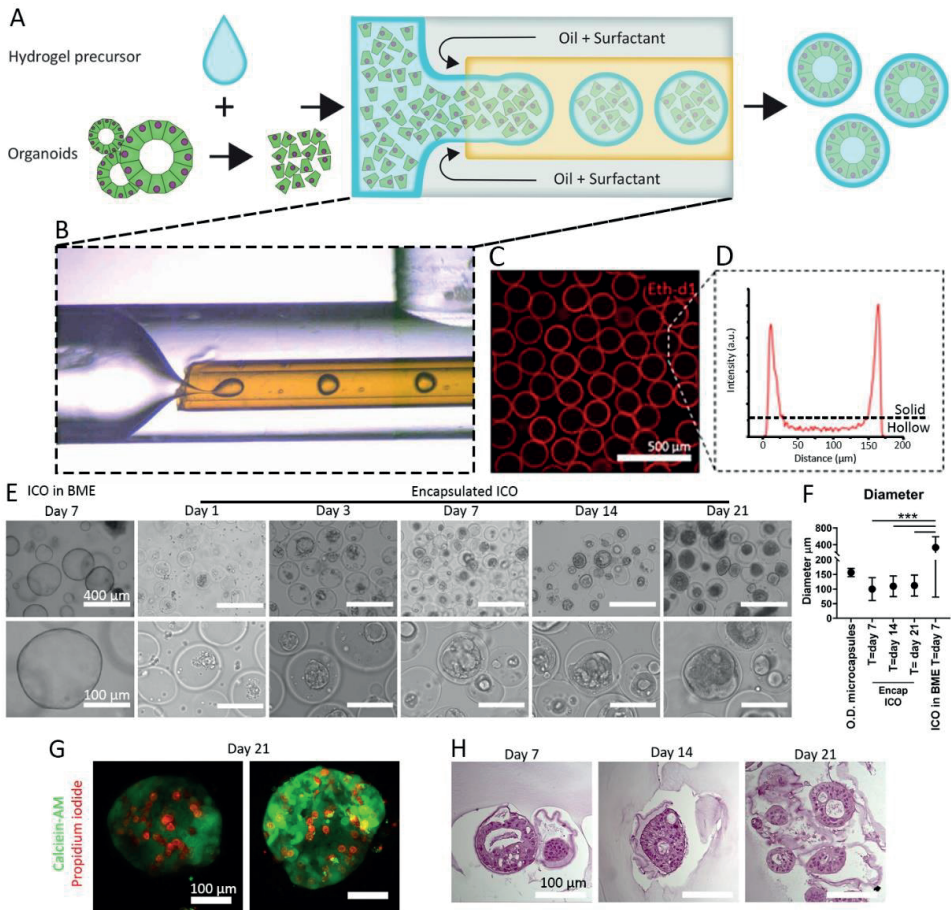
**Figure 4.1. Production of microcapsules containing ICO and liver ECM.** (A) Schematic of cell encapsulation process with single cells derived from organoids. (B) Micrograph of droplet formation in PMMA microfluidic device. (C) Confocal fluorescence images of microcapsules of which the Dex-Ta is stained with Ethidium homodimer-1 (Eth-d1). (D) Fluorescence intensity histogram of Eth-d1 stained microcapsules. (E) Bright-field microscope images of cholangiocytes cultured in BME control for 7 days or cultured in microcapsules for 1, 3, 7, 14, and 21 days. (F) Average diameter of microcapsules (O.D. = outer diameter) encapsulated ICO at days 7, 14, and 21, and control ICO grown in BME at day 7. The graph indicates mean diameter + standard deviation. Significance was tested using ANOVA. *** $p < 0.001$. (G) Representative fluorescence images of ICO in microcapsules stained with calcein-AM in green for live cells and propidium iodide in red for dead cells. (H) Bright-field microscope images of hematoxylin and eosin-stained ICO cultured for 7, 14, and 21 days.

enzymatic covalent crosslinking of Dextran-TA results in stable microcapsules, which allow for long-term cell culture and microaggregation of microencapsulated cells[24].

Cells derived from healthy ICO were encapsulated in microcapsules of 5% Dextran-TA and 0.1% human liver extracellular matrix (HLECM) microcapsules. Dextran was chosen as it is a versatile and cytocompatible biomaterial that can be modified

with relative ease (e.g., the addition of the functional tyramine group to the polymer)[31]. However, the addition of 0.1% HLECM was necessary as Dex-Ta hydrogel without HLECM did not support the self-organization of ICO (**Figure S4.1b,c**). Alternative (synthetic) ECM components, such as collagen[14], cell adhesion motifs (fibronectin or RGD)[32], or laminin-111[13,33], can be used to augment the inert polymeric backbone and to create a more tissue-mimetic or tumor surrounding[9,14,34]. These components were considered, but fine-tuning and optimizing the concentrations in designer hydrogels with ECM components can be cumbersome and challenging[15]. Alternatively, ECM extracts from decellularized tissues can be used[35]. Different publications have shown that organoids can be grown in hydrogels derived from different decellularized tissues, which include small intestinal submucosa[36] or stomach[37]. However, it was also shown that there is a tissue-specific effect of the ECM hydrogels on the organoids[37]. HLECM can successfully replace BME as a tissue-specific culture substrate for ICO; therefore, we tested this liver ECM extract to augment the Dex-Ta hydrogels[21].

The use of HLECM allowed for the formation of ICO inside Dex-Ta hydrogels and the Dex-Ta microcapsules. The cells formed aggregates after one day of culture, and these aggregates were cultured for up to 21 days inside the microcapsules (**Figure 4.1e**). The average diameter of encapsulated ICO did not significantly increase between day 7 (98 µm, SD: ±37 µm), day 14 (109 µm, SD: ±35 µm), or day 21 (112 µm, SD: ±36 µm). The average diameter of the ICO did not exceed the outer diameter (O.D.) of the microcapsules, which was 157 µm (SD: ±14 µm). Moreover, the difference between the average diameter for ICO grown in BME (332 µm, SD: ±259 µm) was significant ($p < 0.001$) when compared to encapsulated ICO. This indicates that encapsulated ICO are more size-controlled than ICO grown in BME, as there is less variation in organoid size (**Figure 4.1f**). ICO cells remained viable during the 21-day culture period (**Figure 4.1g**). Dead cells were observed inside the microcapsules; however, it remains unclear whether this is the result of the encapsulation process or normal cell death during the culture period. Similar levels of cell death are also seen in ICO grown in BME. However, in BME-grown ICO, dead cells typically accumulate in the lumen of the organoids, whereas with the encapsulated organoids, dead cells appear to accumulate in between the organoid and the capsule. Hematoxylin and eosin staining on FFPE sections showed that the encapsulated ICO has a lumen that is similar to the control ICO grown in BME (**Figure 4.1h** and **Figure S4.1c**). Of note, the thickness of the cell layers appeared thicker in the encapsulated ICO, which could be due to the columnar polarization of the cholangiocytes inside the microcapsules. Similar phenotypes were seen for cholangiocyte organoids grown on ductal ECM when cell growth was limited by space (e.g., confluent cell layers)[38,39].

Encapsulated ICO stained positive for the cholangiocyte marker KRT7 (**Figure 4.2a–c**). Proliferation marker KI67 was found to be present at day 7 but was decreased at day 21 (**Figure 4.2d**), which might be due to the organoid size restriction due to

the set microcapsule size. The zonula occludens 1 (ZO1) honeycomb structure was found both on days 7 and 21 (**Figure 4.2e–g**), indicating the formation of tight junctions at the interface of the lumen. Interestingly, in vivo ZO1 is only present inside the lumen of the bile duct, while the encapsulated ICO revealed the ZO1 honeycomb structure on both the inside and the outside of the organoids. This could indicate multiple polarized cell layers sandwiched together, with the outermost layer turned inside out. On a transcriptome level, encapsulated ICO maintained a similar expression profile as BME-cultured ICO for cholangiocyte markers KRT7, KRT19, and EPCAM, MUC1 (**Figure 4.2h**). This was also seen for stem cell marker LGR5, which in vivo is only upregulated in damaged liver tissue[40], but can be regarded as a marker for the cholangiocyte organoids. Hepatocyte-like cell marker albumin did not significantly change over the culture period. The proliferation marker KI67 appeared to decrease on the protein level by day 21 (**Figure 4.2d**) but not on the mRNA level (**Figure 4.2h**). Actually, an increasing trend of KI67 gene expression was observed at 21-day, though this did not reach statistical significance. Average gene expression of epithelial-mesenchymal transition marker vimentin remained stable, indicating that ICO does not undergo this transition after encapsulation. In conclusion, encapsulated ICO resemble ICO grown in BME on gene- and protein expression level for selected markers.

Human cholangiocyte organoids are of interest for regenerative applications, such as ex vivo repair of the damaged biliary epithelium[6,15]. Although not pursued in the current study, the high-throughput nature of the organoid production technique might be beneficiary for the clinical translation of ICO for tissue engineering applications. Alternatively, encapsulation of organoids also is of interest for more fundamental research, as more control over organoid growth, size, and cell number can be exerted, and direct co-culture systems can be engineered for probing cell–cell interactions. This can aid in standardizing assays with complex three-dimensional organoid cultures.

### 4.3.2 Engineering Functional 3D Microtissues in Hollow Hydrogel Microcapsules via Nanoemulsion-induced Crosslinking

In order to probe the versatility of the hybrid microcapsules, we also encapsulated CCAO derived from three distinct cholangiocarcinoma patients. We previously initiated these organoids from patient biopsies and confirmed their tumorigenicity[10]. Similar to ICO, the CCAO aggregated to form cellular spheroids, indicating the beneficial environment for cell encapsulation and proliferation of the tumor organoids (**Figure 4.3a**). After 21 days of culture, organoids of similar size to the microcapsules were formed, albeit with some patient-specific heterogeneity (**Figure 4.3b**). BME-cultured CCAOs utilize their intrinsic capacity to self-organize, which leads to the formation of organoids with high variability in size (**Figure S4.2**). However, as stated before, organoid size influences proliferation, in turn potentially influencing drug responses[17]. Single cells dissociated from organoids in BME can be used to perform drug screenings, but these lack the direct cell–cell interactions of
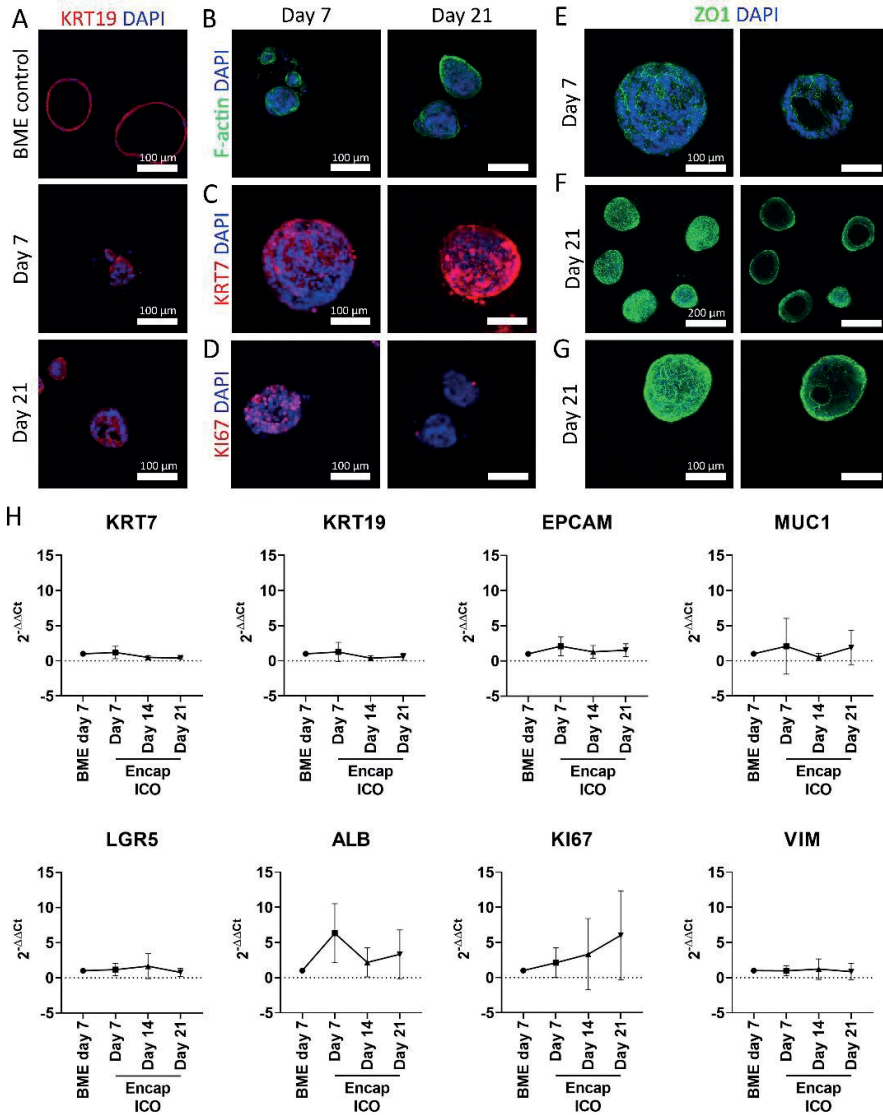
**Figure 4.2. Assessment of cholangiocyte markers of ICO cultured in microcapsules.** (A) Confocal fluorescence images of BME control ICO cultured for 7 days and microencapsulated ICO cultured for 7 and 21 days stained for KRT19 in red and DAPI in blue. (B) Confocal fluorescence images of encapsulated ICO cultured for 7 and 21 days, stained for F-actin in green and DAPI in blue, (C) KRT7 in red and DAPI in blue, (D) KI67 in red and DAPI in blue, (E–G) ZO1 in green and DAPI in blue. The left column represents the max projection of the entire Z-stack, whereas the right column only shows the max projection of a selection of the Z-stack so that the lumen of the ICO is visible. (H) Gene expression of BME control and encapsulated ICO cultured for 7, 14, and 21 days of KRT7, KRT19, EPCAM, MUC1, LGR5, ALB, KI67, and VIM (n = 5). No statistically significant differences were observed. Scale bars for (A–E) and (G) indicate 100 μm. Scale bar for (F) indicates 200 μm.

organoids. The encapsulated tumor organoids generated herein show a tight regulation of size over time, particularly when compared to gold-standard BME culture (**Figure 4.3c**). This demonstrates the efficient generation of standardized tumor organoids using the droplet-generating microfluidic system.

To quantitatively evaluate the potential change in transcriptome due to encapsulation, real-time PCR was employed. KI67, a marker for proliferation, remained constant over time, although with inter-patient heterogeneity, similar to the observations with bright-field microscopy (**Figure 4.3d** and **Figure S4.2**). Importantly, we found that the stemness of the organoids, as represented by LGR5 and PROM1 expression, was similar in encapsulated CCAO and BME-cultured CCAO (**Figure 4.3e**). Thus, the cancer stem cell phenotype, an important characteristic of organoids in BME[41], is not lost during encapsulation. Lastly, integrins play a crucial part in the reciprocal signaling occurring between cells and the extracellular matrix[42]. Integrin signaling is affected by encapsulation within the microcapsules, as ITGB1 is significantly upregulated after 14 and 21 days of encapsulation, suggesting different ECM-cell interactions occur (**Figure 4.3f**). Immunofluorescent staining confirmed the cholangiocyte-origin of the tumor organoids with high KRT7 positivity at day 7 and day 21 in all three patient lines (**Figure 4.3g**). Furthermore, F-actin was stained to visualize actin bundle alignment, which suggested actin re-arrangement over time (**Figure 4.3h**). Overall, encapsulated CCAO exhibit a relatively similar gene and protein expression profile compared to conventional BME culture, and thus, hybrid HLECM and Dex-Ta microcapsules can provide a more standardized, scalable microenvironment.

## 4.3.3 Encapsulated Cholangiocarcinoma Organoids (CCAO) Are Amendable to Drug Screening

We next investigated the feasibility of the hybrid capsules to be applied to (personalized) drug screens in a controlled format. Gemcitabine and cisplatin combinational chemotherapy is the gold standard for the palliative treatment of CCA patients[43]; thus, we incubated encapsulated CCAO for 72 h with these drugs. After combining 10 µM of cisplatin with different doses of gemcitabine, a clear dose-dependent response on cell viability was detected (**Figure 4.4a**). Differences in response were observed between patients, with CCA3 showing the highest sensitivity (IC50 0.1 µM, compared to CCA1 IC50 9.4 µM, CCA2 IC50 2.2 µM). Since dead cells were not able to escape the hybrid microcapsule, drug response could also qualitatively be observed by bright-field microscopy, which showed the accumulation of dead cells (**Figure 4.4b**). Encapsulated organoids from CCA1 show a significant difference compared to BME-cultured CCAO after gemcitabine and cisplatin exposure (10 µM: p = 0.04, Figure 4C), indicating that encapsulation influences chemo resistance of CCAO in a patient-dependent manner. To expand upon these initial findings, a large-scale drug response experiment was performed to further investigate the potential of encapsulated tumor organoids for throughput personalized medicine drug screening applications. For this, 51 FDA-approved anti-

4
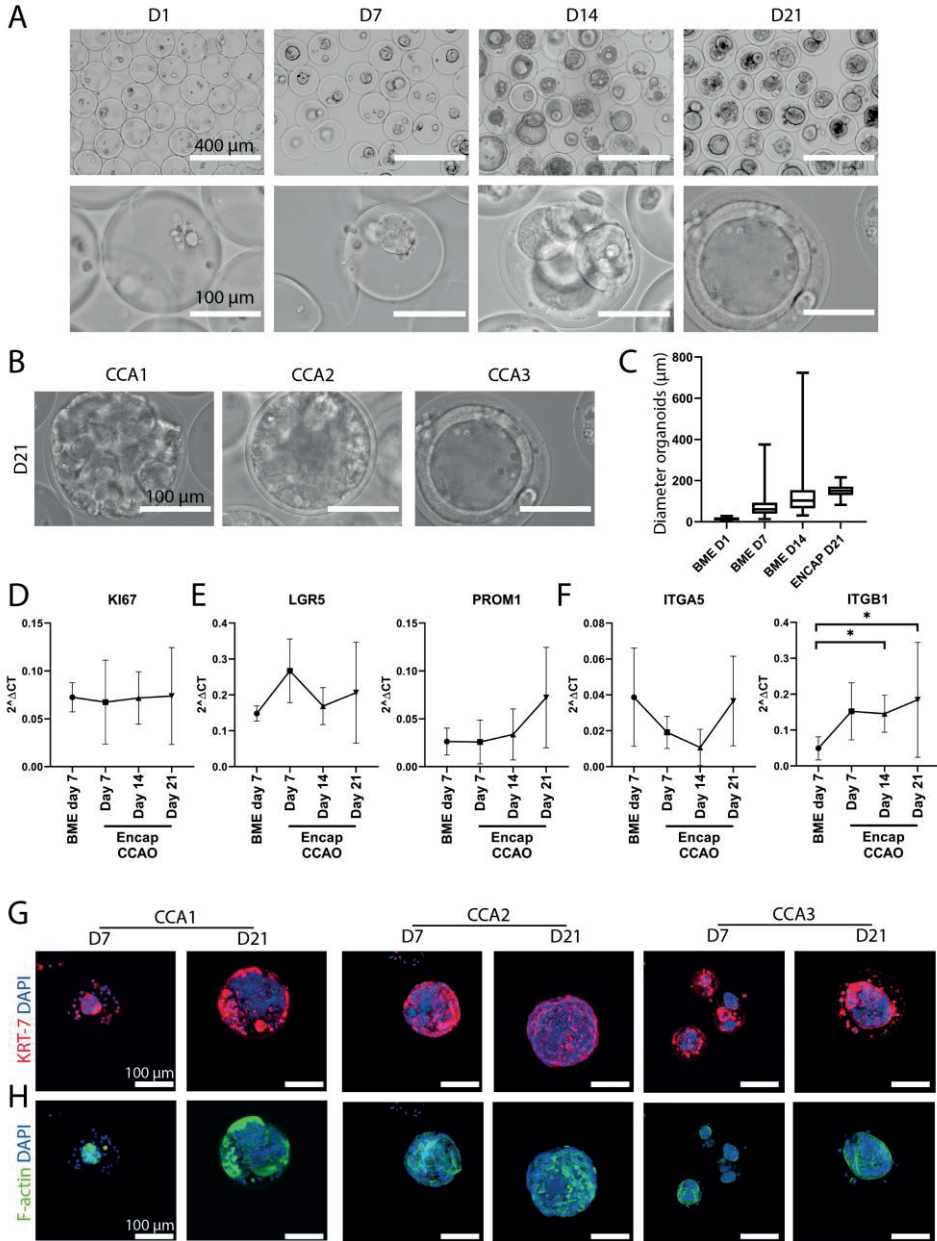
**Figure 4.3. CCAO formation and characterization in microcapsules.** (A) Representative bright-field microscope images of cholangiocarcinoma tumor cells cultured in microcapsules for 1, 7, 14, and 21 days. Scale bar indicates 400 µm in the top row and 100 µm in the bottom row. (B) Representative bright-field micrographs of three distinct patient-derived CCAO after 21 days of culture in microcapsules. Scale bar indicates 100 µm. (C) Size analysis of CCAO in BME or encapsulated in microcapsules. Shown is the mean and standard deviation of individual organoids grown in BME (Day 1: n = 46, Day 7: n = 73, Day 14: n = 73) or microcapsules (n = 117). Standard deviation was smallest in microcapsules. (D–F) Gene expression analysis using real-time PCR of BME control and encapsulated CCAO cultured for 7, 14, and 21 days of KI67

(D), LGR5, PROM1 (E), and ITGA5 and ITGB1 (F). * p < 0.05 (G,H) Confocal fluorescence imaging of encapsulated CCAO cultured for 7 or 21 days, which stained for KRT7 in red (G) and F-actin in green (H). Both images also contain DAPI staining in blue. Scale bar indicates 100 μm.

cancer drugs were tested on encapsulated CCAO of the three patients. Patient-derived organoids showed relatively high heterogeneity in drug response to the drug screening panel (**Figure 4.4d**). CCA1 had a slightly higher average relative cell viability (0.47 ± 0.41) compared to CCA2 (0.36 ± 0.33) and CCA3 (0.43 ± 0.34). However, no significant differences were present due to the large inter-drug differences. Interestingly, this encapsulated throughput approach identified both drugs that showed resistance in all three patients as well as pan-effective drugs, although the majority of responses showed high patient heterogeneity (**Figure 4.4e**). Ceritinib and Romidepsin exhibited the best pan-effective response, with preclinical data in CCA cell lines showing Romidepsin's ability to induce G2/M phase arrest[44], indicating that future research is warranted. Ceritinib was recently used in a phase I trial for solid tumors, including CCA, with a manageable toxicity profile, paving the way for further development as well[45]. Diving more into potential patient-specific effects, it is clear there is variation in the drug response to singular therapies (**Figure 4.4f**). As an example, selumetinib, which previously failed in a phase II study in CCA[42], revealed overall cell viability of 0.01, 0.9, and 1.2 for CCA1, CCA2, and CCA3, respectively. This shows a large difference in response between patients and confirms the observed overall lack of efficacy in the clinical trial. These results stress the need for personalized drug testing and demonstrate the opportunity for high-throughput-produced organoids for scalable personalized medicine. However, probing the similarities between patient and organoid drug response in the future is necessary to validate the ability of standardized production of tumor organoids to uncover pan-effective or patient-specific therapeutics.

## 4.4 Conclusion

In summary, we established a strategy for the one-step fabrication of hybrid capsules composed of dextran-tyramine and native extracellular matrix using a capillary-based flow focus microfluidic droplet generator that enabled the self-assembly and 3D culture of human cholangiocyte and cholangiocarcinoma organoids. The microcapsules are produced via an easily scalable method that allows for the size-standardized generation of organoids. The established system can facilitate the reduction of size variability conventionally seen in organoid culture by providing uniform scaffolding. As a proof-of-concept, we show the potential of the convergence of organoid technology and microfluidics for drug screening applications by observing patient-specific drug responses. This research offers a scalable platform for fundamental organoid research on cell-ECM interactions as well as translational transplantation and drug discovery applications.
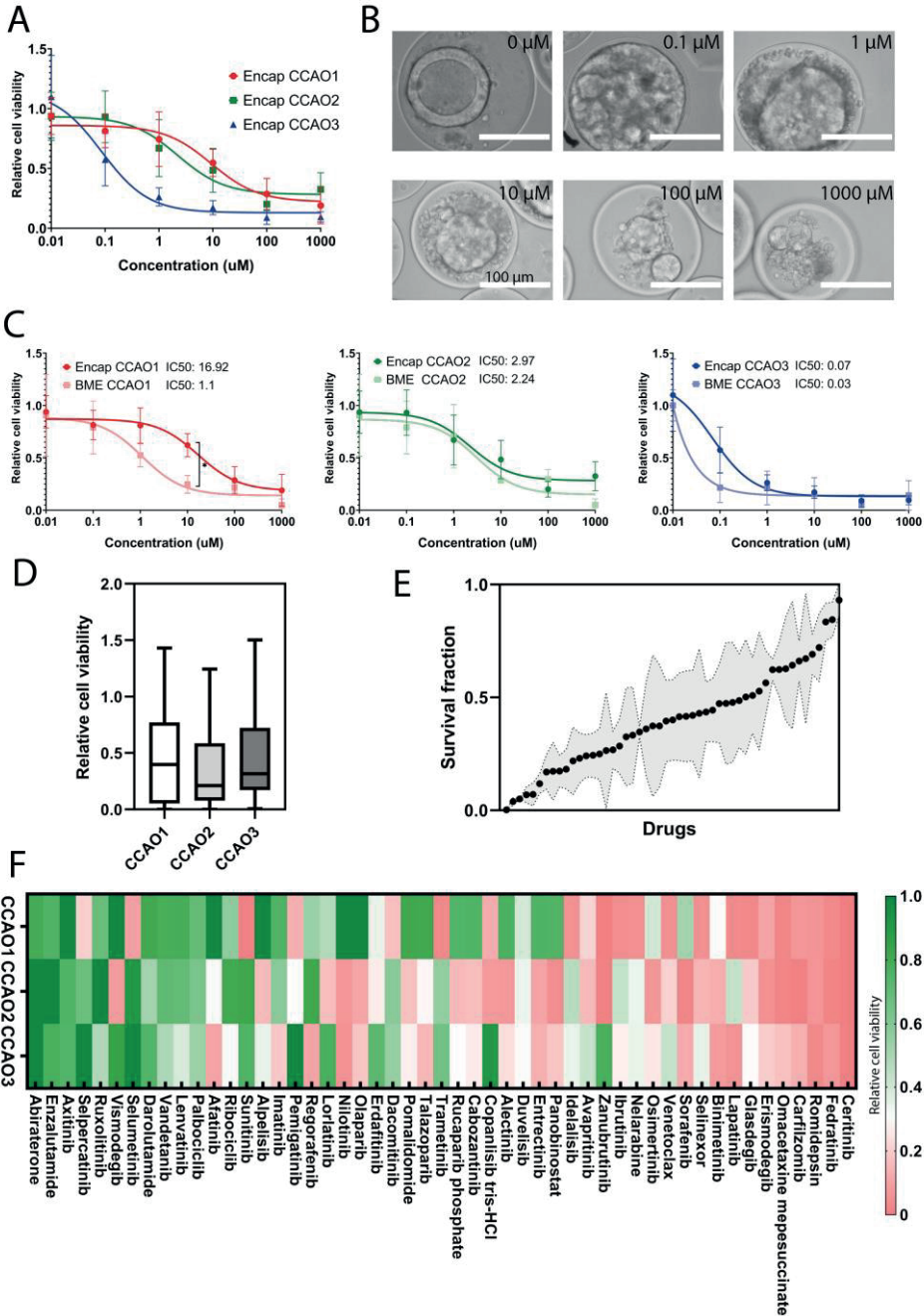
**Figure 4.4. Cell response of encapsulated CCAO in drug screening applications.** (A) Quantification of relative cell viability in encapsulated CCAO of 3 distinct donors after exposure to a fixed concentration of cisplatin and variable concentrations of gemcitabine after 72 h. Error bars indicate standard error of mean. Nonlinear regression curves were fitted to the data to determine IC50 values. (B) Representative bright-field micrographs of encapsulated CCAO1 organoids after exposure to 0 μM, 0.1 μM, 1 μM, 10 μM, 100 μM, and 1000 μM gemcitabine and 10 μM cisplatin. Scale bar indicates 100 μm. (C) Comparison of relative cell

viability for encapsulated CCAO and BME-cultured CCAO after exposure to a fixed concentration of cisplatin and variable concentrations of gemcitabine after 72 h. Error bars indicate standard error of mean. Nonlinear regression curves were fitted to the data to determine IC50 values. * indicates a statistically significant difference in drug response between CCAO1 in BME and encapsulation. (D) Quantification of average cell viability upon exposure to 51 different chemotherapeutic drugs. (E) Box plot displaying the average survival fraction of CCAO ranked from most effective to the least effective drug. Black dot indicates the average survival fraction, and the gray area represents the standard deviation. (F) Cluster map of the three different patient-derived CCAO responses to the drug response panel. Color corresponds to the relative cell viability: green represents resistance to the drugs, and red represents a sensitive response.

## 4.5 Supplementary Information
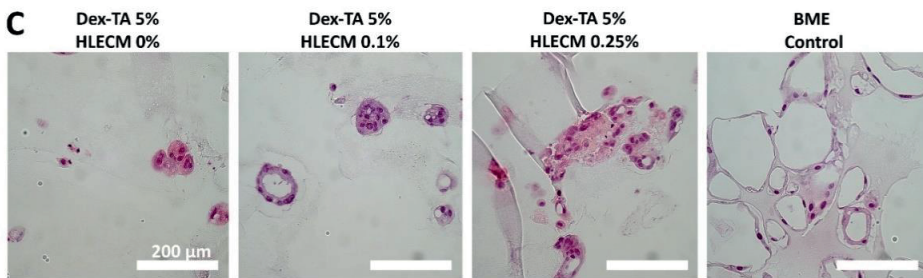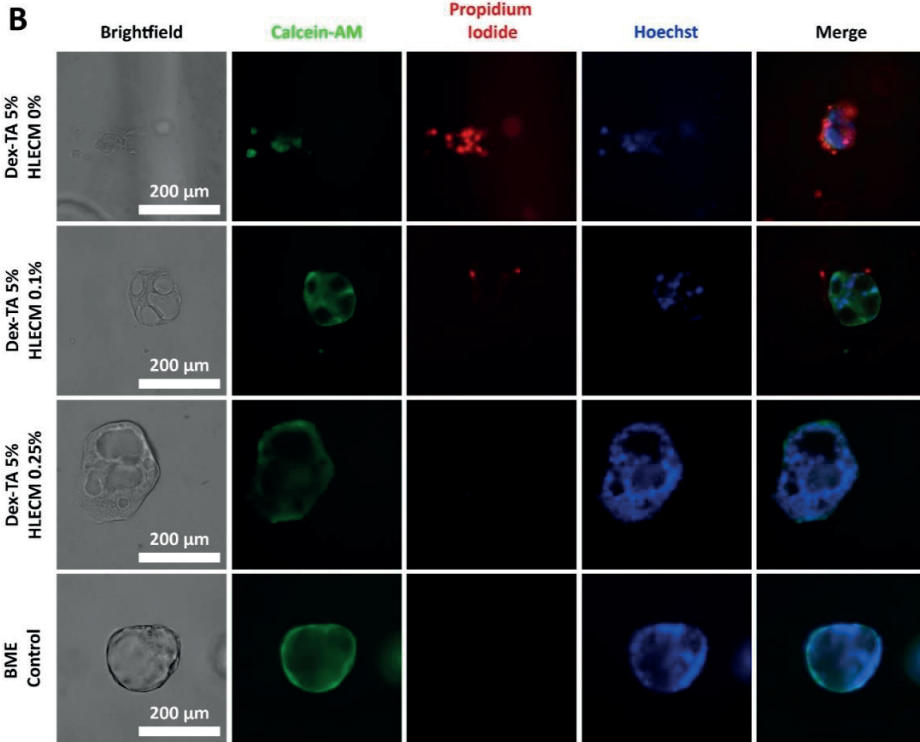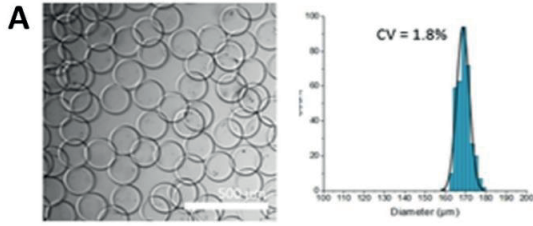
**Figure S4.1. ICO can self-assemble within Dex-Ta microgel, but can only survive with the addition of HLECM.**
A) Microcapsules can be produced with high monodispersity (CV=1.8%). B) Addition of HLECM to Dex-Ta increases cell viability, C) and allows for the self-organization of cells into organoid-like structures.
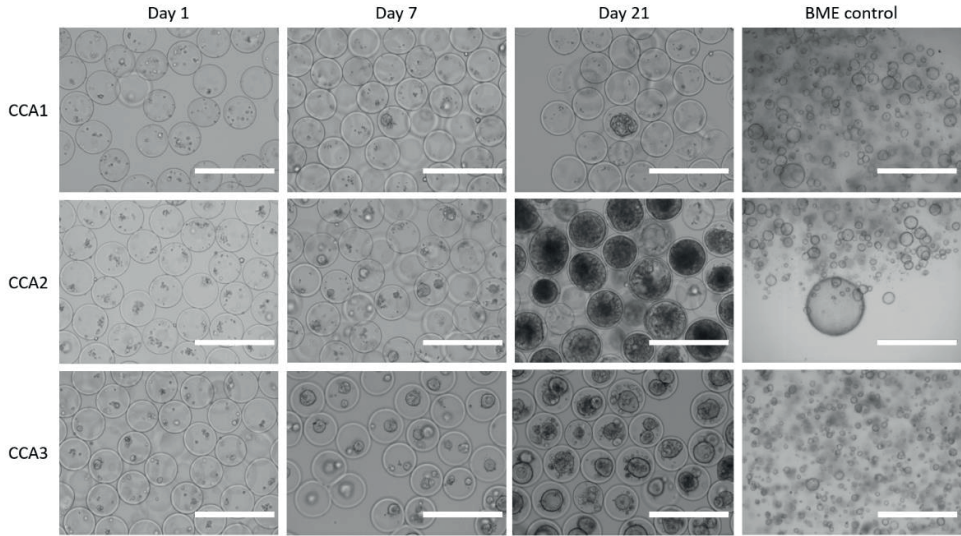
**Figure S4.2. CCAO formation in microcapsules.** Representative bright field micrographs of CCAO cultured in BME control for 7 days or cultured in microcapsules for 1, 7, and 21 days. Scale bar indicates 400 μm.

**Table S4.1.** Medium components required for the formulation of basal medium (ADV+)

| Component | Amount | Concentration | Brand |
|---|---|---|---|
| Advanced DMEM/F12 | 500ml | | Gibco |
| HEPES | 5ml | 1M | Life technologies |
| L-Glutamin | 5ml | 100X | Life technologies |
| Primocin | 1ml | 500mg/ml | Invivogen |
| Pen/Strep | 5ml | 10000 U/ml | Life technologies |

**Table S4.2.** Medium components required for the formulation of Start Up Medium (SEM) or Expansion Medium (EM). Medium components with a * are only added to SEM.

| Component | Concentration | Brand |
|---|---|---|
| Adv+ | - | Gibco |
| N2 | 1% | Gibco |
| B27 | 2% | Gibco |
| N-Acetylcystein | 1mM | Sigma-Aldrich |
| gastrin | 10 nM | Sigma-Aldrich |
| EGF | 50 ng/ml | Peprotech |
| FGF10 | 100 ng/ml | Peprotech |
| HGF | 25 ng/ml | Peprotech |
| nicotinamide | 10nM | Sigma-Aldrich |

| A83.01 | 5 µM | Tocris |
|---|---|---|
| Forskolin | 10 µM | Torcris |
| R-Spondin | 10% | Conditioned medium |
| WNT* | 30% Wnt | Conditioned medium |
| Noggin* | 25 ng/ml | Conditioned medium |
| Y27632* | 10µM | Tocris |
| hES cell cloning recovery solution* | 1:1000 dilution | Stemgent |

**Table S4.3**. List of primary antibodies used in this study

| Primary antibody | Raised in | Dilution | Supplier |
|---|---|---|---|
| ZO1 | Rabbit | 1:100 | Proteintech |
| KRT7 | Mouse | 1:100 | Dako |
| KRT19 | Mouse | 1:100 | Dako |
| KI67 | Rabbit | Ready –to-use | Kind gift from pathology |

**Table S4.4.** List of fluorescent labeled secondary antibodies used in this study

| Secondary antibody | Raised in | Against | Dilution | Supplier |
|---|---|---|---|---|
| Alexa 555 | Goat | Mouse | 1:100 | Fisher scientific |
| Alexa 488 | Goat | Rabbit | 1:100 | Fisher scientific |

**Table S4.5**. List of qPCR primers used in this study

| Primer | Species | Forward sequence 5'to 3' | Reverse sequence 5'to 3' |
|---|---|---|---|
| GAPDH | Human | CTTTTGCGTCGCCAGCCGAG | CCAGGCGCCCAATACGACCA |
| HPRT1 | Human | ACCAGTCAACAGGGGACATAA | CTTCGTGGGGTCCTTTTCACC |
| B2M | Human | GTGTCTGGGTTTCATCCATC | GGCAGGCATACTCATCTTTT |
| LGR5 | Human | GTCAGCTGCTCCCGAATCCC | TGAAACAGCTTGGGGGGCACA |
| PROM1 | Human | CCTGGGGCTGCTGTTTATTA | ATCACCAACAGGGAGATTGC |
| KRT7 | Human | GGGGACGACCTCCGGAATAC | CTTGGCACGCTGGTTCTTGA |
| KRT19 | Human | GCACTACAGCCACTACTACACGA | CTCATGCGCAGAGCCTGTT |

| EPCAM | Human | GACTTTTGCCGCAGCTCAGGA | AGCAGTTTACGGCCAGCTTGT |
| MUC1 | Human | CTGTCACTGCCGCCGAAGA | CGTGCCCCTACAAGTTGGCA |
| KI67 | Human | CTACGGATTATACCTGGCCTTCC | AGGAAGCTGGATACGGATGTCA |
| Vimentin | Human | CGGGAGAAATTGCAGGAGG | TGCTGTTCCTGAATCTGAGC |
| Albumin | Human | CTGCCTGCCTGTTGCCAAAGC | GGCAAGGTCCGCCCTGTCATC |
| CYP3a4 | Human | AGCAAAGAGCAACACAGAGCTGAA | CAGAGGTGTGGGCCCTGGAAT |
| HNF4a | Human | GTACTCCTGCAGATTTAGCC | CTGTCCTCATAGCTTGACCT |
| ITGB1 | Human | GGACGCCGCGCGGAAAAGAT | CACCCACAATTTGGCCCTGCT |
| ITGA5 | Human | AGGGTCGGGGGCTTCAACTTA | GAGCGGCAGGGTGCATACTC |

# References

1.  Clevers, H. Modeling Development and Disease with Organoids. *Cell* **165**, 1586–1597 (2016).
2.  Kim, J., Koo, B.-K. & Knoblich, J. A. Human organoids: model systems for human biology and medicine. *Nat. Rev. Mol. Cell Biol.* **21**, 571–584 (2020).
3.  Lancaster, M. A. & Knoblich, J. A. Organogenesis in a dish: modeling development and disease using organoid technologies. *Science* **345**, 1247125 (2014).
4.  Marsee, A. *et al.* Building consensus on definition and nomenclature of hepatic, pancreatic, and biliary organoids. *Cell Stem Cell* **28**, 816–832 (2021).
5.  Huch, M. *et al.* Long-Term Culture of Genome-Stable Bipotent Stem Cells from Adult Human Liver. *Cell* **160**, 299–312 (2015).
6.  Sampaziotis, F. *et al.* Cholangiocyte organoids can repair bile ducts after transplantation in the human liver. *Science (80-. ).* **371**, 839–846 (2021).
7.  Hallett, J. M. *et al.* Human biliary epithelial cells from discarded donor livers rescue bile duct structure and function in a mouse model of biliary disease. *Cell Stem Cell* **29**, 355-371.e10 (2022).
8.  Zhou, G. *et al.* Modelling immune cytotoxicity for cholangiocarcinoma with tumour-derived organoids and effector T cells. *Br. J. Cancer* **127**, 649–660 (2022).
9.  van Tienderen, G. S., Groot Koerkamp, B., IJzermans, J. N. M., van der Laan, L. J. W. & Verstegen, M. M. A. Recreating Tumour Complexity in a Dish: Organoid Models to Study Liver Cancer Cells and their Extracellular Environment. *Cancers* **11**, (2019).
10. Broutier, L. *et al.* Human primary liver cancer–derived organoid cultures for disease modeling and drug screening. *Nat. Med.* **23**, 1424–1435 (2017).
11. Hughes, C. S., Postovit, L. M. & Lajoie, G. A. Matrigel: A complex protein mixture required for optimal growth of cell culture. *Proteomics* **10**, 1886–1890 (2010).
12. Benton, G., Arnaoutova, I., George, J., Kleinman, H. K. & Koblinski, J. Matrigel: From discovery and ECM mimicry to assays and models for cancer research. *Adv. Drug Deliv. Rev.* **79**–**80**, 3–18 (2014).
13. Cavo, M. *et al.* A new cell-laden 3D Alginate-Matrigel hydrogel resembles human breast cancer cell malignant morphology, spread and invasion capability observed "in vivo". *Sci. Rep.* **8**, 5333 (2018).

14. Nii, T., Makino, K. & Tabata, Y. Three-Dimensional Culture System of Cancer Cells Combined with Biomaterials for Drug Screening. *Cancers* **12**, (2020).

15. Willemse, J., van der Laan, L. J. W., de Jonge, J. & Verstegen, M. M. A. Design by Nature: Emerging Applications of Native Liver Extracellular Matrix for Cholangiocyte Organoid-Based Regenerative Medicine. *Bioengineering* **9**, (2022).

16. Ng, E. S., Davis, R. P., Azzola, L., Stanley, E. G. & Elefanty, A. G. Forced aggregation of defined numbers of human embryonic stem cells into embryoid bodies fosters robust, reproducible hematopoietic differentiation. *Blood* **106**, 1601–1603 (2005).

17. DeStefanis, R. A. *et al.* Impact of baseline culture conditions of cancer organoids when determining therapeutic response and tumor heterogeneity. *Sci. Rep.* **12**, 5205 (2022).

18. Yoon, W. H. *et al.* Use of inkjet-printed single cells to quantify intratumoral heterogeneity. *Biofabrication* **12**, 35030 (2020).

19. Schneeberger, K. *et al.* Large-Scale Production of LGR5-Positive Bipotential Human Liver Stem Cells. *Hepatology* **72**, (2020).

20. Schot, M., Araújo-Gomes, N., van Loo, B., Kamperman, T. & Leijten, J. Scalable fabrication, compartmentalization and applications of living microtissues. *Bioact. Mater.* **19**, 392–405 (2023).

21. Willemse, J. *et al.* Hydrogels derived from decellularized liver tissue support the growth and differentiation of cholangiocyte organoids. *Biomaterials* **284**, 121473 (2022).

22. Broutier, L. *et al.* Culture and establishment of self-renewing human and mouse adult liver and pancreas 3D organoids and their genetic manipulation. *Nat. Protoc.* **11**, 1724–1743 (2016).

23. Willemse, J. *et al.* Fast, robust and effective decellularization of whole human livers using mild detergents and pressure controlled perfusion. *Mater. Sci. Eng. C* **108**, 110200 (2020).

24. van Loo, B. *et al.* Enzymatic outside-in cross-linking enables single-step microcapsule production for high-throughput three-dimensional cell microaggregate formation. *Mater. Today Bio* **6**, 100047 (2020).

25. Sakai, S. *et al.* Enzymatically fabricated and degradable microcapsules for production of multicellular spheroids with well-defined diameters of less than 150μm. *Biomaterials* **30**, 5937–5942 (2009).

26. Correia, C. R., Bjørge, I. M., Zeng, J., Matsusaki, M. & Mano, J. F. Liquefied Microcapsules as Dual-Microcarriers for 3D+3D Bottom-Up Tissue Engineering. *Adv. Healthc. Mater.* **8**, 1901221 (2019).

27. Agarwal, P. *et al.* One-step microfluidic generation of pre-hatching embryo-like core-shell microcapsules for miniaturized 3D culture of pluripotent stem cells. *Lab Chip* **13**, 4525–4533 (2013).

28. Chen, Q. *et al.* Controlled assembly of heterotypic cells in a core–shell scaffold: organ in a droplet. *Lab Chip* **16**, 1346–1349 (2016).

29. Kleinberger, R. M., Burke, N. A. D., Dalnoki-Veress, K. & Stöver, H. D. H. Systematic study of alginate-based microcapsules by micropipette aspiration and confocal fluorescence microscopy. *Mater. Sci. Eng. C* **33**, 4295–4304 (2013).

30. Lee, K. Y. & Mooney, D. J. Alginate: properties and biomedical applications. *Prog. Polym. Sci.* **37**, 106–126 (2012).

31. Jin, R., Hiemstra, C., Zhong, Z. & Feijen, J. Enzyme-mediated fast in situ formation of hydrogels from dextran–tyramine conjugates. *Biomaterials* **28**, 2791–2800 (2007).

32. Gjorevski, N. *et al.* Designer matrices for intestinal stem cell and organoid culture. *Nature* **539**, 560–564 (2016).

33. Ye, S. *et al.* A Chemically Defined Hydrogel for Human Liver Organoid Culture. *Adv. Funct. Mater.* **30**, 2000893 (2020).

34. Ye, S., Boeter, J. W. B., Penning, L. C., Spee, B. & Schneeberger, K. Hydrogels for Liver Tissue Engineering. *Bioengineering* **6**, (2019).

35. Saldin, L. T., Cramer, M. C., Velankar, S. S., White, L. J. & Badylak, S. F. Extracellular matrix hydrogels from decellularized tissues: Structure and function. *Acta Biomater.* **49**, 1–15 (2017).

36. Giobbe, G. G. *et al.* Extracellular matrix hydrogel derived from decellularized tissues enables endodermal organoid culture. *Nat. Commun.* **10**, 5658 (2019).

37. Kim, S. *et al.* Tissue extracellular matrix hydrogels as alternatives to Matrigel for culturing gastrointestinal organoids. *Nat. Commun.* **13**, 1692 (2022).

38. Willemse, J. *et al.* Scaffolds obtained from decellularized human extrahepatic bile ducts support organoids to establish functional biliary tissue in a dish. *Biotechnol. Bioeng.* **118**, 836–851 (2021).

39. Roos, F. J. M. *et al.* Cholangiocyte organoids from human bile retain a local phenotype and can

repopulate bile ducts in vitro. *Clin. Transl. Med.* **11**, e566 (2021).

40.    Huch, M. *et al.* In vitro expansion of single Lgr5+ liver stem cells induced by Wnt-driven regeneration. *Nature* **494**, 247–250 (2013).

41.    Aisenbrey, E. A. & Murphy, W. L. Synthetic alternatives to Matrigel. *Nat. Rev. Mater.* **5**, 539–551 (2020).

42.    Doherty, M. K. *et al.* Randomised, Phase II study of selumetinib, an oral inhibitor of MEK, in combination with cisplatin and gemcitabine chemotherapy for patients with advanced biliary tract cancer. *Br. J. Cancer* **127**, 1473–1478 (2022).

43.    Banales, J. M. *et al.* Cholangiocarcinoma 2020: the next horizon in mechanisms and management. *Nat. Rev. Gastroenterol. Hepatol.* **17**, 557–588 (2020).

44.    Li, P., Liu, L., Dang, X. & Tian, X. Romidepsin Induces G2/M Phase Arrest and Apoptosis in Cholangiocarcinoma Cells. *Technol. Cancer Res. Treat.* **19**, 1533033820960754 (2020).

45.    Fountzilas, C. *et al.* A phase I study of the anaplastic lymphoma kinase inhibitor ceritinib in combination with gemcitabine-based chemotherapy in patients with advanced solid tumors. *Int. J. Cancer* **149**, 2063–2074 (2021).

**4**

# 5

# Mass Production of Lumenogenic Human Embryoid Bodies and Functional Cardiospheres using In Air Generated Microcapsules

Organoids are engineered 3D miniature tissues that are defined by their organ-like structures, which drive fundamental understanding of human development. However, current organoid generation methods associate with low production throughputs and poor control over size and function including due to organoid merging, which limits their clinical and industrial translation. Here, we present a microfluidic platform for mass production of lumenogenic embryoid bodies and functional cardiospheres. Specifically, we apply triple-jet in air microfluidics for the ultra-high throughput generation of hollow, thin-shelled, hydrogel microcapsules that can act as spheroid forming bioreactors in a cytocompatible, oil-free, surfactant-free, and size-controlled manner. Uniquely, we show that microcapsules generated by in air microfluidics provide a lumenogenic microenvironment with near 100% efficient cavitation of spheroids. We demonstrate that upon chemical stimulation, human pluripotent stem cell-derived spheroids undergo cardiomyogenic differentiation, effectively resulting in the mass production of homogeneous and functional cardiospheres that are responsive to external electrical stimulation. These findings drive clinical and industrial adaption of stem cell technology in application areas, such as tissue engineering and drug testing.

Bas van Loo, Simone A. ten Den, Nuno Araújo-Gomes, Vincent de Jong, Rebecca R. Snabel, Maik Schot, José M. Rivera-Arbeláez, Gert Jan C. Veenstra, Robert Passier, Tom Kamperman, and Jeroen Leijten.

## 5.1 Introduction

Organoids are engineered 3D miniature tissues characterized by tissue or organ structures, which can advance our fundamental understanding of human development and has the potential to revolutionize our healthcare system.[1–4] Specifically, organoids enable the study and treatment of diseases in a biomimetic, human-based, patient-specific, ethical, and animal-free manner.[1,5,6] Organoids have, amongst others, been successfully applied to study infectious and hereditary diseases, screen active pharmaceutical ingredients, model cancer, and develop personalized therapies including regenerative medicine approaches.[7–19] Despite these successes, the translation of organoids to many real world applications has been hampered by our inability to upscale the engineering of organoids while maintaining reproducibility and quality.[20]

Cell fate within embryoid bodies (EBs) and organoids is highly dependent on morphogenic signaling. Therefore, control over their composition, size, and shape is essential to recapitulate organogenesis *in vitro*.[21] Yet, engineering well-defined microenvironments that offer size-controlled, reproducible, and scalable EB and organoid production still remains among the biggest hurdles for clinical and industrial translation of this technology.[22,23] Lab-scale EB and organoid production conventionally relies on well-plate-format suspension cultures where stem cells are grown atop low-adhesive (micropatterned) materials[24,25] or within hydrogels,[26] resulting in limited size control. Compartmentalization in (micro)wells[3,27–31] or within hanging droplets[32] can offer improved size control. While these studies frequently claim high throughput, they often rely on batch-based processes that can only facilitate limited and small-scale investigative studies, which are unable to facilitate large-scale studies, clinical translation, and industrial valorization.[20] In contrast, microfluidic production processes allow for continuous production of size-controlled organoids.[20] Consequently, microfluidic encapsulation of (human) pluripotent stem cells (hPSCs) into semi-permeable and chemically defined microcapsules holds the potential for scalable and size-controlled organoid production. As an additional benefit, microencapsulation of pluripotent stem cells in microcapsules also prevents the clumping/fusion of engineered organoids, which currently adversely affects the upscaling of suspension cultures.[33] Currently available microfluidic microencapsulation approaches often claim high throughput while operating in the dripping regime, which is archetyped by limited throughputs in the µl/min range. Furthermore, conventional microfluidic technologies are associated with reliance on emulsifications using oils and surfactants[34–37] which are known for immune adjuvant effects,[36] and contribute to development of autoimmune diseases.[36] While microfluidic organoid production approaches are moving towards all-in-water technologies, these often rely on operation in dripping regime and its inherent limited throughputs that are in the µl/min range,[38–43] or have difficulties in achieving monodispersity.[44–48] Due to this combination between low-throughput, low control or a non-clean (e.g. oil and surfactant containing) production process these

technologies do not support clinically or industrially translation of organoid production. Consequently, an innovative microfluidic technology that allows for scalable, size-controlled, reproducible, and clean (e.g. oil-free and surfactant-free) organoid production has remained urgently wanted.

In this work, we report on the ultra-high throughput generation of uniform and functional pluripotent stem cell derived EBs and cardiospheres using a production platform based on in-air microfluidics (IAMF). Specifically, we pioneer in-air coalescence of three independently tunable liquid microjets to enable the continuous on-the-fly encapsulation of (pluripotent stem) cells in ultrathin-shelled hydrogel microcapsules. Due to its oil-free, chip-free, and jet-based nature, the triple-jet IAMF method overcomes the impermeability,[49] material degradation,[49] biocompatibility [35,36,50–52], and throughput challenges of current on-chip stem cell compartmentalization approaches with ml/min-range throughputs, while retaining high control and resolution. This unique combination distinguishes the triple-jet in-air microfluidic technology from conventional microfluidics by offering both true scalability and accurate control, which is essential for clinical and industrial translation. The microcapsules offer a highly lumenoconductive microenvironment as near 100% efficient lumen formation (i.e., lumenogenesis) and facilitates radial cell/nucleus polarization under physically and chemically defined conditions. Moreover, upon chemical stimulation, the cell spheroids undergo cardiomyogenic differentiation effectively yielding large amounts of functional (i.e., beating) cardiospheres that are responsive to external electrical stimulation. In short, we report on the continuous, ultra-high throughput production of homogeneous, size-controlled, cellular aggregates, cavitated spheroids, and functional cardiospheres, which is anticipated to drive the clinical and industrial adaption of spheroid and organoid technology in application areas that need ultra-high throughput tissue production such as tissue engineering, drug testing, and cultured meat.

## 5.2 Materials and Methods

### 5.2.1 Triple-jet in air microfluidic setup

The IAMF setup for hollow microgel formation consisted of three tapered nozzles with various diameters of which the second and third nozzle were placed under ± 40° on the left and right of the central nozzle respectively, and were aligned using micrometer-precision XYZ-stages. The nozzles were connected with fluorinated ethylene propylene tubing (FEP) to Luer-lock glass syringes, of which the flow rate was controlled by Cetoni neMESYS low-pressure syringe pumps. The central nozzle was vibrated using a piezoelectric actuator, which was operated at 5 Vpp and frequencies between 1 and 10 kHz, allowing controlled break-up of the microjet. Depending on the nozzle diameter used, an optimized piezoelectric frequency was used to achieve monodisperse break-up of the microjet in microdroplets. The microjet of the second nozzle was aligned such that it coalesced with the formed droplet train in a stable manner, which was repeated for the microjet of the third

nozzle. Proper droplet break-up and coalescence of the microjets was confirmed using a high-speed microscope camera (IDS, UI-3240CP Rev. 2).

## 5.2.2 Alginate hollow microcapsule production and analysis

Production method of alginate hollow microcapsules was, unless stated otherwise, achieved as follows. The first microjet consisted of 10% (w/v) dextran and 50 mM calcium chloride ($CaCl_2$) in $dH_2O$, the second microjet consisted of 0.2% (w/v) alginate and 10% (v/v) ethanol (EtOH) in $H_2O$, and the third microjet consisted of 0.2 M $CaCl_2$ and 55% (v/v) EtOH in $dH_2O$. By using different nozzle diameters, it was possible to produce alginate hollow microcapsules in 3 different size regimes; being small (180 ± 8 μm), medium (243 ± 9 μm), or large (459 ± 17 μm). For small microcapsules, nozzle diameters of 50 μm, 50 μm, and 100 μm, with flow rates of 0.9 ml/min, 1.1 ml/min, and 1.5 ml/min were used respectively for the first, second, and third microjet with an actuator frequency of 5.5 kHz. For medium size microcapsules, nozzle diameters of 100 μm, 100 μm, and 150 μm with flow rates of 2 ml/min, 2.2 ml/min, and 2.6 ml/min were used respectively for the first, second, and third microjet with an actuator frequency of 5.5 kHz. For large size microcapsules, nozzle diameters of 150 μm, 150 μm, and 250 μm with flow rates of 3 ml/min, 3.2 ml/min, and 4.6 ml/min were used respectively for the first, second, and third microjet with an actuator frequency of 2.5 kHz. Produced hollow microcapsules were collected in a 0.1 M $CaCl_2$ in $dH_2O$ collection bath. The microjets were characterized by We ± 25. Using collisional angles of ± 40°, this corresponded to $We_{impact}$ ± 10. Produced hollow microcapsules were visualized using brightfield microscopy (EVOS FL Imaging System, ThermoFisher). Size distribution, monodispersity, circularity, amount of cores and shell thickness were analyzed using ImageJ software. To visualize the hollow nature of the microcapsules, 0.5 mg/ml 2000 kDa Dextran-FITC was added to the second microjet when producing the hollow microcapsules in order to achieve a fluorescent shell of the hollow microcapsules. Fluorescently labeled hollow microcapsules were then analyzed by confocal z-stack microscopy analysis (Nikon A1 confocal laser microscope). Permeability experiments were performed by 30 minute incubation of microcapsules in a bath containing 0.5 mg/ml Dextran-FITC of 150 kDa, 500 kDa, and 2000 kDa before visualization using fluorescent confocal microscopy (Nikon A1 confocal laser microscope).

## 5.2.3 PEGDA hollow microcapsule production

Poly(ethylene glycol) diacrylate (PEGDA) hollow microcapsules were produced in identical manner as small alginate microcapsules, with the exceptions that 10% (v/v) PEGDA and 0.25% (w/v) and Irgacure 2959 were additionally added to the second microjet. The third microjet was aligned such that the impact took place 8.9 ms after the second microjet coalesced with the first microjet, which corresponded to a height difference of 8 cm between the second and third microjets. A UV lamp (LAMP) was aimed at the collection bath and was used to photocrosslink the PEGDA in the shell of the alginate hollow microcapsules during production and for 1 minute after collection at 25% UV power. After this, a 1% EDTA in $dH_2O$ wash was

used to remove the alginate. The resulting PEGDA hollow microcapsules were analyzed using brightfield microscopy.

## 5.2.4 Dex-TA hollow microcapsule production and analysis

Tyramine-conjugated dextran (Dex-TA) was synthesized as described previously[53]. In short, dextran was activated with a p-nitrophenyl carbonate group (PNC), dissolved in DMF, after which TA was added under nitrogen. The degree of substitution of the produced Dex-TA was determined to be 15 by proton-NMR. Dex-TA hollow microcapsules were produced in identical manner as small alginate microcapsules, with the exceptions that 5% (w/v) Dex-TA and 57.5 U/ml horseradish peroxidase (HRP) were additionally added to the second microjet. The collection bath additionally contained 0.1% $H_2O_2$ in $H_2O$ to allow for enzymatic crosslinking. After 1 minute of the enzymatic crosslinking post-cure, the hollow microcapsules were washed with 1% EDTA to remove the alginate. The resulting Dex-TA hollow microcapsules were stained with 30 µM of ethidium homodimer (EthD-1), and analyzed using brightfield microscopy and fluorescence confocal microscopy.

## 5.2.5 Oil residue in chip based approaches

Chip-based hollow microcapsule production was performed as described previously[54,55]. In short, a polymethyl methacrylate (PMMA) microfluidic chip was used in a flowfocusing setup to produce droplets consisting of 5% Dex-TA and 250 U/ml HRP within an oil phase of n-hexadecane with the addition of 1% (v/v) Oil-red-O and 1% span 80 as a surfactant. The resulting emulsion was broken by three consecutive washes using n-hexadecane without surfactant and a subsequent wash with phosphate buffered saline (PBS). Absorption of n-hexadecane with and without Oil-red-O and hollow microcapsules produced using chip-based microfluidics or IAMF was measured using spectrophotometry (Multiskan Go Microplate; Thermo Scientific) at 512 nm.

## 5.2.6 Cell culture

3T3 Fibroblasts (ATCC, CRL-1658) were cultured in Dulbeco's Modified Eagle Medium (DMEM) supplemented with 10% Fetal Bovine Serum (FBS), 50 µM 2-mercapto-ethanol, 100 U/ml penicillin and 100 µg/ml streptomycin. Culture medium was changed biweekly, when 80% confluency was reached. Cells were kept in a humidified environment at 37 °C with 5% $CO_2$ before use.

The dual fluorescent human pluripotent stem cells (human embryonic stem cells) reporter lines MESP1(mCherry/NKX2-5(eGFP)[56] derived from hESC HES3 (female) (ESIBI), hPSCreg database: ESIBIe003-A clone 3A1 hetero zygote, and ACTN2(mRubyII)/NKX2-5(eGFP)[57] derived from hESC HES3 (female) (ESIBI), hPSCreg database: ESIBIe003-A clone 3A1 hetero zygote. were cultured in Essential 8 medium (E8) (Thermo Fisher) supplemented with 50 U/ml penicillin and 50 µg/ml streptomycin (Thermo Fisher) on Vitronectin (Thermo Fisher) coated plates. Cells

were passaged twice a week and refreshed the day after passaging. Cells were cultured in a humidified environment at 37 °C with 5% CO2.

## 5.2.7 Cell encapsulation

To optimize the cell loading concentration, 3T3 cells were fixed using a 10% buffered formalin solution (ThermoFisher), and added to the first microjet solution in concentrations ranging from $10^6$ to $10^7$ cells/ml. The number of cells per gel was confirmed based on confocal microscopy analysis following EthD-1 staining of the fixed cells. For the production of live cell-laden alginate hollow microcapsules, $dH_2O$ in all microjet solutions was exchanged with DMEM without phosphates. Detached cells were washed with medium, flown through a 40 μm cell strainer, and suspended in the first microjet solution at a concentration of $10^7$ cells/ml. The cell-laden first microjet solution was loaded into an ice-cooled gastight syringe. Cell sedimentation and subsequent clumping in the syringe was prevented through the dextran crowder, the addition of a frequently stirred magnet, and by keeping the syringe on ice. Nozzle diameter and flow rate parameters were selected for medium-sized microcapsule production. Cell-laden hollow microcapsules were collected in a large collection bath containing 50 ml of 0.1 M $CaCl_2$ in DMEM without phosphates in order to immediately dilute the EtOH to cell-viable concentrations below 2% (v/v). Cell-laden microcapsules were then immediately washed using a 70 μm cell strainer and resuspended in cell culture medium within 2 minutes upon collection. The cell-laden hollow microcapsules were transferred to culture plates for cell culture. For additional analyses, cell-laden hollow microcapsules were first washed with PBS and fixated using a 10% formalin solution. Cells were permeabilized using 0.1% Triton X-100 and subsequently stained with 2.5 U/ml of phalloidin-AF488 and 10 of μg/ml DAPI to stain F-actin and nuclei respectively and analyzed by confocal microscopy (Nikon confocal A1). Cell viability of cell-laden hollow microcapsules was studied using calcein AM and ethidium homodimer-1 staining according to manufacturer's protocol (Invitrogen) and imaging using a digital fluorescence microscope (EVOS FL Imaging System, ThermoFisher) in multiple independent experiments. Spheroids were retrieved from their microcapsules via exposure to 10 U/ml of alginate lyase at day 0-4 or exposure to PBS after day 4.

## 5.2.8 Pluripotent spheroid production

Human pluripotent stem cells (human embryonic stem cells, derived from hESC HES3 (female), hPSCreg database: ESIBIe003-A. Sequencing, karyotyping and marker analysis was performed for identification) were encapsulated using the In Air cell encapsulation method as described above, using a concentration of $2*10^6$ cells/ml such that approximately 20 cells were encapsulated per microcapsule. During the first 24 hours, cell-laden microcapsules were cultured in Essential 8 (E8) medium[58] supplemented with PVA and ROCK inhibitor. Afterwards, cell-laden microcapsules were cultured in E8 medium, which was refreshed every other day. Encapsulated embryoid bodies were analyzed for aggregation efficiency, cavitation efficiency, embryoid body diameter, and cavity diameter by brightfield microscopy. Cell

viability analysis was performed as described above. For microwell-mediated production of embryoid bodies, round-bottom 96-wells plates were used for the production of 5000 cell aggregates, and alginate microwells with a diameter of 200 µm per well were used to produced 500 and 20 cell aggregates, as described by Moreira Teixeira et al.[59] Cavitation was assessed via nuclei staining using DAPI as described above. Distance of nuclei to hPSC spheroid centroid was measured in fluorescent confocal z-stacks of DAPI stained embryoid bodies using ImageJ software. To analyze cellular orientation as well as nuclear position within the cell, live cells were exposed to Draq5 (5 µM) to stain nuclei, and CellMask Green (1000X dilution of stock) to stain cell membranes, which were analyzed using fluorescence confocal microscopy. To analyze pluripotency, cells were stained for Sox2 and Oct3/4 using antibodies (Sox2: eBioscience, 53-9811-82, 1:100 dilution. Oct3/4: Santa Cruz Biotechnology, sc-5279 AF647, 1:100 dilution). In short, embryoid bodies that were cultured for six days were permeabilized with 0.1% Triton in 0.5% BSA, blocked with 5% FBS, and stained with Sox2 and Oct3/4 antibodies at 1:100 and DAPI at 1:4000 in 1% BSA overnight. Stained embryoid bodies were analyzed using fluorescence confocal microscopy.

## 5.2.9 Cardiosphere production

The dual fluorescent hPSC reporter lines MESP1(mCherry/NKX2-5(eGFP) and ACTN2(mRubyII)/NKX2-5(eGFP) (human embryonic stem cells, derived from hESC HES3 (female), hPSCreg database: ESIBIe003-A. Sequencing, karyotyping and marker analysis was performed for identification) were encapsulated using the In Air encapsulation method as described above, using a concentration of $2*10^6$ cells/ml. During the first 24 hours, cultures were exposed to E8 medium supplemented with PVA and Y-27632 ROCK inhibitor. From day 1 till day 4 cultures were exposed to BPEL medium[60] containing, 30 ng/ml Activin A, 30 ng/ml BMP-4, 1.5 µM CHIR99021, 30 ng/ml VEGF, and 40 ng/ml SCF (Stem Cell Factor) in order to induce mesoderm differentiation.[61] Medium was refreshed at the end of day 2. From day 4 till day 22 cultures were exposed to BPEL medium without supplements, which was refreshed 2/3 times per week. Activation of the *MESP1* and *NKX2-5* genes were analyzed for encapsulated cardiospheres using fluorescence confocal microscopy (mCherry and eGFP, respectively). The percentage of NKX2-5/eGFP positive cells was determined by FACS analysis after trypsinization of cardiospheres, which were cultured for 22 days. Calcium flux of encapsulated cardiospheres was analyzed using Fluo-4 AM (Thermo Fisher) calcium imaging (5 µM) measuring fluorescence intensity over time using fluorescence microscopy. To electrically stimulate encapsulated cardiospheres, two platinum electrodes (Advent Research Materials) connected to a custom-made pacing device were placed in a cardiosphere containing well of a 96 wells plate, and paced with 5V (10 ms biphasic pulses, 7–10 V/cm²) at frequencies ranging from 0.5 to 2 Hz. α-Actinin (mRubyII) was imaged using fluorescence microscopy (Nikon ECLIPSE Ti2 inverted microscope). Both sarcomere contraction and contraction amplitude was analyzed by means of fraction area change using ImageJ software.

5

## 5.2.10 Single cell RNA sequencing

Encapsulated EBs and cardiospheres were harvested at day 6 and day 21 respectively by dissolving the microcapsule using alginate-lyase as described in the cell encapsulation section. Cells were dissociated into single cell suspensions using TrypLE (Gibco) and sorted into 384-wells plates containing primers with unique molecular identifiers (UMI), unique cellular barcodes and an oligo-(dT-N) for tagging the mRNA molecules. Single cell RNA sequencing barcode file is added as a supplementary data file Supplementary Data 2.tab. Directly after sorting, the plates were spun down and stored at -80°C until library preparation. The sorted 384-well plates were processed using a modified CEL-Seq2 protocol.[62] In short, ERCC spike-in (1:50,000) were dispensed using a Nanodrop II (BioNex Solutions Inc.) in each well. After a 5 min. incubation step at 65°C, 150 nL of the Reverse Transcription (RT) mix was dispensed into each well and the first strand synthesis was performed with the following thermal cycles: 4°C 5 min, 25°C 10 min, 42°C 1 hrs, 70°C 10 min. Within an incubation of 2 hrs at 16°C the second strand synthesis with E. coli DNA polymerase and E. coli DNA ligase (New England Biolabs), supplemented with E. coli RNase H (Invitrogen), was performed in the plate. After each of the dispensing steps, the plates were spun down at 1000 xg for 1 min at 4°C. Subsequently, the cDNA from the wells were pooled per plate and purified using AmpureXP (Beckman Coulter). Overnight in vitro transcription (Ambion MEGAScript; Invitrogen) for 14 hrs at 37°C, was followed by a 20 min at 37°C exonuclease step and chemical fragmentation of the amplified RNA. The sample was purified using the AmpureXP beads, after which a library RT and amplification PCR (with 9 cycles) was performed to introduce unique sample indices to the plate libraries. After a final beads purification, the sample was quantified using the Denovix HS dsDNA assay and checked for library quality using the BioAnalyzer (Agilent Technologies). The samples were sequenced on the NextSeq 500 (Illumina) platform, at a depth of 20 million reads per plate. Trimming of the reads and alignment was performed with seq2science v0.6.0 (available in Zenodo, https://doi.org/10.5281/zenodo.4451349). In short, kb-python v0.26.4[63] was used (kb count with the setting '--technology 1,8,16:1,0,8:0,0,0') for mapping against the GRCh38 genome and quantified the UMI counts per cell. The Scater package v1.20.1[63] was used for pre-processing and quality control. Only cells with a minimum of 500 detected genes and 1,000 total counts, and a maximum of 50% mitochondrial transcripts and 20% of ERCC transcripts were kept in the analysis. Genes with an expression of 1 count in at least 2 cells were kept. Normalization and downstream analysis, such as dimensionality reduction and Louvain clustering was performed with the Seurat package v4.0.4.[64] The SCTransform function was used to normalize the data and select the 2000 highly variable genes (HVG) in the dataset. The cells were clustered using a shared nearest neighbor (SNN) modularity optimization based clustering algorithm with a resolution of 0.9 and were projected onto Uniform Manifold Approximation and Projection (UMAP) using the first 10 principle components (PCs). Differential gene expression analysis between conditions was performed with a t-test in the FindMarkers function of Seurat, on the

genes expressed in at least 20% of the cells in either of the clusters. The resulting differential gene lists were filtered for a log-fold change > 1 and a p-adjusted value of < 0.05 and the ComplexHeatmap package[64] was used to visualize the sets of genes. Gene Ontology enrichment analysis was performed with the clusterProfiler v4.0.5 package.[65]

### 5.2.11 Statistics

Sample size per experiment is reported in figure descriptions. Significance was determined based on one-way Anova analysis. Significance of $p < 0.05$ is indicated by *. All statistical analyses were performed in OriginPro2017.

### 5.2.12 Data availability

The single cell RNA sequencing data generated in this study have been deposited in the Gene Expression Omnibus database under accession number "GSE219249 [https://www.ncbi.nlm.nih.gov/geo/query/acc.cgi?acc=GSE219249]".

## 5.3 Results and Discussion

### 5.3.1 Triple-jet IAMF enables high-throughput fabrication of monodisperse, hollow, thin-shelled microcapsules for controlled spheroid, embryoid body, and cardiosphere formation

In-air microfluidics (IAMF) is a recently invented jet-based microfluidic technology that enables ultra-high-throughput, oil-free, chip-free, and cytocompatible production of monodisperse solid microparticles.[66] However, creating monodisperse, hollow, micrometer-sized hydrogel capsules (e.g., microcapsules) has remained a challenge and has thus prevented its use in organoid production. Conventionally, in IAMF, a first monodisperse hydrogel precursor droplet train is produced by superimposing a vibration on a jetting micronozzle that is combined with a second crosslinker jet, which results in a stream of monodisperse compound droplets. The use of a rapidly crosslinking material combination (e.g., alginate and a divalent cation such as calcium) results in on-the-fly stabilized particles of controlled size. However, producing microcapsules with the existing IAMF approaches cannot be reliably achieved as they associate with the merging of capsules into larger, poorly defined multi-core constructs (**Figure S5.1**).[66] Here, we report on an IAMF strategy that prevents the merging of microcapsules via the introduction of a third microjet, which allows for the stable in-air production of triple-layered aqueous droplets (**Figure 5.1a, Figure S5.2 Supplementary Video 5.1**). The addition of a third microjet enables the Marangoni-driven encapsulation of the droplets to occur twice, which enabled simultaneous inside-out and outside-in crosslinking of the alginate shell (i.e., middle phase) by calcium ions in the crosslinker liquids (i.e., inner and outer phases). Importantly, this allows for the jet-based production of thin shelled microcapsules at a rate that is more than two orders of
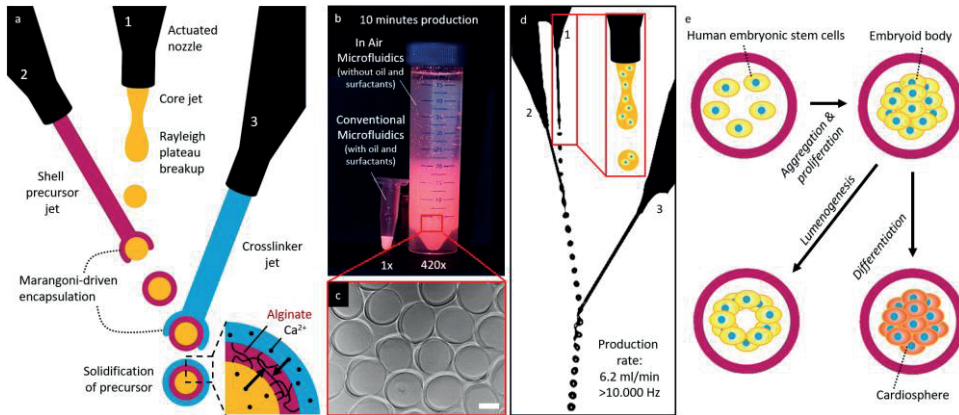
**Figure 5.1. Triple jet In Air microfluidic production of cellular spheroid forming hollow microcapsules.** (a) Schematic of three nozzle In Air Microfluidics for production of alginate microcapsules. (b) Photograph of fluorescently labelled microcapsules that could be produced within a 10 minute time-span using either In Air Microfluidics or conventional microfluidics.[117] (c) Microphotograph of hollow microcapsules produced using In-Air Microfluidics. (d) Microphotograph of in air production of triple-layered aqueous droplets. (e) By addition of human pluripotent stem cells to the core microjet (f) cell-laden microcapsules are formed, which self-assemble into cellular spheroids that autonomously self-organize into cavitated embryoid bodies and can be differentiated into functional cardiospheres. Scale bar is 200 μm.

magnitude faster than competing fabrication techniques (e.g., conventional microfluidics[55]) (**Figure 5.1b-c**).

To demonstrate that in-air produced hollow microcapsules can function as cellular spheroid forming bioreactors, human pluripotent stem cells (hPSCs) were introduced into the first microjet (**Figure 5.1d,e**). After successful encapsulation of hPSCs within calcium-alginate microcapsules at a production frequency of over 10 kHz, the cells rapidly aggregated and subsequently self- organized to form a lumen (**Figure 5.1f**).[67] Furthermore, encapsulated hPSCs could be differentiated into functional cardiospheres that contain highly organized sarcomeres (**Figure 5.1f**).

## 5.3.2 Achieving ultrafast, controlled, and clean microcapsule production by balancing Marangoni flows and ionic crosslinking in flying droplets

In-air encapsulation of liquid droplets by another liquid phase can be achieved via Marangoni spreading, which drives low-surface tension liquids to encapsulate high-surface tension liquids (**Figure 5.2a**). We hypothesized that consecutive spreading of alginate and calcium containing solutions over a calcium-laden droplet could be achieved by exploiting two distinct surface tension gradients, as Marangoni spreading is proportional to the difference in surface tension ($\sigma$).[68] Indeed, on-the-fly colliding water droplets containing 50 mM calcium chloride and 10% dextran (surface tension $\sigma_1$ ~ 73 mN/m) with a liquid jet containing 0.2% (w/v) sodium alginate and 10% ethanol ($\sigma_2$ ~ 48 mN/m), which subsequently collides with a liquid
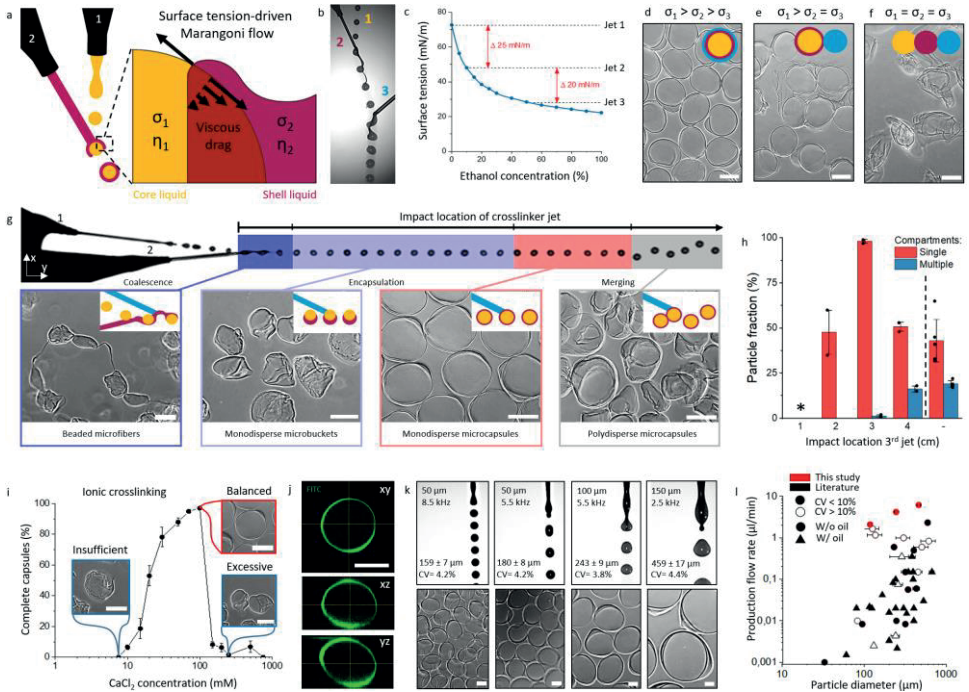
**Figure 5.2. Ultra-high throughput production of hollow microcapsules using In Air microfluidics.** (a) Schematic of the surface tension-driven in-air encapsulation process. (b) Microphotograph of in-air aqueous layering process that enables microcapsule production. (c) Used surface tension differences between microjets were obtained using distinct EtOH concentrations. (d-f) Microphotographs of microparticles formed with stepwise tuning of microjet surface tensions. Schematics indicate the surface tension-driven encapsulation status per condition. Yellow indicates the core solution, red indicates the shell precursor solution and blue indicates the crosslinker solution. (g) Schematic showing the effect of the impact location of the crosslinker microjet with microphotographs of resulting micromaterials. Insert schematics indicate the surface tension-driven encapsulation status per condition. Yellow indicates the core solution, red indicates the shell precursor solution and blue indicates the crosslinker solution. (h) Quantification of microcapsule formation efficiency and number of compartments per microcapsule dependent on $3^{rd}$ jet impact location (n=60 microparticles per condition). * Indicates the formation of beaded microfibers void of individual microcapsules. Data is presented as mean values +/- SD. (i) Analysis and microphotographs of insufficient, balanced, and excessive ionic crosslinking at different core-microjet $CaCl_2$ concentrations (n=350 microparticles). Data is presented as mean values +/- SD. (j) Confocal analysis of a representative FITC-conjugated dextran (2000 kDa)-alginate microcapsule (n=3 experiments). A representative microparticle (k) Microphotographs and analysis of droplet formation and resulting microcapsules using different nozzle sizes and different piezo-electric actuator frequencies (n>100). (l) Literature study for continuously produced hollow core-shell microcapsules. Data from this study is indicated in red, while data from literature is indicated in black. CV < 10% Is indicated in filled data points, while CV > 10% is indicated in empty data points. Horizontal bars indicate particle diameter range found in literature. Circular data points indicated studies without the use of oil, while triangular data points indicate studies with the use of oil. Scale bars represent 100 μm.

jet containing 100 mM calcium chloride and 55% ethanol ($\sigma_3 \sim 28$ mN/m) effectively yielded triple layered aqueous droplets that ionically crosslinked into water-filled thin-walled calcium-alginate microcapsules within milliseconds (**Figure 5.2b-d**). Creating two surface tension gradients was indeed key to producing individual

monodisperse capsules, as confirmed by the merging of capsules when using $\sigma_1 > \sigma_2 = \sigma_3$ (**Figure 5.2e**) and the absence of capsules when using $\sigma_1 = \sigma_2 = \sigma_3$ (**Figure 5.2f, Figure S5.2**).

Systematic examination of the on-the-fly microcapsule formation by triple-jet IAMF revealed that the relative impact location of the third (crosslinker) jet had a dominant effect on microparticle morphology (**Figure 5.2g** and **Figure S5.3**). Quantification reveals that 99.5% ± 0.5% of the microcapsules contained a single compartment upon third-jet optimization, which is in stark contrast to the 43% ± 12% obtained using a two-jet approach (**Figure 5.2h**). In principle, the third crosslinker jet arrested the in-flight droplet formation and encapsulation processes in its temporally defined state. Specifically, introducing the third jet before full droplet pinch-off occurred resulted in beaded microfibers, whereas coalescing the third jet with the pinched-off calcium-alginate droplets resulted in partly formed (i.e., microbuckets) or fully formed microcapsules. Coalescing the third jet too far downstream produced polydisperse multi-core capsules that looked similar to microcapsules produced with conventional two-jet IAMF. To further characterize and optimize the in-air production of ionically crosslinked microcapsules, the concentration of calcium in the core liquid of the triple layered aqueous droplets was varied. A calcium concentration of <10 mM associated with the collapse of the core upon impact with the third jet or with the collection bath (**Figure 5.2i**). A calcium concentration of >100 mM impaired the formation of microcapsules, which can be attributed to the accelerated calcium-alginate crosslinking when using higher calcium concentrations causing the viscosity of the alginate solution to increase, thereby causing larger viscous drag and hampering Marangoni spreading.[69] This resulted in reproducible production of crescent shaped microbuckets. Indeed, reducing the calcium diffusion speed by increasing viscosity through adding dextran to the core aided the stable formation of intact calcium-alginate microcapsules (**Figure S5.4**). Of note, adding a viscous crowder (e.g., 10% dextran) to the core microjet also reduced droplet deformations upon pinch-off owing to increased liquid viscosity of the triple-layered droplet's core (**Figure S5.4**). Overall, these results revealed that balancing of liquid viscosity, surface tension, crosslinking rate, and collision timing enable optimized ultra-high throughput production of hollow microcapsules.

Single-core microcapsules composed of FITC-labeled alginate revealed the micrometer thin (6.4 ± 3.9 µm) nature of the microcapsule's hydrogel shell, which was visualized using confocal microscopy (**Figure 5.2j, Figure S5.5a**). Microcapsule size was monodisperse (coefficient of variation; CV < 5%) and could be produced over a wide range of diameters, for example 159 ± 7 µm, to 243 ± 9 µm, and to 459 ± 17 µm when using 50 µm, 100 µm, and 150 µm nozzles for the core liquid, respectively (**Figure 5.2k** and **Figure S5.5b**). Furthermore, capsule size could be fine-tuned by adjusting the nozzle vibration frequency. Interestingly, adjusting the frequency also provided control over the number of hollow compartments per

microgel. While a typical hollow microgel containing a single compartment was achieved with a stable droplet train using a frequency of 5.5 kHz, other frequency regimes produced droplet trains where droplets traveled in doublets (**Figure S5.6**), or even triplets. This results in 83 ± 2% dual-core microcapsules at 2.7 kHz (**Figure S5.6**), and 88 ± 6% triple-core microcapsules at 2 kHz (**Figure S5.6**). Consequently, triple-jet IAMF allowed for ultra-high throughput production of multi-compartment microcapsules, which offers opportunities for various biomedical, chemical, pharmaceutical, and cosmetic applications.[70–73] Of note, triple-jet IAMF technology also facilitates such variety of uses as it can produce compartmentalized micromaterials from materials other than alginate, as demonstrated by the fabrication of microcapsules composed of interpenetrating hydrogel networks of ionically crosslinked calcium-alginate and photocrosslinked poly(ethylene glycol) (PEGDA) or calcium-alginate and enzymatically crosslinked dextran-tyramine (Dex-TA) (**Figure S5.7**).

To determine the operational window for monodisperse hollow microcapsule production, flow rates were systematically investigated and optimized. Single compartment hollow microcapsules of 180 ± 8 μm having a highly circular morphology (circularity > 0.9) and monodisperse size (CV < 5%) were obtained at core and shell microjet flow rates of 900 μm/min and 1100 μl/min, respectively (**Figure S5.8**). Importantly, an extensive literature study[39–49,54,55,74–96] revealed and confirmed that no other platform rivals triple-jet IAMF microcapsule production as in terms of production throughput, resolution, oil-free production, and monodispersity (**Figure 5.2l, Figure S5.9**). Specifically, triple-jet IAMF represents the first platform that offers ultra-high throughput production (2 ml/min, 4.2 ml/min and 6.4 ml/min for 159 μm, 243 μm and 459 μm microcapsules, respectively), high resolution (i.e. the possibility for producing particles < 500 μm) and highly monodisperse (CV < 5%) microcapsules in an oil-free manner.

### 5.3.3 Engineered microcapsules as bioreactors for mass production of long-term stable cellular spheroids

Triple-jet IAMF was then explored for the encapsulation of living cells. Specifically, a well characterized fibroblast cell line (3T3) was used to establish the cytocompatibility of the microcapsule production process. On-the-fly encapsulated cells were collected in a bath composed of cell culture medium to ensure near-instant >20 times dilution of ethanol levels, which reached maximally ~1% concentrations. While a 1% ethanol concentration is considered non-toxic when exposing it to cells shorter than 24 hours, microencapsulated cells were washed extensively within 1 minute upon collection to further ensure reproducible cytocompatibility (**Figure 5.3a**).[97–99] Similarly, physiological calcium concentrations were retained upon the before mentioned extensive washes within 1 minute upon collection. Indeed, triple-jet IAMF offered excellent cytocompatibility with the viable cell fraction as high as 97 ± 2% directly post-encapsulation and 91 ± 4% after 14 days of culturing (**Figure 5.3b**). Permeability experiments with Dextran-FITC
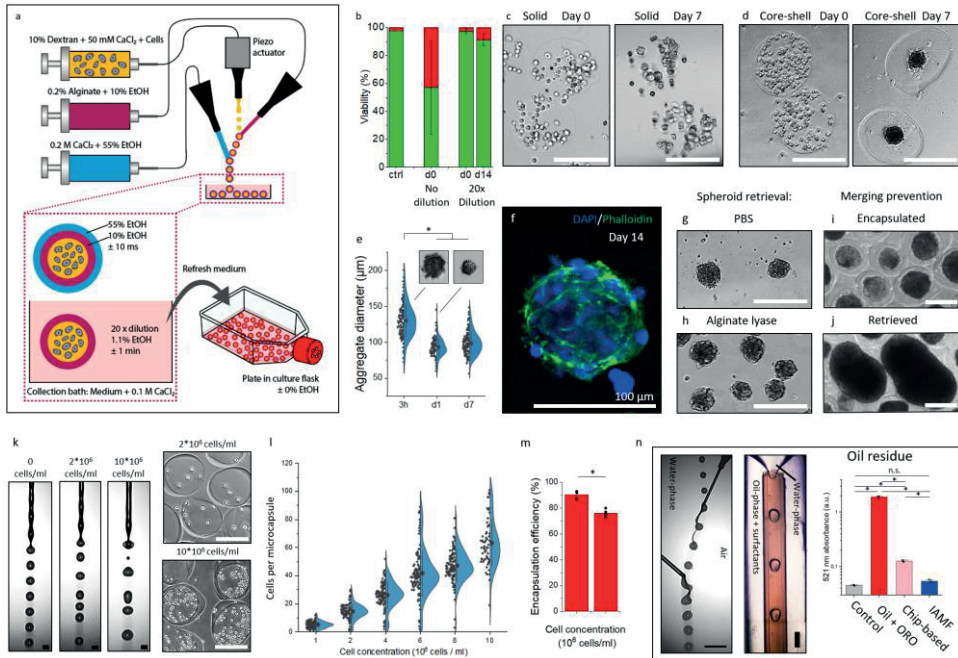
**Figure 5.3 Clean mass production of viable spheroids using in-air generated cell-laden microcapsules.** (a) Schematic of triple-jet in-air microfluidic cell encapsulation in microcapsules. (b) Viability quantification of encapsulated 3T3 fibroblasts with and without 20x dilution upon collection (n=85 microcapsules). Data is presented as mean values +/- SD. Microphotographs of (c) solid microgels and (d) hollow microcapsules containing $10^7$ 3T3 fibroblasts/ml after 0 and 7 days culture. (e) Quantification and microphotographs of 3T3 fibroblast spheroid diameter within microcapsules during seven days of culture (n=60, p=1.37E-29). Data is presented as mean values +/- SD. (f) Confocal fluorescence microphotograph of a microcapsule and its 3T3 spheroid of which the nuclei are stained with DAPI (blue) and its F-actin is stained with phalloidin (green) after 14 days of culture. Microphotographs of spheroids of which their respective microcapsule was instantly dissolved using (g) PBS or (h) alginate lyase after 14 days of culture. Microphotographs of (i) non-merging encapsulated spheroids and (j) merging de-encapsulated spheroids. (k) Microphotographs of droplet formation using solutions containing 0, $2*10^6$ and $10^7$ cells/ml. (l) Quantification of cells per microcapsule for various cell concentrations ranging up to $10^7$ cells/ml (n=60). Data is presented as mean values +/- SD. (m) Encapsulation efficiency of microcapsule production using $2*10^6$ or $10^7$ cells/ml was quantified (n=60, p=1.01E-4). Data is presented as mean values +/- SD. (n) Microphotograph of conventional oil-based microfluidic droplet formation using oil and surfactants, microphotograph of samples obtained with oil-based microfluidics using Oil Red O (ORO) stained oil, and absorbance at 521 nm for residue oil quantification. Chip-based sample was obtained through 3 thorough washing steps (n=3). Data is presented as mean values +/- SD. Significance was determined based on one-way Anova analysis. Significance of p <0.05 is indicated by *. A.U. Indicates arbitrary units. Scale bar is 200 μm unless stated otherwise.

conjugates revealed excellent permeability with an approximate diffusion cutoff of 2000 kDa (**Figure S10**), While conventional matrix-type (i.e., solid) calcium-alginate microgels did not support spheroid formation of 3T3 cells (**Figure 5.3c**), hollow microcapsules readily enabled rapid cell aggregation, which resulted in 3D microtissues formation with aggregate diameters of 99 ± 16 μm (CV = 16%) (**Figure 5.3d-f**). The cell spheroids could be straightforwardly retrieved from the

microcapsules in an enzyme-free manner by exposing the microcapsules to phosphate-buffered saline (PBS) solution, which dissolved the calcium-alginate by competitively binding and extracting the calcium that ionically crosslinked the polymer network to form calcium phosphate, which is not dissolvable in water (Figure 3g). In addition, cell spheroids could be retrieved by bio-orthogonal enzymatic digestion of the alginate using alginate lyase (**Figure 5.3h**). Notably, while encapsulated spheroids remained separate (**Figure 5.3i**), retrieved non-encapsulated spheroids merged upon further culture (**Figure 5.3j**), which underlined the advantage of microcapsule culture to obtain and maintain controlled spheroid sizes.[20] The optimized microencapsulation platform was then tested for different cell concentrations. Although introducing cells into the polymer solution associates with introducing a granularity into the liquids that at high concentrations could adversely affect jet breakup (**Figure 5.3k**), 3T3 fibroblasts using cell concentrations ranging from $10^6$ cells/ml to $10^7$ cells/ml, which corresponded to payloads of $5 \pm 2$ to $63 \pm 17$ cells/microcapsule, readily allowed for reproducible and stable microencapsulation (**Figure 5.3l,m** and **Figure S5.11**).

A key advantage of IAMF over conventional chip-based microfluidics encapsulation strategies is its oil-free nature. As oil residue is known to comprise cell viability,[35,37] associate with immune adjuvant effects,[36] and contribute to development of autoimmune diseases,[36] clinical translational potential of conventional microfluidic strategies is limited. We demonstrated that micromaterials produced with IAMF-based cell encapsulation does not contain oil while microcapsules produced via chip-based microfluidic emulsification, even after extensive washing (i.e., $>10^6$ times diluted via 3 washing steps using $>100x$ excess of liquid) contains oil residues (**Figure 5.3n**). Together, these results highlight the clean nature of triple-jet IAMF encapsulation, which is expected to facilitate clinical and industrial translation of this technology for the clean mass production of 3D microtissues for clinical or biomedical applications.

## 5.3.4 Engineering embryoid bodies using size-controlling microcapsules

We then investigated whether microcapsules could act as bioreactors, enabling mass production of high quality EBs. To this end, microcapsules were laden with ~20 human pluripotent stem cells and suspension-cultured in Essential 8 (E8) stem cell medium, which was supplemented with PVA and ROCK inhibitor during the first 24 hours only (**Figure 5.4a**). Microencapsulated hPSCs aggregated into compact 3D cell spheroids within two days (**Figure 5.4b, Figure S5.12**). Within six days, the vast majority (92% $\pm$ 1%) of hPSC spheroids underwent lumenogenesis, which was progressively developing and did not associate with the formation of a necrotic core (**Figure 5.4c-f**). Specifically, the volume of the average lumen grew by >30 fold between day two and six of microencapsulated suspension culture (**Figure 5.4f**). In mammalian embryogenesis, lumenogenesis of blastocyst is essential for the formation of the trophoblast lineage, its separation from the inner cell mass, and the

subsequent formation of the three germ layers of the embryo proper.[100] Subsequently, cavitation plays a key role at the rosette-stage in formation of the amniotic cavity.[101] Hence, high efficiency lumenogenesis is of high value for both embryonic self-organization and EB-mediated organoid formation[25,27,28,102–105]. The pluripotent character of the hPSC-spheroids was confirmed by pluripotency markers Sox2 and Oct3/4, which were expressed in 98% ± 4% and 89% ± 9% of the PSC-microspheres, respectively, which was comparable to pluripotency marker levels observed in conventional monolayer cultures (100% ± 1% Sox2 and 94% ± 10% Oct3/4) (**Figure 5.4g** and **Figure S5.13**).

hPSC-Spheroids cell population variation was investigated through single cell RNA sequencing, which revealed that the populations of single cells of microencapsulated hPSCs and conventional hPSCs were near-identical regarding transcriptional expression of naïve pluripotency markers (e.g., *NANOG*) and primed pluripotency (e.g., *SALL2*, *CD24*, *ZLC3*, *SFRP2,* and *CDH1*) (**Figure 5.4h**). This is advantageous as it indicates that this production platform is highly comparable in quality to conventional techniques, while supporting upscaling via suspension culture. Although highly similar, several interesting distinctions were observed: while gene expression of biosynthesis markers (*HMGCS1*, *HMGCR*, *CYP51A1*, *ACLY*, *DHCR24*, *SCD*, *FDFT1*, *IDH1*, and *MSMO1*) was higher in conventional non-encapsulated hPSCs, the gene expression of glycolytic markers (*APP*, *PGM1*, *GPI*, *PKM*, *LDHA*, and *PGK1*) was higher in encapsulated EBs (Figure 4i,j). This is likely of value as high glycolytic flux is critical in obtaining and maintaining pluripotency,[106–108] and it is known that primed pluripotent stem cells are typically exclusively glycolytic as compared to naïve pluripotent stem cells, which rely relatively more on oxidative metabolism.[109,110]

To further investigate the cytoarchitecture of the self-organizing spheroids, we visualized and measured nucleus position, cell orientation, and cell aspect ratio (**Figure 5.4k-m, Figure S5.13**). Cells within spheroids were consistently characterized by peripherally located nuclei with a $d_{nucleus}/d_{cell}$ of 0.68 ± 0.11, an aspect ratio $d_{radial}/d_{tangent}$ of 0.44 ± 0.18 and a predominantly radial orientation $\theta_{cell}$-$\theta_{rad}$ of 2.3° ± 19.7° (**Figure 5.4l-n**). This highly anisotropic cytoarchitecture indicated formation of columnar epithelium, which, combined with the observed lumenogenesis and positive primed pluripotency markers including *OTX2*, *FGF2*, *ZIC2* and *SFRP2* (**Figure. 5.4h**),[100] indicate resemblance to rosette-stage epiblast .[101] However, more research is needed to confirm this hypothesis.

Timelapse observations of growing microencapsulated hPSCs revealed that lumenogenesis was strongly correlated with a physical size threshold. Specifically, lumenogenesis exclusively and rapidly occurred in spheroids with $D_{spheroid}$ ≳100 μm (**Figure 5.4o**). Spheroid formation and lumen formation was more controlled, homogeneous, and monodisperse in microcapsules as compared to microwell culture, with 172 μm ± 31 μm (CV 18%) and 92.4% ± 0.8% of lumenogenesis in
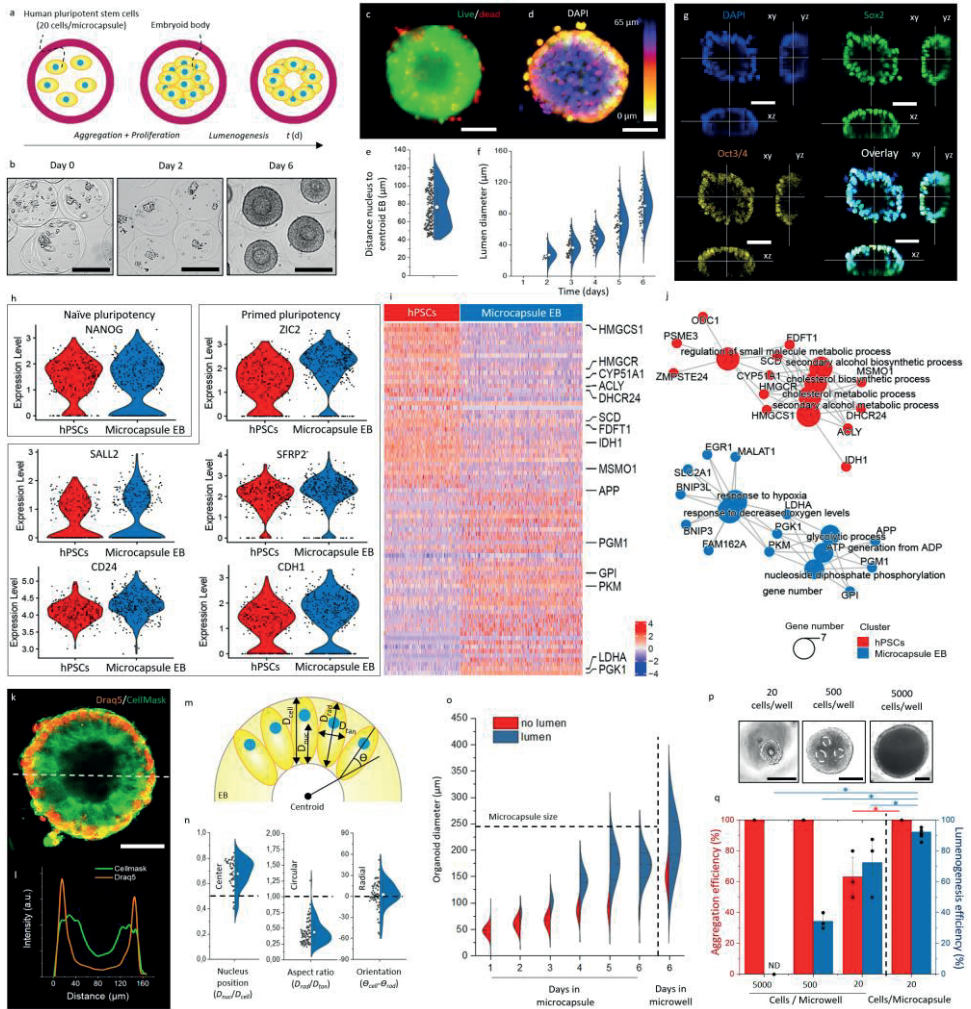
**Figure 5.4. Microencapsulated human pluripotent stem cells self-organize into polarized cavitated embryoid bodies.** (a) Schematic and (b) representative microphotographs of aggregation, compaction, and cavitation of human pluripotent stem cell (hPSC)-laden microcapsules. (n=3 experiments) (c) Fluorescence microphotograph of embryoid body (EB) stained with calcein AM (green) and ethidium homodimer (red) to visualize life and dead cells, respectively. (d) Confocal fluorescence Z-projection of a DAPI stained cavitated EB. (e) Quantification of distance between nuclei and centroid of EBs (n=250 cells). Data presented as mean values +/- SD. (f) Quantification of diameter of lumen of microencapsulated EBs over time (day2: n=8, other conditions: n=48). Data presented as mean values +/- SD. (g) Confocal fluorescence microphotographs of EB fluorescently stained for nuclei (blue), SOX2 (green), and Oct3/4 (yellow). (h) Gene expression analysis for naïve pluripotency (NANOG) and primed pluripotency (SALL2, CD24, ZLC2, SFRP2, CDH1) for conventional microwell cultured EB control (red) and microencapsulated EBs (blue) (hPSCs n=208, Microcapsule EB n=333). (i) Single cell RNA sequencing heatmap of marker genes with highlighted genes related to biosynthesis (HMGCS1-MSMO1) and glycolysis (APP-PGK1). (j) GO-term networks of differences between conventional microwell cultured EB control (red) and microencapsulated EBs (blue). (k) Fluorescence confocal microphotograph of EB stained with Draq5 (orange) for nuclei, and Cellmask (green) for cell membrane. White dotted line indicates (l) histogram of Draq5 and Cellmask. A.U. Indicates arbitrary units. (m) Schematic of EB with distance of nucleus perpendicular to the cavity ($d_{Nucleus}$), length of

the cell perpendicular to the cavity ($d_{Cell}$), distance of the cell radial ($d_{radial}$) and perpendicular ($d_{perpendicular}$), and orientation of the cell compared to the EB's centroid ($\theta_{cell}$-$\theta_{rad}$). (n) Quantification of nucleus position and the aspect ratio and orientation of the cells. (n=57 cells) Data is presented as mean values +/- SD. (o) Quantification of embryoid body diameter over time, with individual denomination for EBs without cavity (red) and with cavity (blue) (n>110). (p) Microphotographs hPSCs aggregates at different cell concentrations formed using the conventional microwell technique. (q) Quantification of aggregation and cavitation process of hPSCs at different cell concentrations using microwells and in-air microencapsulation (microwells: n=30 microtissues, microcapsules: n=175 microtissues). Data presented as mean values +/- SD. Black scale bar represents 100 μm. White scale bar represents 50 μm.

microcapsules and 198 μm ± 65 μm (CV 33%) and 72.5% ± 16% of lumenogenesis in microwells. It was observed that when microcapsules became fully confluent (e.g., after five days of culture) the size of the cell mass stabilized. Since microcapsule size remained constant upon confluency, this offers an elegant manner of spheroid size control by imposing a designable spatial confinement defined by microcapsule size. To investigate if lumen formation indeed correlated with cell mass size, we prepared small, medium, and large spheroids by seeding 20, 500, and 5000 hPSCs per conical non-cell-adhesive culture chamber. As hypothesized, lumenogenesis efficiency correlated with the number of cells per microwell and thus size (**Figure 5.4p,q**). Specifically, no cavitation was observed in the larger spheroids while 34.4% ± 4.1% of medium-sized encapsulated hPSC spheroids underwent lumenogenesis, albeit in an uncontrolled manner characterized by the formation of multiple lumens of various sizes (**Figure 5.4p**). In marked contrast, only small spheroids developed into single-lumen 3D cell spheroids in a fairly reproducible manner (i.e., 72% ± 16% lumenogenesis efficiency), albeit with a significantly lower efficiency than triple-jet IAMF microencapsulated EBs (i.e. 92.4% ± 0.8% lumenogenesis efficiency) (**Figure 5.4q**). This improved performance of 3D microcapsules could potentially be explained by the conformal encapsulation, which unlike microwells controls molecule transport via diffusion by locally preventing convection, therefore allowing for the more efficient buildup of an autocrine microenvironment.[111]

### 5.3.4 Engineering monodisperse functional cardiospheres using IAMF-generated bioreactors

To further explore the translational potential of IAMF-generated microcapsules as bioreactors, microencapsulated EBs were differentiated into functional cardiospheres. Immediately following aggregation and compaction of on average 20 hPSCs per microcapsules, mesoderm transition and cardiac differentiation were induced by exposing the resulting microencapsulated EBs to mesoderm differentiation medium for three days and subsequently to cardiac differentiation medium for 22 days (**Figure 5.5a**). Successful cardiosphere development was investigated and confirmed by visualizing the expression of Mesoderm Posterior BHLH Transcription Factor 1 (MESP1) and homeobox protein NKX2-5 using genetically engineered reporter hPSC cell lines (**Figure 5.5b,c**).[56] After 22 days, 94.3% ± 0.5% of encapsulated cells expressed Green Fluorescent Protein (GFP) (**Figure 5.5d**), which indicated activation of *NKX2-5*
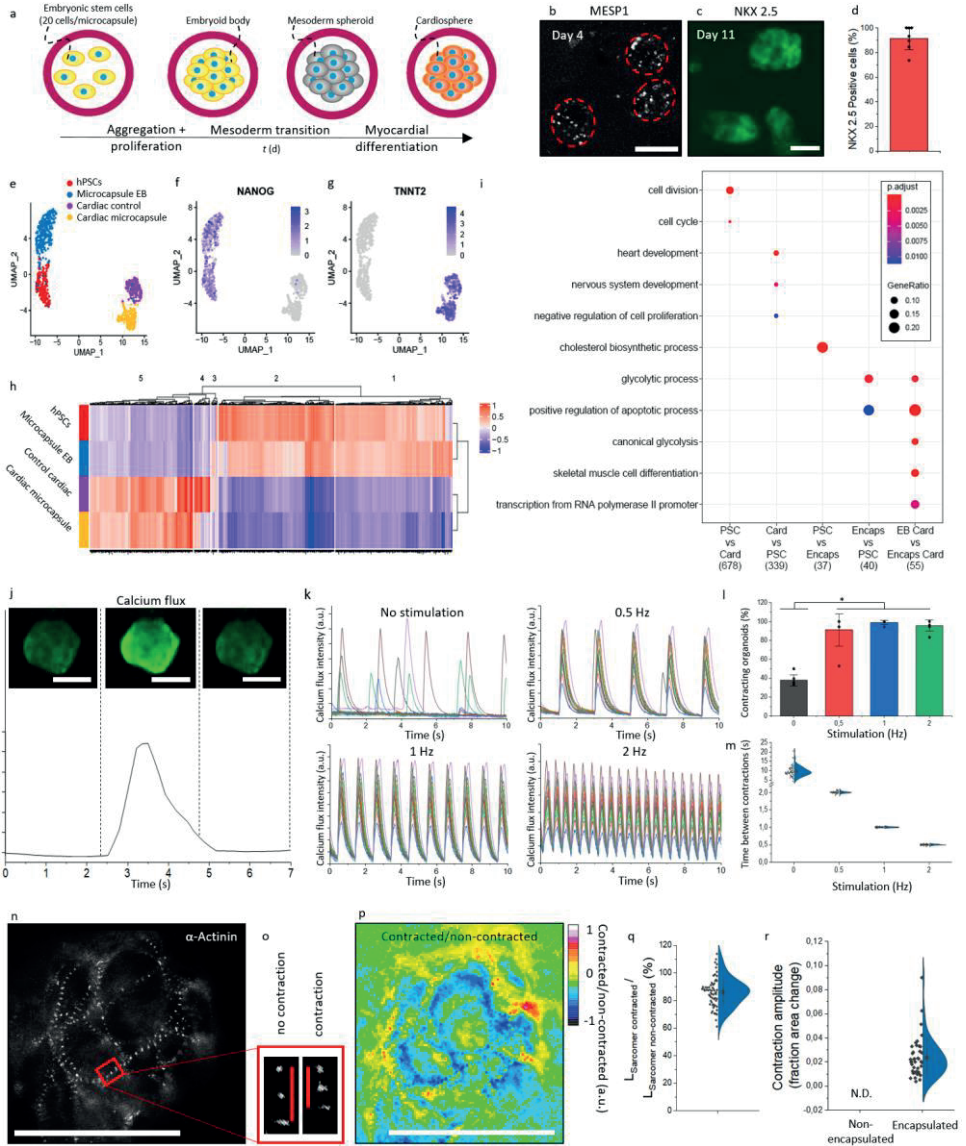
**Figure 5.5. Mass production of functional cardiospheres using in-air generated human pluripotent stem cell-laden microcapsules.** (a) Schematic of aggregation, mesoderm transition, and myocardial differentiation of human pluripotent stem cells (hPSC)-laden microcapsules. (b) Fluorescence microphotograph of MESP1 mesoderm marker in hPSC-laden microcapsules after four days of culture. (c) Fluorescence microphotograph of NKX-2.5 myocardial marker in hPSC-laden microcapsules after 11 days of culture. (d) Quantification of NKX-2.5 positive cells after 22 days of encapsulated culture (n=126). Data presented as mean values +/- SD. (e) Uniform manifold approximation and projection (UMAP) plot of non-differentiated hPSCs (blue) (n=208), microencapsulated EBs (purple) (n=333), control cardiac culture (red) (n=162) and microencapsulated cardiospheres (green) (n=193). UMAP heatmaps of (f) NANOG and (g) TNNT2. (h) Single cell RNA sequencing heatmap of marker genes corresponding to identified clusters. (i) Gene ontology heatmap of differential genes per cluster. Columns from left to right: 1) Upregulated in PSC conditions vs cardiac conditions, 2) Upregulated in cardiac conditions vs PSC, 3) Upregulated in hPSC versus pluripotent EB microcapsule, 4) Upregulated in pluripotent EB microcapsule versus hPSC, 5) Upregulated in cardiac EB

versus cardiac microcapsule. GO-terms with a gene ratio > 0.05 were visualized. P-adjust corrected using Benjamini-Hochberg correction for multiple comparisons. (j) Fluorescence microphotographs and analysis of calcium flux by Fluo-4 staining (green). A.U. Indicates arbitrary units. (k) Analysis of calcium flux intensity in encapsulated cardiospheres without stimulation, or with stimulation using an electrical current with a frequency of 0.5 Hz, 1 Hz, and 2 Hz (n=17). (l) Quantification of contracting encapsulated cardiospheres with or without electrical stimulation (n=120, p=5.19E-6). Data presented as mean values +/- SD. (m) Quantification of time between contractions with or without electrical stimulation (n=50). Data presented as mean values +/- SD. (n) Fluorescence microphotograph of hPSC α-actinin reporter (mRubyII) in differentiated encapsulated cardiomyocytes after 18 days of culture. (o) Fluorescence microphotograph showing shortening of sarcomeres during contraction in encapsulated hPSC-derived cardiomyocytes. (p) Ratiometric image of contracted/non-contracted microphotographs of encapsulated cardiospheres. (q) Quantification of contraction by assessment of single sarcomeres in encapsulated cardiospheres (n=66 sarcomeres). Data presented as mean values +/- SD. (r) Quantification of contraction by assessment of fraction area change of non-encapsulated and encapsulated cardiospheres (n=40 cardiospheres). Data presented as mean values +/- SD. Scale bar represents 100 μm.

expression and highly efficient cardiac differentiation comparable to previously reported optimized yet low-throughput cardiac differentiation strategies.[112]

Next, the quality of cardiac differentiation within the microcapsules in terms of population heterogeneity was investigated. To this end, single cell RNA sequencing was performed on cardiac differentiated hPSCs that were cultured in microcapsules or with conventional cardiac culture in cell culture wells, which were compared to undifferentiated hPSCs and microencapsulated cavitated hPSCs (**Figure 5.5e**). It is important to note that conventional cardiac culture in 2D cell culture wells will form 3D tissues and therefore does not resemble traditional monolayer culture. Differentiation towards the cardiac lineage associated with loss of pluripotency markers (e.g., *NANOG*) (**Figure 5.5f**) and transcription of cardiac markers (e.g., *TNNT2, RYR2*, and *MYL7)* (**Figure 5.5g, Figure S5.14**) in both microencapsulated and conventional cardiac culture. Importantly, no notable subpopulation was observed among the microencapsulated cardiospheres, indicating that the hPSC-derived cardiomyocyte population was highly similar at the single cell level. This is a highly desirable feat as it demonstrates that IAMF-generated microcapsules can act as bioreactors for the mass production of high quality (e.g., homogeneous) hPSC-derived cardiomyocyte populations.

Heatmap analysis of the genes that were differentially expressed between the obtained single cell RNA sequencing data sets (i.e., undifferentiated hPSCs, hPSC-derived cavitated EBs, conventional cardiac culture, and microcapsule cardiospheres) revealed that the gene expression profiles of conventional cardiac cultures and microcapsule-mediated mass-produced cardiospheres were near-identical (**Figure 5.5h, Figure S5.15**). Gene ontology analysis of identified cell clusters revealed that non-differentiated hPSCs differentially expressed genes relating to cell proliferation and metabolism as compared to differentiated cardiospheres (**Figure 5.5i** and **Figure S5.15**). Compared to non-differentiated hPSCs, both encapsulated cardiospheres and conventional cardiac culture showed increased expression for cardiac tissue formation markers with no major differences between microencapsulated and conventional conditions. Consequently, this suggested

that in-air mass production using bioreactors offers similar high quality cardiomyocytes and cardiac culture as conventional non-scalable production methods.

Time-resolved microscopy confirmed that microencapsulated cardiospheres underwent spontaneous contraction (**Supplementary Video 5.2**), which coincided with a calcium flux as visualized using a fluorescently labeled calcium indicator Fluo-4 AM (**Supplementary Video 5.3** and **Figure 5.5j**). Furthermore, exposure to cyclical electrical stimulation at various physiologically relevant frequencies (0.5 Hz, 1 Hz and 2 Hz) resulted in synchronized corresponding contractile behavior of all observed mass produced cardiospheres at near 100% efficiency (**Figure 5.5k-m**), which corroborated successful cardiac differentiation and function[113]. Interestingly, the possibility of pacing cardiospheres within microcapsules facilitates controlled electrical stimulation of cardiosphere suspension cultures, for example, to mature engineered cardiac tissue constructs *in vitro* while still allowing for safe and facile (down-stream) handling of mass produced cardiospheres.[113–115]

Microencapsulated cardiospheres contractility was quantified using hPSCs that were genetically modified to express fluorescent a-Actinin/mRubyII fusion protein to visualize the cell's sarcomere Z-lines, which allowed for time-resolved analysis in live cells (**Figure 5.5n, Figure S5.16, Supplementary Video 5.4**).[57,116] Specifically, we measured shortening of sarcomeres on a single-cell level by determining the length between two adjacent Z-lines during contraction events. This revealed that sarcomeres contracted to 82 ± 9% of their original length upon 5 V external pacing (1.68 μm ± 0.17 μm in original state and 1.43 μm ± 0.17 μm in contraction) (**Figure 5.5o-q**), which is in line with findings in literature (1.73 μm ± 0.015 μm in original state and 1.54 ± 0.014 μm in contraction, which correlates to 89% of its original length).[116] In addition, contraction was also quantified in terms of fraction area change, which revealed a 0.024 ± 0.016 fraction area change upon contraction (**Figure 5.5r**), which was not readily quantifiable using fraction area change within conventional cardiac cultures (**Supplementary Video 5.5**), thus offering improved functional read-outs for various applications such as developmental biology and drug testing.

To conclude, we report on a microfluidic production platform that can produce cellular spheroids in a clean manner (i.e., oil-free and surfactant-free) at a rate that is orders of magnitude faster than conventional approaches, with high control and resolution, which uniquely enables the production of these living 3D microtissues at clinically and industrially relevant scales. Specifically, a triple-jet strategy was designed to controllably collide microdroplets of distinct chemical compositions in-air, in an in-line fashion, to produce hollow thin-shelled hydrogel microcapsules, which were demonstrated to be capable of acting as highly efficient microtissue-forming bioreactors. These mass produced microcapsules allowed hPSCs to autonomously undergo lumenogenesis to form cavitated pluripotent spheroids with polarized cytoarchitecture. Exposing mass produced hESC-laden microcapsules to myocardial differentiation medium resulted in production of high quality functional

5

cardiospheres that were composed of a homogenous cell population, as confirmed by single cell RNAseq. Taken together, we here present a microfluidic platform for the mass production of 3D functional living microtissues which opens new areas of research and drives clinical and industrial adoption in application areas such as tissue engineering, drug testing, and cultured meat.

5

## 5.4 Supplementary Information
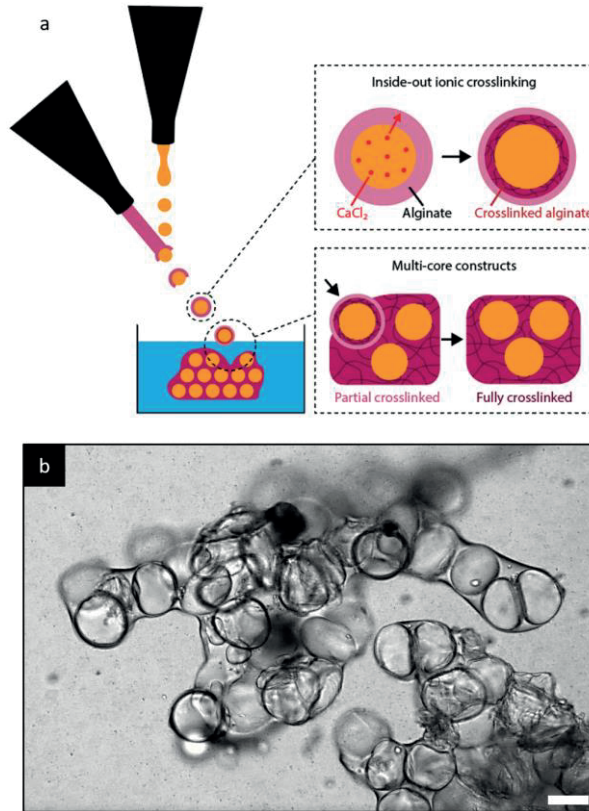


**Figure S5.1. In Air microfluidics using a two-nozzle setup results in formation of uncontrolled multi-compartment microparticles.** (a) Schematic of two-nozzle setup, inside-out crosslinking process, and mechanism by which multi-compartment microparticles are formed. (b) Microphotograph of formed microparticle using two-nozzle in-air microfluidics. Scale bar represents 200 µm.

5
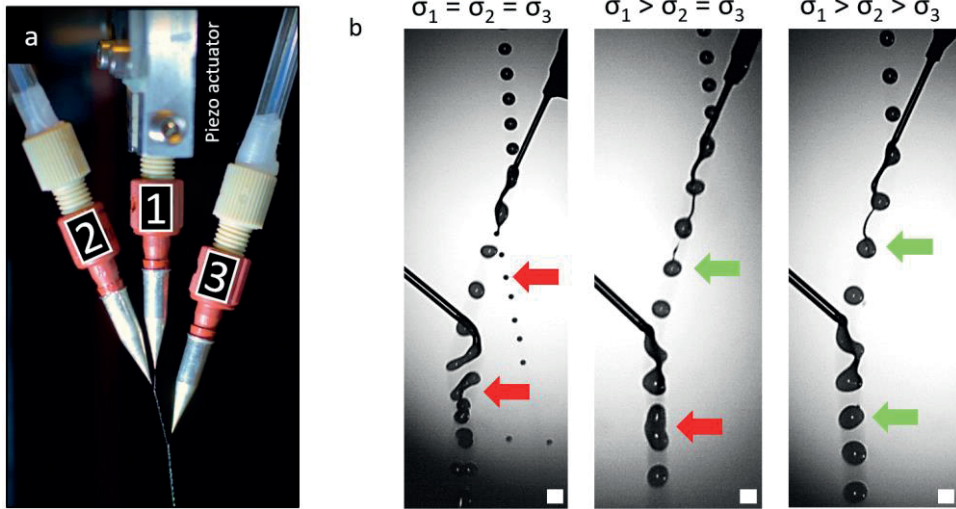
**Figure S5.2. In Air microfluidics three-nozzle setup for In Air droplet encapsulation.** (a) Photograph of a three nozzle In Air microfluidics setup, with a piezo-electric actuator attached to the first nozzle. (b) Microphotographs of the encapsulation process with $\sigma_1 = \sigma_2 = \sigma_3$, $\sigma_1 > \sigma_2 = \sigma_3$ and $\sigma_1 > \sigma_2 > \sigma_3$. Red arrows indicate spraying and improper encapsulation, green arrows indicate proper encapsulation. Scale bar represents 200 μm.
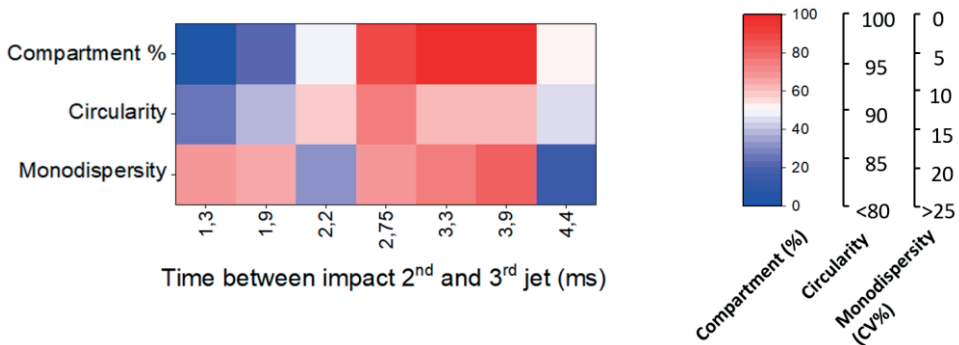


**Figure S5.3. Third jet coalescence location dictates hollow microcapsule formation.** Effect of in-air flight time before third jet coalescences with the droplet train as analyzed in terms of percentage of single compartment, circularity, and monodispersity of produced microparticles (n>85).
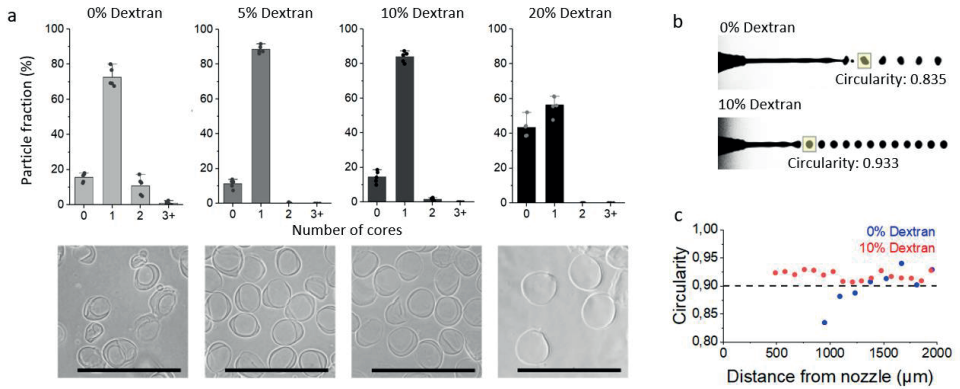
**Figure S5.4. Effect of dextran in core liquid on hollow microcapsule formation.** (a) Number of hollow compartments per microparticle using dextran core liquid concentrations of 0%, 5%, 10%, and 20%, including corresponding microphotographs (n=60). Data is presented as mean values +/- SD. (b) Microphotographs and (c) quantification of circularity of formed droplets with and without 10% dextran. Scale bar represents 400 μm.
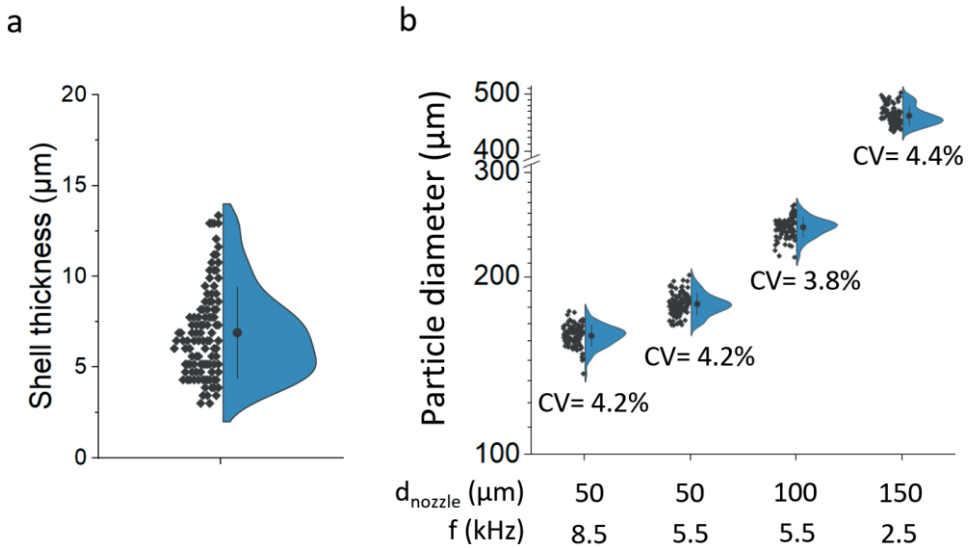


**Figure S5.5. Hollow microcapsule morphology.** (a) Quantification of shell thickness of in-air produced microcapsules (n=107). Data is presented as mean values +/- SD. (b) Quantification of microcapsule diameter and monodispersity using different nozzle sizes and different piezo-electric actuator frequencies (n=100). Data is presented as mean values +/- SD.
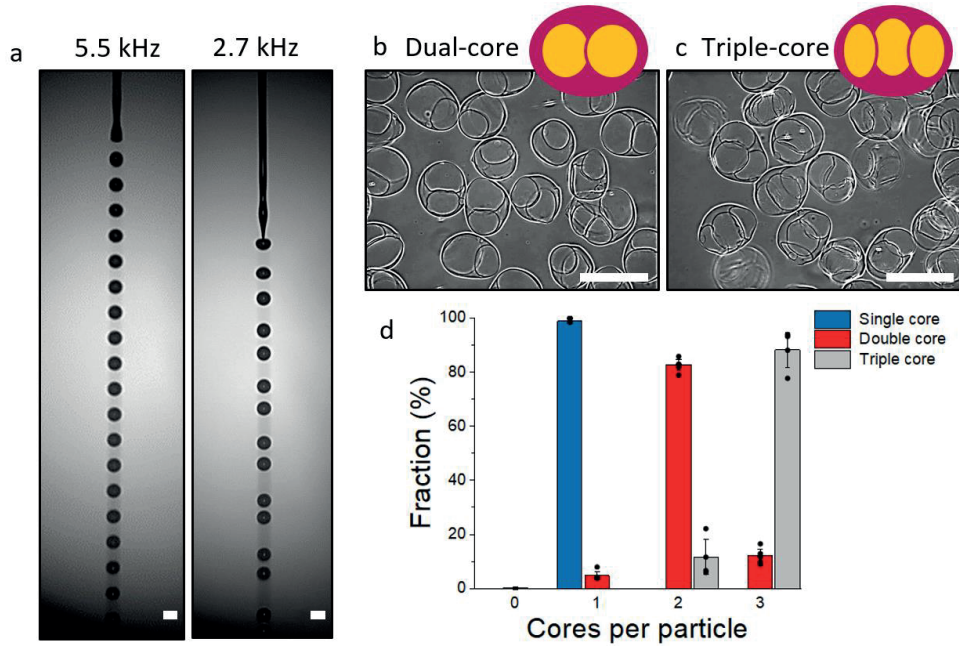
**Figure S5.6. Controlled production of multi-core microparticles by adjusting piezo-actuator frequency.** (a) Microphotographs of droplet formation at 5.5 kHz and 2.7 kHz. (b) Microphotograph of dual-core microcapsules (c) and triple-core microcapsules. (d) Quantification of percentage single-, dual-, and triple-core microcapsules (n=169 microparticles). Data is presented as mean values +/- SD. Scale bar represents 200 μm.
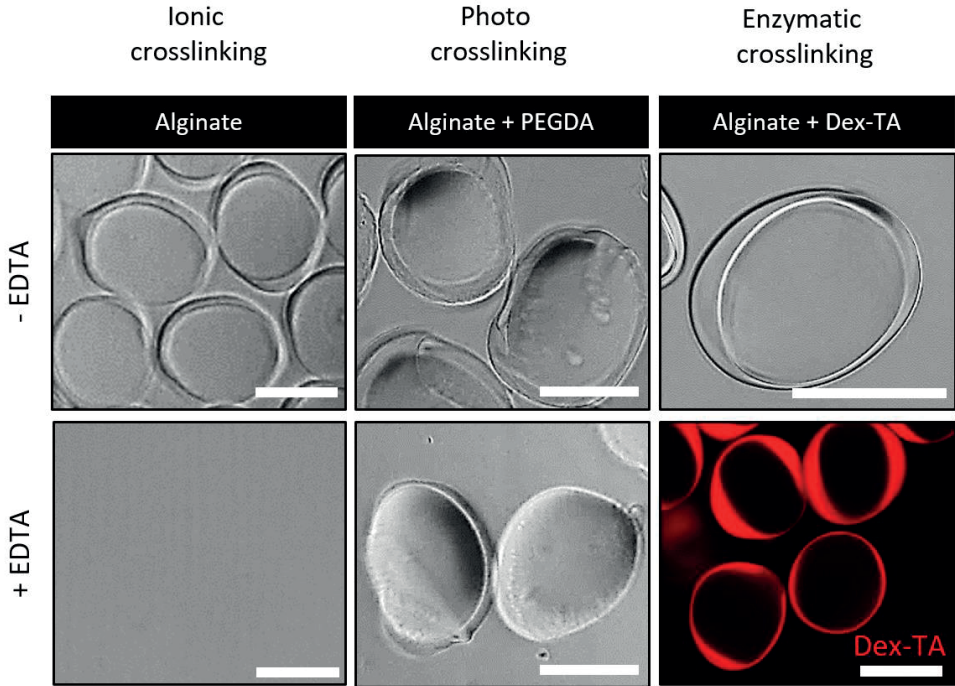
**Figure S5.7. In Air production of microcapsules using photocrosslinkable and enzymatic crosslinkable materials.** Microphotographs of ionically crosslinked alginate microcapsules, photocrosslinked PEGDA microcapsules, and enzymatic crosslinked dextran-tyramine microcapsules, before and after EDTA treatment. Dex-TA microcapsules post-EDTA were stained with ethidium homodimer (red). Scale bar represent 100 μm.
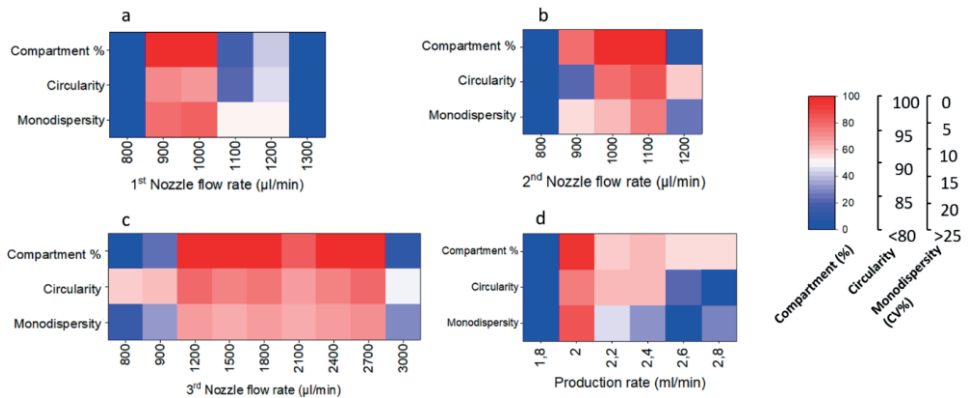


**Figure S5.8. Flow rate optimization for microcapsules production.** Quantification of the percentage of microparticles containing a single compartment, circularity of formed microparticles, and microparticle monodispersity. Setup used: Nozzle 1 (50 μm) at 900 μl/min, nozzle 2 (50 μm) at 1100 μl/min, nozzle 3 (100 μm) at 1500 μl/min. (a) Effect of first nozzle flow rate on microparticle formation (n=100). (b) Effect of second nozzle flow rate on microparticle formation (n=100). (c) Effect of third nozzle flow rate on microparticle formation (n=100). (d) Effect of total production flow rate on microparticle formation (n=100). Ratios between flow rates were kept constant at the ratio described above.
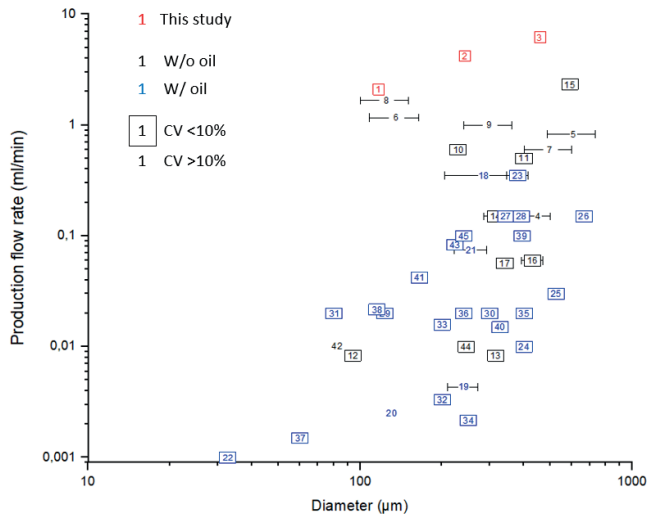
| 1-3 | This work |
| 4 | Aghdam et al.[96] |
| 5 | Correia et al.[44] |
| 6 | Alessandri et al.[46] |
| 7 | Ma et al.[47] |
| 8 | Alessandri et al.[45] |
| 9 | Rutkowski et al.[48] |
| 10 | Sakai et al.[48] |
| 11 | Ren et al.[80] |
| 12-13 | Song et al.[80] |
| 14 | Zhao et al.[89] |
| 15 | Domejean et al.[76] |
| 16 | Rao et al.[40] |
| 17-18 | Nguyen et al.[43] |
| 19 | Agarwal et al.[41] |
| 20 | Kim et al.[78] |
| 21 | Ashida et al.[75] |
| 22 | Seuss et al.[75] |
| 23 | Agarwal et al.[74] |
| 24 | Siltanen et al.[82] |
| 25 | Zhao et al.[88] |
| 26-28 | Watanabe et al.[85] |
| 29-31 | van Loo et al.[54] |
| 32 | Sun et al.[84] |
| 33 | Hu et al.[77] |
| 34 | Xie et al.[86] |
| 35 | Yang et al.[87] |
| 36 | Kamperman et al.[55] |
| 37 | Yu et al.[90] |
| 38 | Lin et al.[79] |
| 39 | Fattahi et al.[95] |
| 40 | Zhu et al.[94] |
| 41 | Jeong et al.[93] |
| 42 | Mytnyk et al.[49] |
| 43 | Wang et al.[91] |
| 44 | Liu et al.[39] |
| 45 | Liu et al.[92] |

**Figure S5.9. Literature study for continuously produced hollow core-shell microcapsules.** Elaboration of figure 2l with corresponding studies per datapoint.
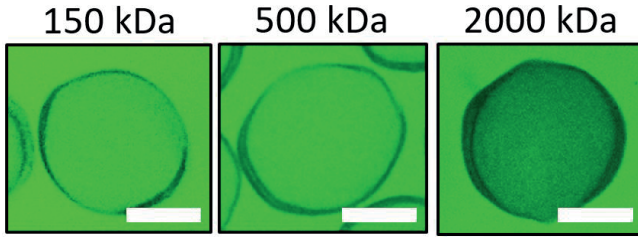
**Figure S5.10. Permeability of microcapsules.** Fluorescent confocal micrographs of microcapsules incubated for 30 minutes in Dextran-FITC containing solutions of 150 kDa, 500 kDa and 2000 kDa. Representative micrographs out n=3 experiments. Scale bars represent 100 μm.
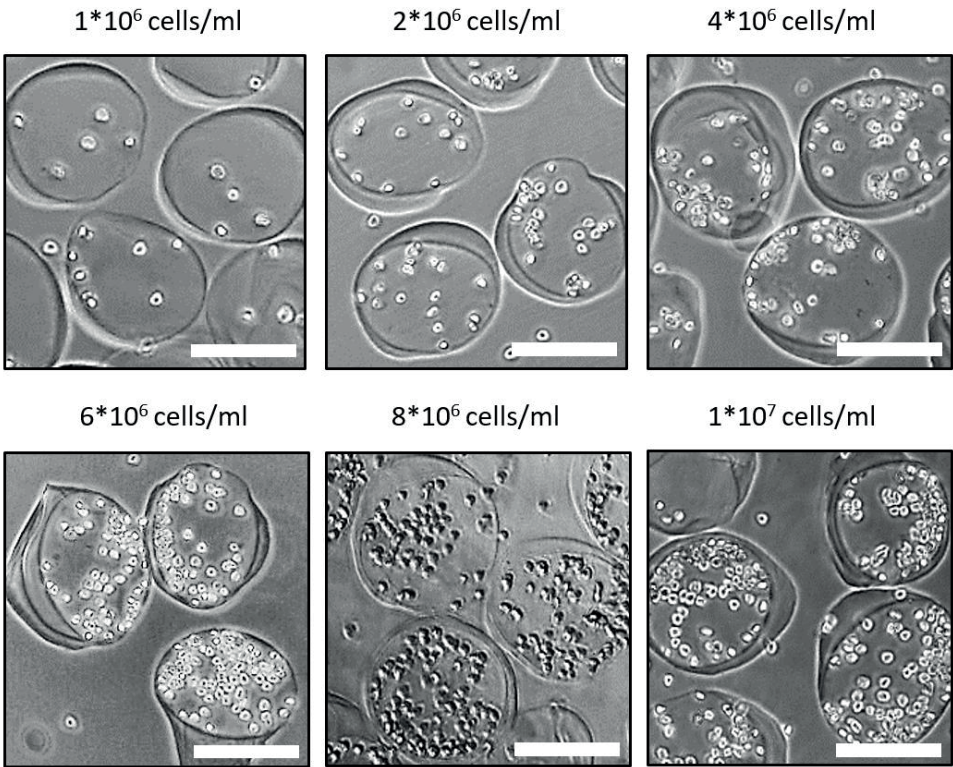


**Figure S5.11. In Air microencapsulation of 3T3 Fibroblast within alginate microcapsules.** Microphotographs of 3T3 fibroblast-laden microcapsules produced using a variety of cell concentrations. Representative micrographs out n=3 experiments. Scale bars represent 200 μm.
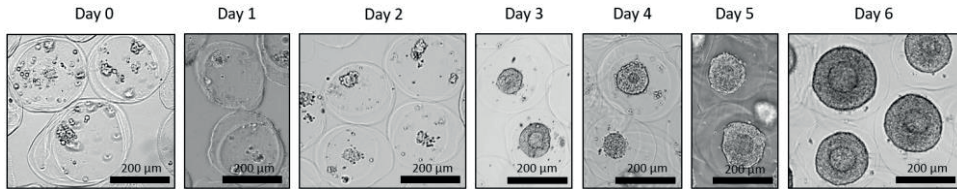
**Figure S5.12. Embryoid body formation by in-air microcapsulated hPSCs.** Microphotographs of encapsulated hPSCs show aggregation and lumenogenesis. Representative micrographs out n=3 experiments. Scale bar represents 200 μm.
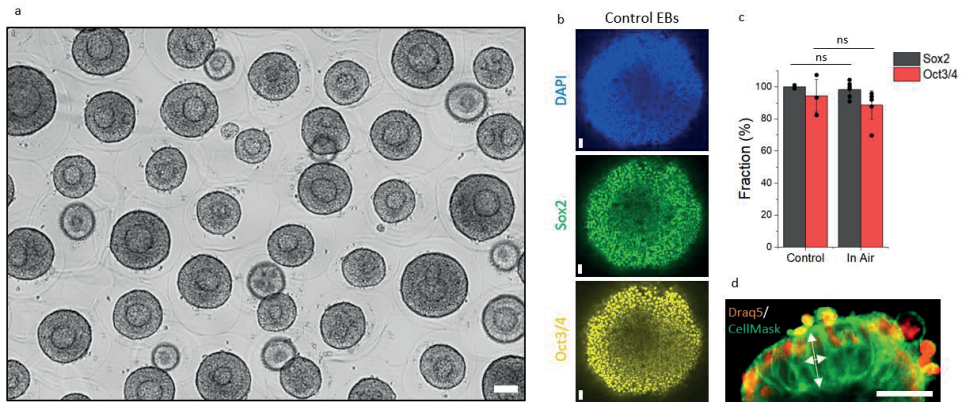


**Figure S5.13. Mass production of embryoid body by in-air microcapsulating hPSCs.** (a) Microphotograph of EBs formed within in-air produced alginate microcapsules. Representative micrographs out n=3 experiments. (b) Fluorescence microphotograph of EBs produced using microwells with 5000 cells/microwell, which were stained with DAPI for nuclei (blue), SOX2 (green), and OCT3/4 (yellow) for pluripotency. (c) Quantification and comparison of pluripotency by percentage of cells positive for SOX2 and OCT3/4 between EBs produced with conventional microwells or In Air microfluidics (n=300 cells). Data is presented as mean values +/- SD. Significance was determined based on one-way Anova analysis. Significance was determined based on one-way Anova analysis. Significance of p <0.05 is indicated by *. (d) Confocal microphotograph of an EB with its nucleus stained with Draq5 (orange) and its cell membrane stained with CellMask (green). Scale bars represent 50 μm.
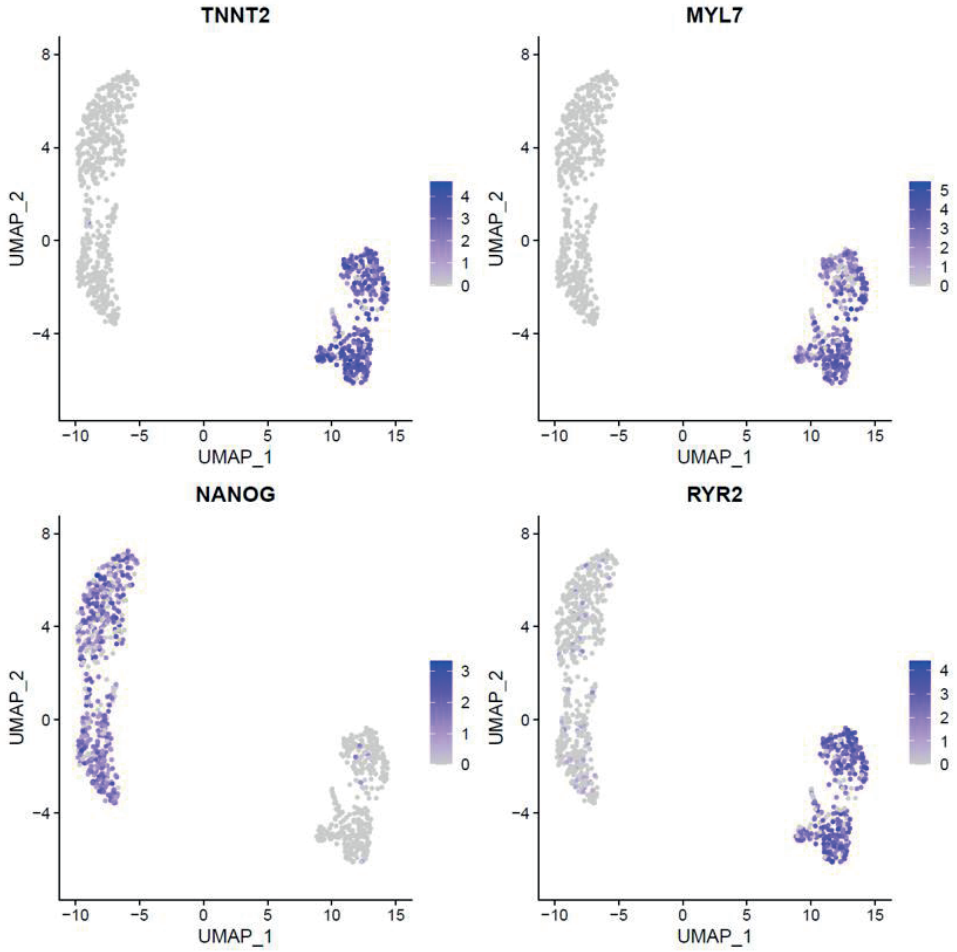
**Figure S5.14. Single cell RNA sequencing UMAP plots for pluripotency and cardiac markers.** Heatmap of NANOG, TNNT2, MYL7 and RYR2 gene expression in UMAP plots.

5
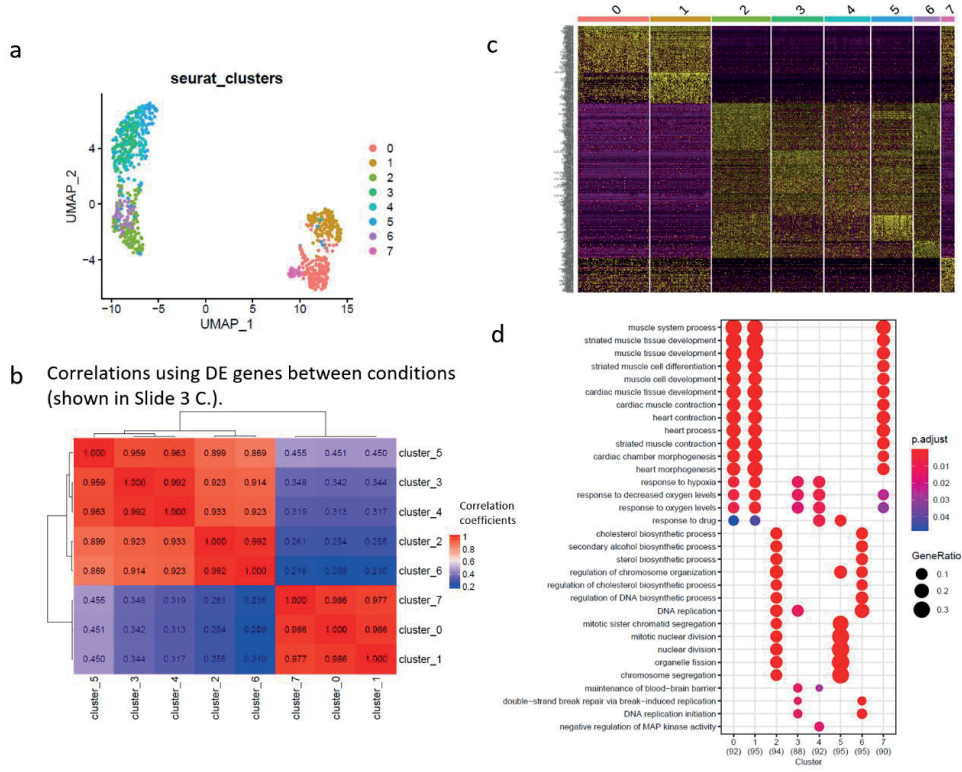
**Figure S5.15. Single cell RNA sequencing Seurat cluster data.** (a) Seurat clusters. (b) Correlation using differential expression genes between conditions. (c) Heatmap of marker genes corresponding to identified clusters. (d) Gene ontology heatmap of differential genes per cluster. P-adjust corrected using Benjamini-Hochberg correction for multiple comparisons.
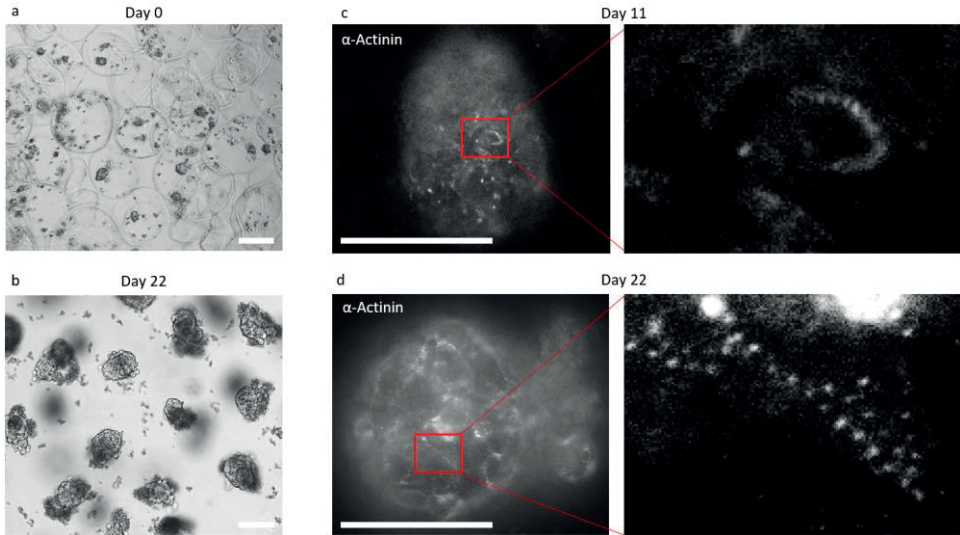
**Figure S5.16. Functional *human* cardiospheres produced in mass using in-air microfluidics.** (a) Microphotograph of encapsulated *human* pluripotent stem cells immediate after microencapsulation. (b) Microphotograph of encapsulated cardiospheres after 22 days of cardiac differentiation. Fluorescence microphotograph of a-actinin reporter in differentiated cardiomyocytes cultured after (c) 11 days and (d) 22 days of culture. Scale bars represent 100 μm.

**5**
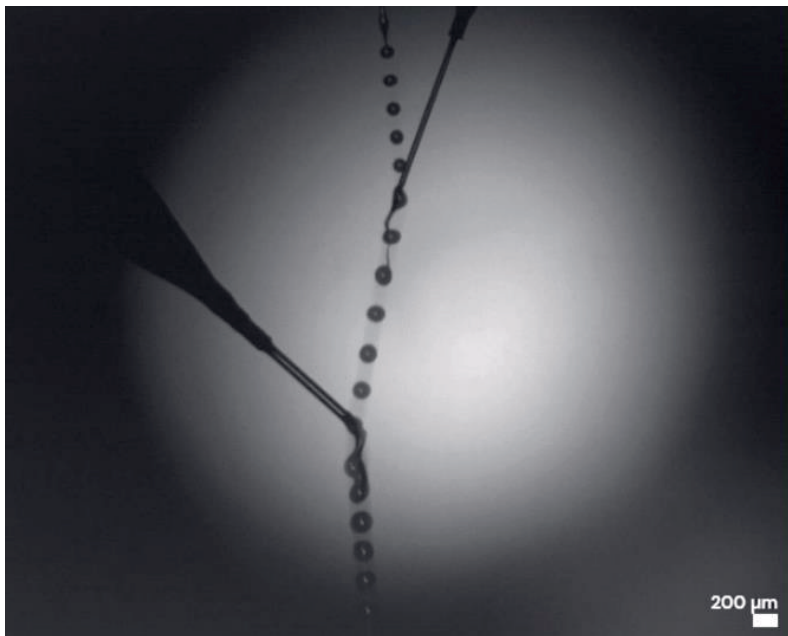


**Supplemental movie S5.1 (still). In Air Microfluidic setup for mass production of microcapsules.** Sequential start flow of core jet, actuation of piezo element at 5.5 kHz, start flow shell-precursor jet and start flow crosslinker jet.
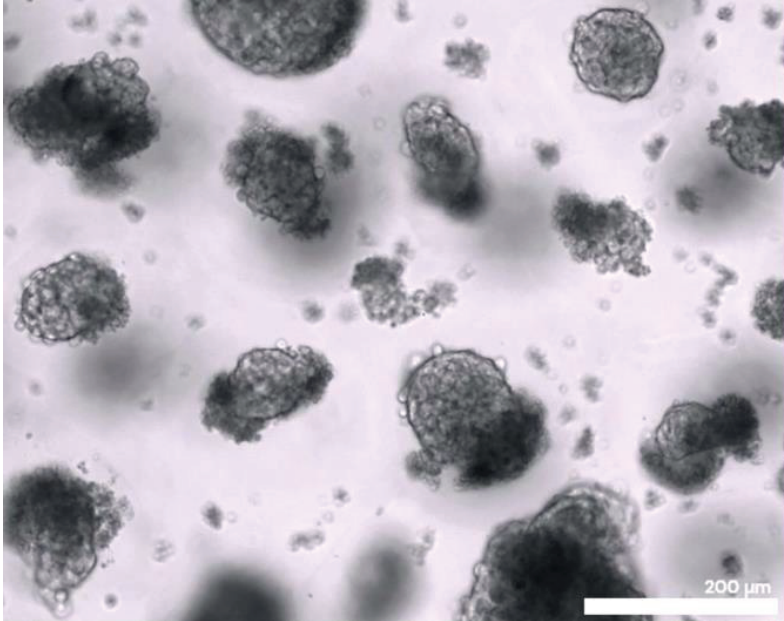
**Supplemental movie S5.2 (still). Spontaneous contraction of cardiospheres.** Brightfield microscopy video of spontaneously contracting cardiospheres within In Air generated microcapsules.
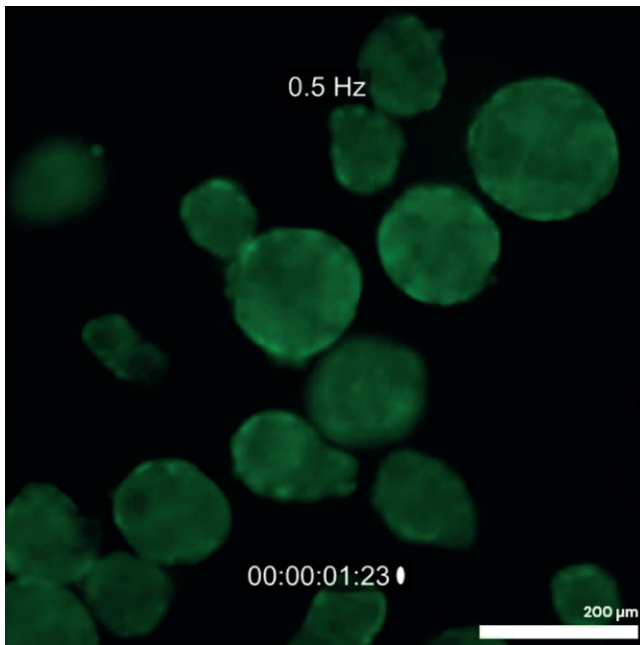


**Supplemental movie S5.3 (still). Calcium flux of (non-)stimulated cardiospheres.** Calcium flux of cardiospheres within In Air generated microcapsules as visualized by Fluo-4 AM. Cardiospheres were stimulated at 0Hz, 0.5 Hz, 1 Hz and 2 Hz.
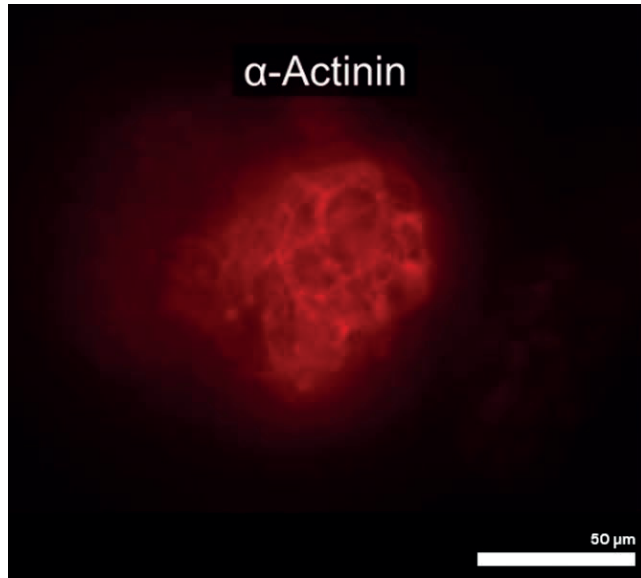
**Supplemental movie S5.4 (still). Sarcomere contraction in non-stimulated cardiospheres.** Brightfield video, fluorescent microscopy video for NKX 2-5 GFP-positive and fluorescent microscopy video for alpha-actinin mCherry-positive sarcomeres in a cardiospheres within an In Air generated microcapsule
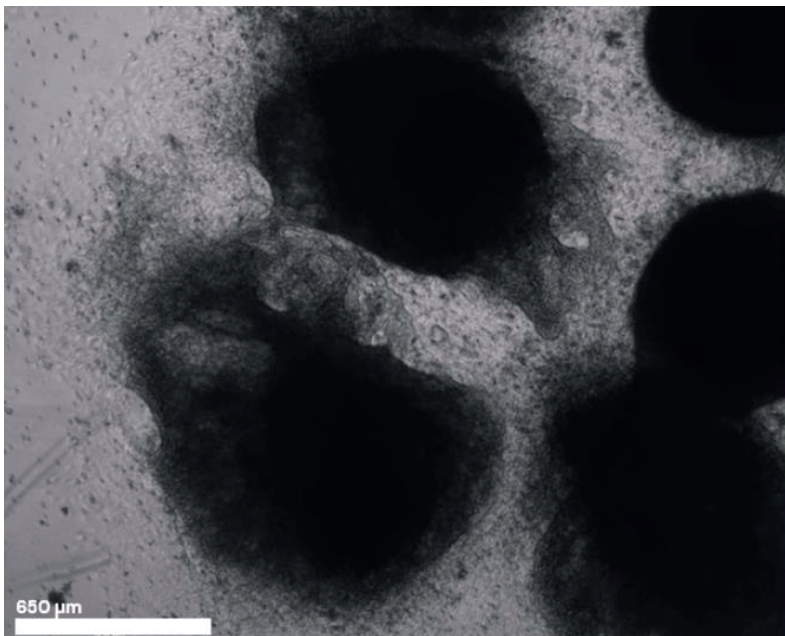


**Supplemental movie S5.5 (still). Control plated cardiospheres.** Brightfield video of control cardiospheres which were plated on a culture plate.

# References

1.     Lancaster, M. A. & Knoblich, J. A. Organogenesis in a dish: modeling development and disease using organoid technologies. *Science* **345**, 1247125 (2014).

2.     Eiraku, M. & Sasai, Y. Self-formation of layered neural structures in three-dimensional culture of ES cells. *Curr. Opin. Neurobiol.* **22**, 768–777 (2012).

3.     Drakhlis, L. *et al.* Human heart-forming organoids recapitulate early heart and foregut development. *Nat. Biotechnol.* **39**, 737–746 (2021).

4.     Lancaster, M. A. & Knoblich, J. A. Generation of cerebral organoids from human pluripotent stem cells. *Nat. Protoc.* **9**, 2329–2340 (2014).

5.     Kim, J., Koo, B.-K. & Knoblich, J. A. Human organoids: model systems for human biology and medicine. *Nat. Rev. Mol. Cell Biol.* **21**, 571–584 (2020).

6.     Dutta, D., Heo, I. & Clevers, H. Disease Modeling in Stem Cell-Derived 3D Organoid Systems. *Trends Mol. Med.* **23**, 393–410 (2017).

7.     Qian, X. *et al.* Brain-Region-Specific Organoids Using Mini-bioreactors for Modeling ZIKV Exposure. *Cell* **165**, 1238–1254 (2016).

8.     McCracken, K. W. *et al.* Modelling human development and disease in pluripotent stem-cell-derived gastric organoids. *Nature* **516**, 400–404 (2014).

9.     Sahu, S. & Sharan, S. K. Translating Embryogenesis to Generate Organoids: Novel Approaches to Personalized Medicine. *iScience* **23**, 101485 (2020).

10.    Mills, R. J. *et al.* Drug Screening in Human PSC-Cardiac Organoids Identifies Pro-proliferative Compounds Acting via the Mevalonate Pathway. *Cell Stem Cell* **24**, 895-907.e6 (2019).

11.    Richards, D. J. *et al.* Human cardiac organoids for the modelling of myocardial infarction and drug cardiotoxicity. *Nat. Biomed. Eng.* **4**, 446–462 (2020).

12.    Lancaster, M. A. *et al.* Cerebral organoids model human brain development and microcephaly. *Nature* **501**, 373–379 (2013).

13.    Boj, S. F. *et al.* Organoid models of human and mouse ductal pancreatic cancer. *Cell* **160**, 324–338 (2015).

14.    Gao, D. *et al.* Organoid cultures derived from patients with advanced prostate cancer. *Cell* **159**, 176–187 (2014).

15.    van de Wetering, M. *et al.* Prospective derivation of a living organoid biobank of colorectal cancer patients. *Cell* **161**, 933–945 (2015).

16.    Dekkers, J. F. *et al.* Characterizing responses to CFTR-modulating drugs using rectal organoids derived from subjects with cystic fibrosis. *Sci. Transl. Med.* **8**, 344ra84 (2016).

17.    Yui, S. *et al.* Functional engraftment of colon epithelium expanded in vitro from a single adult Lgr5^{+} stem cell. *Nat. Med.* **18**, 618–623 (2012).

18.    Fordham, R. P. *et al.* Transplantation of expanded fetal intestinal progenitors contributes to colon regeneration after injury. *Cell Stem Cell* **13**, 734–744 (2013).

19.    Clevers, H. Modeling Development and Disease with Organoids. *Cell* **165**, 1586–1597 (2016).

20.    Schot, M., Araújo-Gomes, N., van Loo, B., Kamperman, T. & Leijten, J. Scalable fabrication, compartmentalization and applications of living microtissues. *Bioact. Mater.* **19**, 392–405 (2023).

21.    Ng, E. S., Davis, R. P., Azzola, L., Stanley, E. G. & Elefanty, A. G. Forced aggregation of defined numbers of human embryonic stem cells into embryoid bodies fosters robust, reproducible hematopoietic differentiation. *Blood* **106**, 1601–1603 (2005).

22.    Hofer, M. & Lutolf, M. P. Engineering organoids. *Nat. Rev. Mater.* **6**, 402–420 (2021).

23.    Velasco, V., Shariati, S. A. & Esfandyarpour, R. Microtechnology-based methods for organoid models. *Microsystems Nanoeng.* **6**, 76 (2020).

24.    Nelson, C. M., VanDuijn, M. M., Inman, J. L., Fletcher, D. A. & Bissell, M. J. Tissue geometry determines sites of mammary branching morphogenesis in organotypic cultures. *Science (80-. ).* **314**, 298–300 (2006).

25.    Warmflash, A., Sorre, B., Etoc, F., Siggia, E. D. & Brivanlou, A. H. A method to recapitulate early embryonic spatial patterning in human embryonic stem cells. *Nat. Methods* **11**, 847–854 (2014).

26.    Gjorevski, N. *et al.* Designer matrices for intestinal stem cell and organoid culture. *Nature* **539**, 560–564 (2016).

27.    Rivron, N. C. *et al.* Blastocyst-like structures generated solely from stem cells. *Nature* **557**, 106–111

(2018).

28.   Sozen, B. *et al.* Self-assembly of embryonic and two extra-embryonic stem cell types into gastrulating embryo-like structures. *Nat. Cell Biol.* **20**, 979–989 (2018).

29.   Hofbauer, P. *et al.* Cardioids reveal self-organizing principles of human cardiogenesis. *Cell* **184**, 3299-3317.e22 (2021).

30.   Lewis-Israeli, Y. R. *et al.* Self-assembling human heart organoids for the modeling of cardiac development and congenital heart disease. *Nat. Commun.* **12**, 5142 (2021).

31.   Ming, Y. *et al.* Longitudinal morphological and functional characterization of human heart organoids using optical coherence tomography. *Biosens. Bioelectron.* **207**, 114136 (2022).

32.   Beauchamp, P. *et al.* Development and Characterization of a Scaffold-Free 3D Spheroid Model of Induced Pluripotent Stem Cell-Derived Human Cardiomyocytes. *Tissue Eng. - Part C Methods* **21**, 852–861 (2015).

33.   Przepiorski, A. *et al.* A Simple Bioreactor-Based Method to Generate Kidney Organoids from Pluripotent Stem Cells. *Stem Cell Reports* **11**, 470–484 (2018).

34.   Utada, A. S., Fernandez-Nieves, A., Stone, H. A. & Weitz, D. A. Dripping to Jetting Transitions in Coflowing Liquid Streams. *Phys. Rev. Lett.* **99**, 94502 (2007).

35.   Prastowo, A., Feuerborn, A., Cook, P. R. & Walsh, E. J. Biocompatibility of fluids for multiphase drops-in-drops microfluidics. *Biomed. Microdevices* **18**, 114 (2016).

36.   Yau, A. C. Y., Lönnblom, E., Zhong, J. & Holmdahl, R. Influence of hydrocarbon oil structure on adjuvanticity and autoimmunity. *Sci. Rep.* **7**, 14998 (2017).

37.   Kamelia, L., Louisse, J., de Haan, L., Rietjens, I. M. C. M. & Boogaard, P. J. Prenatal developmental toxicity testing of petroleum substances: Application of the  mouse embryonic stem cell test (EST) to compare in vitro potencies with potencies observed in vivo. *Toxicol. In Vitro* **44**, 303–312 (2017).

38.   Song, Y., Sauret, A. & Cheung Shum, H. All-aqueous multiphase microfluidics. *Biomicrofluidics* **7**, 61301 (2013).

39.   Liu, H. *et al.* A Droplet Microfluidic System to Fabricate Hybrid Capsules Enabling Stem Cell Organoid Engineering. *Adv. Sci.* **7**, 1903739 (2020).

40.   Rao, W. *et al.* Enhanced enrichment of prostate cancer stem-like cells with miniaturized 3D culture in liquid core-hydrogel shell microcapsules. *Biomaterials* **35**, 7762–7773 (2014).

41.   Agarwal, P. *et al.* One-step microfluidic generation of pre-hatching embryo-like core-shell microcapsules for miniaturized 3D culture of pluripotent stem cells. *Lab Chip* **13**, 4525–4533 (2013).

42.   Sakai, S. *et al.* Enzymatically fabricated and degradable microcapsules for production of multicellular spheroids with well-defined diameters of less than 150 microm. *Biomaterials* **30**, 5937–5942 (2009).

43.   Nguyen, D. K., Son, Y. M. & Lee, N.-E. Hydrogel Encapsulation of Cells in Core-Shell Microcapsules for Cell Delivery. *Adv. Healthc. Mater.* **4**, 1537–1544 (2015).

44.   Correia, C. R., Bjørge, I. M., Zeng, J., Matsusaki, M. & Mano, J. F. Liquefied Microcapsules as Dual-Microcarriers for 3D+3D Bottom-Up Tissue Engineering. *Adv. Healthc. Mater.* **8**, 1901221 (2019).

45.   Alessandri, K. *et al.* Cellular capsules as a tool for multicellular spheroid production and for investigating the mechanics of tumor progression in vitro. *Proc. Natl. Acad. Sci. U. S. A.* **110**, 14843–14848 (2013).

46.   Alessandri, K. *et al.* A 3D printed microfluidic device for production of functionalized hydrogel microcapsules for culture and differentiation of human Neuronal Stem Cells (hNSC). *Lab Chip* **16**, 1593–1604 (2016).

47.   Ma, M. *et al.* Core-shell hydrogel microcapsules for improved islets encapsulation. *Adv. Healthc. Mater.* **2**, 667–672 (2013).

48.   Rutkowski, S. *et al.* Magnetically-guided hydrogel capsule motors produced via ultrasound assisted hydrodynamic electrospray ionization jetting. *J. Colloid Interface Sci.* **541**, 407–417 (2019).

49.   Mytnyk, S. *et al.* Microcapsules with a permeable hydrogel shell and an aqueous core continuously produced in a 3D microdevice by all-aqueous microfluidics. *RSC Adv.* **7**, 11331–11337 (2017).

50.   Yasuga, H., Kamiya, K., Takeuchi, S. & Miki, N. Self-generation of two-dimensional droplet array using oil–water immiscibility and replacement. *Lab Chip* **18**, 1130–1137 (2018).

51.   Jeyhani, M., Thevakumaran, R., Abbasi, N., Hwang, D. K. & Tsai, S. S. H. Microfluidic Generation of All-Aqueous Double and Triple Emulsions. *Small* **16**, 1906565 (2020).

52.   Deng, Y. *et al.* Rapid purification of cell encapsulated hydrogel beads from oil phase to aqueous phase in a microfluidic device. *Lab Chip* **11**, 4117–4121 (2011).

**5**

53.    Wennink, J. W. H. *et al.* Injectable Hydrogels by Enzymatic Co-Crosslinking of Dextran and Hyaluronic Acid Tyramine Conjugates. *Macromol. Symp.* **309-310**, 213–221 (2011).

54.    van Loo, B. *et al.* Enzymatic outside-in cross-linking enables single-step microcapsule production for high-throughput three-dimensional cell microaggregate formation. *Mater. Today Bio* **6**, 100047 (2020).

55.    Kamperman, T. *et al.* On-the-fly exchangeable microfluidic nozzles for facile production of various monodisperse micromaterials. *Lab Chip* **19**, 1977–1984 (2019).

56.    Den Hartogh, S. C. *et al.* Dual reporter MESP1 mCherry/w-NKX2-5 eGFP/w hESCs enable studying early human cardiac differentiation. *Stem Cells* **33**, 56–67 (2015).

57.    Elliott, D. A. *et al.* NKX2-5eGFP/w hESCs for isolation of human cardiac progenitors and cardiomyocytes. *Nat. Methods* **8**, 1037–1040 (2011).

58.    Chen, G. *et al.* Chemically defined conditions for human iPSC derivation and culture. *Nat. Methods* **8**, 424–429 (2011).

59.    Moreira Teixeira, L. S. *et al.* High throughput generated micro-aggregates of chondrocytes stimulate cartilage formation in vitro and in vivo. *Eur. Cell. Mater.* **23**, 387–399 (2012).

60.    Schwach, V., Cofiño-Fabres, C., ten Den, S. A. & Passier, R. Improved Atrial Differentiation of Human Pluripotent Stem Cells by Activation of Retinoic Acid Receptor Alpha (RAR&alpha;). *Journal of Personalized Medicine* **12**, (2022).

61.    Birket, M. J. *et al.* Contractile Defect Caused by Mutation in MYBPC3 Revealed under Conditions Optimized for Human PSC-Cardiomyocyte Function. *Cell Rep.* **13**, 733–745 (2015).

62.    Hashimshony, T. *et al.* CEL-Seq2: sensitive highly-multiplexed single-cell RNA-Seq. *Genome Biol.* **17**, 77 (2016).

63.    Melsted, P. *et al.* Modular, efficient and constant-memory single-cell RNA-seq preprocessing. *Nat. Biotechnol.* **39**, 813–818 (2021).

64.    Hao, Y. *et al.* Integrated analysis of multimodal single-cell data. *Cell* **184**, 3573-3587.e29 (2021).

65.    Wu, T. *et al.* clusterProfiler 4.0: A universal enrichment tool for interpreting omics data. *Innov. (Cambridge* **2**, 100141 (2021).

66.    Visser, C. W., Kamperman, T., Karbaat, L. P., Lohse, D. & Karperien, M. In-air microfluidics enables rapid fabrication of emulsions, suspensions, and 3D modular (bio)materials. *Sci. Adv.* **4**, (2018).

67.    Su, K. Y. *et al.* Deciphering epiblast lumenogenesis reveals proamniotic cavity control of embryo growth and patterning. *Sci. Adv.* **7**, eabe1640 (2022).

68.    Koldeweij, R. B. J., van Capelleveen, B. F., Lohse, D. & Visser, C. W. Marangoni-driven spreading of miscible liquids in the binary pendant drop geometry. *Soft Matter* **15**, 8525–8531 (2019).

69.    Li, J., Wu, Y., He, J. & Huang, Y. A new insight to the effect of calcium concentration on gelation process and physical properties of alginate films. *J. Mater. Sci.* **51**, 5791–5801 (2016).

70.    Yoshida, K., Sekine, T., Matsuzaki, F., Yanaki, T. & Yamaguchi, M. Stability of vitamin A in oil-in-water-in-oil-type multiple emulsions. *J. Am. Oil Chem. Soc.* **76**, 1–6 (1999).

71.    Wang, W. *et al.* Controllable microfluidic production of multicomponent multiple emulsions. *Lab Chip* **11**, 1587–1592 (2011).

72.    Seiffert, S., Thiele, J., Abate, A. R. & Weitz, D. A. Smart Microgel Capsules from Macromolecular Precursors. *J. Am. Chem. Soc.* **132**, 6606–6609 (2010).

73.    Lee, M.-H., Oh, S.-G., Moon, S.-K. & Bae, S.-Y. Preparation of Silica Particles Encapsulating Retinol Using O/W/O Multiple Emulsions. *J. Colloid Interface Sci.* **240**, 83–89 (2001).

74.    Agarwal, P. *et al.* A Biomimetic Core-Shell Platform for Miniaturized 3D Cell and Tissue Engineering. *Part. Part. Syst. Charact. Meas. Descr. Part. Prop. Behav. powders other disperse Syst.* **32**, 809–816 (2015).

75.    Ashida, T., Sakai, S. & Taya, M. Competing two enzymatic reactions realizing one-step preparation of cell-enclosing duplex microcapsules. *Biotechnol. Prog.* **29**, 1528–1534 (2013).

76.    Doméjean, H. *et al.* Controlled production of sub-millimeter liquid core hydrogel capsules for parallelized 3D cell culture. *Lab Chip* **17**, 110–119 (2017).

77.    Hu, Y. & Perez-Mercader, J. Microcapsules with Distinct Dual-Layer Shells and Their Applications for the Encapsulation, Preservation, and Slow Release of Hydrophilic Small Molecules. *ACS Appl. Mater. Interfaces* **11**, 41640–41648 (2019).

78.    Kim, C. *et al.* Generation of core-shell microcapsules with three-dimensional focusing device for efficient formation of cell spheroid. *Lab Chip* **11**, 246–252 (2011).

79.    Lin, Z. *et al.* Precisely controlled delivery of magnesium ions thru sponge-like monodisperse

PLGA/nano-MgO-alginate core-shell microsphere device to enable in-situ bone regeneration. *Biomaterials* **174**, 1–16 (2018).

80. Ren, Y. *et al.* Tuning the formation and stability of microcapsules by environmental conditions and chitosan structure. *Int. J. Biol. Macromol.* **91**, 1090–1100 (2016).

81. Seuss, M., Schmolke, W., Drechsler, A., Fery, A. & Seiffert, S. Core–Shell Microgels with Switchable Elasticity at Constant Interfacial Interaction. *ACS Appl. Mater. Interfaces* **8**, 16317–16327 (2016).

82. Siltanen, C. *et al.* One step fabrication of hydrogel microcapsules with hollow core for assembly and cultivation of hepatocyte spheroids. *Acta Biomater.* **50**, 428–436 (2017).

83. Song, Y., Chan, Y. K., Ma, Q., Liu, Z. & Shum, H. C. All-Aqueous Electrosprayed Emulsion for Templated Fabrication of Cytocompatible Microcapsules. *ACS Appl. Mater. Interfaces* **7**, 13925–13933 (2015).

84. Sun, M., Durkin, P., Li, J., Toth, T. L. & He, X. Label-Free On-Chip Selective Extraction of Cell-Aggregate-Laden Microcapsules from Oil into Aqueous Solution with Optical Sensor and Dielectrophoresis. *ACS sensors* **3**, 410–417 (2018).

85. Watanabe, T., Motohiro, I. & Ono, T. Microfluidic Formation of Hydrogel Microcapsules with a Single Aqueous Core by Spontaneous Cross-Linking in Aqueous Two-Phase System Droplets. *Langmuir* **35**, 2358–2367 (2019).

86. Xie, X. *et al.* Microfluidic Fabrication of Colloidal Nanomaterials-Encapsulated Microcapsules for Biomolecular Sensing. *Nano Lett.* **17**, 2015–2020 (2017).

87. Yang, X.-L. *et al.* Core–Shell Chitosan Microcapsules for Programmed Sequential Drug Release. *ACS Appl. Mater. Interfaces* **8**, 10524–10534 (2016).

88. Zhao, G., Liu, X., Zhu, K. & He, X. Hydrogel Encapsulation Facilitates Rapid-Cooling Cryopreservation of Stem Cell-Laden Core-Shell Microcapsules as Cell-Biomaterial Constructs. *Adv. Healthc. Mater.* **6**, (2017).

89. Zhao, S. *et al.* Coaxial electrospray of liquid core-hydrogel shell microcapsules for encapsulation and miniaturized 3D culture of pluripotent stem cells. *Integr. Biol. (Camb).* **6**, 874–884 (2014).

90. Yu, L. *et al.* Microfluidic formation of core-shell alginate microparticles for protein encapsulation and controlled release. *J. Colloid Interface Sci.* **539**, 497–503 (2019).

91. Wang, D., Zheng, X., Chen, X. & Hu, G. Flow-pattern-altered syntheses of core–shell and hole–shell microparticles in an axisymmetric microfluidic device. *Acta Mech. Sin.* (2021). doi:10.1007/s10409-021-01096-w

92. Liu, Z. *et al.* Mild formation of core-shell hydrogel microcapsules for cell encapsulation. *Biofabrication* (2020). doi:10.1088/1758-5090/abd076

93. Jeong, H.-S. *et al.* Hydrogel Microcapsules with a Thin Oil Layer: Smart Triggered Release via Diverse Stimuli. *Adv. Funct. Mater.* **31**, 2009553 (2021).

94. Zhu, Z. *et al.* Perfluorocarbon-Loaded Hydrogel Microcapsules from Interface Shearing for Magnetic Guided Ultrasound and Laser Activation . *Frontiers in Physics* **8**, 477 (2020).

95. Fattahi, P. *et al.* Core–shell hydrogel microcapsules enable formation of human pluripotent stem cell spheroids and their cultivation in a stirred bioreactor. *Sci. Rep.* **11**, 7177 (2021).

96. Khodabakhsh Aghdam, S., Khoshfetrat, A. B., Rahbarghazi, R., Jafarizadeh-Malmiri, H. & Khaksar, M. Collagen modulates functional activity of hepatic cells inside alginate-galactosylated chitosan hydrogel microcapsules. *Int. J. Biol. Macromol.* **156**, 1270–1278 (2020).

97. Worley, S. L., Vaughn, B. J., Terry, A. I., Gardiner, C. S. & DeKrey, G. K. Time- and dose-dependent effects of ethanol on mouse embryonic stem cells. *Reprod. Toxicol.* **57**, 157–164 (2015).

98. Wang, Q., Song, J., Liu, Y. & Zhao, X. Involvement of Wnt pathway in ethanol-induced inhibition of mouse embryonic stem cell differentiation. *Alcohol* **58**, 13–18 (2017).

99. Tapani, E., Taavitsainen, M., Lindros, K., Vehmas, T. & Lehtonen, E. Toxicity of ethanol in low concentrations. Experimental evaluation in cell culture. *Acta Radiol.* **37**, 923–926 (1996).

100. Zeevaert, K., Elsafi Mabrouk, M. H., Wagner, W. & Goetzke, R. Cell Mechanics in Embryoid Bodies. *Cells* **9**, (2020).

101. Neagu, A. *et al.* In vitro capture and characterization of embryonic rosette-stage pluripotency between naive and primed states. *Nat. Cell Biol.* **22**, 534–545 (2020).

102. Taniguchi, K. *et al.* Lumen Formation Is an Intrinsic Property of Isolated Human Pluripotent Stem Cells. *Stem cell reports* **5**, 954–962 (2015).

103. Shao, Y. *et al.* A pluripotent stem cell-based model for post-implantation human amniotic sac development. *Nat. Commun.* **8**, 208 (2017).

**5**

104. Harrison, S. E., Sozen, B., Christodoulou, N., Kyprianou, C. & Zernicka-Goetz, M. Assembly of embryonic and extraembryonic stem cells to mimic embryogenesis in vitro. *Science (80-. ).* **356**, eaal1810 (2017).

105. Poh, Y.-C. *et al.* Generation of organized germ layers from a single mouse embryonic stem cell. *Nat. Commun.* **5**, 4000 (2014).

106. Folmes, C. D. L., Dzeja, P. P., Nelson, T. J. & Terzic, A. Metabolic Plasticity in Stem Cell Homeostasis and Differentiation. *Cell Stem Cell* **11**, 596–606 (2012).

107. Panopoulos, A. D. *et al.* The metabolome of induced pluripotent stem cells reveals metabolic changes occurring in somatic cell reprogramming. *Cell Res.* **22**, 168–177 (2012).

108. Ezashi, T., Das, P. & Roberts, R. M. Low O2 tensions and the prevention of differentiation of hES cells. *Proc. Natl. Acad. Sci. U. S. A.* **102**, 4783–4788 (2005).

109. Cha, Y. *et al.* Metabolic control of primed human pluripotent stem cell fate and function by the miR-200c–SIRT2 axis. *Nat. Cell Biol.* **19**, 445–456 (2017).

110. Mu, W.-L. *et al.* Sox2 Deacetylation by Sirt1 Is Involved in Mouse Somatic Reprogramming. *Stem Cells* **33**, 2135–2147 (2015).

111. Esteves, T. C. *et al.* A microfluidic system supports single mouse embryo culture leading to full-term development. *RSC Adv.* **3**, 26451–26458 (2013).

112. Lian, X. *et al.* Directed cardiomyocyte differentiation from human pluripotent stem cells by modulating Wnt/β-catenin signaling under fully defined conditions. *Nat. Protoc.* **8**, 162–175 (2013).

113. Ronaldson-Bouchard, K. *et al.* Advanced maturation of human cardiac tissue grown from pluripotent stem cells. *Nature* **556**, 239–243 (2018).

114. Nunes, S. S. *et al.* Biowire: a platform for maturation of human pluripotent stem cell–derived cardiomyocytes. *Nat. Methods* **10**, 781–787 (2013).

115. Chan, Y.-C. *et al.* Electrical stimulation promotes maturation of cardiomyocytes derived from human embryonic stem cells. *J. Cardiovasc. Transl. Res.* **6**, 989–999 (2013).

116. Ribeiro, M. C. *et al.* A cardiomyocyte show of force: A fluorescent alpha-actinin reporter line sheds light on human cardiomyocyte contractility versus substrate stiffness. *J. Mol. Cell. Cardiol.* **141**, 54–64 (2020).

**5**

5
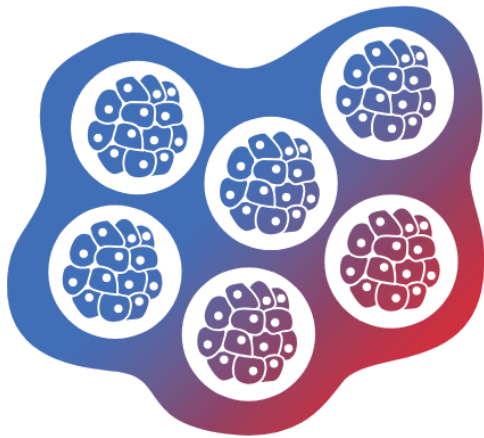
# 6

# Single-step biofabrication of in situ spheroid-forming compartmentalized hydrogel for clinical sized cartilage tissue formation

3D cellular spheroids offer more biomimetic microenvironments than conventional 2D cell culture technologies, which has proven value for many tissue engineering applications. Despite the beneficiary effects of 3D cell culture, clinical translation of spheroid tissue engineering is challenged by the limited scalability of current methods of spheroid formation. Although the recent adoption of droplet microfluidics can provide a continuous production process, the use of oils and surfactants, the generally low throughput, and requirement of additional biofabrication steps hinder clinical translation of spheroid culture. Here we report on the use of clean (e.g., oil-free and surfactant-free), ultra-high throughput (e.g., 8.5 ml/min, 10.000 spheroids/s), single-step, in-air microfluidic biofabrication of spheroid forming compartmentalized hydrogels. We demonstrated that this novel technique could reliably produce 1D, 2D, and 3D compartmentalized hydrogel constructs in the form of fibers, plane, and volumes, which each allowed for distinct (an)isotropic orientation of hollow spheroids forming compartments. The spheroids that were produced within ink-jet bioprinted compartmentalized hydrogels outperformed 2D cell cultures in terms of chondrogenic behavior. Moreover, we demonstrated that the cellular spheroids could be harvested from compartmentalized hydrogels and used to build shape-stable centimeter-sized biomaterial-free living tissues in a bottom-up manner. Consequently, it is anticipated that in-air microfluidic production of spheroid forming compartmentalized hydrogels could advance the production and use of cellular spheroids for various biomedical applications.

## 6.1 Introduction

Two dimensional (2D) *in vitro* cell culture has historically been the gold standard in the field of tissue engineering, which aims to repair, regenerate, or replace damaged living tissues. However, conventional 2D cell culture environments do not resemble their natural *in vivo* counterpart and thus adversely affect cellular behavior.[1–5] Three dimensional (3D) cell cultures such as cellular spheroid or organoids have allowed for a more biomimetic approach towards cell culture.[6–8] It has been widely reported that biomimetic 3D spheroid cultured cells outperform 2D cultured cells when utilized for tissue engineering, [9–13] and can facilitate more reliable drug target discovery and enable engineering of macroscopic tissue constructs with improved functionalities.[14–19] For example, 3D printing of stem cell spheroid-laden bioinks improves functional behavior (e.g., chondrogenic differentiation and cartilage matrix deposition) of biofabricated constructs.[20] Although promising, 3D culture techniques such as spheroid culture are hindered in their clinical translation by their production methods, which are often batch processes that are characterized by low production rates. These batch production technologies such as microwells[9,10,12,21–24] and hanging drops[13,25–27] require multiple complex and time-consuming steps that only offer a limited yield of spheroids. Although specific bioreactor approaches could allow for higher production yields, they are still limited to being batch processes that often associate with low levels of control of spheroid diameter as compared to compartmentalized technologies such as microwells and hanging drops.[28] While this might be sufficient for the small lab scale experimentation, a robust single step biofabrication technology with high production rates and high monodispersity remains needed to facilitate the clinical translation of spheroid technology for clinically sized tissues.[29,30]

Microfluidic compartmentalization has recently been explored to evolve spheroid production from a batch process towards a continuous process. Microfluidic encapsulation of cells in hollow biomaterial compartments allows for the controlled continuous production of cellular spheroid forming microbioreactors, which offers a higher production rate than conventional batch-based processes.[31–39] However, the design of conventional on-chip microfluidic droplet generators prevents the widespread clinical use of microfluidic produced spheroids owing to a variety of reasons. Firstly, conventional on-chip microfluidics requires the use of immiscible fluids for droplet formation which often necessitates the use of oils and surfactants that are known to be potentially harmful and often incompatible with clinical applications.[40–44] Produced spheroid-forming compartments therefore need extensive washing in an attempt to remove the oil and surfactants before culture/use, which associates with time-demanding artisanal processes that adversely affect cell viability.[45,46] Secondly, while conventional on-chip microfluidics allows for continuous spheroid production, droplet formation is often limited to the dripping regime resulting in low throughputs (<10 µl/min), which is still insufficient for

most clinical applications.[47] Lastly, retrieving spheroids from their compartments to enable further biofabrication processing typically requires a complex multistep process that can adversely affects cell survival.[44] Consequently, a clean, fast, cell-friendly, and single step biofabrication strategy that can endow large engineered tissues with *in situ* spheroid forming properties has remained wanted.

Here, we introduce a novel In Air microfluidics (IAMF)[48] based bioprinting technique that overcomes the translational limitations of spheroid use. Specifically, IAMF enabled the engineering of living matter that contained biomaterial-free cell-laden compartments, which acted as spheroid forming microreactors. Advantageously, this innovative approach represents a single step biofabrication technique for the engineering of clinically-sized hydrogels that contain a high density of cellular spheroids that are produced at clinically relevant rates (1-8.5 ml/min equaling 10.000 spheroids/s). This significant increase in production throughput is achieved by IAMF's ability to monodispersly endow ink-jet bioprinted bioinks with hollow compartments in the jetting regime, while conventional on-chip approaches are limited to the much slower dripping regime.[49] This novel biofabrication process is also remarkably clean as IAMF obviates the traditional need for oils, surfactants, or sacrificial templates to create the hollow compartments within engineered tissues. In addition to conventional machine-based ink-jet bioprinting, we demonstrated that our in-line bottom-up biofabrication could also be used in the form of a simple handheld device to manually print spheroid-forming compartmentalized hydrogels with multiple complexities, which further facilitates the technology's compatibility with clinical applications. While the translational challenges of upscaled production of microtissues are important for a plethora of distinct tissue types,[28] we produced clinical-sized cartilage tissues to function as a model tissue while acknowledging that a wide range of other (organ) shapes could also be produced using this approach.

## 6.2 Materials and Methods

### 6.2.1 IAMF setup
The IAMF setup for compartmentalized hydrogel consisted of two tapered nozzles (Idex Health&Science) of similar nozzle diameter, positioned at an angle of ± 40°, which were aligned using micrometer-precision XYZ-stages (Thorlabs). The nozzles were connected to Luer-lock glass syringes (Hamilton) with fluorinated ethylene propylene (FEP) tubing (ID 250 μm, DuPont). Flow rate was controlled by low-pressure syringe pumps (neMESYS, Cetoni). The primary nozzle was connected to a piezoelectric actuator, which was operated at 5 Vpp with frequencies between 1 and 10 kHz, depending on the used nozzle diameter, allowing controlled break-up of the microjet. The secondary nozzle was aligned such that its microjet coalesces with the monodisperse droplet train of the primary microjet. Controlled droplet break-up and coalescence of the microjet with the droplet train was confirmed

using a high-speed microscope camera (SMZ800N, Nikon attached with a uEye usb camera, IDS).

## 6.2.2 Alginate compartmentalized hydrogel production and analysis

The primary microjet consisted of 10% (w/v) dextran (40 kDa, Pharmacosmos) and 50 mM calcium chloride ($CaCl_2$) (Sigma-Aldrich) in $dH_2O$. The secondary microjet consisted of 0.5% (w/v) sodium alginate (80 ~120 cP, FUJIFILM Wako) (and 10% (v/v) ethanol (EtOH) in $dH_2O$. Different nozzle diameters (50 μm, 100 μm, 150 μm, and 200 μm) were used to produce compartments of different compartment sizes. For 50 μm diameter nozzles, flow rates of 0.9 ml/min and 1.1 ml/min were used respectively for the primary and secondary microjets with an actuator frequency of 6.5 kHz. For 100 μm diameter nozzles, flow rates of 2 ml/min and 2.2 ml/min were used respectively for the primary and secondary microjets with an actuator frequency of 5.5 kHz, or flow rates of 4 ml/min and 4.5 ml/min were used respectively for the primary and secondary microjets if indicated that the total flow rate was 8.5 ml/min with an actuator frequency of 5.5 kHz. For 150 μm diameter nozzles, flow rates of 3 ml/min and 3.2 ml/min were used respectively for the primary and secondary microjets with an actuator frequency of 4.5 kHz. For 200 μm diameter nozzles, flow rates of 4 ml/min and 4.2 ml/min were used respectively for the primary and secondary microjets with an actuator frequency of 3.5 kHz. The microjets were characterized by We ± 25 using collisional angles of ± 40°, which corresponded to $We_{impact}$ ± 10.

Compartmentalized hydrogels were produced using multiple fabrication options. For the first option, nozzles were fixed in position and the in-air formed compartments were collected in a petri dish on a moveable XZ-collection stage for the production of compartmentalized hydrogels. For the second option, nozzles were fixed upon the moveable printhead (1 m/s) of a 3D printer (Inkredible+, CELLINK) and the in-air formed compartments were collected in a petri dish for the production of compartmentalized hydrogels. For the third option, nozzles were fixed upon a handheld device, allowing manual deposition of in-air formed compartments for the production of compartmentalized hydrogels. Regardless of which setup was being used, 1D fibers, 2D planes, and 3D volumes of compartmentalized hydrogel could be produced by controlled movement of either nozzles or collection petri dish.

Compartmentalized hydrogels were visualized using brightfield microscopy (EVOS FL Imaging System, ThermoFisher). Compartment diameter was measured using the Feret diameter. The hollow nature of the compartments was investigated via the addition of 0.5 mg/ml 2000 kDa Dextran-TRITC (Sigma-Aldrich) to the primary microjet and 0.5 mg/ml 2000 kDa Dextran-FITC (Sigma-Aldrich) to the alginate containing secondary microjet. Fluorescently labeled compartmentalized hydrogels were analyzed using confocal z-stack microscopy analysis (Nikon A1

confocal). Size distribution, monodispersity, angle orientation, ellipsoid elongation, and fluorescent intensity was analyzed using ImageJ software.

### 6.2.3 Cell culture

C20A4 chondrocytes were cultured in Dulbecco's Modified Eagle Medium (DMEM, Gibco) with 10% fetal bovine serum (FBS, Sigma-Aldrich), 100 U/ml penicillin (Gibco), and 100 µg/ml streptomycin (Gibco). Culture medium was changed biweekly. Human chondrocytes were cultured in proliferation medium containing DMEM, 10% FBS, 100 U/ml penicillin, 100 µg/ml streptomycin, 0.1 mM L-proline (Sigma-Aldrich), 1% non-essential amino acids (NEAA, Sigma-Aldrich), and 1% ascorbic acid (ASAP, Sigma-Aldrich), or in chondrogenic medium containing DMEM, 100 U/ml penicillin, 100 µg/ml streptomycin, 0.1 mM L-proline (Sigma-Aldrich), 1% non-essential amino acids (NEAA, Sigma-Aldrich), and 1% ascorbic acid (ASAP, Sigma-Aldrich), 10 ng/ml TGFb3 (R&D systems) and 0.1 µM dexamethasone (Sigma-Aldrich). Cells were passaged when 80% confluency was reached. Cell cultures were kept in a humidified environment at 37 °C with 5% $CO_2$.

### 6.2.4 Cell encapsulation

When preparing cell-laden compartmentalized hydrogels, $dH_2O$ in the microjet solutions was replaced with DMEM without phosphates (Gibco). Cells were detached using trypsin-EDTA (Invitrogen), washed with medium and subsequently flown through a 40 µm cell strainer (EASYstrainer, Greiner) to ensure a single cell suspension. Cells were then suspended at $10^7$ cells/ml in the primary microjet solution unless stated otherwise. The cell-laden solution was then loaded into and kept in an ice-cooled gastight syringe for the duration of the encapsulation procedure (<10 minutes). Nozzle diameters of 100 µm were used in cell encapsulation experiments, with flow rates of 2 ml/min and 2.2 ml/min for the primary and secondary microjets respectively, with a frequency of 5.5 kHz applied by the piezo actuator. Cell-laden compartmentalized hydrogels were collected in a petri dish or directly into culture plates. Immediately after production, the compartmentalized hydrogel was washed with medium in order to wash away excess ethanol to maintain high cell-viability. Finally, fresh culture medium was added upon which the compartmentalized hydrogels that were placed in culture.

Cellular aggregation upon cell encapsulation was monitored by brightfield microscopy (EVOS FL Imaging System, ThermoFisher). Cell viability was studied by staining with calcein AM and ethidium homodimer-1 according to manufacturer's protocol (Invitrogen) and imaging using a digital fluorescence microscope (EVOS FL Imaging System, ThermoFisher).

For additional analyses, cell-laden compartmentalized were washed with PBS and fixated using a 10% buffered formalin solution (Sigma-Aldrich). Cells were permeabilized using 0.1% Triton X-100 (Sigma-Aldrich) and were subsequently stained with 2.5 U/ml phalloidin-AF488 (Thermo Fisher Scientific) and 10 µg/ml DAPI (Thermo Fisher Scientific) to stain for F-actin and nuclei respectively. Fluorescently

**6**

stained samples were analyzed using confocal microscopy (Nikon confocal A1) and ImageJ software.

## 6.2.5 Gene expression analysis

Primary human chondrocytes were encapsulated in compartmentalized hydrogels and cultured for 21 days in chondrogenic medium. As a control, primary human chondrocytes were cultured in monolayer. Samples for qPCR analysis were prepared with TRIzol (Invitrogen) lysis buffer and processed for RNA isolation using the miRNeasy kit (QIAGEN) following the protocol provided by the supplier. cDNA was synthesized using the iScript cDNA synthesis kit (Bio-Rad). cDNA was then subjected to qPCR using SensiMix SYBR & fluorescein kit (Bioline) on a CFX Connect Real-time System (Bio-Rad).

## 6.2.6 Cartilage production analysis

Primary human chondrocytes were encapsulated in compartmentalized hydrogels and cultured for 21 days in chondrogenic medium. Spheroids were fixated using 10% buffered formalin solution, permeabilized using 0.1% Triton-X (Sigma-Aldrich), blocked using 10% bovine serum albumin (Sigma-Aldrich), and stained using 1:100 anti-collagen 1 (Novus biological), 1:100 anti-collagen 2 (Abcam), 1:100 anti-aggrecan (Abcam), or 1:200 anti-hyaluronansynthase 1 (Abcam), in combination with 1:250 AF488- (Invitrogen) and 1:200 AF647- (Abcam) labeled secondary antibodies, and 1:100 DAPI as counter staining.

## 6.2.7 Large cellular tissue formation

C20A4 cells were encapsulated in compartmentalized hydrogels and cultured for four days, upon which the cellular spheroids were retrieved by PBS washing and 10 U/ml alginate lyase (Sigma-Aldrich) incubation for 30 minutes at 37 °C. Approximately 540.000 spheroids ($\pm 4*10^7$ cells) were injected into an agarose bone-shaped mold to form a large cellular tissue. As a control, $4*10^7$ single cells were injected in the bone mold. The total mold volume in which the cells could be injected was 315 µl, and was produced as previously described.[50] Agarose molds were incubated in culture medium for 24 hours prior to use. Formed large tissues were analyzed using macroscopic photography (Canon EOS 6D) and brightfield microscopy (EVOS FL Imaging System, ThermoFisher). Cell size/volume was analyzed by brightfield imaging upon trypsinization of spheroids that were cultured for 0, 1, or 4 days. Large tissue surface area, shape, and cell volume was analyzed using ImageJ software.

## 6.2.8 Statistics

Sample size per experiment is reported in figure descriptions. Significance was determined based on one-way Anova analysis. Significance of p <0.05 is indicated by *. All statistical analyses were performed in OriginPro2017.

## 6.3 Results and Discussion

### 6.3.1 Preparation and Characterization of Crosslinker Nanoemulsion

In-air microfluidics (IAMF) is a microfluidic approach that enables controlled micrometer-sized droplet production by in air colliding a liquid jet with a constant period stream of aqueous droplets that were created by piezo-actuating a liquid jet, which allows for chip-free, oil-free, and cytocompatible production of monodisperse microparticles at ultra-high throughputs.[48] In this study, we combined IAMF with ink-jet bioprinting to allow for controlled merging of in-air formed hollow microcapsules that enables the production of large scale compartmentalized hydrogels. To this end, a two micronozzle setup was used in combination with a moveable XYZ collection stage (**Figure 6.1a**).

To form hollow microcapsules, a core microjet solution containing calcium chloride (CaCl$_2$) was collided with a controlled droplet train that was produced by superimposing a vibration onto the micronozzle using piezo-actuation (**Figure 6.1b**). Drop-jet coalescence with an alginate precursor microjet with lowered surface tension ($\sigma_{core} > \sigma_{alginate}$) allows for Marangoni driven encapsulation (**Figure 6.1c**). This encapsulation process occurs on a time scale of $\tau_e \sim (\rho\mu D^4/\Delta\sigma^2)^{1/3}$, with $\rho$, D, $\mu$, and $\sigma$ denoting the microjet density, diameter, viscosity, and surface tension respectively, which is typically within a few milliseconds.[48] This allows for complete encapsulation within the 10 to 100 ms droplet flight time before the droplets are collected. This enables the production of two-layered droplets containing a CaCl$_2$ core and an alginate precursor shell. The resulting core-shell (i.e., calcium-alginate) compound droplets were crosslinked in an inside-out manner by CaCl$_2$ diffusion from the core layer towards the alginate layer (**Figure 6.1d**). Since ionic alginate crosslinking occurs in the range of milliseconds[51] and because of the inside-out nature of the crosslinking, the inner alginate layer was crosslinked while the compound droplet was still in the air, while the outer alginate layer crosslinking occurred over time via inside-out diffusion of Ca$^{2+}$ ions. The partially crosslinked microcapsules were then collected in a controlled manner by either a moveable XYZ collection or micronozzle stage. Of note, at the moment of impact the crosslinking of the in-air formed microcapsules is still ongoing, allowing them to crosslink with the already collected microcapsules upon landing, thereby effectively forming an instantaneously solid 3D construct containing hollow microcompartments (**Figure 6.1e**).

We hypothesized that 1D Fibers, 2D planes, and 3D volumes of compartmentalized hydrogels could be formed in a robust, predictable, and controllable manner by tuning microcapsule placement using standard droplet-based biofabrication methods (**Figure 6.1f**). This biofabrication approach was demonstrated using a hand-held bioprinting device, (**Figure 6.1g,h**) which allowed for manual direct defect-filling using the shape-stable compartmentalized hydrogel (**Figure 6.1i-k**). The hand-held approach is anticipated to facilitate clinical applications such as in

**6**
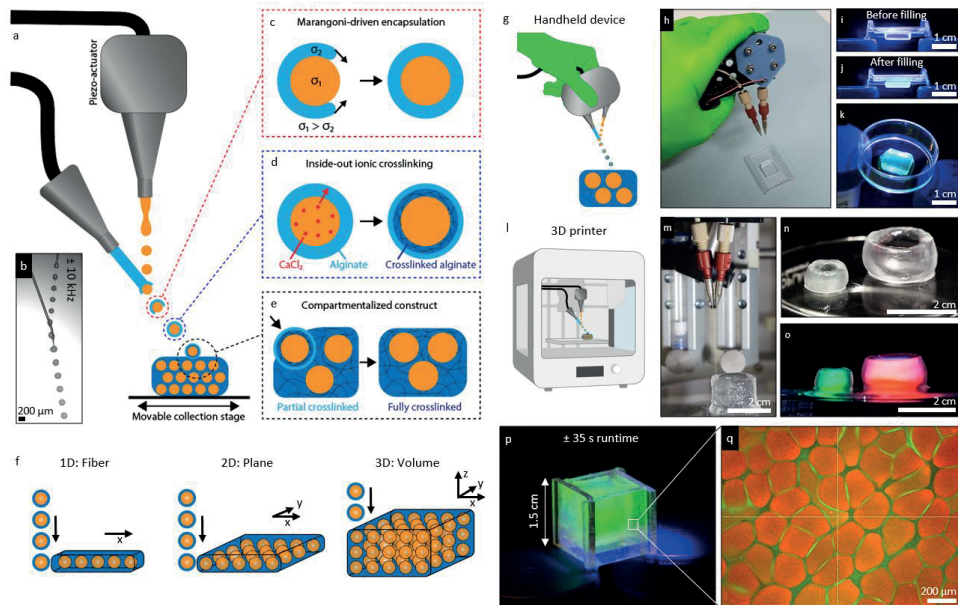
**Figure 6.1. In Air microfluidic biofabrication of highly compartmentalized hydrogels.** (a) Schematic of compartmentalized hydrogel production process using a two nozzle in air microfluidics approach. (b) Micrograph of droplet formation and droplet/compartment encapsulation in air. (c) Surface tension Marangoni flow enables encapsulation of the core droplet by a hydrogel precursor solution. (d) CaCl$_2$ diffuses from the inside of the two-layered all-aqueous droplet towards the alginate layer, allowing for an inside-out ionic crosslinking mechanism, which results in crosslinked alginate at the interface between the two droplet layers, while the crosslinking in the shell remains ongoing. (e) The ongoing crosslinking in the microcompartment's shell upon impact was leveraged to engineer solid multi-compartmentalized hydrogels. (f) Controlled deposition of compartments allowed for 1D fiber, 2D planes, and 3D volumes of compartmentalized hydrogels. (g) Schematic and (h) photograph of a 3D printer with integrated In Air microfluidic setup. (i) Photograph of hollow tube-like compartmentalized hydrogel structures printed using a 3D printer that (j) are non-leaking as visualized by containment of dextran-FITC (green) and dextran-TRITC (red) staining solutions. (k) Schematic of handheld IAMF device for manual ink-jet bioprinting of compartmentalized hydrogel bioinks. (l) Photograph of handheld IAMF device being used for direct defect filling of a plastic mold. Fluorescent photographs of the mold (m) before and (n) after being conformally filled with compartmentalized hydrogel via handheld ink-jet bioprinting, (o) which was demonstrated shape stable even after being removed from the mold. (p) Photograph of compartmentalized fluorescent hydrogel produced with a production rate of 8.5 ml/min, which enabled the filling of a 1.5 x 1.5 x 1.5 cm mold in 35 seconds. (q) Confocal fluorescence microscopy confirmed the formation of compartmentalized hydrogels, with alginate stained in green with dextran-FITC and hollow core stained in red with dextran-TRITC.

situ bioprinting during surgical procedures. Moreover, we demonstrated that this novel biofabrication approach could be also combined with programmable 3D bioprinters (**Figure 6.1l,m**), which we demonstrated allowed for the production of large scale structures composed of more complex geometries such as a shape-stable tube-like compartmentalized hydrogel (**Figure 6.1n,o, Movie S6.1**). The ultra-high throughput nature of IAMF (up to 8.5 ml/min) (**Figure S6.1**) allows for the

biofabrication of clinically sized compartmentalized hydrogels in a fast, direct, and single-step manner (**Figure 6.1p,q**).

Owing to the ultra-high throughputs and short in-air flight time of IAMF produced droplets, a fast (millisecond) crosslinking strategy such as the proposed ionic crosslinking of alginate or photopolymerization is typically required.[52] However, materials relying on slower (seconds to minutes) crosslinking mechanisms such as silk fibroin can still be utilized by leveraging alginate as sacrificial structural interpenetrating network template.[53]

## 6.3.2 Size, shape, and isotropic control of microcompartments and macrogel using In Air microfluidic biofabrication

The size and shape of alginate hydrogel as well as their incorporated hollow compartments were controlled based on the placement of different sized micronozzles on a moveable XYZ stage. Micronozzles with an inner diameter of 50 µm, 100 µm, 150 µm, and 200 µm produced monodisperse (CV < 10%) compartment sizes of 140±5 µm, 219±14 µm, 277±12 µm, and 347±18 µm respectively (**Figure 6.2a,b**). This represents a significant improvement over conventional high throughput technologies such as large bioreactors which are often associated with polydispersity of tissue sizes.[28]

Compartmentalized hydrogels with distinct dimensions such as 1D fibers, 2D sheets, and 3D volumes can be achieved through movement of micronozzles in multiple dimensions with theoretical resolutions similar to the compartment sizes (140±5 µm, 219±14 µm, 277±12 µm, and 347±18 µm for core jet micronozzles with an inner diameter of 50 µm, 100 µm, 150 µm, and 200 µm respectively). The ability to produce these fundamental shapes offers the opportunity for fabrication of larger arbitrary-shaped tissues by further assembling these shapes.[54] Compartmentalized fibers were produced by movement of the micronozzles in a single dimension (**Figure 6.2c,d**). Uniquely, this created hydrogel fibers containing ellipsoidal compartments with an elongation ratio of 1.7 +/- 0.5 (**Figure 6.2e**), which were consistently oriented with their ellipsoidal shape following the fiber's orientation (**Figure 6.2f**). This compartment shape control offers interesting possibilities since it is known that endowing elongation ratio's in physical space in which microtissues are cultured/grown result in consistent and distinct behaviors that guide amongst others morphogenesis.[55] Furthermore, multiple material writings can be formed with this biofabrication technique using a variety of payloads in microcompartments by utilizing the moveable micronozzle stage in 2D as demonstrated using dextran-TRITC and dextran-FITC (**Figure 6.2g**). Moreover, formed fibers were associated with good handleability (e.g., facile manual manipulation), which could potentially be used for applications such as weaving (**Figure 6.2g**), knitting, and braiding without inevitable fiber failure.[56–59] The ability to align cell-laden fibers has been reported to be capable of improving tissue engineering applications in which alignment is important such as muscle tissue engineering applications.[60–62] Additionally, cell-
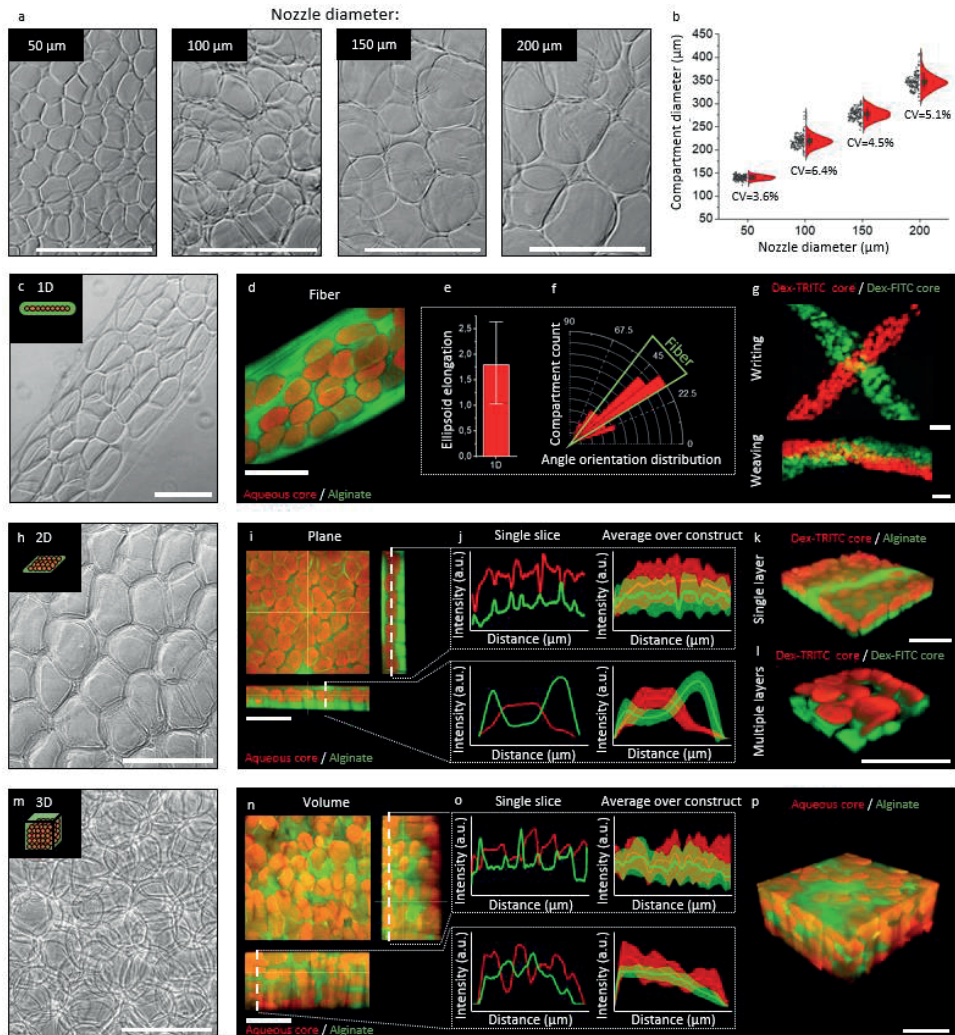
**Figure 6.2. Controlled yet distinct morphologies in 1D, 2D, and 3D compartmentalized hydrogels produced by in air microfluidic biofabrication.** (a) Micrographs of hollow alginate microcapsules that were produced using a variety of nozzle with distinct diameters, which effectively controlled the hydrogel compartment's diameter (b) with high monodispersity (n=150). (c) Brightfield micrograph of 1D compartmentalized fiber. (d) Fluorescent confocal micrograph of compartmentalized fiber with alginate stained green with dextran-FITC and compartments red with dextran-TRITC. (e) Quantification of compartment alignment as compared to its compartmentalized fiber (n=54). (f) Ellipsoid elongation of compartments in 1D fibers as compared to the 3D volume of its compartmentalized hydrogel (n=54). (g) Fluorescent confocal micrograph of compartmentalized fibers used for writing and weaving with multiple compartment payloads (green dextran-FITC and red dextran-TRITC). (h) Brightfield micrograph of a 2D compartmentalized hydrogel sheet. (i) Fluorescent confocal z-stack of compartmentalized sheet with alginate stained green using dextran-FITC and compartments stained red using dextran-TRITC. (j) Fluorescence intensity histograms of compartmentalized plane along the xy-plane (top) and x plane (bottom) for a single slice (left) and as an average over the construct (right). (k) Fluorescent confocal 3D reconstruction of a single layer compartmentalized sheet with alginate stained green using dextran-FITC and compartments stained red using dextran-TRITC. (l) Fluorescent confocal 3D reconstruction of a double layer compartmentalized plane

with multiple compartment payloads (green dextran-FITC and red dextran-TRITC). (m) Brightfield micrograph of a 3D compartmentalized hydrogel volume. (n) Fluorescent confocal z-stack of compartmentalized volume with alginate stained green using dextran-FITC and compartments stained red using dextran-TRITC. (o) Fluorescence intensity histograms of compartmentalized volume along the xy-plane (top) and x plane (bottom) for a single slice (left) and as an average over the construct (right). (p) Fluorescent confocal 3D reconstruction of a single layer of compartmentalized hydrogel volume with alginate stained green using dextran-FITC and compartments stained red using dextran-TRITC. Scale bars equal 500 µm.

laden microfibers are also utilized for islet cell encapsulation, making use of the easy retrievability of fibers when implanted in a patient body.[56,63]

While moving the micronozzles in a single dimension creates hydrogel microfibers, a two dimensional movement allowed for the formation of spatially organized single-layer hydrogel sheets (**Figure 6.2h**). Confocal z-stack analysis confirmed the hollow (e.g., aqueous and non-crosslinked) nature of the compartments within the printed hydrogel sheet (**Figure 6.2i**). Notably, the formed hydrogel sheets where characterized by an symmetrical yet anisotropic nature, which was corroborated by semi-quantitative histograms analysis of individual confocal slices (**Figure 6.2j**). Averaging histogram data of the X or Y plane indicated random placement of compartments, while the Z plane was shown to be consistently organized in terms of compartment placement at a specific height. Complexity in the planes such as multi-layers and multiple materials can be added by repeating the controlled process of plane formation, which results in hydrogels composed of multiple layered planes, which provides the potential to use multiple materials or material properties in a height defined manner (**Figure 6.2k,l**). 2D cell-laden sheets can function as patches, which have been proven to be successful for amongst others cardiac tissue engineering applications and wound healing patches.[64–66] and can be rolled up to mimic tubular structures.[67]

In-air printing of annealing microcapsules was also demonstrated to be readily capable of rapidly creating voluminous 3D compartmentalized hydrogels (**Figure 6.2m,n**). 3D Hydrogels containing spheroids have been shown to be relevant for a wide variety of biomedical applications, for example, it has consistently been shown to increase chondrogenesis and cartilage formation.[10,12] While compartment placing in 2D compartmentalized sheets was reproducibly anisotropic, the average over construct histograms of 3D volumes revealed that 3D volumes were characterized by isotropic compartment placement (**Figure 6.2o,p**). Packing density (compartments/volume) can be controlled by tuning the compartment sizes through the use of core jet micronozzles with different inner diameters as well as via the relative flow rates. No kinetic displacement of the fabricated structure upon collision with newly jetted compartments has been observed.

In-air microfluidics biofabrication of compartmentalized hydrogels of 1D, 2D, and 3D materials offers, amongst others, an increased handleability as compared to traditional 0D hydrogel compartments such as microcapsules. Specifically, hydrogel

**6**

microcapsules are typically suspended in liquid and thus have to be handled by for instance pipetting techniques, causing microparticles to be easily lost or physically damaged due to adherence to culture plastic or pipette tips. In contrast, larger structures such as the here described 1D fibers, 2D sheets, and 3D volumes, can be handled on a macroscopic level using tools such as spatulas and/or tweezers, which allow for facile complex manipulation such as writing, weaving, or stacking of separate materials, which minimizes loss or damage.

### 6.3.3 Ultra-high throughput production of chondrogenic spheroid within cell-laden compartmentalized hydrogels

Using IAMF, large compartmentalized hydrogels can be produced at throughputs of >850 fold higher than conventional microfluidics (10 µl/min for conventional microfluidics[31] versus 8,5 ml/min for IAMF compartmentalized hydrogels). This approach could be leveraged for the mass production of cellular spheroids at an unprecedented rate (10.000 spheroids per second).

To demonstrate this, C20A4 chondrocytes were encapsulated in compartmentalized hydrogels by introduction of the cells in the core microjet solution (**Figure 6.3a**). Upon cell-laden compartmentalized hydrogels formation, the hydrogel was immediately washed with a surplus of culture medium and subsequently provided with fresh culture medium. Cellular spheroids formed within the hydrogel compartments within 24 hours, and were able to be cultured inside the compartments for at least 21 days within 3D hydrogels (**Figure 6.3b**) and 1D fibers (**Figure S6.2**), which remained stable for at least 21 days of culture. Cell viability remained high upon cell encapsulation (96±3%) as well as during subsequent cell culture (96±3%) (**Figure 6.3c,d**).

The number of encapsulated cells is controlled by tuning the cell concentration in the core microjet solution, with 13±5, 38±10, and 73±15 cells/compartment for $2*10^6$, $5*10^6$, and $10^7$ cells/ml in the core microjet solution respectively (**Figure S6.3**). Formed cellular spheroids possessed monodisperse size distributions (CV ≤ 10% at day 1), which demonstrated controlled formation of cellular spheroids within the IAMF-produced compartmentalized hydrogels (**Figure 6.3e,f**). The ability to control the number of encapsulated cells and thus the formed spheroid diameter is especially important as spheroid diameter is known to influence biological function.[12] Previous studies reported that creating 50-100 cells/spheroids improves chondrogenic performance by increasing expression of *SOX9*, *ACAN*, and *COL2A1* while lowering expression of *COL1* as compared to both single cells and larger spheroids.[12] Therefore, chondrogenic experiments were performed encapsulating primary human chondrocytes at $10^7$ cells/ml, which equaled 73±15 cells/compartment.

Spheroids of primary human chondrocytes were formed and cultured within compartmentalized hydrogels or as monolayers in chondrogenic medium for 21 days. As compared to monolayers, chondrocytes in compartmentalized hydrogels expressed significantly higher levels of the chondrogenic master transcription factor
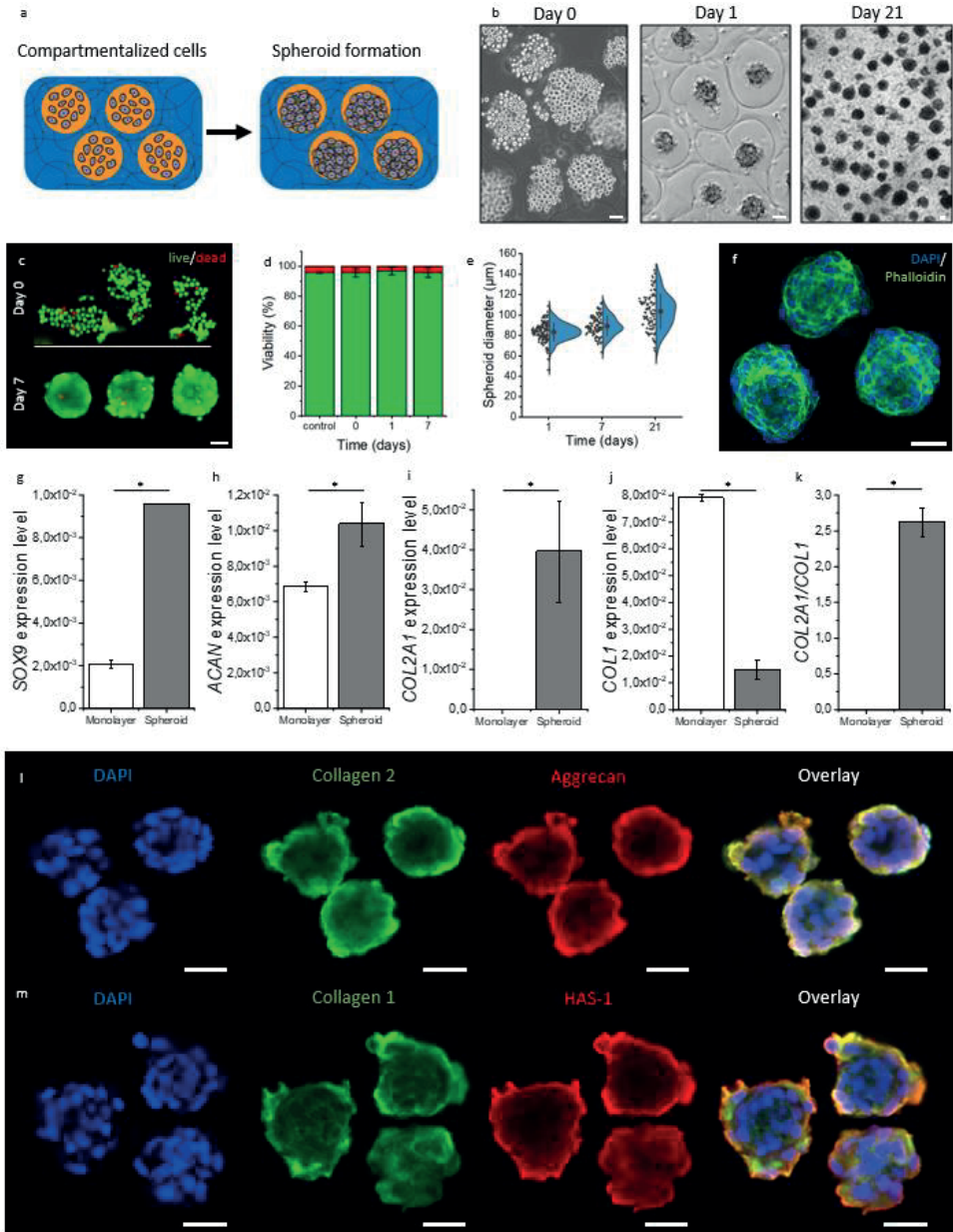
**Figure 6.3. In-situ spheroid formation in in-air bioprinted compartmentalized hydrogels.** (a) Schematic of spheroid formation within compartmentalized hydrogel. (b) Brightfield micrograph of encapsulated chondrocytes at day 0, day 1, and day 21. (c) Fluorescent micrograph of viability staining at day 0 (top) and day 7 (bottom) with live cells stained green using calcein-AM and dead cells stained red using ethidium homodimer. (d) Quantification of the fraction of viable chondrocytes after 0, 1, and 7 days of culture within compartmentalized hydrogels. (n=136 spheroids). (e) Quantification of spheroid diameter over 21 days of culture within compartmentalized hydrogels. (n=100). (f) Confocal fluorescence micrograph of spheroids with nuclei stained blue using DAPI and F-actin stained green using Alexa fluor 488 phalloidin after 21 days

of culture within compartmentalized hydrogels. (g) Relative mRNA levels of the chondrogenic markers (g) *SOX9*, (h) *ACAN*, and (i) *COL2A1*, and of the fibrocartilage marker (j) *COL1*, as well as (k) relative ratio between *COL2A1* and *COL1* as an indication of cartilage phenotype from human primary chondrocytes cultured as either monolayer or spheroid within compartmentalized hydrogel for 21 days (n=2, 50.000 spheroids each). Fluorescence micrographs of cellular spheroids formed in compartmentalized hydrogels visualized using Immunofluorescence staining of (l) DAPI (blue), collagen 2 (green), aggrecan (red), and (m) DAPI (blue), collagen 1 (green), and hyaluronan synthase 1 (HAS1) (red) after 21 days of culture in chondrogenic medium. Scale bars equal 50 μm.

*SOX9* (**Figure 6.3g**) as well as other key cartilage extracellular matrix components *ACAN* (**Figure 6.3h**) and *COL2A1* (**Figure 6.3i**), while expressing lower levels of the undesired fibrocartilage marker *COL1* (**Figure 6.3j**) resulting in a higher *COL2A1/COL1* ratio in the cellular spheroids as compared to monolayer cultures (**Figure 6.3k**). Combined, the gene expression profile corroborated that the cellular microspheroids that had autonomously formed within the hollow compartmentalized hydrogels indeed associated with a stronger chondrogenic phenotype than cells that were individually dispersed throughout solid hydrogels. To confirm whether true chondrogenic behavior of the spheroids in compartmentalized hydrogels had occurred, immunofluorescent staining of spheroids exposed to chondrogenic differentiation medium for 21 days was performed. Indeed, spheroids within compartmentalized hydrogels expressed cartilage markers such as collagen 1, collagen 2, aggrecan, and hyaluronan synthase 1 (**Figure 6.3l,m**). These results demonstrated that autonomously formed spheroids in compartmentalized hydrogels, which outperform conventional monolayer cultures in terms of chondrogenic performance, can now be considered for the engineering of cartilage, and specifically as a novel method to enable the clinical translation of the benefits of cellular spheroids in a clean, cytocompatible, single-step, and clinically scalable manner.

### 6.3.3 In Air microfluidic spheroid forming compartmentalized hydrogels allows for formation of shape-stable clinically-sized biomaterial-free cellular tissues

The ultra-high throughput production of spheroid-forming compartmentalized hydrogels allows for clinically sized engineered tissue formation. However, spheroid culture has also been found beneficial for engineering of biomaterial-free living tissues in the form of bottom-up tissue engineering by using spheroids as modular building blocks. In comparison with conventional single cell techniques, cellular spheroids allow for the production of more shape stable tissues[15]. This tight shape and volume control  is highly important in predictable tissue engineering and conformal defect filling as onset of construct shrinkage will inevitably lead to formation of unwanted defects and cavities. Unfortunately, due to the existing spheroid batch production processes these clinical-sized constructs have remained out of reach due to the required amount of spheroids to form large scale tissue constructs; conventional spheroid production processes only offer low production

**Figure 6.4. Compartmentalized hydrogel as a 3D platform for spheroid production for the engineering of clinically-sized cellular tissues.** (a) Schematic of clinically-sized cellular tissue formation, including high-throughput (HT) spheroid production in compartmentalized hydrogel, retrieving spheroids from the compartmentalized hydrogels, injection molding of spheroids in a agarose mold, and subsequent tissue formation. (b) Theoretical representation of microwells needed versus In Air microfluidic runtime needed to create ±540.000 spheroids, which was required to fill the model injection mold. (c) Brightfield micrograph of retrieved chondrocyte spheroids following alginate lyase treatment. (d) Photograph of a centimeter-sized tissue formed in an agarose mold in a 12 wells-plate well after 24 hours of culture. (e) Stitched micrograph of formed tissue after 24 hours of culture. (f) Projection of formed tissues produced with spheroids (top) or single cells (bottom) on top of an outline of the original mold shape. (g) Tissue projection area of formed tissues produced with spheroids or single cells relative to mold projection area (n=4). (h) Overlap of formed tissue with spheroids or single cells relative to shape of mold (corrected for tissue projection area) (n=4). (i) Projection of formed tissue produced with spheroids (top) or single cells (bottom) with representation of angle in red and measured angle in white (n=4). (j) Cell volume of chondrocytes upon culture and spheroid formation within compartmentalized hydrogels after 0 (control), 1, and 4 days of culture (n=500).

rates. To address this, we hypothesized that the compartmentalized hydrogels could be sacrificed and thus act as temporary and discretionary 3D picoreactors to facilitate the mass production of monodisperse cellular spheroids. Indeed, scaling into the third dimension would significantly enhance spheroid production rate as the gold standard production platforms are all 2D in their nature. We reasoned that the ultra-high throughput spheroid production nature of the compartmentalized hydrogel would enable the production of shape stable, clinical-sized biomaterial-free cellular tissues (**Figure 6.4a**).

To produce the quantity of spheroids needed to engineer a fully cellular tissue with only a volume of 315 µl, which estimates a common full thickness cartilage defect

of 1.5 cm²[268], would require a total of 150 individual wells of 12 wells plate (3600 spheroids per well[9]) (**Figure 6.4b**). The amount of trained manual labor is therefore considered non-scalable, which thus challenges wide-spread clinical translation of spheroid-based cellular tissues. However, utilizing the continuous IAMF compartmentalized hydrogel method, a runtime of only 60 seconds is needed in order to produce the same amount of spheroids (**Figure 6.4b**). It is noted that specific medical applications require a larger tissue size to be considered as clinically-sized, which can easily be achieved by prolonging the production runtime from a single minute to several minutes. The evolution of multiple sequential artisan batch processes into a single continuous sub-minute runtime process is anticipated to facilitate the feasibility of using bottom-up engineering large tissues using cellular spheroid building blocks. Moreover, our novel approach also is more ecologically friendly as it strongly reduces the amount of plastic plates needed to create large living tissues in this bottom-up approach.

Chondrocyte spheroids were mass produced in alginate compartmentalized hydrogels and enzymatically retrieved using alginate lyase after four days of culture (**Figure 6.4c**). Approximately ~540.000 spheroids or an equal total amount ($4*10^7$) of individual cells were injected in a centimeter-sized bone-shaped mold to allow for the formation of a centimeter-sized engineered tissues. The symbolic shape of a bone was chosen owing to its suitability to assess shape-stability of formed tissues (**Figure 6.4d,e**). It was observed that utilizing spheroids for injection molding of large scale tissues resulted in superior shape stability as compared to single cells (**Figure 6.4f**). Specifically, mass produced spheroids associated with a lower tissue shrinkage as indicated by tissue projection area, which was 71.7±7.3% for spheroids and 47.5±0.4% for single cells respectively after a single day of culture (**Figure 6.4g**). Moreover, produced tissues showed a higher overlap with the injection mold's shape when seeded with spheroids (90.3±0.2%) then when single cells (84.0±0.1%) were used. (**Figure 6.4h**). This observation was corroborated by the measurements of the angle of the physical ends of the fully cellular bone-shaped tissues. The curve of the bone-shaped tissues of spheroids (122±14°) maintained a high fidelity to that of the used injection mold (116±2°), while the angle was virtually lost when using single cell suspensions (176±19°) (**Figure 6.4i**). We reasoned that cellular shrinkage during the condensation phase that occurs during the formation of 3D microtissues might offer an explanation for the observed differences in the shape stability of engineered large cellular tissues. Cell volume analysis revealed that placing cells from a 2D environment into a 3D environment resulted in a cell volume decrease from 6.0±2.7 pl to 4.4±2.3 pl after a single day of culture (**Figure 6.4j**). Moreover, cell volume remained stable (5.0±2.1 pl) during further 3D culture. This indicates that the initial spheroid formation in the compartmentalized hydrogels created microtissue building blocks that would – unlike individual cells from 2D cultures - not shrink when used to engineer large cellular tissues thus offering improved shape stability when used for injection mold engineering of living tissues.

## 6.4 Conclusion

In Air microfluidics allowed for the successful production of cell-laden hollow compartmentalized hydrogels that enabled *in-situ* formation of cellular spheroids in an ultra-high throughput, clean, and single-step manner. This innovative technology was proven to be compatible with conventional ink-jet bioprinting technology, which facilitated the production of compartmentalized hydrogels with multiple complexities, while handheld ink-jet bioprinting allowed for quick and easy freeform biofabrication of compartmentalized spheroid forming hydrogels. Utilizing the ultra-high throughput of In Air microfluidics, the scalable production of spheroid based clinically sized cartilage tissues was realized in relevant timeframes, which represents a significant step towards clinical translation of cellular spheroids.

**6**

## 6.5 Supplementary Information
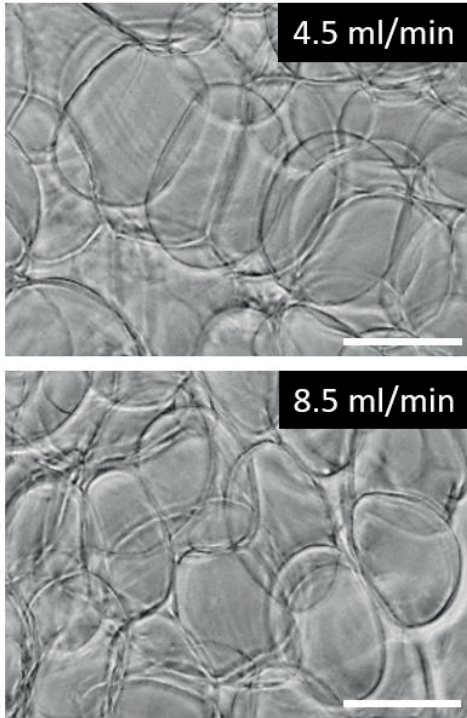


**Figure S6.1. Compartmentalized hydrogel produced at different total flowrates.** Brightfield micrographs of compartmentalized hydrogels produced with a total flow rate of 4.5 ml/min and 8.5 ml/min. Scale bars equal 300 μm.
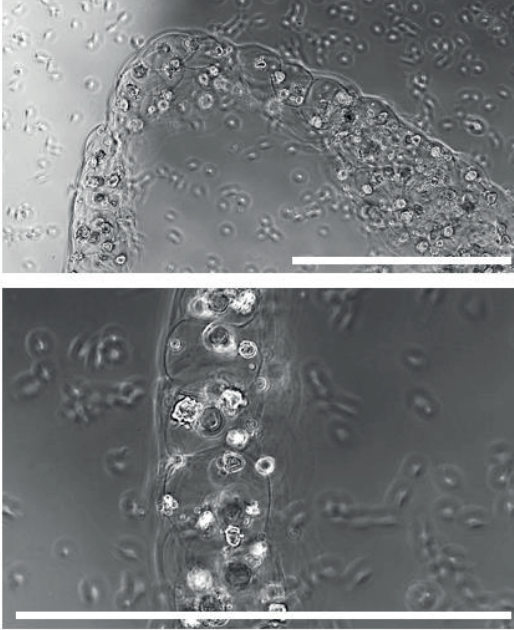
**Figure S6.2. Spheroid formation in compartmentalized fibers.** Brightfield micrographs of spheroid formation in compartmentalized fibers. Scale bars equal 1000 μm.

6
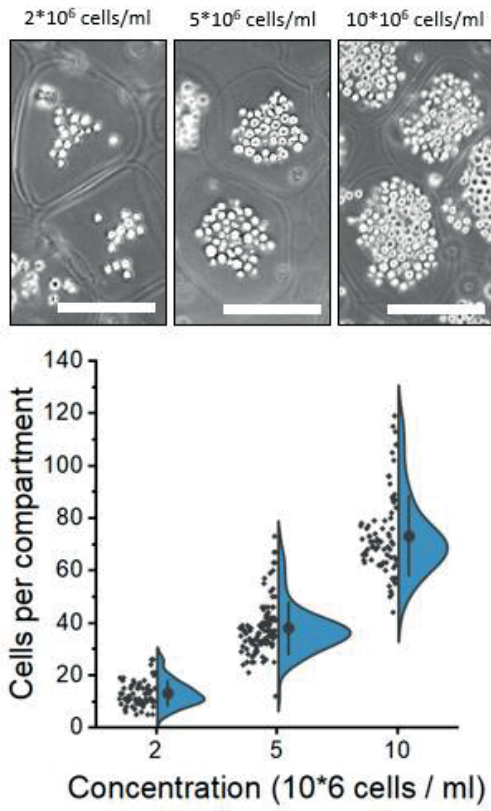
**Figure S6.3. Control over amount of encapsulated cells by tuning cell concentration.** (a) Brightfield micrographs of encapsulated cells at 2*10⁶, 5*10⁶, and 10*10⁶ cells/ml. (b) Quantification of cells per compartment (n=72). Scale bars equal 200 μm.
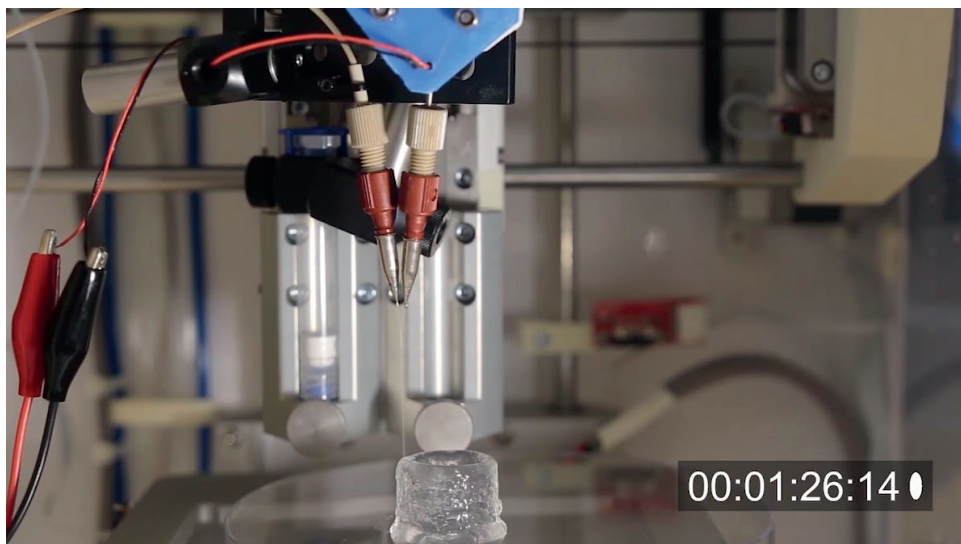
**Supplemental movie S6.1 (still). In Air microfluidic ink-jet printing of tube-like compartmentalized hydrogel.**

6

# References

1.  Pampaloni, F., Reynaud, E. G. & Stelzer, E. H. K. The third dimension bridges the gap between cell culture and live tissue. *Nat. Rev. Mol. Cell Biol.* **8**, 839–845 (2007).
2.  Baker, B. M. & Chen, C. S. Deconstructing the third dimension – how 3D culture microenvironments alter cellular cues. *J. Cell Sci.* **125**, 3015 LP – 3024 (2012).
3.  Fitzgerald, K. A., Malhotra, M., Curtin, C. M., O' Brien, F. J. & O' Driscoll, C. M. Life in 3D is never flat: 3D models to optimise drug delivery. *J. Control. Release* **215**, 39–54 (2015).
4.  VON DER MARK, K., GAUSS, V., VON DER MARK, H. & MÜLLER, P. Relationship between cell shape and type of collagen synthesised as chondrocytes lose their cartilage phenotype in culture. *Nature* **267**, 531–532 (1977).
5.  Edna, C., Roumen, P., R., S. D. & M., Y. K. Taking Cell-Matrix Adhesions to the Third Dimension. *Science (80-. ).* **294**, 1708–1712 (2001).
6.  Fennema, E., Rivron, N., Rouwkema, J., van Blitterswijk, C. & de Boer, J. Spheroid culture as a tool for creating 3D complex tissues. *Trends Biotechnol.* **31**, 108–115 (2013).
7.  Benya, P. D. & Shaffer, J. D. Dedifferentiated chondrocytes reexpress the differentiated collagen phenotype when cultured in agarose gels. *Cell* **30**, 215–224 (1982).
8.  Caron, M. M. J. *et al.* Redifferentiation of dedifferentiated human articular chondrocytes: comparison of 2D and 3D cultures. *Osteoarthr. Cartil.* **20**, 1170–1178 (2012).
9.  Moreira Teixeira, L. S. *et al.* High throughput generated micro-aggregates of chondrocytes stimulate cartilage formation in vitro and in vivo. *Eur. Cell. Mater.* **23**, 387–399 (2012).
10. Bolander, J. *et al.* Healing of a Large Long-Bone Defect through Serum-Free In-Vitro Priming of Human Periosteum-Derived Cells. *Stem Cell Reports* **8**, 758–772 (2017).
11. Wolf, F. *et al.* Cartilage tissue engineering using pre-aggregated human articular chondrocytes. *Eur. Cell. Mater.* **16**, 92–99 (2008).
12. Leijten, J. *et al.* Bioinspired seeding of biomaterials using three dimensional microtissues induces chondrogenic stem cell differentiation and cartilage formation under growth factor free conditions. *Sci. Rep.* **6**, 36011 (2016).
13. Beauchamp, P. *et al.* Development and Characterization of a Scaffold-Free 3D Spheroid Model of Induced Pluripotent Stem Cell-Derived Human Cardiomyocytes. *Tissue Eng. - Part C Methods* **21**, 852–861 (2015).
14. Matsunaga, Y. T., Morimoto, Y. & Takeuchi, S. Molding Cell Beads for Rapid Construction of Macroscopic 3D Tissue Architecture. *Adv. Mater.* **23**, H90–H94 (2011).
15. Vrij, E. *et al.* Directed Assembly and Development of Material-Free Tissues with Complex Architectures. *Adv. Mater.* **28**, 4032–4039 (2016).
16. Lin, H., Li, Q. & Lei, Y. Three-dimensional tissues using human pluripotent stem cell spheroids as biofabrication building blocks. *Biofabrication* **9**, 25007 (2017).
17. Kato-Negishi, M., Morimoto, Y., Onoe, H. & Takeuchi, S. Millimeter-Sized Neural Building Blocks for 3D Heterogeneous Neural Network Assembly. *Adv. Healthc. Mater.* **2**, 1564–1570 (2013).
18. Luo, H. *et al.* Fabrication of viable centimeter-sized 3D tissue constructs with microchannel conduits for improved tissue properties through assembly of cell-laden microbeads. *J. Tissue Eng. Regen. Med.* **8**, 493–504 (2014).
19. Langhans, S. A. Three-Dimensional in Vitro Cell Culture Models in Drug Discovery and Drug Repositioning. *Frontiers in Pharmacology* **9**, (2018).
20. de Melo, B. A. G. *et al.* 3D Printed Cartilage-Like Tissue Constructs with Spatially Controlled Mechanical Properties. *Adv. Funct. Mater.* **29**, 1906330 (2019).
21. Sozen, B. *et al.* Self-assembly of embryonic and two extra-embryonic stem cell types into gastrulating embryo-like structures. *Nat. Cell Biol.* **20**, 979–989 (2018).
22. Rivron, N. C. *et al.* Blastocyst-like structures generated solely from stem cells. *Nature* **557**, 106–111 (2018).
23. Branco, M. A. *et al.* Transcriptomic analysis of 3D Cardiac Differentiation of Human Induced Pluripotent Stem Cells Reveals Faster Cardiomyocyte Maturation Compared to 2D Culture. *Sci. Rep.* **9**, (2019).
24. Hu, Y. *et al.* Lung cancer organoids analyzed on microwell arrays predict drug responses of patients within a week. *Nat. Commun.* **12**, 2581 (2021).
25. Frey, O., Misun, P. M., Fluri, D. A., Hengstler, J. G. & Hierlemann, A. Reconfigurable microfluidic hanging drop network for multi-tissue interaction and analysis. *Nat. Commun.* **5**, 4250 (2014).
26. Kuo, C.-T. *et al.* Three-dimensional spheroid culture targeting versatile tissue bioassays using a PDMS-based hanging drop array. *Sci. Rep.* **7**, 4363 (2017).
27. Tung, Y.-C. *et al.* High-throughput 3D spheroid culture and drug testing using a 384 hanging drop array. *Analyst* **136**, 473–478 (2011).
28. Schot, M., Araújo-Gomes, N., van Loo, B., Kamperman, T. & Leijten, J. Scalable fabrication, compartmentalization and applications of living microtissues. *Bioact. Mater.* **19**, 392–405 (2023).

29. Menasché, P. Cell therapy trials for heart regeneration — lessons learned and future directions. *Nat. Rev. Cardiol.* **15**, 659–671 (2018).

30. Hofer, M. & Lutolf, M. P. Engineering organoids. *Nat. Rev. Mater.* **6**, 402–420 (2021).

31. van Loo, B. *et al.* Enzymatic outside-in cross-linking enables single-step microcapsule production for high-throughput three-dimensional cell microaggregate formation. *Mater. Today Bio* **6**, 100047 (2020).

32. Liu, H. *et al.* A Droplet Microfluidic System to Fabricate Hybrid Capsules Enabling Stem Cell Organoid Engineering. *Adv. Sci.* **7**, 1903739 (2020).

33. Agarwal, P. *et al.* One-step microfluidic generation of pre-hatching embryo-like core-shell microcapsules for miniaturized 3D culture of pluripotent stem cells. *Lab Chip* **13**, 4525–4533 (2013).

34. Alessandri, K. *et al.* Cellular capsules as a tool for multicellular spheroid production and for investigating the mechanics of tumor progression in vitro. *Proc. Natl. Acad. Sci. U. S. A.* **110**, 14843–14848 (2013).

35. Chen, Q. *et al.* Controlled assembly of heterotypic cells in a core–shell scaffold: organ in a droplet. *Lab Chip* **16**, 1346–1349 (2016).

36. Kim, C. *et al.* Generation of core-shell microcapsules with three-dimensional focusing device for efficient formation of cell spheroid. *Lab Chip* **11**, 246–252 (2011).

37. Sakai, S. *et al.* Enzymatically fabricated and degradable microcapsules for production of multicellular spheroids with well-defined diameters of less than 150 microm. *Biomaterials* **30**, 5937–5942 (2009).

38. Yu, L., Ni, C., Grist, S. M., Bayly, C. & Cheung, K. C. Alginate core-shell beads for simplified three-dimensional tumor spheroid culture and drug screening. *Biomed. Microdevices* **17**, 33 (2015).

39. Correia, C. R., Bjørge, I. M., Zeng, J., Matsusaki, M. & Mano, J. F. Liquefied Microcapsules as Dual-Microcarriers for 3D+3D Bottom-Up Tissue Engineering. *Adv. Healthc. Mater.* **8**, 1901221 (2019).

40. Prastowo, A., Feuerborn, A., Cook, P. R. & Walsh, E. J. Biocompatibility of fluids for multiphase drops-in-drops microfluidics. *Biomed. Microdevices* **18**, 114 (2016).

41. Yau, A. C. Y., Lönnblom, E., Zhong, J. & Holmdahl, R. Influence of hydrocarbon oil structure on adjuvanticity and autoimmunity. *Sci. Rep.* **7**, 14998 (2017).

42. Yasuga, H., Kamiya, K., Takeuchi, S. & Miki, N. Self-generation of two-dimensional droplet array using oil–water immiscibility and replacement. *Lab Chip* **18**, 1130–1137 (2018).

43. Jeyhani, M., Thevakumaran, R., Abbasi, N., Hwang, D. K. & Tsai, S. S. H. Microfluidic Generation of All-Aqueous Double and Triple Emulsions. *Small* **16**, 1906565 (2020).

44. Deng, Y. *et al.* Rapid purification of cell encapsulated hydrogel beads from oil phase to aqueous phase in a microfluidic device. *Lab Chip* **11**, 4117–4121 (2011).

45. Noudeh, G. D., Khazaeli, P., Mirzaei, S., Sharififar, F. & Nasrollahosaiani, S. Determination of the Toxicity Effect of Sorbitan Esters Surfactants Group on Biological Membrane. *J. Biol. Sci.* **9**, 423–430 (2009).

46. Choi, C.-H. *et al.* One-step generation of cell-laden microgels using double emulsion drops with a sacrificial ultra-thin oil shell. *Lab Chip* **16**, 1549–1555 (2016).

47. Utada, A. S., Fernandez-Nieves, A., Stone, H. A. & Weitz, D. A. Dripping to Jetting Transitions in Coflowing Liquid Streams. *Phys. Rev. Lett.* **99**, 94502 (2007).

48. Visser, C. W., Kamperman, T., Karbaat, L. P., Lohse, D. & Karperien, M. In-air microfluidics enables rapid fabrication of emulsions, suspensions, and 3D modular (bio)materials. *Sci. Adv.* **4**, (2018).

49. Nunes, J. K., Tsai, S. S. H., Wan, J. & Stone, H. A. Dripping and jetting in microfluidic multiphase flows applied to particle and fiber synthesis. *J. Phys. D. Appl. Phys.* **46**, (2013).

50. Kamperman, T. *et al.* Spatiotemporal material functionalization via competitive supramolecular complexation of avidin and biotin analogs. *Nat. Commun.* **10**, 4347 (2019).

51. Lin, S. H. Gelation of sodium alginate in a batch process. *Chem. Eng. Sci.* **46**, 651–655 (1991).

52. Jiang, J. *et al.* Continuous High-Throughput Fabrication of Architected Micromaterials via In-Air Photopolymerization. *Adv. Mater.* **33**, 2006336 (2021).

53. Compaan, A. M., Christensen, K. & Huang, Y. Inkjet Bioprinting of 3D Silk Fibroin Cellular Constructs Using Sacrificial Alginate. *ACS Biomater. Sci. Eng.* **3**, 1519–1526 (2017).

54. Morimoto, Y., Hsiao, A. Y. & Takeuchi, S. Point-, line-, and plane-shaped cellular constructs for 3D tissue assembly. *Adv. Drug Deliv. Rev.* **95**, 29–39 (2015).

55. Samal, P., Maurer, P., van Blitterswijk, C., Truckenmüller, R. & Giselbrecht, S. A New Microengineered Platform for 4D Tracking of Single Cells in a Stem-Cell-Based In Vitro Morphogenesis Model. *Adv. Mater.* **32**, 1907966 (2020).

56. Onoe, H. *et al.* Metre-long cell-laden microfibres exhibit tissue morphologies and functions. *Nat. Mater.* **12**, 584–590 (2013).

57. Moutos, F. T., Freed, L. E. & Guilak, F. A biomimetic three-dimensional woven composite scaffold for functional tissue engineering of cartilage. *Nat. Mater.* **6**, 162–167 (2007).

58. Chen, G. *et al.* Culturing of skin fibroblasts in a thin PLGA–collagen hybrid mesh. *Biomaterials* **26**, 2559–2566 (2005).

59. Fan, H., Liu, H., Toh, S. L. & Goh, J. C. H. Anterior cruciate ligament regeneration using mesenchymal stem cells and silk scaffold in large animal model. *Biomaterials* **30**, 4967–4977 (2009).

**6**

60.   Kim, J. *et al.* A Microfluidic Device to Fabricate One-Step Cell Bead-Laden Hydrogel Struts for Tissue Engineering. *Small* **18**, 2106487 (2022).

61.   Costantini, M. *et al.* Microfluidic-enhanced 3D bioprinting of aligned myoblast-laden hydrogels leads to functionally organized myofibers in vitro and in vivo. *Biomaterials* **131**, 98–110 (2017).

62.   Hsiao, A. Y. *et al.* Smooth Muscle-Like Tissue Constructs with Circumferentially Oriented Cells Formed by the Cell Fiber Technology. *PLoS One* **10**, e0119010 (2015).

63.   Jun, Y. *et al.* Microfluidics-generated pancreatic islet microfibers for enhanced immunoprotection. *Biomaterials* **34**, 8122–8130 (2013).

64.   Shimizu, T. *et al.* Fabrication of pulsatile cardiac tissue grafts using a novel 3-dimensional cell sheet manipulation technique and temperature-responsive cell culture surfaces. *Circ. Res.* **90**, e40 (2002).

65.   Sekine, H. *et al.* In vitro fabrication of functional three-dimensional tissues with perfusable blood vessels. *Nat. Commun.* **4**, 1399 (2013).

66.   Liu, J. *et al.* A Dual-Cross-Linked Hydrogel Patch for Promoting Diabetic Wound Healing. *Small* **18**, e2106172 (2022).

67.   Yuan, B. *et al.* A Strategy for Depositing Different Types of Cells in Three Dimensions to Mimic Tubular Structures in Tissues. *Adv. Mater.* **24**, 890–896 (2012).

68.   Ding, C. *et al.* Knee cartilage defects: association with early radiographic osteoarthritis, decreased cartilage volume, increased joint surface area and type II collagen breakdown. *Osteoarthr. Cartil.* **13**, 198–205 (2005).

6

6
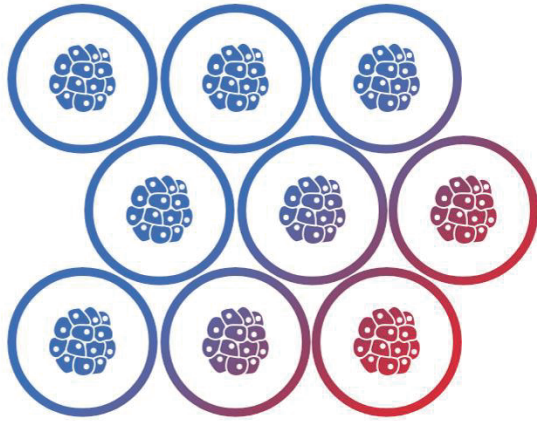
# 7    Reflection and Outlook

This thesis describes multiple microfluidic technologies in order to overcome the challenges in the process of clinical and industrial translation of cellular 3D microtissues. Utilizing the developed microcapsule production technologies, several types of microtissues are produced in a simple, clean, continuous and high-throughput manner. While each of the in this thesis described technologies solve some of these translational challenges, it is clear that no perfect solution exists as of yet. In order to achieve the full potential of these microfluidic technologies additional research is needed. The following chapter focusses on the shared points of potential improvements and the remaining challenges that lie ahead for true clinical and industrial translation of cellular 3D microtissues.

## 7.1 Cell Source

In this thesis we have used several distinct cell types, which demonstrates the versatility of the here reported microencapsulation systems. Dependent on the used cell type, specific (micro)tissues can be formed. For the on-chip approach in chapter 2 and 3, we set up a proof-of-principle for continuous cellular spheroid production using either 3T3 fibroblasts or human mesenchymal stem cells (hMSCs). The use of hMSCs is popular in the field of tissue engineering for its osteogenic, adipogenic and chondrogenic capacities, enabling the formation of bone, adipose and cartilage tissue. However, the encapsulation of other cell types might allow for the formation of microtissues of other tissue types. As an example, in another project not discussed in this thesis, insulin-producing MIN6 β-cells were encapsulated in immune-protective polyethylene glycol-tyramine (PEG-TA) microcapsules using the enzymatic outside-in crosslinking method described in chapter 3. β-Cell microtissues restored normoglycemia 5 days post implantation in type 1 diabetic mice and remained glucose responsive for 28 days in vivo[1], showcasing the functionality of microfluidically-formed microtissues.

In literature, spheroids are used for many more types of tissues. Also, there is a special interest in cancer microtissues for cancer research[2–9]. Although briefly touched upon in chapter 4 with the production of cholangiocarcinoma organoids, microfluidically produced cancer microtissues of all different types of tissues have the potential to revolutionize drug research and personalized medicine.

While spheroids offer a 3D cellular environment and its subsequent benefits over conventional 2D cell culture[2,8,10], they often consist of a single cell type which is homogeneously dispersed throughout the spheroid. Organoids however are formed from a single or a couple pluripotent stem cells and are able to produce multiple cell types within a single microtissue. They have an additional layer of complexity in their cellular organization, can mimic organ function and revolutionize our fundamental understanding of human development[11–13]. In this thesis microfluidically-formed intrahepatic cholangiocyte organoids are demonstrated in chapter 4. However, continuous production of a multitude of other organoid types might be interesting for future endeavors.

Pluripotent stem cells are an interesting source for spheroid and organoid production. While pluripotent stem cells are used to produce the embryoid bodies and cardiospheres, pluripotent stem cells allow for the formation of various organoids[14–20]. Moreover, patient-derived pluripotent stem cells such as iPSCs can be used to create personalized microtissues which might be useful for personalized tissue engineering and drug screening purposes[21].

The microcapsules might also be used for the encapsulation of multiple cell types in a single compartment. As an example, it might be interesting to perform co-encapsulation of embryonic stem cells and *trophoblasts* to produce blastocyst-like structures as described by Rivron et al. in a high-throughput manner[22].

## 7.2 Microcapsule Material

Microcapsules of several materials have been introduced in this thesis. In chapter 3, we demonstrate the formation of microcapsules using tyramine-conjugates such as dextran-tyramine and hyaluronic acid tyramine. In chapter 4, we demonstrate the formation of extracellular matrix-enriched dextran-tyramine microcapsules. In chapter 5, we demonstrate the formation of microcapsules using alginate, and by utilizing a mixture of alginate and an additional material such as dextran-tyramine or PEGDA an enzymatic- or photo-crosslinking postcure can be performed respectively to produce dextran-tyramine or PEGDA microcapsules using the In Air microfluidic system. Material choice in this thesis was mostly based on the limitation of cell-material attachment, since an absence of cell-material attachment is needed to allow efficient cellular aggregation. However, other materials might allow for interesting characteristics for certain applications.

For instance, while chapter 3 demonstrates spheroid formation in dextran-tyramine microcapsules, other experiments were performed using PEG-tyramine (PEG-TA) utilizing the same enzymatic outside-in crosslinking mechanism[1]. The immunoprotective characteristics of PEG-TA can play an important role in regulating the immune response post-injection by acting as an immunoprotective semi-permeable shield. This strategy is of particular interest for organs with an endocrine function, such as the pancreas[23] or the adrenal gland[24] under pathological conditions that associate with autoimmune destruction of native tissues. Injected encapsulated pancreatic islets from an allogeneic source show improved implant survival, integration, and retrievability compared to non-encapsulated islets, while maintaining the ability to restore normoglycemia in diabetic mice[25]. In addition, immunoprotective biomaterials may further enable the use of allogeneic or xenogeneic cell for a wider set of clinical applications. In another project not described in this thesis, we demonstrate this by the production of immunoprotective PEG-TA microcapsules for the formation of glucose-responsive MIN6 spheroids, which were used treat diabetic mice. Diabetic mice retained normoglycemia 5 days post implantation of MIN6 spheroid containing immunoprotective microcapsules[1]. Another potentially interesting material with biological function for spheroid-forming microcapsules that is worth investigating can for instance be heparin-tyramine for its anti-coagulant characteristics[26].

As described in chapter 4, extracellular matrix additives can also be added to the microcapsule material in order to induce cell-matrix interactions. While this chapter focusses on human liver extracellular matrix, it is worth exploring other possible additives[27].

While this thesis describes microcapsules made out of single materials, it might be interesting to explore multi-layer microcapsules build from multiple materials with distinct mechanical properties. In combination with crosslink reversibility, such as described for alginate in chapter 6 but also worth investigating for other materials, this might give the opportunity to have temporal control over mechanosensing, which is known to be an important factor in differentiation processes[28].

7

## 7.3 Microtissues for Tissue Engineering

For tissue engineering applications, chapter 5 demonstrates how IAMF enables the direct biofabrication of spheroid-forming hydrogel tissues for large scale tissue formation, and how spheroids can be used as building blocks for clinical sized cellular tissue formation. Utilizing the ultra-high throughput nature of the IAMF approach we are now able to produce the high quantity of spheroids needed for clinical sized tissues. Large tissue engineered constructs often face challenges concerning diffusion limitations due to the lack of vascularization. Limited diffusion of oxygen, nutrients, and waste products result in low cell viability in the core of the produced constructs and therefore low construct efficiency[29,30]. Since cartilage tissue does not contain vascularization, these challenges are limited in the cartilage tissue engineering applications demonstrated in chapter 5. However, for other biological tissues these challenges remain and additional engineering approaches are needed for the formation of viable clinical sized tissues.

Pre-vascularization of engineered tissues is a common approach to improve viability of clinically relevant sized tissues. Microtissues allow for some interesting possibilities in this aspect. The shear thinning properties of microcapsules and microtissues allow for embedded 3D printing, enabling the printing of producing pre-vascularized structures from microcapsules and/or microtissues[31–33]. Moreover, instead of being used as an embedded bath, microtissues can also be used as bio-inks in 3D printing technologies[34,35]. Upscaling of microtissues for 3D printing technologies often happens using stirred bioreactors, which are associated with large polydispersity due to microtissue fusion and mechanical stress[36]. The use of microcapsules are likely to overcome these challenges and is thus being able to meaningfully impact this field of research. Furthermore, incorporating microtissues in both bio-ink and printing bath could allow for the production of highly complex tissue constructs. The high throughput production of controlled microtissues described in this thesis could provide the large quantities of microtissues necessary for these endeavors. Micro annealed particles (MAPs), which are large constructs of connected microparticles, can offer built-in vasculature because of the inherent empty space between the microparticles[37]. In an ongoing project, a proof-of-principle experiment was performed using PEG-TA microcapsules produced with the on-chip enzymatic outside-in crosslinking method as described in chapter 2 and 3. These PEG-TA microcapsules were injected in a mold and treated with ruthenium-based post-cure crosslink to connect the microcapsules to form PEG-TA MAPs. Combined with MIN6 encapsulation as discussed previously in the current chapter 7[1], this might enable immunoprotective, glucose-responsive MAPs for diabetes treatment.

As described in this thesis, microcapsules can function as a versatile system for the formation of a multitude of microtissues which can be used either to repair or replace biological tissues *in vivo*. This thesis focuses on use of single cell type tissues. Complexity of formed tissues can however be increased by modular biofabrication of tissues using multiple distinct cell types[22], utilizing different microtissue-types/microcapsule-materials for tissue engineering building blocks[38–40], or even

using different micromaterial morphologies such as the fibers described in chapter 2 and chapter 5.

An interesting prospect in tissue engineering is the engineering of artificial meat, which promises an alternative to animal products and its accompanied environmental impact. Although the first successfully studies are out[41,42], there are several challenges that need to be solved in order to provide feasible mass production. One of these challenges is the amount of cells and tissues that will be needed for the mass production of cultured meat in a highly cytocompatible manner[43]. Another challenge is the texture of the meat, and therefore different cell types, which are important for taste and thus the acceptance and adaptation towards cultured meat[44]. For both these challenges ultra-high throughput compartmentalized microtissue production might be an interesting technology because of the large quantities and the fact that separated microtissues can be easily assembled later in the desired architecture[45]. It is anticipated that microcapsule material, microcapsule size and microtissue size allow high level of control over texturization of these constructs.

## 7.4 Reflection on different microfluidic approached for continuous microtissue production

In chapter 1 of this thesis it is stated that clinical and industrial translation of 3D cell culture techniques such as microtissue culture is limited due to non-scalable production processes. While microfluidics allows for a continuous, and thus scalable, production process of microtissue-forming microcapsules, current state-of-the-art microfluidics remains to have limitations hindering clinical and industrial translation. In this thesis, two different microfluidic approaches for the production of microtissue-forming microcapsules are being introduced in order to overcome these limitations, being a PMMA microfluidic chip approach which operates in the dripping regime, and an in air microfluidic approach which operates in the jetting regime.

In contrast with conventional PDMS-based microfluidics[46–49], two platforms that are described in this thesis offer a cleanroom-free approach, which allows for more widespread availability. Furthermore, while conventional PDMS-based microfluidics are single-use, the here presented approaches are both reusable and off-the-shelf, which can contribute to limiting waste production. Moreover, utilizing the exchangeable nozzles in the PMMA-chip and the IAMF setup, multiple microcapsule size ranges can be produced using a single system, which is in stark contrast with conventional single-purpose PDMS-based microfluidic approaches. This is especially important in setting up systems that can universally be applied for different microtissue applications since the amount of cells per microtissue, which can easily be tuned by microcapsule size, which is commonly accepted as an important factor for microtissue performance.

However, although we successfully showed the universality of the PMMA microfluidic chip and the enzymatic outside-in crosslinking through the encapsulation of human mesenchymal stem cells (hMSCs), 3T3 fibroblasts, MIN6[1],

7

and cholangiocytes, we found that encapsulation of certain cell types will lead to inefficient microtissue formation, and it was observed that enzymatic outside-in crosslinking for microtissue-forming microcapsule production was not viable for bovine chondrocyte encapsulation in dextran-tyramine microcapsules. Instead of forming aggregates, it was observed that bovine chondrocytes often stick to the microcapsule shell causing deformation of the microcapsule or preventing aggregation altogether. We hypothesize that the high extracellular matrix (ECM) production of bovine chondrocytes[50] provides a larger amount of tyrosine groups at the outer cell layer compared to low ECM producing cells such as the previously described hMSCs, cholangiocytes and min6 cells. These tyramine groups are then possibly available for direct on-cell crosslinking (DOCKING)[51] of the dextran-tyramine and the bovine chondrocytes, preventing the migration and aggregation of bovine chondrocytes. If this hypothesis is deemed to be correct, temporary coatings[52] might lead to successful encapsulation of bovine chondrocytes. However, this challenge indicates that the enzymatic outside-in crosslinking method might need tuning for the encapsulation of some cell types. In contrast with enzymatic outside-in crosslinking, it is possible to prevent the before mentioned cell-shell attachment by utilizing ionic crosslinking-based IAMF, resulting in successful encapsulation of human chondrocytes for cartilage repair purposes as described in chapter 5.

Moreover, the PMMA microfluidic chip described in chapter 2 and 3 suffers some more limitations, which it has in common with conventional PDMS-based microfluidics, such as relative low throughput (<1 ml/min) and need for oil and surfactants. These wall-induced limitations are removed by transferring the droplet production process towards the described in air approach, resulting in a microfluidic approach, which allows for the fast and clean production of microtissue-forming microcapsules for clinical and industrial applications.

This does not say that the IAMF approach is the best solution for every application. While the confined nature of on-chip approaches requires the need for oil and surfactants and offer a more limited throughput, it also provides high control over the droplet production process. The loss of control in a wall-free setup is regained by microvibrations produced by a piezo-actuator[53]. However, although it was found that this is successful for non-granular liquids, the introduction of cells disrupts the monodisperse droplet production as is demonstrated in chapter 4 by the broadening of cell/microcapsule distribution at higher cell densities. Therefore, although the clean, ultra-high throughput nature of IAMF is a major advantage towards clinical and industrial application, the high degree of control of on-chip approaches might be beneficial for research applications where a limited quantity of highly controlled microtissues is needed such as drug discovery studies. It is anticipated that further research on the optimization of the IAMF hollow cell-laden microcapsule formation would be beneficial to gain greater control over the production of microcapsules when using granular liquids such as high density cell suspensions.

7

## 7.5 Remaining Challenges of High Throughput Microtissue Production

As previously stated, microtissue production rate is an important factor towards feasible clinical and industrial applications. However, it must be noted that for ultra-high production rates, as achievable with IAMF, there also is a need for high quantity of cells. In other words; without a sufficient amount cells, no microtissue production will take place. During work on this thesis, it was observed that conventional 2D culture is limited in terms of obtainable cell quantities. For example, in order to produce the cartilage tissues of chapter 5, approximately 860 cm² of culture area was needed to obtain the required number of cells. Therefore, in order to truly overcome the limitations hindering clinical and industrial translation of microtissue culture, and cell-based technologies in general, clinical/industrial scale cell culture techniques are needed. Dynamic bioreactors are often investigated for this purpose, with the first laboratory-scale bioreactors for cell culture now reaching the market. As stated in chapter 1, bioreactors often suffer from poor microtissue size control due to microtissue merging[54,55]. However, it might be interesting to utilize microcapsules in combination with bioreactors to obtain better microtissue size control and simplify the microcapsule culture process. As described previously in this chapter, microcapsules have the potential to overcome the challenges concerning microtissue polydispersity using bioreactors[36].

Finally, when microtissues are produced continuously with high throughput, high (continuous) screening capacity technologies are needed as well to further accelerate clinical and industrial translation of microtissues. Screening techniques currently mostly focus on multiwall formats[56]. However, continuous screening methods are needed for true scalability and clinical and industrial translation. Although the high-throughput method fluorescence activated cell sorting (FACS) is commonly used for single cell analysis, it has been utilized for microtissue analysis as well[57]. Microcapsule-cultured microtissues could help advance continuous microtissue analysis technology by functionalizing microcapsules with biochemical sensors. This could allow for rapid assays without the need for multi-step protocols after adding drug compounds[58]. Furthermore, commonly used cellular analysis methods are often designed for 2D monolayer cultures. For true transition from 2D to 3D there also needs to be a change of focus towards 3D microtissue assays[56].

## 7.6 Conclusion

In conclusion, this thesis introduces multiple microfluidic systems for scalable microcapsule and microtissue production with the aim to remove the hurdles towards clinical and industrial translation of cellular 3D microtissues. Regardless of the work that is still ahead, the work described in this thesis demonstrates that microcapsule technology has indeed the potential to overcome the translational

challenges for the use of cellular 3D microtissues in clinical and industrial environments.

## References

1. Araújo-Gomes, N. *et al.* Microfluidic Generation of Thin-Shelled Polyethylene Glycol-Tyramine Microgels for Non-Invasive Delivery of Immunoprotected β-Cells. *Adv. Healthc. Mater.* **n/a**, 2301552 (2023).
2. Fitzgerald, K. A., Malhotra, M., Curtin, C. M., O' Brien, F. J. & O' Driscoll, C. M. Life in 3D is never flat: 3D models to optimise drug delivery. *J. Control. Release* **215**, 39–54 (2015).
3. Hoffmann, O. I. *et al.* Impact of the spheroid model complexity on drug response. *J. Biotechnol.* **205**, 14–23 (2015).
4. Langhans, S. A. Three-Dimensional in Vitro Cell Culture Models in Drug Discovery and Drug Repositioning. *Frontiers in Pharmacology* **9**, (2018).
5. Friedrich, J., Seidel, C., Ebner, R. & Kunz-Schughart, L. A. Spheroid-based drug screen: considerations and practical approach. *Nat. Protoc.* **4**, 309–324 (2009).
6. Tung, Y.-C. *et al.* High-throughput 3D spheroid culture and drug testing using a 384 hanging drop array. *Analyst* **136**, 473–478 (2011).
7. Thoma, C. R., Zimmermann, M., Agarkova, I., Kelm, J. M. & Krek, W. 3D cell culture systems modeling tumor growth determinants in cancer target discovery. *Adv. Drug Deliv. Rev.* **69–70**, 29–41 (2014).
8. Edmondson, R., Broglie, J. J., Adcock, A. F. & Yang, L. Three-Dimensional Cell Culture Systems and Their Applications in Drug Discovery and Cell-Based Biosensors. *Assay Drug Dev. Technol.* **12**, 207–218 (2014).
9. Mosaad, E. O., Chambers, K. F., Futrega, K., Clements, J. A. & Doran, M. R. The Microwell-mesh: A high-throughput 3D prostate cancer spheroid and drug-testing platform. *Sci. Rep.* **8**, 253 (2018).
10. Shamir, E. R. & Ewald, A. J. Three-dimensional organotypic culture: experimental models of mammalian biology and disease. *Nat. Rev. Mol. Cell Biol.* **15**, 647 (2014).
11. Lancaster, M. A. & Knoblich, J. A. Organogenesis in a dish: modeling development and disease using organoid technologies. *Science* **345**, 1247125 (2014).
12. Dutta, D., Heo, I. & Clevers, H. Disease Modeling in Stem Cell-Derived 3D Organoid Systems. *Trends Mol. Med.* **23**, 393–410 (2017).
13. Clevers, H. Modeling Development and Disease with Organoids. *Cell* **165**, 1586–1597 (2016).
14. Beauchamp, P. *et al.* Development and Characterization of a Scaffold-Free 3D Spheroid Model of Induced Pluripotent Stem Cell-Derived Human Cardiomyocytes. *Tissue Eng. - Part C Methods* **21**, 852–861 (2015).
15. Shadrin, I. Y. *et al.* Cardiopatch platform enables maturation and scale-up of human pluripotent stem cell-derived engineered heart tissues. *Nat. Commun.* **8**, 1825 (2017).
16. Lin, H., Li, Q. & Lei, Y. Three-dimensional tissues using human pluripotent stem cell spheroids as biofabrication building blocks. *Biofabrication* **9**, 25007 (2017).
17. Shao, Y. *et al.* A pluripotent stem cell-based model for post-implantation human amniotic sac development. *Nat. Commun.* **8**, 208 (2017).
18. McCracken, K. W. *et al.* Modelling human development and disease in pluripotent stem-cell-derived gastric organoids. *Nature* **516**, 400–404 (2014).
19. Thavandiran, N. *et al.* Functional arrays of human pluripotent stem cell-derived cardiac microtissues. *Sci. Rep.* **10**, 6919 (2020).
20. Przepiorski, A. *et al.* A Simple Bioreactor-Based Method to Generate Kidney Organoids from Pluripotent Stem Cells. *Stem Cell Reports* **11**, 470–484 (2018).
21. Turhan, A. G. *et al.* iPSC-Derived Organoids as Therapeutic Models in Regenerative Medicine and Oncology . *Frontiers in Medicine* **8**, (2021).
22. Rivron, N. C. *et al.* Blastocyst-like structures generated solely from stem cells. *Nature* **557**, 106–111 (2018).
23. Jun, Y. *et al.* Microfluidics-generated pancreatic islet microfibers for enhanced immunoprotection. *Biomaterials* **34**, 8122–8130 (2013).
24. Balyura, M. *et al.* Transplantation of bovine adrenocortical cells encapsulated in alginate. *Proc. Natl. Acad. Sci.* **112**, 2527–2532 (2015).
25. Weaver, J. D. *et al.* Synthetic poly(ethylene glycol)-based microfluidic islet encapsulation reduces graft volume for delivery to highly vascularized and retrievable transplant site. *Am. J. Transplant.* **19**, 1315–1327 (2019).
26. Li, Z. *et al.* Injectable gelatin derivative hydrogels with sustained vascular endothelial growth

factor release for induced angiogenesis. *Acta Biomater.* **13**, 88–100 (2015).

27. Bae, S.-W., Kim, J. & Kwon, S. Recent Advances in Polymer Additive Engineering for Diagnostic and Therapeutic Hydrogels. *International Journal of Molecular Sciences* **23**, (2022).

28. Kamperman, T. *et al.* Steering Stem Cell Fate within 3D Living Composite Tissues Using Stimuli-Responsive Cell-Adhesive Micromaterials. *Adv. Sci.* **10**, 2205487 (2023).

29. Place, T. L., Domann, F. E. & Case, A. J. Limitations of oxygen delivery to cells in culture: An underappreciated problem in basic and translational research. *Free Radic. Biol. Med.* **113**, 311–322 (2017).

30. Cheng, G., Markenscoff, P. & Zygourakis, K. A 3D Hybrid Model for Tissue Growth: The Interplay between Cell Population and Mass Transport Dynamics. *Biophys. J.* **97**, 401–414 (2009).

31. Hinton, T. J. *et al.* Three-dimensional printing of complex biological structures by freeform reversible embedding of suspended hydrogels. *Sci. Adv.* **1**, e1500758 (2023).

32. Skylar-Scott, M. A. *et al.* Biomanufacturing of organ-specific tissues with high cellular density and embedded vascular channels. *Sci. Adv.* **5**, eaaw2459 (2023).

33. Bhattacharjee, T. *et al.* Liquid-like Solids Support Cells in 3D. *ACS Biomater. Sci. Eng.* **2**, 1787–1795 (2016).

34. Daly, A. C., Davidson, M. D. & Burdick, J. A. 3D bioprinting of high cell-density heterogeneous tissue models through spheroid fusion within self-healing hydrogels. *Nat. Commun.* **12**, 753 (2021).

35. Highley, C. B., Song, K. H., Daly, A. C. & Burdick, J. A. Jammed Microgel Inks for 3D Printing Applications. *Adv. Sci.* **6**, 1801076 (2019).

36. Schot, M., Araújo-Gomes, N., van Loo, B., Kamperman, T. & Leijten, J. Scalable fabrication, compartmentalization and applications of living microtissues. *Bioact. Mater.* **19**, 392–405 (2023).

37. Griffin, D. R., Weaver, W. M., Scumpia, P. O., Di Carlo, D. & Segura, T. Accelerated wound healing by injectable microporous gel scaffolds assembled from annealed building blocks. *Nat. Mater.* **14**, 737–744 (2015).

38. Daly, A. C. & Kelly, D. J. Biofabrication of spatially organised tissues by directing the growth of cellular spheroids within 3D printed polymeric microchambers. *Biomaterials* **197**, 194–206 (2019).

39. Anada, T., *et al.* Vascularized Bone-Mimetic Hydrogel Constructs by 3D Bioprinting to Promote Osteogenesis and Angiogenesis. *Int. J. Mol. Sci.* **20**, (2019).

40. Machino, R. *et al.* Replacement of Rat Tracheas by Layered, Trachea-Like, Scaffold-Free Structures of Human Cells Using a Bio-3D Printing System. *Adv. Healthc. Mater.* **8**, e1800983 (2019).

41. Furuhashi, M. *et al.* Formation of contractile 3D bovine muscle tissue for construction of millimetre-thick cultured steak. *npj Sci. Food* **5**, 6 (2021).

42. Post, M. J. Cultured beef: medical technology to produce food. *J. Sci. Food Agric.* **94**, 1039–1041 (2014).

43. Post, M. J. Cultured meat from stem cells: Challenges and prospects. *Meat Sci.* **92**, 297–301 (2012).

44. Bodiou, V., Moutsatsou, P. & Post, M. J. Microcarriers for Upscaling Cultured Meat Production . *Frontiers in Nutrition*  **7**, (2020).

45. Lanza, R., Langer, R., Vacanti, J. P. & Atala, A. *Principles of tissue engineering*. (Academic press, 2020).

46. Okushima, S., Nisisako, T., Torii, T. & Higuchi, T. Controlled Production of Monodisperse Double Emulsions by Two-Step Droplet Breakup in Microfluidic Devices. *Langmuir* **20**, 9905–9908 (2004).

47. Nisisako, T., Okushima, S. & Torii, T. Controlled formulation of monodisperse double emulsions in a multiple-phase microfluidic system. *Soft Matter* **1**, 23–27 (2005).

48. Seo, M., Paquet, C., Nie, Z., Xu, S. & Kumacheva, E. Microfluidic consecutive flow-focusing droplet generators. *Soft Matter* **3**, 986–992 (2007).

49. Chang, F.-C. & Su, Y.-C. Controlled double emulsification utilizing 3D PDMS microchannels. *J. Micromechanics Microengineering* **18**, 65018 (2008).

50. Callahan, L. A. S. *et al.* ECM production of primary human and bovine chondrocytes in hybrid PEG hydrogels  containing type I collagen and hyaluronic acid. *Biomacromolecules* **13**, 1625–1631 (2012).

51. Kamperman, T. *et al.* Tethering Cells via Enzymatic Oxidative Crosslinking Enables Mechanotransduction in Non-Cell-Adhesive Materials. *Adv. Mater.* **33**, 2102660 (2021).

52. Davis, K. A. *et al.* Coatings on mammalian cells: interfacing cells with their environment. *J. Biol. Eng.* **13**, 5 (2019).

53. Visser, C. W., Kamperman, T., Karbaat, L. P., Lohse, D. & Karperien, M. In-air microfluidics enables rapid fabrication of emulsions, suspensions, and 3D modular (bio)materials. *Sci. Adv.* **4**, (2018).

54. Sumi, S. *et al.* A multiple-funnels cell culture insert for the scale-up production of uniform cell spheroids. *Regen. Ther.* **7**, 52–60 (2017).

55. Allen, L. M., Matyas, J., Ungrin, M., Hart, D. A. & Sen, A. Serum-Free Culture of Human Mesenchymal Stem Cell Aggregates in Suspension Bioreactors for Tissue Engineering Applications. *Stem Cells Int.* **2019**, 4607461 (2019).

56. Mehta, G., Hsiao, A. Y., Ingram, M., Luker, G. D. & Takayama, S. Opportunities and challenges for use of tumor spheroids as models to test drug  delivery and efficacy. *J. Control. release Off. J. Control. Release  Soc.* **164**, 192–204 (2012).

**7**

57. Durand, R. E. & Olive, P. L. Evaluation of bioreductive drugs in multicell spheroids. *Int. J. Radiat. Oncol. Biol. Phys.* **22**, 689–692 (1992).
58. Battista, E., Causa, F. & Netti, P. A. Bioengineering Microgels and Hydrogel Microparticles for Sensing Biomolecular Targets. *Gels* **3**, (2017).

7

# Acknowledgements

Nu mijn PhD tijdperk in Enschede er bijna op zit is het duidelijk dat dit proefschrift er niet had gelegen zonder de hulp van anderen. Ik wil dan ook graag iedereen bedanken die me ofwel direct maar vooral ook indirect heeft geholpen tijdens deze tijd.

Ten eerste wil ik Jeroen bedanken voor het bieden van de kans om dit PhD traject te starten, en alles waar dit toe heeft geleid. Zoals gezegd tijdens een van onze meetings; groeien doet pijn. Maar ik ben vooral heel erg dankbaar voor de grote hoeveelheid aan lessen die deze groei op zowel persoonlijk als op professioneel vlak mogelijk heeft gemaakt en me heeft gebracht tot waar ik nu sta. Hier zal ik je altijd dankbaar voor blijven.

Daarnaast wil Marcel bedanken voor de mooie tijd bij de vakgroep. Vooral ook voordat ik het PhD traject in ging voor je kookkunsten tijdens de student-assistent BBQs. Daarbij wil ik vooral ook Janneke bedanken voor deze tijd als student-assistent. Het starten met het student-assistentschap is voor mij een belangrijk moment geweest in de richting van mijn professionele pad (en indirect de focus van bier op de kroeg  heeft verlegd naar wat er daarna allemaal te wachten staat). Hier ben ik je nog altijd erg dankbaar voor.

Voor al het labwerk dat nodig is geweest om tot dit proefschrift te komen is in eerste instantie een lab nodig om gebruik van te maken. Hier wil ik vooral Jacqueline en Irene voor bedanken. De data in deze thesis is mogelijk gemaakt door het werk wat jullie in de laboratoria stoppen. Zonder jullie was de Zuidhorst al 22x afgebrand. Daarbij wil ik ook graag Ingrid bedanken voor het blussen van alle administratieve brandjes en alle hulp die daarbij komt kijken.

Dan de Powergroup. Maik, Melvin, Malin, Carlo en later ook Nuno, ontzettend bedankt voor de ontzettend mooie tijd. Van onze Barcelona trip tot alle borrels, feestjes en etentjes, de tijd met jullie is wat me het meest bijblijft aan de PhD tijd. In tijden waar het trappen van dozen me nader stond dan het lachen heb ik altijd op jullie kunnen rekenen om me er weer bovenop te krijgen. Ik vind het heel mooi hoe we van collega's tot vriendengroep zijn gegroeid, en ik ben blij om te weten dat we elkaar nog lang na onze PhD tijd zullen zien. Bedankt voor alles.

Uiteraard wil ik ook alle andere collega's bedanken voor alles. Tom, ik ben heel dankbaar voor alle lessen die ik van jou heb geleerd. Het was erg prettig om in het begin van de PhD veel met je op te trekken in het lab. Jij staat aan de basis van alle technieken die in dit proefschrift beschreven staan, en je hulp is altijd zeer gewaardeerd. Ik vind het mooi om te zien hoe je aan de weg timmert met je bedrijf, en wens je al het succes mee voor de toekomst. Jan, bedankt voor het regelen van alle borrels. Ik weet dat je me graag als opvolger chef-borrel

had gezien, en ik hoop dat je het me kan vergeven dat ik die rol binnen de vakgroep nooit helemaal waar heb kunnen maken. Wesley, met wie samen met Maik vele lake-breaks zijn gedaan om even bij te komen van al onze lab avonturen. Daarnaast ook een speciaal bedankje voor de collega's van de ESB ~~Porto~~ Zeeland 2021 groep met onder andere Castro, Marieke, Minye, Francisca. In tijden van Covid-19 zonder internationale conferenties was het een hele leuke ervaring om met zijn allen in Zeeland onze eigen conferentie op te zetten.

Alle andere collega's van DBE, maar ook van AST, wil ik graag bedanken voor de gezelligheid tijdens lunches, in de coffeecorner, tijdens de kerstborrels, en in het celkweeklab. Gedeelde smart is halve smart. En in tijden wanneer cellen weer eens besloten om niet mee te werken aan een experiment heb ik toch kunnen genieten van de galgenhumor met jullie allemaal in het celkweeklab.

Ik wil ook alle co-auteurs bedanken voor de fijne samenwerkingen. Simone, ik heb de samenwerking met jou altijd als erg prettig ervaren. Het heeft allemaal even geduurd, maar ik ben trots op het resultaat wat we hebben neergezet. Ik denk dat jij het qua baan het beste voor elkaar hebt van de hele Zuidhorst. Jorke, ik wil jou graag bedanken voor de meest efficiënte samenwerking ooit. Na samen ooit begonnen te zijn aan de bachelor vond ik het ontzettend mooi om na al die Zeezuipers in de Beiaard, fototripjes en gesprekken aan de keukentafel samen een artikel te publiceren.

Als je zo gefocust bent op een langdurig project als een PhD is het belangrijk om dit ook af en toe los te kunnen laten. Hiervoor wil ik graag de leden van Filosofisch Dispuut Panta Rhei bedanken, die me hier al dan niet bewust mee hebben geholpen. De brakke vrijdagen in het lab waren soms een extra uitdaging, maar ik had ze voor geen goud willen missen. Daarnaast de jongens van de "Chippendales lounge" voor de vele feestjes, tripjes en goede gesprekken, met in het speciaal Rutger voor de hulp met het coverdesign waar nog net genoeg tijd voor was naast het racen.

Mijn paranymphs Maik en Tom, met wie ik respectievelijk tijdens studie en dispuutstijd veel heb meegemaakt, maar met wie ik beide ook een mooie tijd in de Zuidhorst heb beleefd. In die zin zijn jullie als paranymphs een mooie samenvatting van mijn tijd in Enschede. Een tijd waar ik met heel veel plezier op terugkijk, en jullie heel erg voor wil bedanken.

Uiteraard is dit ook het moment om mijn familie te bedanken voor alles. Ik wil mijn ouders Sjaak en Marike en broer Tim bedanken voor alle steun door de jaren heen. Het is na al die tijd toch fijn om te zien dat die hulp met wiskunde sommetjes aan de eettafel zijn vruchten heeft afgeworpen. Bedankt voor het zijn wie jullie zijn en alle lessen die jullie mij hebben meegegeven.

Een dankwoord voor een proefschrift is geen dankwoord voor een proefschrift als het niet eindigt met degene die de grootste prestatie heeft geleverd, namelijk degene die constant naar al het gezeur over de PhD heeft moeten luisteren. Suus, ik ben ontzettend dankbaar voor alle steun en liefde die ik van je mag ontvangen. Als er iemand is die me er doorheen heeft gesleept ben jij het, en daar ben ik je enorm dankbaar voor. Nu dit hoofdstuk eindelijk afgesloten is kan de blik weer naar de toekomst, en ik heb ongelooflijk veel zin in ons nieuwe gezamenlijke biomedische project.

Bedankt iedereen.

Bas

# Biography

Sebastiaan Robert (Bas) van Loo was born on the 13th of January in Apeldoorn, The Netherlands. In 2011 he received his diploma for pre-university education (VWO) with a dual specialization (Nature & Technology and Nature & Health) from Veluws College Walterbosch in Apeldoorn, The Netherlands. In 2011, he started Biomedical Engineering at the University of Twente, The Netherlands. Here he worked as a student assistant from 2014 till 2018, assisting courses and practicals in subjects such as cell culture, microscopy and polymer synthesis. In 2015 he defended his Bachelor thesis on the subject of lipodomics in osteoarthritis under supervision of Brenda Bakker and Marcel Karperien at the department of Developmental BioEngineering within the Technical Medical Centre at the University of Twente. During this project, his interests for 3D cell culture methods started to emerge. After an internship where he briefly taught chemistry in pre-university education (VWO) at the Bonhoeffer College in Enschede, The Netherlands, he continued to work on the subject of 3D cell culture during an internship at FUJIFILM Tilburg, The Netherlands under the supervision of Dr. Bas Kluijtmans. Here he focused on the formation of a cell-viable hydrogel out of recombinant peptides, focusing on the chemistry behind the formation of 3D cell culture platforms. In 2018 he defended his Master thesis on the subject of cell-shrinkage induced molecular crowding under supervision of Dr. Jeroen Leijten at the department of Developmental BioEngineering at the University of Twente. After successfully defending the thesis, he immediately started his PhD training under the supervision of Jeroen Leijten at the department of Developmental BioEngineering at the University of Twente. During his PhD training, he combined his interests in 3D cell culture with microfluidics, which resulted in several microfluidic platforms for cellular microaggregate/organoid culture applications. His work was awarded twice with poster awards at the Netherlands society for Biomaterials and Tissue Engineering (NBTE) conferences in 2018 and 2019.
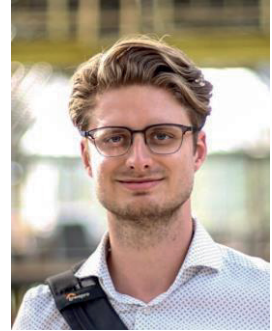
# Scientific Output

## Peer-reviewed Papers

1. **Van Loo SR**\*, Kamperman T**\***, Gurian M, Henke S, Karperien M and Leijten J. On-the-fly exchangeable microfluidic nozzles for facile production of various monodisperse micromaterials. *Published in Lab on a Chip, 2019, DOI: 10.1039/C9LC00054B, Impact Factor 6.8.*

2. **Van Loo SR**, Salehi SS, Henke S, Shamloo A, Kamperman T, Karperien M, and Leijten, J. Enzymatic outside-in cross-linking enables single-step microcapsule production for high-throughput three-dimensional cell microaggregate formation. *Published in Materials Today Bio, 2020, DOI: 10.1016/j.mtbio.2020.100047, Impact Factor 7.3.*

3. **Van Loo SR**\*, van Tienderen GS\*, Willemse J\*, van Hengel EVA, de Jonge J, van der Laan LJW, Leijten J, and Verstegen MMA. Scalable Production of Size-Controlled Cholangiocyte and Cholangiocarcinoma Organoids within Liver Extracellular Matrix-Containing Microcapsules. *Published in Cells, 2022, DOI: 10.3390/cells11223657, Impact Factor 6.0.*

4. **Van Loo SR**, ten Den SA, Araújo-Gomes N, de Jong V, Snabel RR, Schot M, Rivera-Arbeláez JM, Veenstra GJC, Passier R, Kamperman T, and Leijten J. Mass Production of Lumenogenic Human Embryoid Bodies and Functional Cardiospheres using In Air Generated Microcapsules. *Published in Nature Communications, 2023, DOI: 10.1038/s41467-023-42297-0, Impact Factor: 16.6.*

5. **Van Loo SR**, Schot M, Gurian M, Kamperman T, and Leijten J. Single-step biofabrication of in situ spheroid-forming compartmentalized hydrogel for clinical sized cartilage tissue formation. *Published in Advanced Healthcare Materials, 2023, DOI: 10.1002/adhm.202300095, Impact Factor: 11.1.*

6. Schot M, Araújo-Gomes N, **van Loo SR**, Kamperman T, and Leijten J. Scalable fabrication, compartmentalization and applications of living microtissues. *Published in Bioactive Materials, 2023, DOI: 10.1016/j.bioactmat.2022.04.005, Impact Factor 18.9.*

7. Araújo-Gomes N, Zoetebier-Liszka B, **van Loo SR**, Becker M, Nijhuis S, Smink AM, de Haan BJ, de Vos P, Karperien M, and Leijten J. Microfluidic Generation of Thin-Shelled Polyethylene Glycol-Tyramine Microgels for Non-Invasive Delivery of Immunoprotected β-Cells. *Published in Advanced Healthcare Materials, 2023, DOI: 10.1002/adhm.202301552, Impact Factor: 11.1.*

8. Johnbosco C, Karbaat L, Korthagen N, Warmink K, Koerselman M, Coeleveld K, Becker M, Zoetebier B, **Van Loo SR**, Both S, Karperien M, Leijten J. Microencapsulated stem cells reduce cartilage damage in a material dependent manner following minimally invasive intra-articular injection in an

OA rat model. *Published in Materials Today Bio, 2023, DOI: 10.1016/j.mtbio.2023.100791. Impact Factor: 8.5.*

**\* Co-first authorship**

## Conference Abstracts (<u>presenter</u>; non-exhaustive list)

1. <u>**S.R. van Loo**</u>, S. Salehi, T. Kamperman, S. Henke, M Gurian, M. Karperien, and J. Leijten. Microfluidically generated hollow microgels enable high throughput production of micro-aggregates. *Annual Netherlands society for Biomaterials and Tissue Engineering (NBTE) meeting, 2018, Lunteren, The Netherlands.*

2. <u>**S.R. van Loo**</u>, S. Henke, T. Kamperman, M. Karperien, and J. Leijten. Enzymatic Outside-In Crosslinking Enables Single-Step Hollow Core-Shell Microgel Production for Controlled High Throughput Aggregate Formation. *Annual Netherlands society for Biomaterials and Tissue Engineering (NBTE) meeting, 2019, Lunteren, The Netherlands.*

3. <u>**S.R. van Loo**</u>, Nuno Araújo-Gomes, Vincent de Jong, Tom Kamperman, and Jeroen Leijten. Ultra-High Throughput Production of Hollow Micromaterials by In-Air Microfluidics for Tissue Engineering Applications. *Annual Netherlands society for Biomaterials and Tissue Engineering (NBTE) meeting, 2020, Lunteren, The Netherlands.*

4. <u>**S.R. van Loo**</u>, Nuno Araújo-Gomes, Vincent de Jong, Tom Kamperman, and Jeroen Leijten. Ultra High Throughput Production of Hollow Micromaterials by In-Air Microfluidics for Tissue Engineering Applications. *World congress of the Tissue Engineering and Regenerative Medicine International Society (TERMIS), 2021, Maastricht, The Netherlands.*

5. <u>**S.R. van Loo**</u>, Nuno Araújo-Gomes, Simone ten Den, Vincent de Jong, Robert Passier, Marcel Karperien, Tom Kamperman, and Jeroen Leijten. Ultra-High Throughput Production of Human Cardiac Organoids using In-Air Microfluidics generated Hollow Core-Shell Microgels. *Conference of the European Society for Biomaterials (ESB), 2021, Porto, Portugal.*

6. <u>**S.R. van Loo**</u>, Nuno Araújo-Gomes, Simone ten Den, Vincent de Jong, Robert Passier, Marcel Karperien, Tom Kamperman, and Jeroen Leijten. Ultra-High Throughput Production of Human Cardiac Organoids using In-Air Microfluidic generated Hollow Core-Shell Microcapsules.

7. <u>N. Araújo-Gomes</u>, B.M. Liszka-Zoetebier, **S.R. van Loo**, S. Nijhuis, T. Kamperman, P. de Vos, A.M. Smink, B. de Haan, M. Karperien, and J. Leijten. High-Throughput Production of Polyethylene Glycol-Tyramine Microcapsules for Non-Invasive Delivery of Immunoprotected Beta Cells. *Conference of the European Society for Biomaterials (ESB), 2021, Porto, Portugal. Annual Netherlands society for*

*Biomaterials and Tissue Engineering (NBTE) meeting, 2021, Lunteren, The Netherlands.*

8. <u>N. Araújo-Gomes</u>, B.M. Liszka-Zoetebier, **S.R. van Loo**, S. Nijhuis, T. Kamperman, P. de Vos, A.M. Smink, B. de Haan, M. Karperien, and J. Leijten. Generation of Immunoprotective and Enzymatically Crosslinked Polyethylene Glycol-Tyramine Microcapsules for Beta-cell Delivery using Microfluidics. *Annual Netherlands society for Biomaterials and Tissue Engineering (NBTE) meeting, 2020, Lunteren, The Netherlands.*

9. <u>Nuno Araújo-Gomes</u>, Barbara Liszka, **S.R. van Loo**, Suzanne Nijhuis, Tom Kamperman, Marcel Karperien, and Jeroen Leijten. Microfluidic Generation of Immunoprotective and Enzymatically Crosslinked Ultra-Thin Polyethylene Glycol-Tyramine Microcapsules for Minimally Invasive Delivery of Beta Cells. *World congress of the Tissue Engineering and Regenerative Medicine International Society (TERMIS), 2021, Maastricht, The Netherlands.*

10. <u>Barbara Zoetbier-Liszka</u>, **S.R. van Loo**, Marcel Karperien, and Jeroen Leijten. Microfluidic Generation of Enzymatically Crosslinked Ultrathin Polyethylene Glycol-Tryamine Microcapsules for Minimally Invasive Delivery of Immunoprotected Beta Cells. *World Biomaterials Congress, 2020, Glasgow, Scotland.*

# Awards

1. NBTE Poster Award (2018) at the *Annual Netherlands society for Biomaterials and Tissue Engineering (NBTE) meeting, 2018, Lunteren, The Netherlands.*

2. NBTE Poster Award (2019) *Annual Netherlands society for Biomaterials and Tissue Engineering (NBTE) meeting, 2019, Lunteren, The Netherlands.*

# Teaching and Supervision

## Courses

2018-2019   BMT M5, Tutor, lecturer and practical instructor.

BMT M2, Practical instructor.

2019-2020   BMT M5, Tutor and practical instructor.

2020-2021   BMT M5, Tutor and practical instructor.

## Students

1. Martijn Kern (2018). Increased molecular crowding in 3D micro-aggregates: Mechanism and biological effects. MSc.

2. Marieke Meteling (2019). Unravelling the mechanisms behind microaggregate shrinkage. MSc.

3. Ceri-Anne Suurmond (2020). Characterizing the effect of 3D cellular aggregate size on cell shrinkage, molecular crowding, and cellular functionality. MSc.

4. Marlize Kramer (2021). Cartilage formation in microcapsules. BSc.

# Public Outreach

1. Presentation at ReumaNederland Developmental BioEngineering Centre of Excellence open day (2019). Celtherapie voor behandeling van kraakbeendefecten.